UNIVERSITY OF SOUTHAMPTON

Faculty of Engineering and the Environment

Energy Technology Research group

Heteropolyacids and non-carbon electrode materials for fuel cell and battery applications

by

Maria Kourasi

Thesis for the degree of Doctor of Philosophy

February 2015

UNIVERSITY OF SOUTHAMPTON

ABSTRACT

FACULTY OF ENGINEERING AND THE ENVIRONMENT

Doctor of Philosophy

HETEROPOLYACIDS AND NON-CARBON ELECTRODE MATERIALS FOR FUEL CELL AND BATTERY APPLICATIONS

by Maria Kourasi

Heteropolyacids (HPAs) are a group of chemicals that have shown promising results as catalysts during the last decades. Since HPAs have displayed encouraging performance as electrocatalysts in acidic environment, in this project their redox activity in acid and alkaline aqueous electrolytes and their electrocatalytic performance as additives on a bifunctional gas diffusion electrode in alkaline aqueous electrolyte are tested.

The results from the electrochemical characterisation of two different HPAs, the phosphomolybdic acid (PMA) and the phosphotungstic acid (PWA) dissolved in acidic and alkaline environment showed that both heteropolyacids demonstrate a redox activity but they also suffer from low stability issues.

A series of gas diffusion electrodes were manufactured having PMA and PWA incorporated in their catalyst layer. The electrode support was carbon Toray paper and each heteropolyacid was mixed with Ni to create the catalyst layer of the electrode. From the electrochemical characterisation oF these electrodes in alkaline electrolyte, it was shown that the addition of HPAs enhances the activity of the nickel towards OER and ORR.

During the constant current measurements on the manufactured gas diffusion electrodes it was noticed that the electrodes fail after a period of time which could be attributed to the corrosion of the carbon support. In order to find alternative, non-carbon materials to be used as the electrode support, electrochemical characterisation on Magnéli phase bulk materials, Magnéli spray coated electrodes and PVD coated electrodes was performed.

The results from this investigation showed that Magnéli phase materials can support electron transfer reactions but their electron conductivity is rather low and it needs to be enhanced. Additionally, it was presented that the Magnéli coating protects the substrate over the potential region where OER and ORR take place. Hence, Magnéli materials could be used as a support for the bifunctional HPA gas diffusion electrodes.

Contents

List of Figures

List of Tables

Declaration of Authorship

I, Maria Kourasi, declare that the thesis entitled *Heteropolyacids and non-carbon electrode materials for fuel cell and battery applications* and the work presented in the thesis are both my own, and have been generated by me as the result of my own original research. I confirm that:

- this work was done wholly or mainly while in candidature for a research degree at this University;
- where any part of this thesis has previously been submitted for a degree or any other qualification at this University or any other institution, this has been clearly stated;
- where I have consulted the published work of others, this is always clearly attributed;
- where I have quoted from the work of others, the source is always given. With the exception of such quotations, this thesis is entirely my own work;
- I have acknowledged all main sources of help;
- where the thesis is based on work done by myself jointly with others, I have made clear exactly what was done by others and what I have contributed myself;
- parts of this work have been published as:

  1. R. G. A. Wills, **M. Kourasi**, A. A. Shah, and F. C. Walsh, "Molybdophosphoric acid based nickel catalysts as bifunctional oxygen electrodes in alkaline media", Electrochemistry Communications, vol. 22, pp. 174-176, 2012.
  2. M. Gardon, S. Dosta, J. M. Guilemany, **M. Kourasi**, B. Mellor, and R. Wills, "Improved, high conductivity titanium sub-oxide coated electrodes obtained by Atmospheric Plasma Spray", Journal of Power Sources, vol. 238, pp. 430-434, 2013.
  3. **M. Kourasi**, R.G.A. Wills, A.A. Shah and F.C. Walsh, "Heteropolyacids for fuel cell applications", Electrochimica Acta, vol. 127, pp. 454-466, 2014

Signed:.....

Date:.....

Acknowledgements

Foremost, I would like to thank my PhD supervisor, Dr Richard Wills. He has been guiding me and supporting me more than I would expect for the last three years and I would not have been able to accomplish this important step in my life and career, if he wasn't there for me. Dr Akeel Shah is another person that I would like to thank, because he had supported me when I was his MSc project student and he had believed in me. Additionally, I should aknowledge the financial support of the Faculty of Engineering and the Environment at the University of Southampton for funding of my PhD.

Additionally, I would like to thank Dr Dmitry Bavykin for his very constructive comments and feedback during 9 month and 18 month assessment of my project. I would also like say thank you to Dr Carlos Ponce de Leon Albarann for selecting me to be his teaching assistant during the third year of my PhD, since it was something that I have really enjoyed and also because it has helped me to understand a bit more about how academia works. A big thank you must go to the technicians from the Glassblowing facility and the Chemistry faculty for providing me with equipment which was essential for my research.

At this point, I would like to say thank you to a number of colleagues and friends who helped me either by their technical suggestions or their psychological support throughout these three years of my PhD project. Rachel, Derek, Krishna, Scott, Mihaela, Irene, Recep, Luis Fernando, Ruben, Badr, I would like to thank you for your valuable help and support in the lab and in the office mostly during the last few months of my PhD. Gogo and Gianni, you know that words are not enough to express my gratitude for everything you have done for me the last years and I promise that I will never forget it, thanks. A big thanks goes also to all my lovely housemates and friends, Vassili, Lauren, Gisela, Marco, Hugh, Hannah and Vera who made me feel like being at home.

Last and of course not least, a great thank you to my wonderful parents and sister who even if they were many miles away from me, they were always trying to support me with any means they had. Efharisto poli.

Nomenclature

ABPI poly (2,5-benzimidazole)

APS atmospheric plasma spray

BET Brunauer Emmett Teller

CHP combined heat and power systems

CNT carbon nanotube

CV cyclic voltammetry

DAFC direct alcohol fuel cell

DEFC direct ethanol fuel cell

DFT density functional theory

DME dimethyl ether

DMFC direct methanol fuel cell

DTPA diethylenetriaminepentaacetic acid

EDX energy dispersion x-ray

FC fuel cell

GCE glass carbon electrode

GDE gas diffusion electrode

GDL gas diffusion layer

GNF graphite carbon nanofiber

GNS graphene nanosheet

GPTMS 3-glycidoxypropyl-trimethoxysilane

HER hydrogen evolution reaction

HFP hexafluoropropylene

HPA heteropolyacid

ICR interfacial contact resistance

IPA isopolyacid or isopropyl alcohol

MCM-41 mobil composition of matter No. 41

MEA membrane electrode assembly

MOR methanol oxidation reaction

MWCNT multi-walled carbon nanotube

NHE normal hydrogen electrode

OCV open circuit voltage

OER oxygen evolution reaction

ORR oxygen reduction reaction

PA proton affinity

PAM poyacrylamide

PANI polyaniline

PBI polybenzimidazole

PEG polyethylene glycol

PEI polyethyleneimine

PEK poly(etherketones)

PEM polymer electrolyte or exchange membrane

PEMFC proton exchange membrane fuel cell

PEO polyethylene oxide

PES polyehtersulfone

PFSA perfluorosulfonic acid

PG pyrolytic graphite

PMA phosphomolybdic acid, $H_3PMo_{12}O_{40}$

POM polyoxometallate

PPO polyphenylene oxide

PPSS poly(phenylene sulfide sulfone)

PTFE polytetrafluoroethylene

PVA polyvinylacetate

PVACO polyvinyl alcohol-co-vinyl acetate-co-itaconic acid

PVD physical vapour deposition

PVDF polyvinylidenedifluoride

PWA phosphotungstic acid, $H_3PW_{12}O_{40}$

RDE ring disc electrode

RE reference electrode

RFC regenerative fuel cell

SCE saturated calomel electrode

SEM scanning electron microscopy

SHE standard hydrogen electrode

SPAEK sulfonated poly(arylene ether ketone)

SPAENK sulfonated poly(arylene ether nitrile ketone)

SPAES sulfonated poly(arylene ether sulfone)

SPEEK sulfonated poly(ether-ether ketone)

SPEK sulfonated polyetherketone

SPES sulfonated polyethersulfone

SPI sulfonated polyimides

SPSF solfunated polysulfone

STM scanning tunelling microscopy

TS tunnelling spectroscopy

URFC unitised regenerative fuel cell

WE water electrolyser or working electrode

XRD x-ray diffraction

Chapter 1

Introduction

1.1 Background and motivation

After the establishment of renewable energy sources, such as solar power and wind power, the need of more efficient and less polluting energy storage devices has been increased [3]. An example of this necessity can be confirmed by the content of the *2030 Framework for Climate and Energy* which was approved by the European Council in October 2014 [4]. According to this framework, some of the targets that are to be accomplished by 2030 are that the 27% of the energy which is used in EU level has to come from renewable sources and that the greenhouse gas emissions have to be reduced by 40% compared to the records from 1990 [4].

Fuel cells and metal-air batteries are believed to be some of the devices that satisfy some of the energy storage requirements, such as high energy density, environmentally friendly and low cost [5, 6]. Their operation is based on the conversion of electrochemical energy into electric energy. Electrochemical oxidation (positive electrode) and reduction (negative electrode) take place in the electrochemical device that lead to a current flow in the external circuit.

The main operational difference between fuel cells and batteries is that fuel cells consume fuels that are continuously supplied to the cell, whereas batteries use a finite quantity of reactants which are incorporated in them. Hence, unlike batteries, the electric energy that a fuel cell produces depends primarily on the reactant supply.

Fuel cells exhibit high efficiencies, high power densities and zero harmful emissions, facts that make them suitable for a great variety of applications. Generally, they

can be used in hydrogen transportation, combined heat and power systems (CHP), emergency power systems, portable applications, as well as space applications. The most common fuel cell design is the polymer electrolyte membrane fuel cell (PEMFC) which uses hydrogen gas at the positive electrode and oxygen at the negative electrode as reactants near ambient temperatures. Additionally, there are fuel cells that use methanol, called direct methanol fuel cells (DMFC) or ethanol, the direct ethanol fuel cells (DEFC), alternatively to hydrogen. The fuel which is supplied to the positive electrode (anode) is usually stored in tanks close to the fuel cell but oxygen, which is used at the negative electrode (cathode) can be received from ambient air.

The above fuel cell designs can produce energy as long as the reactants are fed in the cell. However, there is a fuel cell design, the regenerative fuel cells (RFC), which both supply and store electric energy. Two different operations take place in these fuel cells; the fuel cell (FC) mode and the water electrolyser (WE) mode. Hydrogen and oxygen are consumed to produce electricity during the FC mode, and during the WE mode, electricity is consumed while hydrogen and oxygen are produced and consecutively stored in tanks outside the cell. The two different operations (FC and WE mode) take place either in separate compartments or in a single system depending on their design. The fuel cells that combine both different operation modes in the same cell are called unitised regenerative fuel cells (URFC).

There are two different designs of URFCs. In the first design, the electrodes of the fuel cell do not change their redox function when the operation mode changes [7]. Hence, one electrode operates as the anode, where oxygen evolution and hydrogen oxidation take place, and the other electrode operates as the cathode, where hydrogen evolution and oxygen reduction take place, during both operational modes (figure 1.1).

In the second URFC design, two different electrodes, a hydrogen and an oxygen electrode are operating in the cell [8]. Specifically, hydrogen evolution and oxidation take place at one electrode (hydrogen electrode) and oxygen evolution and reduction take place at the other electrode (oxygen electrode) (figure 1.2). Both hydrogen and oxygen electrodes in this cell are bifunctional electrodes which means that one electrode can operate during both the oxidation and the reduction of the same species.

Except of URFCs, another electrochemical device that incorporates an oxygen/air electrode is the metal-air battery. There are two types of metal-air batteries, the

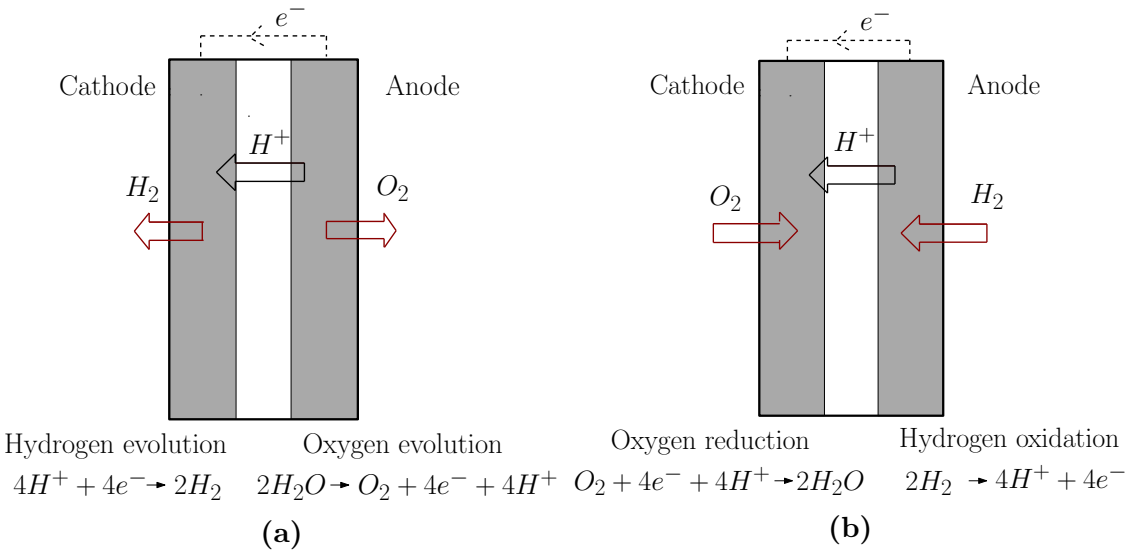

Figure 1.1: *Schematic of a URFC in (a) water electrolyser mode and in (b) fuel cell mode (Design 1).*

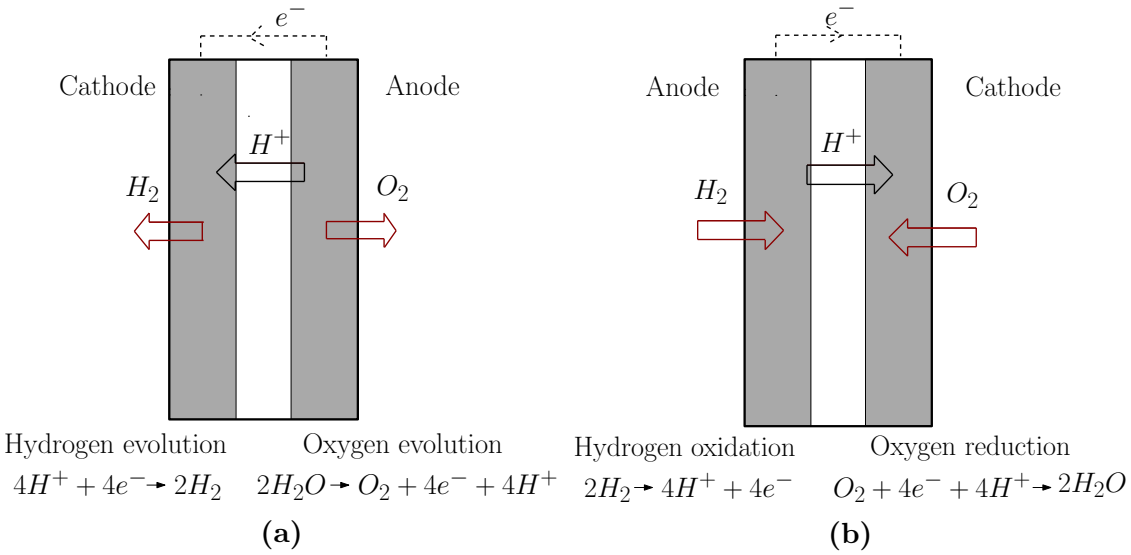

Figure 1.2: *Schematic of a URFC in (a) water electrolyser mode and in (b) fuel cell mode (Design 2).*

primary and the secondary metal-air batteries. The primary batteries are the batteries that can only produce energy, while secondary or rechargeable batteries are the batteries which can also store energy. Hence, fuel cells and primary metal-air batteries can discharge during their operation, while URFCs and secondary metal-air batteries include both discharging and charging functions.

The other electrode in the secondary metal-air batteries is a metal electrode. During the battery discharging, O_2/air is reduced, while the metal at the anode is oxidised and then dissolved in the electrolyte [9]. The battery is then charged, by supplying electrical current back to the battery, so the initial reactants are regenerated. The electrolyte that is commonly used in metal-air batteries is aqueous alkaline electrolyte due to two factors. Primarily, the performance of the bifunctional oxygen electrode is improved in alkaline environment and secondly, the corrosion of the metal electrodes can be limited [10].

Metal-air batteries display high specific energy since ambient air is used as a reactant and the materials that are used at the alternate electrode are light metals, such as zinc, iron, aluminium, magnesium, and lithium [11, 5]. According to Neburchilov et al. (2010), one of the most costly but also significant components for the overall performance of a metal-air battery, is the air electrode [12].

When a bifunctional oxygen/air electrode is incorporated in an electrochemical device, there is only need of the storage and/or the supply of only one reactant into the device, the reactant of the alternate electrode since the bifunctional oxygen/air electrode utilises the atmospheric air. Hence in general, a device with a bifunctional oxygen/air electrode is lighter, has a less complex design and has high energy density [10].

The performance and the cost of bifunctional oxygen/air electrodes is a common concern in the electrochemical devices that utilise them. A lot of research has been focused on the optimisation of these electrodes and different electrode designs and materials have been suggested in order to enhance the electrode's performance [13, 10].

A simple design of a bifunctional oxygen/air electrode is shown in figure 1.3.

The bifunctional electrode consists of a catalyst layer and a catalyst support while two oxygen reactions, oxygen reduction (ORR) and oxygen evolution reactions (OER) are taking place on the electrode. The catalyst layer incorporates catalysts that can enhance the kinetics of both oxygen reactions. Unfortunately, the kinetics of both oxygen reactions (ORR and OER) are rather slow and the electrochemistry

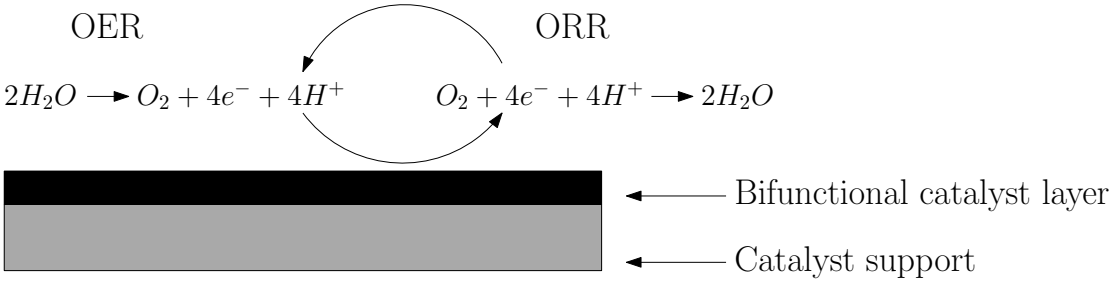

Figure 1.3: *Schematic of a bifunctional oxygen/air electrode*

of oxygen is rather complex [10]. The electrode's substrate varies depending on the electrochemical device but it is important to consist of materials that can survive the highly oxidative conditions that exist during the operation of the electrode. Hence, due to these high requirements a lot research has been focused on finding an optimum design for bifunctional oxygen/air electrodes.

There is a wide range of related processes and technologies that would benefit from a low cost, bifunctional oxygen/air, electrode. Table 1.1 summarises the oxygen reactions that take place in a range of electrochemical devices, and the nature of the electrolyte in each of them.

Oxygen reaction	Electrolyte	Electrochemical device	Reference
ORR	Acidic	polymer electrolyte membrane fuel cells (PEMFCs)	[11]
		solid oxide fuel cells (SOFCs)	[14]
		phosphoric acid fuel cells (PAFCs)	[15]
	Alkaline	Alkaline fuel cells	[15]
		chlor-alkali cells	[16]
		metal-air batteries	[5]
OER	Acidic	PEM electrolysers	[17]
	Alkaline	Alkaline electrolysers	[18]
ORR & OER	Acidic	unitised regenerative fuel cells (URFCs)	[13]
		reversible solid oxide fuel cells (RSOFCs)	[14]
	Alkaline	secondary metal-air batteries	[5]

Table 1.1: *Oxygen reactions which take place in various electrochemical devices*

A group of chemicals, called heteropolyacids have been used as additives in fuel cell electrodes and electrolytes to enhance their performance [19]. Heteropolyacids

have shown encouraging performance when added in acidic fuel cell systems but there is not enough research focused on the behaviour of heteropolyacids in alkaline fuel cell systems.

Heteropolyacids are also known for their high redox activity and their high solubility in polar solvents which could be advantageous in other electrochemical applications, such as redox flow cells. Redox flow cells are electrochemical devices that incorporate redox active liquid electrolytes which are stored in tanks outside the cell and flow in the cell during their operation. During charging, the electrolytes are pumped into the cell and their redox species get oxidised and/or reduced in order to produce energy, while during discharging electricity is provided in the cell, the electrolytes are regenerated and are stored back in the storage tanks. Hence, the main principles of redox flow cells are different to the principles of fuel cells or batteries, since the electrochemical reactions in redox flow cells take place in liquid electrolytes and not at solid electrodes.

An initial study on the redox activity of heteropolyacids in acidic and alkaline environment is performed and the results are presented in this thesis, in order to investigate whether heteropolyacids can be dissolved in the electrolyte and perform as the redox active species of the liquid electrolytes in redox flow batteries.

It has to be noted that the majority of the systems that have a bifunctional oxygen/air electrode use an alkaline electrolyte because the performance of the oxygen electrode is improved in alkaline environment and non-noble metals can be used at the catalyst layer of the electrode [10]. For that reason, in this project heteropolyacids are incorporated in the catalyst layer of bifunctional air electrodes as additives and their electrochemical performance is tested under an alkaline electrolyte for the first time.

Bifunctional O_2/air electrodes usually contain carbon in their substrates. However, carbon suffers from corrosion under the oxidative environment during the operation of these electrodes. Hence, further to the investigation towards an optimum oxygen/air electrode design, the characterisation of various non-carbon electrode materials in acidic, alkaline and neutral electrolytes is performed and presented in this thesis.

1.2 Aims and Objectives

The main aim of this project is the development of a new electrode architecture and a non-carbon active material for bifunctional OER and ORR electrodes.

In order to satisfy this aim the following objectives were followed:

- selection of the appropriate heteropolyacids for the electrocatalysis of the oxygen reduction and evolution reactions;
- characterisation of the aqueous electrochemistry of phosphomolybdic (PMA) and phosphotungstic acid (PWA) by exploring their different properties in alkali and acidic environment;
- immobilisation of the HPAs (PMA and PWA) on an electrode substrate (i.e. Magnéli phase electrode, glassy carbon electrode);
- manufacture of novel gas diffusion electrodes which include heteropolyacids in their catalyst ink;
- electrochemical characterisation of the HPA gas diffusion electrodes in alkaline environment;
- monitoring of how the variation of the structural characteristics of the HPA gas diffusion electrodes (e.g. catalyst loading, HPA loading etc.) affect their electrochemical performance towards OER and ORR;
- examination of the long term application of the HPA gas diffusion electrodes by microscopy screening and by monitoring the cycling of a battery which incorporates an HPA gas diffusion electrode;
- investigation of alternative non-carbon materials such as Magnéli phase materials and different substrates coated with Magnéli phase materials, titanium nitride (TiN), titanium nitride with carbon (TiN/C), zirconium nitride (ZrN), chromium nitride (CrN), chromium nitride with carbon (CrN/C) and Graphit_iC^{TM} for the electrode substrate;
- electrochemical characterisation of the different non-carbon materials in different electrolytic environments.

1.3 Thesis outline

The thesis consists of 8 chapters, including the introduction and the literature review (chapters 1 and 2), the experimental details (chapter 3), the analysis and the discussion of the results (chapters 4-7) and the conclusions with some suggestions for further work on the project (chapter 8).

Chapter 2 includes a thorough literature review on the heteropolyacids and their applications in fuel cells. Additionally, information on the bifunctional oxygen/air electrodes and on the materials that have been used for catalysts and substrates on these electrodes is included.

Chapter 3 describes the materials, the equipment and the experimental setup that has been used during this project. A few general information about the experimental work is presented in the first few paragraphs, while further details about the experiments are separated into small different sections which correspond to the different chapters with the analysis of the results of the experiments (chapters 4-7).

Chapter 4 introduces the analysis of the results from the electrochemical characterisation of heteropolyacids while being dissolved in supporting electrolytes and while being immobilised on a glassy carbon electrode (GDE).

In chapters 5 and 6, the results from the investigation on the HPA gas diffusion electrodes in alkaline environment are analysed. Chapter 5 presents some initial results from the characterisation of these electrodes, while in chapter 6 the results from a further investigation on the HPA gas diffusion electrodes are presented and analysed.

Chapter 7 includes the analysis of the electrochemical characterisation of some new, non-carbon electrode materials. The characterisation of the electrode materials was under different pH values and applied potential values.

Finally, chapter 8 summarises the main results and the important outcomes of this project, while it also includes some recommendations on further experimental work that can be done as a continuation of this work.

The tree diagram that is presented in figure 1.4 illustrates the experimental paths of this project.

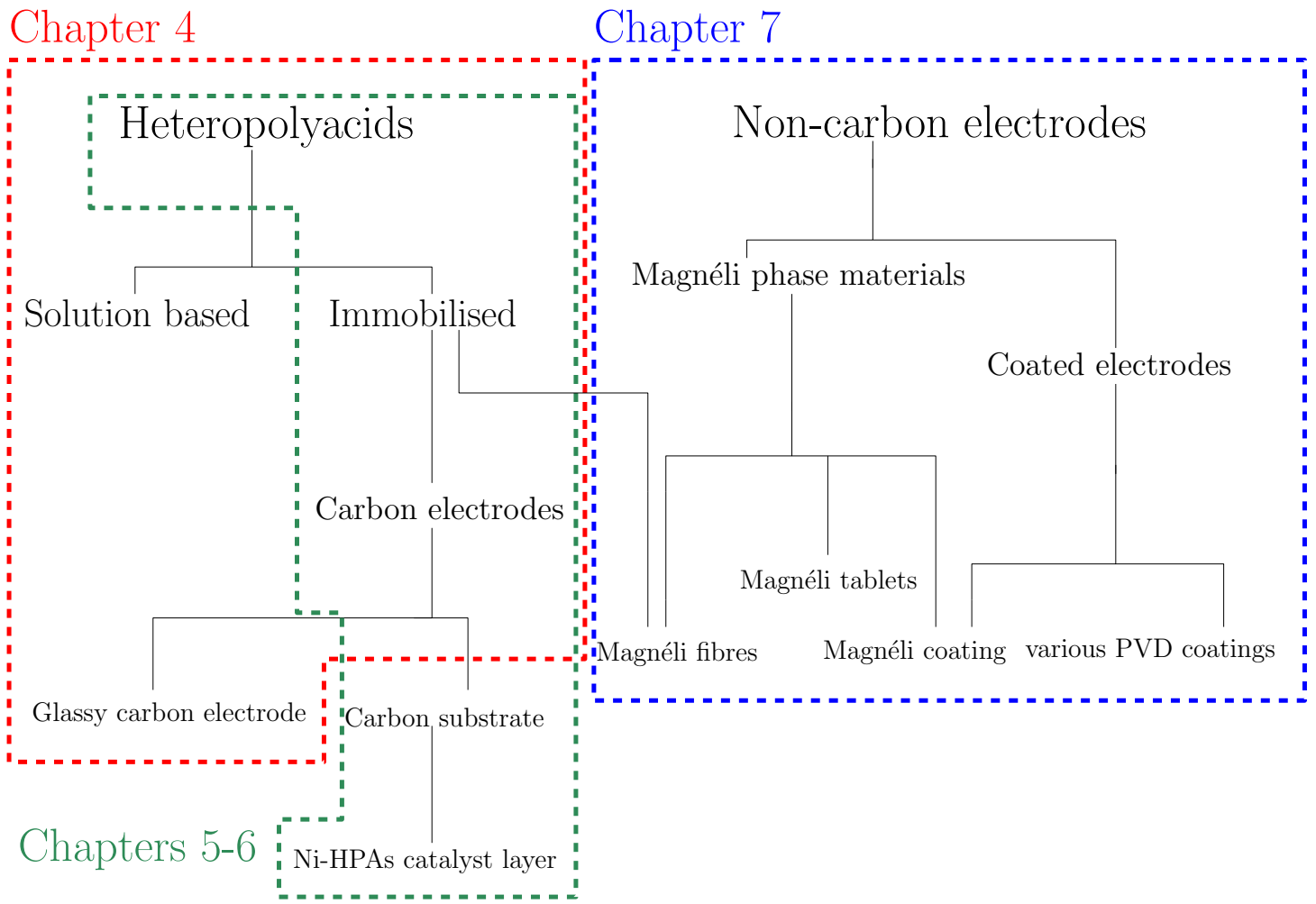

Figure 1.4: *Project's tree diagram*

Chapter 2

Literature review

2.1 Novel electrocatalysts: Heteropolyacids

The first reference to polyoxometalates was made in 1826, when Berzelius described a "yellow precipitate", ammonium 12-molybdophosphate, formed from the reaction of ammonium molybdate with phosphoric acid [20]. By 1908, around 750 heteropoly compounds had been described and characterized by more than 250 different authors [21]. During the process of attempting to describe the inner structure of heteropolyacids it was initially proposed that the rules describing the structure of complex ionic crystals can be employed [22]. Even if these early interpretations subsequently proven not to be entirely correct, they motivated further research on heteropolyacids [21].

In 1933, Keggin used X-ray diffraction to correctly resolve the $H_3[PW_{12}O_{40}] \cdot 5H_2O$ structure, becoming the first person to provide an explicit description of the bonds between the WO_6 octahedra of the molecule. Another HPA structure, the well-known Wells-Dawson structure, was theoretically described by Wells in 1945, and confirmed experimentally by Dawson in 1953 [21, 23].

Polyoxometalates (POMs) are a group of chemicals that have attracted the interest of many researchers due to the variety and selectivity of their properties. POMs can be applied in a broad range of processes, notably catalysis [24]. A vast body of literature on these compounds has contributed to a variety of nomenclatures to describe the entire group, including: polyoxometalates; polyoxoanions [25]; early transition metal oxygen anion clusters [26]; and metal oxygen clusters [27]. According to differences in their structures, POMs are divided into two main

groups: the isopolyacids (IPA) and the heteropolyacids (HPA). For these two subcategories, IPA and HPA, the following terminology is additionally used:

IPA: isopolyacids [28] ; isopolyoxometalates [25].

HPA: heteropolyanions; heteropolyacids; heteropoly electrolytes [28]; heteropoly compounds [29]; and heteropolyoxometalates [25].

The IPA and HPA prefixes can be a source of confusion, with 'metal oxygen clusters' suggested as a more appropriate name for this broad group of compounds [27]. The term 'heteropolyacid' is used to describe those heteropolyanions that contain hydronium cations [25]. For simplicity, the terminology HPA, heteropolyacid (or the chemical formula) is used. Further information about the terminology of specific heteropolyacids discussed within this thesis can be found in Table 2.1.

Full name	**Chemical composition**	**Shorthand**
Phosphomolybdic acid	$H_3PMo_{12}O_{40}$	PMA, PMo_{12}, MPA
Phosphotungstic acid	$H_3PW_{12}O_{40}$	PWA, PTA, PW_{12}, TPA
Silicotungstic acid	$H_4SiW_{12}O_{40}$	STA, SiW_{12}, TSA
Silicomolybdic acid	$H_4SiMo_{12}O_{40}$	SMA, $SiMo_{12}$, MSA

Table 2.1: *HPA nomenclature*

This section focuses on the use of HPAs in fuel cell technologies. A concise introduction to the structure, the properties and some general applications of these compounds is, nevertheless, essential. POMs consist mainly of early transition metal cations in their highest oxidation state (called 'addenda' (M) atoms) and oxide anions. Isopolyanions contain only transition metal ions and oxide ions, whereas heteropolyacids incorporate one or more p, d or f block elements in a positive oxidation state. The latter are termed 'heteroatoms' (X) [29]. The proportion of these atoms in the structure of an HPA to the number of the addenda atoms is small. More than 60 different elements of the periodic table can be used as the heteroatom [21]. This flexibility leads to a great variety of different structures, compositions and properties for HPAs.

Despite this plethora of different HPA varieties, only the structures of Keggin and Wells-Dawson variants (figure 2.1) will be discussed in detail, particularly since they are most applicable to electrochemical energy storage and conversion. The HPA structure is formed by MO_x polyhedra, most commonly distorted octahedra, which surround one or more heteroatoms (figure 2.2). There are strong bonds between the atoms, which support the polyhedral structure and connect it with

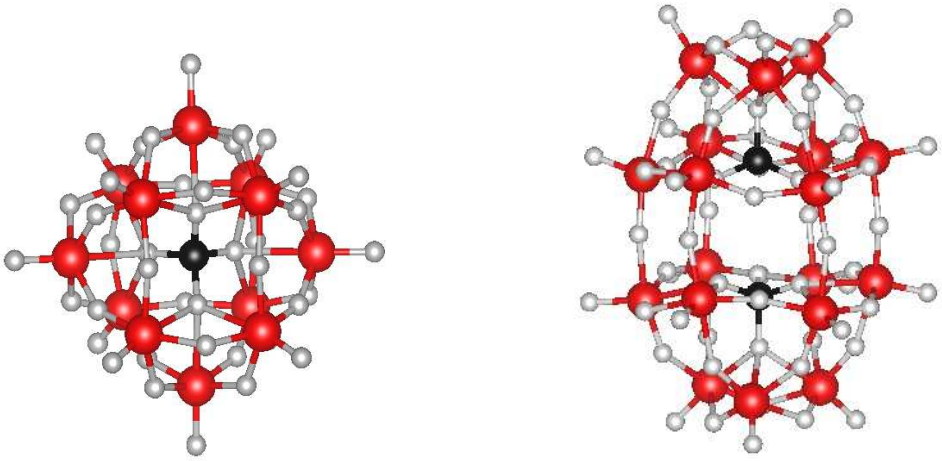

Figure 2.1: *Ball and stick diagrams showing (A) Keggin and (B) Wells-Dawson HPA variant where, heteroatoms are black, addenda atoms are red and oxygen atoms are light grey. The diagrams were designed with Vestra (Ver.3.1.5) software.*

the heteroatoms. The bridging, edge sharing and corner sharing oxygen atoms give rise to the interconnectivity. HPAs are synthesised by polymerisation of the metal-oxygen polyhedra around a heteroatom while acidification of the solution takes place [21]. The most common metals used as addenda atoms in HPAs are tungsten (W), molybdenum (Mo) and vanadium (V).

The Keggin structure, which is the most investigated, includes twelve addenda atoms and one heteroatom, $X^{x+}M_{12}O_{40}^{x-8}$, where X is the heteroatom, x is its oxidation state and M is the addenda atom. It contains one tetrahedron (XO_4), which is surrounded by twelve edge- and corner-sharing metal-oxide octahedra (MO_6). The octahedra form four M_3O_{13} groups and each group has three octahedra sharing edges(figure 2.2). They are connected via strong oxygen bonds, which also connect the central tetrahedron [30]. The Wells-Dawson heteropolyanions, $X_2^{x+}M_{18}O_{62}^{(2x-16)}$, contain eighteen addenda atoms and two heteroatoms (figure 2.2). Their structure can best be described as the addition of two lacunary (see below) Keggin ions, each with one heteroatom and nine addenda atoms.

A further subset is the lacunary HPA ions: ions that have lost one or more MO_6 octahedra. The addenda atoms and the bonding oxygen atoms of these polyhedra are not shared with other atoms [31]. Lacunary ions can be used during the synthesis of more complex HPA molecules because they are able to coordinate cations; they react readily with addenda atoms or octahedrally coordinating metal ions [32]. They can be produced using a controlled treatment with alkaline solution [21].

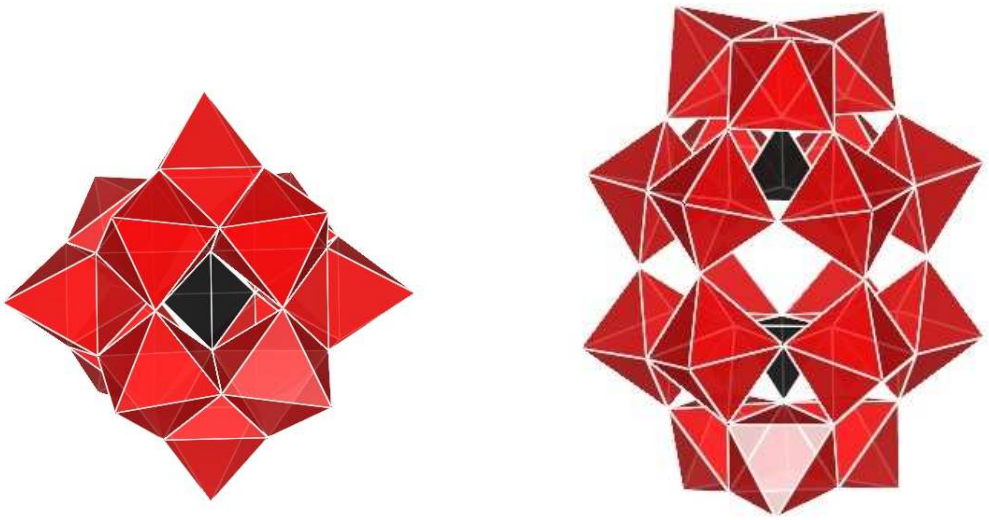

Figure 2.2: *Structural diagrams showing (A) Keggin and (B) Wells-Dawson HPA variant where, heteroatoms tetrahedra are black and addenda octahedra are red. The diagrams were designed with Vestra (Ver.3.1.5) software.*

Theoretically, Keggin ions can form six different isomers, of which only two (α-and β-isomers) are the most common and important. According to Jansen et al., the remaining Keggin isomers do not have the stability required to exist in aqueous solutions and so are unsuitable for most fuel cell applications [32]. The isomerism occurs when one or more of the four M_3O_{13} groups rotate 60° around the three-fold axis and reattaches to the main structure of the molecule [21]. In a similar manner, isomers of Wells-Dawson ions result from the rotation of the two M_3O_{13} groups.

Due to their wide range of different sizes (the diameter of phosphomolybdic acid is approximately 12 Å) and structures (localised clusters of redox active addenda atoms), HPAs exhibit a number of interesting properties, which is perhaps the main reason for the intense research on these compounds in the last decade [33]. HPAs exhibit strong acidity, good solubility in polar solvents, good thermal stability and reversible redox behaviour. One of the most important properties of HPAs is that they can be chemically adjusted or tuned by simple modification of their structures. For example, the redox potential of the HPA is affected by its addenda atoms, so if the HPA is required to have a lower redox potential, this can be accomplished by choosing a specific heteroatom which is more electronegative than others, e.g. tungsten instead of molybdenum (see table 2.2).

The acidity of the HPA is dependent upon the total charge of the anion and the heteroatom involved in its structure [32]. The strong acidity level introduces fast

proton mobility, which leads to a high catalytic activity [30]. The total charge and the heteroatom of the anion are also important for the solubility of the HPA [32], together with the size of the counter ion; for high solubility, the counter ion should not be large. Kozhevnikov [30] studied the stability of several Keggin ions in aqueous solution and found that their thermal stabilities followed the ordering:

$$SiW_{12}O_{40}^{-4} > PW_{12}O_{40}^{-3} > SiMo_{12}O_{40}^{-4} > PMo_{12}O_{40}^{-3}$$

The contribution of the heteroatom to thermal stability is, on the other hand, minimal [32]. The redox behaviour exhibited by HPAs is an important characteristic that motivates their application as redox bi-functional catalysts. The reduction potential of the HPA increases as the electronegativity of the counter cations or the heteroatoms increases [33]. The choice of addenda atom (rather than heteroatom) dominates the redox activity. This is exemplified by the oxidation potentials of the following Keggin structures [34]:

$$H_3PMo_{12}O_{40} > H_4SiMo_{12}O_{40} >> H_3PW_{12}O_{40} > H_4SiW_{12}O_{40}$$

The redox potential values and the proton affinity values of some characteristic heteropolyacids can be found in table 2.2.

Heteropolyacid	**Redox potential in aqueous solution*, E_o (V *vs.* NHE)**	**Proton affinity**, PA (kJ mol^{-1})**
$H_3PMo_{12}O_{40}$	0.65	1140
$H_4SiMo_{12}O_{40}$	0.63	1150
$H_3PW_{12}O_{40}$	0.15	1070
$H_4SiW_{12}O_{40}$	-0.05	1140

Table 2.2: *Characteristic values for the redox potentials and the proton affinities of Keggin HPAs (* from [1],** from [2])*

A notable and significant characteristic of Keggin HPAs is that they can gain several electrons per molecule without changes in their structures [34]. Furthermore, the reduced forms retain their structures when re-oxidised. In other words, they are stable to repeated redox cycling. Heteropolyacids, specifically Keggin structures, are easily synthesized, and hence readily available compared to other classes of POMs. Generally speaking, the most appealing characteristic of heteropolyacids is the freedom to synthesize compounds that exhibit specific properties.

The reduced forms of some HPAs, mostly the Keggin and Dawson structures that contain Mo and W, are called *heteropolyblues* due to the intense blue colour that they produce. The number of the electrons that are added to the HPA depends on the pH and the electropotential of the surrounding chemical environment [21]. Addition of further electrons to the already reduced heteropolyblues results in the formation of *heteropolybrowns*.

2.1.1 Applications of Heteropolyacids

Heteropolyacids have been used in a broad range of applications, including chemical analysis, biochemistry, ion selective membranes, sensors, biodiesels and fuel cells. Most commonly, however, they are employed as catalysts.

HPAs can be effective catalysts for both acid catalysis and redox catalysis, depending on their composition [32]. One of the important characteristics of the heteropolyacids is that by adding different cations to their structures, the molecules can be tuned, allowing for the design of HPAs for specific reactions.

The high selectivity, stabilities, long lifetimes in solution, separation properties and non-corrosive nature of many HPAs mean that they are natural *green catalysts* [35]. A number of industrial applications of HPA catalysis are based on such properties, e.g., the hydration of isobutene and the polymerisation of tetrahydrofuran using heteropolymolybdate [36, 37]. HPAs can be used to simplify processes and are amenable to recycling or renewal, ultimately leading to energy and costs savings. Showa Denko has applied HPAs in two industrial processes: the synthesis of ethyl acetate from ethylene and the direct synthesis of acetic acids by oxidation [35]. Both processes, however, have suffered from severe catalyst deactivation, and research into improving the processes is ongoing [35].

The fact that the majority of the periodic table of elements can potentially function as heteroatoms in heteropolyacids is the main reason that they have found applications in the field of analytical chemistry. There exists a enormous variety of gravimetric and colorimetric analytical methods, as well as several methods for elemental analysis, utilizing HPAs [38].

HPAs have been also used in a number of biochemical and biomedical applications [39], e.g., as precipitants for proteins, analytical reagents for proteins, alkaloids, purines and stains in electron microscopy [38]. The range of proteins or enzymes that can interact with heteropolyacids is broad, and the interaction is specific

to the HPA [40]. HPAs exhibit antiviral and antitumoral activity, which leads to applications in biomedicine [41]. Crystal hydrates of HPA containing molybdenum have shown antitumoral activity with low toxicity. HPAs have also been tested for plant antiviral activity, with encouraging results, particularly using HPAs that include tungsten [42].

A number of attempts have been made to use HPAs in the biodiesel production [43]. One of the most successful attempts was the production of biodiesel from Eruca Sativa Gars (ESG) vegetable oil from the transesterification of ESG, which was catalysed by $Cs_{2.5}H_{0.5}PW_{12}O_{40}$ heteropolyacid salt [44]. The resulting biodiesel properties were in compliance with the US Standard for Biodiesel (ASTM 6751). Encouraging results have been also obtained with a technique that employs microwaves to produce biodiesel from yellow horn oil and the HPA salt as the catalyst for transesterification [45]. The process was shown to be more efficient than the conventional method of producing biodiesel from the same oil.

HPAs have been investigated extensively as dopants in membranes. The attraction of HPAs for membrane applications is a consequence of their high ionic conductivity, thermal stability and ability to form various salts. Composite membranes containing HPAs have been used in ion-selective electrodes, gas detection sensors, electrochromic devices and solid or liquid electrolytes in electrolytic cells [24]. Heteropolyacids have been also incorporated in a variety of ion-selective membranes for molecular selectivity and sensing,as well as into membranes for biosensors and hydrogen gas sensors [24, 46, 47, 48, 38].

Historically, a great deal of research has focused on HPA-incorporated membranes for electrolytic cells, including fuel cells. In 1976, Nakamura et al. were amongst the first to test the performance of polyoxometalates as electrolytes in electrochemical cells [49]. Polyoxometalate acids or their salts were compression moulded under high pressures and used as proton-selective membranes in H_2/O_2 fuel cells. The high ionic conductivities of these membranes were in part responsible for raising the awareness of POMs for fuel cell applications, leading to numerous subsequent investigations. In addition to the applications outlined above, HPAs are used in flame retardants, smoke suppressants, corrosion inhibitors, thin film solar energy materials, recording materials, dyes and wood pulp bleaching. The reader is referred to [24, 38, 50] for further details.

Despite the vast variety of possible structures, the majority of the literature focuses on only a handful of HPAs, namely $H_3PMo_{12}O_{40}$, $H_3PW_{12}O_{40}$, $H_4SiMo_{12}O_{40}$ and $H_4SiW_{12}O_{40}$ [24]. However, several acid forms of these polyoxometalates are

known and they could be potentially examined for further applications in fuel cells.

2.1.1.1 HPAs in fuel cell electrolytes

The main aim of this subchapter is to highlight and assess the different applications of HPAs in fuel cells. Heteropolyacids can be employed in fuel cells in a number of a ways, e.g., solvated in the electrolyte, immobilised on the electrodes or incorporated in the ion exchange membrane. In particular, considerable efforts have been directed towards the incorporation of HPAs into the components of polymer electrolyte fuel cells (PEFCs), direct methanol fuel cells (DMFCs) and direct ethanol fuel cells (DEFCs). These applications typically involve precious metal catalysts [51], with a limited number of investigations on non-precious metals such as Ni [52].

The first attempt to incorporate an HPA into fuel cells was made by Nakamura et al.[53], who used phosphomolybdic acid ($H_3PMo_{12}O_{40}$) as a solid electrolyte, in the form of pellets, inside a H_2/O_2 fuel cell. The fuel cell attained a current density of 100 mA cm^{-2} at 0.5 V, which is low compared to conventional fuel cell systems (ca. 1 A cm^{-2}) but extremely encouraging for a new system, particularly for applications in which the power density is not an issue (e.g. stationary power supplies).

After Nakamuras group first study on the addition of HPAs in fuel cells, the design of these systems has been radically developed but still HPAs have been chosen by a significant amount of researchers in order to enhance the electrolytes performance. The most commonly used fuel cells are possibly the polymer electrolyte fuel cells (PEFCs), where electrolyte membranes are incorporated. The main requirements for an electrolyte membrane are high proton conductivity, chemical, mechanical and thermal stabilities under the fuel cells operating conditions, low fuel permeability, no electron conductivity and low cost.

The most commonly used membranes in fuel cells belong to the PFSA family of membranes, e.g. Nafion®. PFSA membranes exhibit reasonably good performance as electrolyte membranes in fuel cells but they also possess several disadvantages. Their high costs, long-term durability problems, as well high permeabilities to the fuel in DMFCs and DEFCs, have motivated the search for alternative non-fluorinated membranes. Detailed reports of the performance of membranes made from poly(ether ketones) (PEK) and their derivatives sulfonated-PEEK,

poly(arylene thioethilene sulfone), poly(vinyl alcohol) (PVA), polybenzimidazole (PBI), and many more besides, abound in the literature [54, 55].

HPAs have been used as additives in numerous electrolyte membranes in order to improve their proton conductivity and the overall performance of cells. However, HPAs one major obstacle to their deployment in fuel cells is their high solubility in polar media (e.g., water), which is a consequence of their low surface areas (58 m^2 g^1). The high solubility leads to leaching problems that can have a severe effect on the overall performance of the cell [56]. Two different approaches to overcoming this issue have been suggested. The first involves placing the HPAs on support materials such as high surface oxides (e.g. SiO_2, Al_2O_3, ZrO_2, TiO_2) or thermoplastics (e.g. PPO) in order to enhance their stability [57, 56]. The second option is the use of heteropoly salts rather than heteropoly acids, i.e., substituting the protons (H^+) for large cations such as Cs^+, $NH_4{}^+$, Rb^+ and Tl^+ [58]. This technique increases the surface area of the particle and transforms it into an insoluble acid salt, while retaining its original proton conductivity and thermal stability characteristics. A drawback to this technique is the resulting large size of the heteropolysalt particle, which decreases the conductivity, and possibly reduces the thermal stability, of the composite [58].

The table in the Appendix summarises the literature on the incorporation of heteropolyacids in different types of electrolyte membranes for fuel cells. Since each study is conducted under different experimental conditions, e.g. preparation of the hybrid membrane, temperature and humidity environment, characterisation techniques, it is not feasible to compare them all extensively. However, some important trends for the HPA incorporated membranes for PEMFCs and DEMFCs have been spotted and are mentioned. The first subsection that follows is based on the hybrid membranes manufactured for applications in PEMFCs and the second subsection is about the hybrid electrolyte membranes that has been used in DMFCs. Both subsections are focused on the incorporation of HPAs in the most common types of membranes, such as Nafion®, PVA and SPEEK. The table in the Appendix highlights several other membrane/HPA combinations, however they are single cases and therefore difficult to compare directly. It is also clear from the summarising table in the Appendix that only a few specific heteropolyacids have been used as additives in electrolyte membranes so far .

2.1.1.1.1 Heteropolyacids in PEMFC electrolytes

The most common electrolyte membranes belong to the PFSA family of membranes, e.g. Nafion®. However, one of the main drawbacks of Nafion® membranes is that they have to be highly hydrated in order to have high conductivity and when the cells operating temperature is higher than 80°C, their proton conductivity is significantly decreased. High operating temperature is rather beneficial for a PEMFCs overall performance and a great variety of modified Nafion® membranes that are able to remain hydrated and proton conductive at high operating temperatures have been investigated. A typical modification, designed to maintain high water content levels in the Nafion®-type membranes at elevated temperatures, is the addition of an inorganic material with hydrophilic properties with HPAs being suitable candidates [59].

A few studies have incorporated several different heteropolyacids in Nafion membranes for application in PEMFCs [60, 61, 62, 63]. At high temperature values the hybrid membranes show improved proton conductivity values (around 10^{-2} S cm^{-1}) [60, 62, 63]. At low temperature and high relative humidity conditions a membrane with Nafion®-silicotungstic acid showed the highest proton conductivity of 9.5×10^{-2} S cm^{-1} [61]. In general, the membranes with the silicotungstic acid ($H_4SiW_{12}O_{40}$) showed the best enhancing abilities for the proton conductivity of the Nafion® membranes, whereas the membranes with heteropolyacids that included molybdenum had stability issues after their long-term use [60, 61, 62, 63]. Additionally, it was shown that the water content of the modified Nafion® membrane increased with the addition of silicotungstic acid [61] (there is typically a linear relationship between water content and conductivity, at a fixed temperature).

In order to improve the stability of the heteropolyacids, heteropolysalts have been alternatively used as fillers in Nafion® membranes for PEMFCs. Larger cations such as Cs^+, NH_4^+, Rb^+ and Tl^+ were combined with phosphotungstic acid to produce heteropolysalts. The heteropolysalt that exhibited the highest proton conductivity values is the salt with cesium and phosphotungstic acid. It has to be mentioned that all the hybrid membranes had improved proton conductivities ($10^{-2} Scm^{-1}$) compared to the values exhibited by the equivalent Nafion membranes [58, 64]. Nafion® membranes with heteropolyacids supported on different materials (SiO_2, ZrO_2 and TiO_2) have been manufactured and tested by a significant number of researchers [56, 65, 66, 67, 68, 69]. The only heteropolyacid that has been used in these hybrid membranes was the phosphotungstic acid. It is shown that SiO_2 is the best candidate for the supportive material since there is a strong interaction developed between the $H_3PW_{12}O_{40}$, the Nafion® and the SiO_2 molecules

[66]. The proton conductivities exhibited by the hybrid Nafion® membranes were 10^{-3}- 10^{-2} S cm^{-1} at high temperature values and 10^{-1} S cm^{-1} at low temperature values [65, 66, 67, 68, 69]

Membranes made from PVA are low cost and exhibit very good chemical resistance and reduced fuel permeability, but they possess very low proton conductivities (10^{10} - 10^{14} S cm^{1} for pure dry PVA materials) [70]. HPAs can be embedded into PVA membranes in order to provide sufficiently high proton conductivities for application in PEMFCs. Three different heteropolyacids were incorporated in PVA by following three different preparation techniques [70, 71, 72]. All the hybrid membranes showed much enhanced proton conductivities (10^{-1} - 10^{-3} S cm^{-1}) and it can be also noticed that when the temperature rises the proton conductivity of the hybrid PVA membrane is decreased [70, 71, 72].

Heteropolyacids have also been embedded in a number of membranes made of sulfonated polymer materials, mostly SPEEK (sulfonated poly(ether-ether ketone)), in order to improve their performance when used in PEMFCs. HPAs containing tungsten and molybdenum as well as heteropolysalts containing cesium or sodium cations have been used as additives with some of them being supported on materials such as SiO_2, Pt or MCM41 [73, 74, 75, 76, 77, 78]. The addition of HPAs again increases the proton conductivity and improves the thermal stability of the membranes. The HPA-modified SPEEK membranes showed to enhanced proton conductivity values (10^{-3}-10^{-1} S cm^{-1}) compared to the low values exhibited by a plain SPEEK membrane (10^{-4}-10^{-3} S cm^{-1}) [77].

2.1.1.1.2 Heteropolyacids in DMFC electrolytes

An additional major drawback to the use of Nafion®-type membranes is fuel crossover in DMFCs [79]. During operation, methanol passes through the membrane to the cathode of the fuel cell, which results in a reduced cell voltage. HPAs were incorporated into Nafion® membranes in order to create more conductive membranes that would allow for thicker membrane components in the cells which would consequently reduce the rate of methanol crossover [80].

The heteropolyacids that were added in the Nafion® membranes are phosphomolybdic acid ($H_3PMo_{12}O_{40}$), cesium-phosphotungstic salt ($Cs_{2.5}H_{0.5}PW_{12}O_{40}$) and phosphotungstic acid ($H_3PW_{12}O_{40}$) supported on PPO, SiO_2 or ZrO_2 [57, 81, 82, 83, 84, 85]. The hybrid Nafion® membranes showed reduced methanol

crossover, increased water uptake and in some cases led to higher open circuit voltages and higher peak power densities.

The proton conductivity values ranged from 10^3 to 10^1 S cm^1 under different temperature and relative humidity conditions. Among the membranes that incorporated heteropolyacids supported on various materials, the membranes with HPA and SiO_2 exhibited the best results. It is important to be mentioned that the conductivity of the phosphotungstic acid on SiO_2 membranes was decreasing as the temperature was increasing [73, 75]. In the contrary, the conductivity of the membrane with unsupported $H_3PMo_{12}O_{40}$ exhibited an unusually opposite dependence with the temperature [84].

Following the addition of HPAs in PVA membranes for DMFCs, it was shown that PVA hybrid membranes have lower methanol permeabilities, higher proton conductivities and improved thermal stabilities. The most common additives are supported or unsupported tungsten-based HPAs and tungsten-based cesium heteropolysalts [86, 87, 88, 89, 90, 91, 92]. The proton conductivity values of these hybrid PVA membranes are between 10^4 and 10^2 S cm^1, orders of magnitude higher than neat PVA membranes. It is shown that the support not only improves the stability of the HPAs but it contributes to higher proton conductivity values [86, 87, 88].

A few research groups have also tried to incorporate heteropolyacids in SPEEK membrane in order to improve their proton conductivity and methanol crossover behaviour [93, 94, 95]. The heteropolyacids that are used are all tungsten-based HPAs. All the HPA-modified membranes had shown improved proton conductivity and lower methanol permeability values. The proton conductivities vary between 10^{-2} and 10^{-1} S cm^{-1}, with the SPEEK membrane with the $Cs_{2.5}H_{0.5}PW_{12}O_{40}$ exhibiting the highest conductivity [93, 94, 95].

2.1.1.2 HPAs immobilised on fuel cell electrodes

Two of the most common and promising types of fuel cells are the polymer electrolyte fuel cells (PEMFCs) and the direct alcohol fuel cells (DAFCs). The electrodes in both types of cells share the same structure and are referred to as gas diffusion electrodes. Such electrodes consist of a gas diffusion layer and a catalyst layer. The gas diffusion layer is a substrate, commonly a carbon cloth, carbon foam or carbon paper, that ensures a continuous flow of reactants to the catalyst layer and provides a conduction path for electrons. The catalysts are typically noble

metals such as Pt, Pd, Ru and their alloys. The main drawbacks of these traditional catalysts are: (i) high costs; (ii) susceptibility to poisoning by CO, CO_2, H_2S and other fuel impurities; (iii) tendency towards Ostwald ripening, agglomeration and sintering; (iv) susceptibility to dissolution in catalyst layer ionomers; and (v) insufficient electroactivity towards oxygen reduction and methanol oxidation.

Reducing the loading of noble metal catalysts and improving their utilization efficiencies therefore remain important objectives for fuel cell developers and manufacturers. A popular approach is to reduce the size of the catalyst particles to the nano-scale, in order to increase the active surface area for a given loading and to improve dispersion on the support material, e.g. carbon black [96]. Pt particles of sub-3 nm size, on the other hand, exhibit decreased mass activities, despite leading to higher surface areas [97]. This is usually attributed to an increased strength of adsorption for oxygen containing species OH_{ads}, which block the active sites [98].

In many practical PEMFC systems, the hydrogen fuel comes from reformation of hydrocarbon fuels, such as natural gas. When chemical reformation takes place, excess quantities of carbon monoxide (CO) are produced as a co-product:

$$\mathrm{CH_4 + H_2O \longrightarrow 3\,H_2 + CO} \qquad \text{(C 2.1)}$$

For fuel cell applications, high-purity H_2 is essential because CO poisons the anode Pt catalyst (by far the most commonly used) by preferentially adsorbing on the Pt surface and, therefore, blocking the active sites for hydrogen oxidation; ultimately this leads to a severe drop in the cell voltage. CO poisoning is ameliorated using alloys of Pt, Ru and Co as catalysts, but it cannot be eliminated entirely. The water gas shift reaction is, therefore, used to remove CO from the reformate [80]:

$$\mathrm{CO + H_2O \longrightarrow H_2 + CO_2} \qquad \text{(C 2.2)}$$

Unfortunately, traces of CO are still present (on the order of a few ppm). The CO can be desorbed from Pt by operating at around 150°C [99], which would also enhance the rates of hydrogen oxidation and oxygen reduction. Typically, however, PEMFCs are operated at around 80°C in order to prevent dehydration of the PFSA membrane. A second important reason for operating at temperatures below 100°C relates to the chemical degradation of PFSA membranes, which is accelerated at high temperatures and low hydration levels [100].

HPAs have been used as additives to the catalyst layers, both in anodes and cath-

odes, with the aim of addressing the CO-poisoning and other drawbacks of the catalysts, mostly in conjunction with Pt. It has been shown that the addition of HPAs to the catalyst layers of fuel cells can enhance the electrocatalytic activity towards ORR and MOR, and reduce the level of catalyst poisoning by CO when compared to the performance of pure Pt [101, 102]. Additionally, the fact that HPAs can be easily absorbed on Pt and activated carbon substrates to form electroactive absorbates is another advantage to their use in fuel cells, particularly since Pt (either on its own in an alloy) is still the most common catalyst [101].

2.1.1.2.1 Heteropolyacids in PEMFC electrodes

Molecules that can be used as additives to Pt must satisfy certain basic requirements: they must be able to limit the degradation of Pt particles, they should interact with Pt in a manner that improves its performance and they should not react with the inert reactants and/or the intermediates of reaction. With these requirements in mind, heteropolyacids are potentially suitable choices. Due to their large structures, they inhibit the formation of Pt oxides, while promoting proton transport to active Pt sites by virtue of their high proton conductivities [103]

In order to be able to understand how HPA can facilitate the electrocatalytic performance of platinum in PEMFCs' cathodes, it is essential to explain the rather complex mechanism of the oxygen reduction reaction on Pt. O_2 is reduced to water either through a four-electron path or through a two-electron path with intermediate radical and H_2O_2 formation (in an acidic medium).

This model, originally proposed by Damjanovic et al. [104], is depicted in figure 2.3. Several similar models have been proposed, notably those of Wroblowa et al. [105] and Appleby [106]. Step 1 in figure 2.3 is the four-electron (direct) reduction path (1.229 V *vs.* standard hydrogen electrode (SHE)). Steps 2 and 3 represent a series path where O is first reduced to H_2O_2 through two-electron transfer (0.695 V vs. SHE), followed by reduction of H_2O_2 to H_2O (1.77 V vs. SHE). H_2O_2 can also detach from the catalyst surface and enter the bulk (Step 4).

The two pathways occur simultaneously in varying ratios; the four-electron pathway is the dominant mechanism on noble metals such at Pt, whereas the two-electron pathway is favoured on most carbon materials.

$$O_2 + 2\,e^- + 2\,H^+ \longrightarrow H_2O_2 \qquad (C\,2.3)$$

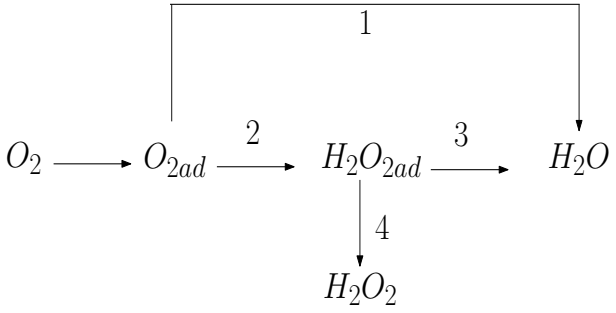

Figure 2.3: *The model of Damjanovic et al. for oxygen reduction on metals in both alkaline and acidic media. Water can either be formed directly via the four-electron pathway, 1, or via the two-electron pathway, 2 and 3 in series. The subscript ad refers to an adsorbed species.*

$$\mathrm{O_2 + 4\,e^- + 4\,H^+ \longrightarrow 2\,H_2O} \qquad \text{(C 2.4)}$$

The role of the HPAs in the enhancement of ORR is to promote the four-electron reaction, with the exact mechanism still requiring elucidation. What has to be highlighted at this point is the suggested mechanism that HPAs follow in order to enhance the oxygen reactions. According to Stanis et al., it is presumed that an enhanced reaction rate is facilitated through increased proton transport and the ability of the HPAs to undergo multiple 1 or 2 e^- reductions without structural deterioration [107].

A wide variety of HPAs, both Keggin and Wells-Dawson structures, have been tested for their abilities to enhance the electrocatalytic performance of Pt towards ORR. According to Stanis et al., the HPA must undergo a 4e^- reduction, as shown below, in order to be considered an efficient catalyst for ORR [107]:

$$\mathrm{HPA + 4\,H^+ + 4\,e^- \longrightarrow H_4HPA} \qquad \text{(C 2.5)}$$

$$\mathrm{H_4HPA + O_2 \longrightarrow HPA + H_2O} \qquad \text{(C 2.6)}$$

Fuel cell tests were conducted by Stanis et al. using a variety of HPAs as cathode catalysts (and a Pt-ELAT anode). Tungsten based HPAs were demonstrated to be ineffective for ORR, since they are not easily reduced. The Mo based HPAs, on other hand, were capable of producing relatively high current densities; at 80°C, the Keggin HPA, $H_3PMo_{12}O_{40}$, produced a current density of 265 mA cm^{-2} at 0.2 V, while the Mo based Wells-Dawson HPA, $H_6P_2Mo_{18}O_{40}$, produced a current

density of 290 mA cm^{-2}, at the same cell voltage, although both cells suffered from high cathode activation losses. The results were improved by vanadium substitution, (e.g. $H_5PMo_{10}V_2O_{40}$, achieved a current density of 290 mA cm^{-2} at 0.2 V), particularly at low current densities, but the performance with these catalysts deteriorated after a conditioning period of 16 h, suggesting that they are not stable in a fuel cell environment [107].

The addition of only 16 wt.% silicotungstic acid ($H_4SiW_{12}O_{40}$) to Pt (unspecified loading) in the cathode of a H_2/air fuel cell was shown by Brooker et al. to decrease the current density at 0.2 V by a factor of three when operating at 118°C [108]. This appeared in large part to be caused by a decrease in the pore volume and subsequent increase in the diffusional resistance by virtue of maintaining the same ionomer wt.% in the preparation of the electrodes. With adjustments to the wt.% of the ionomer, the performance with 16 wt.% silicotungstic acid was comparable to that of the Pt electrode.

It has already been mentioned that heteropolyacids are highly soluble in polar solvents. This characteristic usually causes their detachment/leaching from the electrode of a fuel cell. Hence, Dsoke et al. used a water-insoluble cesium-HPA salt ($Cs_xH_{3-x}PW_{12}O_{40}$) to solve this problem [109]. XRD and BET analyses revealed that the Pt nanoparticles were encapsulated in the mesopores of the HPA salt, thereby avoiding aggregation. Incorporation of the HPA salt on the catalyst layer increased the heterogeneous rate constant for oxygen reduction, which was ascribed to the high surface acidity and high proton mobility of the salt (indirectly, therefore, enhancing the four-electron reduction of O_2) [109].

Another study which is focused on the extent to which adsorbed HPAs may hinder or enhance the ORR is conducted by Chojak et al. [96]. It is shown that ($H_3PW_{12}O_{40}$ and $H_3PMo_{12}O_{40}$) molecules decompose hydrogen peroxide (H_2O_2) so they protect platinum from agglomeration and dissolution of it in the electrolyte. The bonds that HPAs form with Pt are primarily with corner oxygen atoms. Hence, the majority of Pt sites are not blocked. Moreover, O_2 molecules can diffuse through the HPAs to reach the Pt surface [96]. Overall, it was reported that HPAs can enhance the electrocatalytic activity of Pt.

HPAs have been also incorporated into catalyst layers of anodes of PEMFCs. A number of iron-substituted Wells-Dawson HPAs were used by Kuo et al. as dopants for the anode of a PEMFC [110]. Using an anode doped with only 1 mol cm^{-2} of Wells-Dawson $H_{12}[(P_2W_{15}O_{56})Fe_4^{III}(H_2O)_2]$, a remarkable 85% increase in the power density at 0.2 V (0.68 W cm^{-2}) was observed, compared to a Pt control

anode operating in the same configuration under the same conditions. Substantial improvements were also observed with other Fe-substituted Wells-Dawson type HPAs. From curve fitting of the polarisation data, it was concluded that the main reason for the improvements was a dramatic reduction (up to 100%) in the area specific resistance of the membrane electrode assembly to ion transport. There may also have been minor enhancements in the H_2 oxidation catalytic activity of the electrode, which would have been masked by the effects of an increased ionic conductivity.

A few studies have also shown that the incorporation of HPAs into Pt electrodes enhances the performance of the anode when reformate is used because the heteropolyacid promotes CO oxidation [68, 69, 64]. For example, the addition of molybdenum or a HPA that contains Mo (e.g., $H_3PMo_{12}O_{40}$ (phosphomolybdic acid) [111]) to a Pt anode enhances its CO tolerance. Direct comparisons of the performance of $H_3PMo_{12}O_{40}$, $H_4SiW_{12}O_{40}$ and $H_3PW_{12}O_{40}$, along with their vanadium substituted analogues, showed that HPAs containing Mo are the most effective CO oxidation catalysts and that their activities increase when vanadium atoms are present. It is believed that vanadium-containing HPAs possess higher redox activities [112, 113]. $H_4SiW_{12}O_{40}$ exhibits a high proton conductivity but is not as efficient as $H_3PMo_{12}O_{40}$ towards the oxidation of CO.

In a later study by the same group [112] a series of Keggin, Wells-Dawson and Wells-Dawson sandwich ($M_4^{II}(H_2O)_2(P_2W_{15}O_{56})_2^{16-}$, where M=Ni,Fe,Co,Cu,Zn) HPAs were tested in a hydrogen fuel cell in the presence and in the absence of CO in the anode fuel stream. When the cell was fed with H_2 containing 100 ppm CO, doping with phosphomolybdic acid and its di- and tri-vanadium-substituted analogues produced quite dramatic improvements in the performance, although the presence of CO still led to a severe drop in the cell voltage. For example, doping with $H_3PMo_9V_3O_{40}$ produced a current density of 525 mA cm^{-2} at 0.5 V compared to 229 mA cm^{-2} for pure Pt (ca. 950 mA cm^{-2} with pure H_2). The other HPAs tested were not able to improve the performance to any great extent. The reason for the improvement using phosphomolybdic acid ($H_3PMo_{12}O_{40}$) under poisoning conditions is that it acts as an oxidizing agent for the reaction between CO and liquid water in the presence of Au, Pt and Pd [113, 114].

Limoges et al. incorporated HPAs in both the cathode and the anode of a PEMFC. They examined the performance of the series $(PMo_{(12-n)}V_nO_{40})^{(3+n)-}$ (n=0,1,2,3) as pure anode and cathode catalysts for a hydrogen/oxygen fuel cell [115]. The tests were conducted separately using Pt/C for a counter electrode. Increasing

the vanadium content made no discernible difference to the results, which, overall, were disappointing at both the anode and cathode; when used as anode catalysts (Pt/C cathode), the OCV of the cell was between 600 and 700 mV and the maximum current density was on the order of a few mA cm^{-2} at room temperature. More promising results were obtained when $H_5PMo_{10}V_2O_{40}$ was used as the cathode catalyst (Pt/C anode), with an OCV of around 750 mV and a maximum current density of around 140 mA cm^{-2} at 100°C. At such temperatures, however, humidification is required and degradation of the cell components, especially of the membrane, can be severe. These catalysts are, on the other hand, potentially suitable for methanol oxidation at elevated temperatures. One feature of the cell that led to the poor performance was the loading of HPA on the electrode. In mass terms, the HPA loading was around 0.1 mol cm^{-2}, which was extremely low compared to the ca. 2 mol cm^{-2} loading at the Pt/C counter electrode.

A commercial application of HPAs in a PEM-type fuel cell was realised by ACAL Energy Ltd. [116]. This cell consists of a porous electrode, made from carbon, and an aqueous solution in contact with the electrolyte membrane. In the aqueous solution, heteropolyacids namely vanadomolybdates, are used as redox mediators that undergo reduction in the electrode and are re-oxidised by air in an external compartment [116]. The results from varying the flow rates and POM concentrations in the aqueous solution showed that the cathode overpotentials under typical operating conditions can be lower than those in a cell employing a standard MEA but that improvements were still required to match the performance of state-of-the-art conventional cells [117].

2.1.1.2.2 Heteropolyacids in DMFC electrodes

An alternative to the hydrogen PEMFC, which circumvents the problems associated with the use of H_2, is the DMFC. The performance of DMFCs is, however, limited by the slow kinetics of the anode reaction (methanol oxidation), poisoning of the platinum catalyst by carbon intermediates and methanol crossover from the anode to the cathode. These drawbacks result in low energy densities (ca. 2000 Wh kg^{-1}) and low operating voltages (ca. 0.4 V) [118]. Since platinum is regarded as the most active catalyst for alcohol oxidation at low and moderate temperatures, the cost and limited stability of Pt are also significant issues [119].

Heteropolyacids have been also incorporated in electrodes of DMFCs. The results from a few studies have shown that phosphomolybdic acid ($H_3PMo_{12}O_{40}$)

promotes the electro-oxidation of CO to CO_2 on catalysts such as Ru or Co [120, 121, 122]. It is also known that transition metal oxides, when combined with Pt, can enhance CO oxidation by virtue of the formation of oxygen-containing species at low potentials [123]. Additionally, vanadium atoms exhibit good redox activity. $H_3PMo_{12}O_{40}$ with two substituted vanadium atoms, which combines the properties of HPAs with those of transition metal oxides, was tested by Cui et al. as an additive to Pt in a DMFC [123]. The results showed that this combination of Pt with $H_5PMo_{10}V_2O_{40}$ leads to an improved catalytic activity towards MOR, together with enhanced stability. The likely explanation for the increased activity is enhanced proton transfer, which also aids the electro-oxidation of CO and other intermediate species [123]. These results were confirmed by similar experiments on Pt modified with vanadium substituted analogues of phosphomolybdic acid [124]. Additionally, it was found that the electron transfer coefficient of the rate-determining step is higher when the Pt electrode is doped with $H_5PMo_{10}V_2O_{40}$. The highest activity for MOR was seen with the tri-vanadium substituted analogue [124].

Cesium heteropolyacid salts, $Cs_{2.5}H_{0.5}PW_{12}O_{40}$ and $Cs_{2.5}H_{0.5}PMo_{12}O_{40}$, have also been used as promoters for the catalysis of MOR in a DMFC anode. After modification with the HPA salts, the Pt catalyst showed enhanced MOR kinetics, with higher voltammetric and amperometric catalytic currents (25 mA cm^{-2} when $Cs_{2.5}H_{0.5}PW_{12}O_{40}$ is added to the Pt electrode compared to 15 mA cm^{-2} with no HPA addition and 11 mA cm^{-2} for the Pt/$Cs_{2.5}H_{0.5}PW_{12}O_{40}$ vs. 8 mA cm^{-2} for the bare Pt electrode at 0.8 V vs. RHE) [119]. It is also shown that $Cs_{2.5}H_{0.5}PMo_{12}O_{40}$ facilitates the removal of CO from the Pt sites by the action of its oxo-groups.

Ferrell et al. doped the Pt anode of a DMFC with $H_3PMo_{12}O_{40}$ and $H_3PW_{12}O_{40}$ [125]. Incorporation of the HPAs enhanced the catalytic activity of the electrode towards MOR, with $H_3PW_{12}O_{40}$ yielding the best results.

The utilisation of the catalyst is highly dependent upon its dispersion on the support material, as already mentioned [118]. A more uniform dispersion can enhance the performance of Pt electrodes in methanol and hydrogen fuel cells by increasing the active surface area for reaction [126]. A lot of research has been concentrated on the substitution of the state-of-art carbon supports in fuel cells such as carbon papers and carbon cloths by new high surface area materials. Numerous carbon-based materials are available as supports, including Vulcan carbon black, carbon nanotubes (CNTs), graphite carbon nanofibres (GNFs) and carbon

nanohorns [127]. Therefore, there is a variety of studies based on the immobilisation of HPAs on these new high surface area carbon and graphene supports [118, 127, 128, 129, 130, 131].

There are many different techniques for attaching Pt nanoparticles to carbon nanotubes, including electrodeposition, chemical deposition, layer-by-layer deposition and thermal deposition [132, 128]. Some of these techniques involve the addition of linker molecules to enhance the bonds between Pt particles and the CNTs. These linker molecules may be small organic bridging molecules or polymers (e.g. polyethyleneimine (PEI)-metal ion complexes) [128, 133]. High conductivity is required so that they do not affect the electron transfer between the Pt and CNTs and, consequently, the catalytic activity of the electrode.

After addition of the linker molecules, ethylene glycol or sodium borohydride, which is subsequently removed, is used as a reductant in order to reduce the metal particles to nanoparticles of the required size [128]. HPAs, on the other hand, can be used as both bridging molecules and reductants for the attachment of Pt on carbon supports. HPAs have, consequently, been used as additives on Pt or Pt alloys deposited on a variety of carbon supports.

Li et al. developed a simple, room-temperature procedure for the synthesis of a Pt/CNT nanohybrid with the aid of HPAs [128]. Phosphotungstic acid acted as a simultaneous reductant and bridging molecule for synthesising these hybrids, with the $H_3PW_{12}O_{40}$ subsequently acting as co-catalyst for MOR and CO oxidation [128]. In addition to that simple synthesis process, the electrode exhibited an enhanced electrocatalytic activity toward methanol electrooxidation.

Similar results were obtained by Pan et al., who prepared CNTs modified with $H_7PMo_{12}O_{42}$ by sonication followed by electrodeposition of Pt or Pt-Ru on a pyrolytic graphite (PG) electrode coated with the modified CNTs. The electrodes with modified CNTs yielded better results than those with non-modified CNTs [129]. The exchange current density and specific activity of a PG/CNT-HPA/Pt-Ru electrode were respectively 120% and 159% higher than those of a PG/Pt electrode. Moreover, long-term cycle stability tests (500 cycles) showed that the loss of catalytic activity for the PG/CNT-HPA/Pt-Ru electrode was half that of the PG/Pt electrode.

The addition of HPA to Pt-supported carbon nanotubes has shown comparable enhancements [130]. Seo et al., for example, attached $H_3PMo_{12}O_{40}$ to a Pt/CNT hybrid that was prepared via a colloidal method, using ethylene glycol as a reduc-

tant for Pt^{2+}, rather than applying the HPA directly to the CNTs [128, 130]. An enhancement of ca. 50% in the electroactivity towards methanol oxidation was achieved by better dispersion on the CNTs alone. A further 50% enhancement was achieved by using the $H_3PMo_{12}O_{40}$. Voltammetry studies suggested that the main function of the HPA was to facilitate the removal of CO and other adsorbed intermediates from the Pt surface sites [130].

A variety of other materials have also been tested as supports for MOR active electrodes. Maiyalagan used $H_3SiW_{12}O_{40}$ to enhance the MOR on Pt-Ru nanoparticles that were deposited on CNFs functionalised with carboxyl groups [118]. The resulting electrode showed enhanced activity and improved stability as a result of a wider dispersion of the catalyst on the CNFs and enhanced oxidation of CO intermediates by the heteropolyacid.

Multi-walled carbon nanotubes (MWCNTs) have favourable properties as Pt support materials, such as high electrical conductivity, high specific surface area and exceptional chemical stability. In order to attach Pt to MWCNTs, however, functionalization is required [131]. Jin et al. synthesised $H_3PMo_{12}O_{40}$-MWCNT-Pt and $H_3PMo_{12}O_{40}$/MWCNT/Pt-Ru composites using a one-pot procedure. Their results showed that the HPAs provide better dispersion and a higher electrochemical surface area than MWCNTs alone [131][105]. Interestingly, the average diameter of the Pt or Pt-Ru particles was substantially smaller in the presence of the HPA (by 70% in the case of Pt), which was likely to be the main reason for the increase in active surface area.

Graphene nanosheets (GNS) also possess a high electronic conductivity and a high specific surface area. The manufacturing of GNS by chemical reduction of graphene oxide in solution leads to GNS with a low density of oxygen-containing groups, which makes the attachment and dispersion of Pt or Pt-Ru particles on GNS difficult [127]. This problem can be overcome by applying certain molecules or polymers to the GNS. Since $H_3PMo_{12}O_{40}$ is easily and strongly adsorbed on carbon, it was used by Li et al. to modify GNS as a support material for Pt-Ru nanoparticles [127]. Their results showed that the HPA-modified support improved the activity and the cycle stability of the electrode towards MOR when it was compared to analogous results obtained from a Pt-Ru/GNS electrode. After 200 cycles, the potential of the electrode with the HPA was reduced by 10% and the potential of the electrode without the HPA was reduced by 18% [127].

2.1.1.2.3 Heteropolyacids in DAFC electrodes

HPAs have also been used to enhance ethanol electro-oxidation in other direct alcohol fuel cells, such as ethanol and dimethylether fuel cells [119, 134, 135]. The preferred catalyst at the anode of DEFCs is a Pt alloy containing Sn. The catalytic efficiency of this alloy towards ethanol oxidation is, on the other hand, rather low. The reason is that the ethanol oxidation is a complex reaction that involves the breaking of the carbon-carbon bonds and which requires the removal of poisoning carbon intermediates from the catalyst surface. Dimethylether (DME) is also used as a fuel in direct alcohol fuel cells. DME oxidation yields a total of 12 electrons and the vapour pressure of DME means that it is relatively easy to store with incumbent fuel infrastructures. Moreover, the rate of fuel crossover is low when compared to DMFCs [135]. Even though DME can be adsorbed with ease on platinum, DME oxidation on Pt electrodes requires enhancement.

Barczuk et al. used a molybdenum-containing HPA in an attempt to improve the activity of Pt, Pt-Ru and Pt-Sn electrodes towards ethanol oxidation [134]. The voltammetric and the amperometric catalytic current values were improved with the incorporation of the HPA, with the highest activity on Pt-Sn [134]. It is believed that Mo acts as an oxo-group provider, which aids the removal of CO adsorbates from the Pt surfaces.

When Cs HPA salts, $Cs_{2.5}H_{0.5}PW12O_{40}$ and $Cs_{2.5}H_{0.5}PMo_{12}O_{40}$, were used for the enhancement of ethanol oxidation on Pt nanoparticles, $Cs_{2.5}H_{0.5}PW_{12}O_{40}$ exhibited the greatest stability, whereas $Cs_{2.5}H_{0.5}PMo_{12}O_{40}$ exhibited higher current densities [119].

HPAs ($H_3PMo_{12}O_{40}$, $H_3PW_{12}O_{40}$ and $H_4SiW_{12}O_{40}$) have been used as Pt co-catalysts on the anode of a DME fuel cell [135]. $H_3PW_{12}O_{40}$ and $H_4SiW_{12}O_{40}$ yielded higher current densities and the addition of $H_3PW_{12}O_{40}$ increased the cell current density by 10% [135].

2.2 Bifunctional oxygen/air electrodes

An important part of this thesis is based on bifuctional oxygen/air electrodes that incorporate HPAs, hence it is important to include some basic information about bifunctional oxygen/air electrodes.

As already mentioned, two oxygen reactions take place on a bifunctional oxygen/air electrode, the oxygen reduction and the oxygen evolution reactions. Unfortunately, the kinetics of both reactions are rather slow and the electrochemistry of oxygen is rather complex [10].

Oxygen reduction reaction can happen in two different pathways, the two-electron reduction and the four-electron reduction. The two-electron reduction involves the formation of peroxide (H_2O_2) in acidic environment and HO_2 in alkaline environment), whereas the four-electron reduction leads to the formation of water (H_2O) in acidic environment and the formation of hydroxide in alkaline environment (OH^-).

The four-electron and the two-electron reduction reaction of oxygen in acidic solution are shown below:

Four electron ORR:

$$O_2 + 4\,e^- + 4\,H^+ \longrightarrow 2\,H_2O \tag{C 2.7}$$

Two electron ORR:

$$O_2 + 2\,e^- + 2\,H^+ \longrightarrow H_2O_2 \tag{C 2.8}$$

Peroxide reduction:

$$H_2O_2 + 2\,e^- + 2\,H^+ \longrightarrow 2\,H_2O \tag{C 2.9}$$

Peroxide decomposition:

$$2\,H_2O_2 \longrightarrow O_2 + 2\,H_2O \tag{C 2.10}$$

The four-electron and the two-electron reduction reaction of oxygen in alkaline solution are shown below:

Four electron ORR:

$$O_2 + 2\,H_2O + 4\,e^- \longrightarrow 4\,OH^- \tag{C 2.11}$$

Two electron ORR:

$$O_2 + H_2O + 2\,e^- \longrightarrow HO_2{}^- + OH^- \tag{C 2.12}$$

Peroxide reduction:

$$HO_2{}^- + H_2O + 2\,e^- \longrightarrow 3\,OH^- \tag{C 2.13}$$

Peroxide decomposition:

$$2\,HO_2^- \longrightarrow 2\,OH^- + O_2 \qquad (C\,2.14)$$

Peroxide affects the cell since it corrodes the materials that exist in it. Thus, it decreases the overall performance of the device [136]. Hence, the main aim in ORR catalysis is to achieve the four-electron reduction and avoid the formation of peroxide. The four-electron pathway is favoured in noble metal catalysts, transition metal oxides and transition metal macrocycles, with platinum showing the best catalytic results for ORR [10].

The mechanism of oxygen evolution reaction is also complicated and it is affected by the electrode potential and the electrode material [137, 138]. A good electrocatalyst for OER is a metal that can form and deform oxides easily, since the reaction occurs on the metal oxides of the metallic catalysts [136]. Hence, in this case the commonly used catalyst in fuel cells, platinum, is an inadequate catalyst for OER, since the oxides that are formed on Pt are relatively stable.

There are different designs suggested for the bifunctional oxygen/air electrodes with one of them including one catalyst layer on a single electrode [10]. In that design, the catalysts that are incorporated in the catalyst layer have to be able to enhance both oxygen reactions (OER and ORR). A variety of different materials have been tested as catalysts in bifunctional oxygen/air electrodes depending highly on the potential application of the electrode, since the OER and the ORR mechanisms are not the same under alkaline and under acidic environment. Hence, different catalysts are selected for the bifunctional oxygen/air electrodes in URFCs, where acidic environment exists and different catalysts are chosen when the environment is alkaline, i.e. secondary metal-air batteries.

2.2.1 Catalyst layer

Many different materials have been tested as bifunctional electrocatalysts, for both ORR and OER, in URFCs. Even though platinum exhibits the highest electrocatalytic activity for ORR compared to other metals, its activity for OER is rather poor [139].

Swette et al. have introduced the use of IrO_2 as an efficient electrocatalyst for OER, while $Na_xPt_3O_4$ was suggested as a substance that could be used as an

alternative electrocatalyst after further investigation [140]. The $Na_xPt_3O_4$ resulted after the combination of Na_2CO_3 and Pt_2 and its sodium content can be calculated from the unit cell parameter, a_o, $x = (a_o - 5.59)/0.11$ [140]. Ioroi et al. , have used Pt-Ir, combining two electrocatalysts, one for ORR and one for OER while Cisar et al. have used a combination of Pt black and Ir oxides [141, 142]. Altmann et al. claim that IrO_2 is stable as an electrocatalyst at the oxygen electrode but its low activity requires addition of Pt at the catalyst layer [143].

Chen et al. added Ru in the Pt-Ir combination of catalysts in order to stabilise the surface bonds of the catalysts and increase the reaction rate [144]. Seventy-five different combinations of five candidate elements (Pt, Ru, Os, Ir, Rh) have been tested [144]. These studies concluded that $Pt_{4.5}Ru_4Ir_{0.5}$ showed the best stability and efficiency results as a potential bifunctional electrocatalyst for the oxygen electrode in regenerative fuel cells.

When the oxygen reactions are taking place in alkaline environment the employment of non-noble catalyst is applicable due to the nature of the reactions. Nickel materials have been widely used as catalysts for the oxygen evolution and reduction reactions in alkaline fuel cells, batteries and water electrolysers [145, 146]. The two main reasons that nickel is being chosen are its reversible $Ni(OH)_2/NiOOH$ redox couple and the relatively high stability of metallic Ni to corrosion[146].

However, a few noble materials have been used as catalysts in bifunctional oxygen/air electrodes under alkaline environment [10]. Ag and Pt were effective catalysts for ORR but they were dissolving in OER. $CoIrO_3$, $NiIrO_3$,RhO_2 and IrO_2 showed satisfying results for the oxygen evolution reaction. Swette et al. used $PbPdO_2$ as a catalyst in a bifunctional oxygen/air electrode which exhibited enhancing activity and stability results [147].

Additionally to noble metals, a variety of non-noble materials have been investigated for catalysts, such as transition metal oxides, perovskites, pyrochlorides and spinel oxides. Transition metal oxides or mixed transition metal oxides were acting as good catalysts for OER and ORR and they show good stability in alkaline but they were not optimum due to their low conductivity [10, 148].

The catalytic activity towards OER and ORR of perovskites, pyrochlorides and spinel oxides has been widely explored [147, 149, 150, 151, 152, 153]. The majority of these oxides showed good performance when catalysing the oxygen evolution reaction but they were unstable during the oxygen reduction reaction. $La_{0.6}Ca_{0.4}Co_3$ is one of the perovskites that has been widely used as a catalyst in bifunctional air

electrodes [149, 153]. The most enhancing catalytic results by using $La_{0.6}Ca_{0.4}Co_3$ were recorded after the perovskite has been subjected to thermal treatment [153]. By applying the specific thermal treatment, Lee et al. created a high surface area powder which included $La_{0.6}Ca_{0.4}Co_3$ and so the electrocatalytic activity of the catalyst layer was subsequently improved [153].

$Pb_2Ir_2O_{7-y}$ and $PbBiRu_2O_{7-y}$ are two pyrochlorides that have been used as electrocatalysts for OER and ORR in bifunctional air electrodes under alkaline environment [150]. Both molecules showed satisfying electrocatalytic activity towards both oxygen reactions however they were highly soluble in strongly alkaline electrolytes which was limiting their overall performance. In order to avoid their dissolution, they were stabilised by inserting them in a polymer matrix [150]. Lead ruthenate pyrochlores showed great electrocatalytic performance towards both OER and ORR when applied on a catalyst layer of a bifunctional air electrode [151]. Additionally, when iridium was incorporated in the catalyst improved the electrodes activity towards the oxygen reduction reaction and anion conducting polymers were used to coat the catalyst layer in order to diminish the corrosion of Ru [151].

Finally, $NiCo_2O_4$, Co_3O_4 and Li doped Co_3O_4 are all spinel oxides that have been used as catalyst materials for the oxygen evolution and reduction reactions and they have all exhibited satisfying catalysing activity towards oxygen reactions [152, 154].

2.2.2 Catalyst support

An equally significant part in every electrode is the electrocatalyst support. There are many different electrode designs in literature and many different materials have been used with carbon being the most common [10]. It is usually used in a carbon cloth or a carbon paper form, with Vulcan XC72 and Ketjen being the most popular [155, 156]. Carbon is a preferable material as a catalyst support due to its low cost, wettability, high surface area, wide availability and its high electrical conductivity but unfortunately it cannot stand the oxidative environment of the oxygen electrode and it eventually corrodes [157, 155, 158, 159, 160, 161, 149].

With the aim of improving its performance as an electrode substrate, carbon has been doped with a variety of different elements to develop electronically conductive carbon substitutes such as boron carbides, tungsten carbides, tantalum carbides, titanium carbides and perovskite compounds [13, 162].

Studies have shown that the main reason of the failure of a bifunctional oxygen/air electrode is the corrosion of its carbon substrate [157, 149, 163]. Ross and Sokol have investigated the corrosion of carbon black anodes in alkaline environment [163]. From their investigation it was concluded that carbon dissolves in the oxidative environment of OER and gasifies to carbon monoxide at different temperature values and applied potentials [163]. Additionally, Velraj et al. have performed measurements on a degraded carbon containing bifunctional oxygen/air electrode and regardless the deterioration of the electrode, the electrocatalysts were still active [157]. Hence, in order to improve the lifetime of a bifunctional oxygen/air electrode, alternative materials to carbon have to be employed [157, 164].

A lot of research has been focused on the field of alternative non-carbon materials for the catalyst support. According to Wang et al., there is a number of requirements that a material has to satisfy in order to be a sufficient candidate as a catalyst support [156]:

1. high surface area;
2. high resistivity in corrosion;
3. low solubility in acidic and alkaline media;
4. high electrochemical stability under the cell's operating conditions;
5. sufficient electronic conductivity.

Inorganic metal oxides such as Ti-based, Sn-based, Ru-based, W-based and indium tin oxides and SiO_2, have also been suggested as candidate materials for electrocatalysts support [162].

2.2.2.1 Magnéli phase materials

A specific group of titanium oxides that has been particularly investigated as alternative materials for electrode substrates in electrochemical devices, such as fuel cells and batteries, is the Magnéli phase group [165, 166, 167, 168, 169].

The Magnéli phase materials are a group of substoichiometric composition of titanium oxides with the general formula Ti_nO_{2n-1} with n=3-10 [168]. Magnéli phases, with mostly four or five titanium atoms, are commercially known under the name Ebonex®.

Apart from their interesting magnetic properties, Magnéli phase materials show high electrical conductivity (10^5 S m^{-1}) and high electrochemical stability at high and low pH conditions [170, 171, 172]. In addition to their electrocatalytic activity and their low cost, Magnéli phase materials are very attractive candidates as a non-carbon electrode substrate [170, 165].

Li et al. investigated the electrochemical performance of a glassy carbon modified electrode with Ti_4O_7 (Magnéli phase material) in alkaline environment [165]. They showed that the Magnéli phase modified electrode was active towards both OER and ORR and stable under the existing oxidative conditions [165].

Another study based on the use of Magnéli phase materials as an electrode support of a bifunctional oxygen/air electrode was conducted by Rashkova et al. [169]. Electrocatalytic films of Co-Te-O on Ebonex® were used as a bifunctional electrode for OER and ORR and the obtained results were satisfying for both oxygen reactions [169].

In a US patent based on fuel cells and fuel cell plates, Ebonex® materials have been suggested as substrates for bipolar fuel cell electrodes [173].

Finally, the idea that Magnéli phase materials can be used in electrochemical devices is further justified by a bipolar lead acid battery constructed and commercialised by Atraverda that incorporates Ebonex® into its electrodes [174]. The Ebonex® composite electrodes were highly electrical conductive and chemically resistant to sulphuric acid [168].

2.3 Summary

Based on the literature review some key points were identified.

- Firstly, a great amount of research has been based on heteropolyacids and their application in fuel cells. However, the most of the research has been focused on the investigation of the HPAs in acidic environment.
- Additionally, heteropolyacids have shown that can enhance the ORR in acid but there has not been a similar study in alkaline media.
- It is suggested HPAs show this enhancing ability towards oxygen reactions due to their increased proton mobility and the ability of the HPAs to undergo multiple 1 or 2 e^- reductions without structural deterioration [107].
- Another point that has been raised is the high demand on new materials and designs for the bifunctional electrodes for fuel cells and metal-air batteries which do not include platinum catalysts and can operate under alkaline environment.
- Finally, it has been shown by multiple research groups that carbon corrodes under OER and ORR and hence is not an appropriate candidate as a substrate in O_2/air bifunctional gas diffusion electrodes. For that reason, a lot of research has been based on the investigation of alternative non-carbon materials (e.g. Magnéli phase materials, transition metal oxides, etc.) as candidates for electrode substrates.

Hence, based on these observations, the research of this project is focused on:

- the investigation of the redox activity of HPAs in acidic and alkaline environment;
- the development of a novel gas diffusion electrode architecture for OER and ORR which can operate in alkaline environment and incorporates heteropolyacids and non-carbon active materials.

Chapter 3

Experimental details

3.1 Materials and chemicals

The chemicals used for the electrolytes were: potassium hydroxide (KOH), potassium chloride (KCl) and potassium nitrate (KNO_3) purchased from Fischer Scientific, sulphuric acid (H_2SO_4) from ReAgenta, potassium ferricyanide ($K_3Fe(CN)_6$) from Acros organics. All of them were used as received.

The materials that were used for the formation of the HPA gas diffusion electrodes are: nickel (Ni) nano-powder purchased from Sigma-Aldrich (particle size ¡100nm), nickel carbonate ($NiCO_3{\cdot}2Ni(OH)_2$) (38-40% nickel) purchased from BDH Chemicals Ltd., nickel micro-powder (2-10 μm particle size determined by SEM) purchased from Huizhou Wallyiking Battery Ltd., phosphomolybdic acid ($H_3PMo_{12}O_{40}$), phosphotungstic acid ($H_3PW_{12}O_{40}$) and molybdenum powder (Mo) purchased from Sigma-Aldrich and Toray TGP-H-060 carbon paper based gas diffusion substrate with a carbon black coating base layer purchased by Jonhson Matthey Fuel Cells. All chemicals and materials were used as received. Nafion® (DE-521, 5.0 wt.% in IPA/H_2O) was purchased from DuPont de Nemours and following distillation the final concentration of the solution was 10.7 wt.% Nafion®.

The materials used for the bulk Magnéli electrodes were: Magnéli fibres (2.5 w.t.% organic binder with 260μm diameter) and Magnéli porous tablets (7.5-50 w.t.% organic binder with 1.0 cm diameter) supplied by Vana Adamaki from the University of Bath, aluminium paste purchased from Gwent Electronic Materials Ltd., silver wires (diameter 0.125 mm) from Goodfellow, Epoxy (Quick Set Epoxy Adhesive)

and silver paste and copper tinned wire from RS Chemicals.

The APS titanium sub-oxide coated electrodes were supplied by the Thermal Spray Centre (CPT), University of Barcelona and the PVD coatings of titanium nitride (TiN), titanium nitride with carbon (TiN/C), zirconium nitride (ZrN), chromium nitride (CrN), chromium nitride with carbon (CrN/C) and Graphit_iC^{TM} on stainless steel electrodes were provided by C-Tech Innovation Ltd. They were all used as received.

3.2 Electrolyte preparation

The electrolytes that were used for the experiments were aqueous solution of sulphuric acid (1.0 M H_2SO_4), aqueous solution of potassium chloride (1.0 M KCl), aqueous solution of potassium hydroxide (4.0 M KOH), aqueous solutions of potassium ferricyanide (5.0 mM $K_3Fe(CN)_6$) in potassium nitrate (0.1 M KNO_3), aqueous solutions of potassium ferricyanide (10μM $K_3Fe(CN)_6$) in potassium chloride (1.0 M KCl), aqueous solutions of phosphomolybdic acid (5×10^{-2} M $H_3PMo_{12}O_{40}$ and 10×10^{-2} M $H_3PMo_{12}O_{40}$) in sulphuric acid (1.0 M H_2SO_4), phosphotungstic acid (5×10^{-2} M $H_3PW_{12}O_{40}$) in sulphuric acid (1.0 M H_2SO_4), phosphomolybdic acid (5×10^{-2} M $H_3PMo_{12}O_{40}$) in potassium hydroxide (4.0 M KOH) and phosphotungstic acid (5×10^{-2} M $H_3PW_{12}O_{40}$) in potassium hydroxide (4.0 M KOH). The solutions were prepared by using distilled water from a Purite water purifier.

3.3 Electrochemical techniques

The electrochemical characterisation was performed using an Autolab PGSTAT 30 potentiostat/galvanostat controlled via a PC running Autolab GPES Manager and NOVA by Metrohm Autolab software. The operating temperature was 20°C. During the measurements where fixed air was fed in the electrochemical cell, the air source was unprocessed laboratory air which was supplied using an air pump (Dymax5 Charles Austen Pumps). The oxygen source during the measurements with the fixed oxygen flow was pure O_2 with a steady flow of $100\,cm^3\,min^{-1}$ or $300\,cm^3\,min^{-1}$ and pressure of 30 bar, venting from the cell to atmospheric pressure. The pure oxygen was supplied by a compressed oxygen cylinder (99.5% pure O_2) purchased by BOC.

Cyclic voltammetry is a popular electroanalytical technique which is used to determine the electrochemical performance of new systems and to investigate complex electrode reactions [175]. During cyclic voltammetry, a potential is swept through a range of potentials where an electrode reaction takes place and subsequently the potential is reversed so as to investigate the stability of the products of the reaction and the formation of any other electroactive species [176].

The setup of the experiment in this thesis is based on a three-electrode cell system where a working electrode, a counter electrode and a reference electrode are involved. The three electrodes are immersed in an electrolyte. The reaction which needs to be investigated takes place on the working electrode, the reference electrode monitors the current response of the working electrode during the experiment and the counter electrode is used to balance the potential of the cell.

Important parameters for the cyclic voltammetry are [177]:

- the scanning potential limits;
- the scan rate;
- the initial potential;
- the scan direction;
- the number of cycles;
- the final potential.

In figure 3.1, the results from a cyclic voltammetry where a redox reaction takes place are presented.

Let us assume that the following electron transfer reaction takes place on the working electrode:

$$\mathrm{Ox} + \mathrm{ne}^- \longleftrightarrow \mathrm{Red} \qquad (\mathrm{C}\,3.1)$$

When the scanning is directed towards positive potentials oxidation occurs, while after it is reversed towards negative potentials reduction takes place. Each peak corresponds to an electrode reaction, hence in figure 3.1 two reactions take place, an oxidation reaction (at positive potentials) and a reduction reaction (at negative

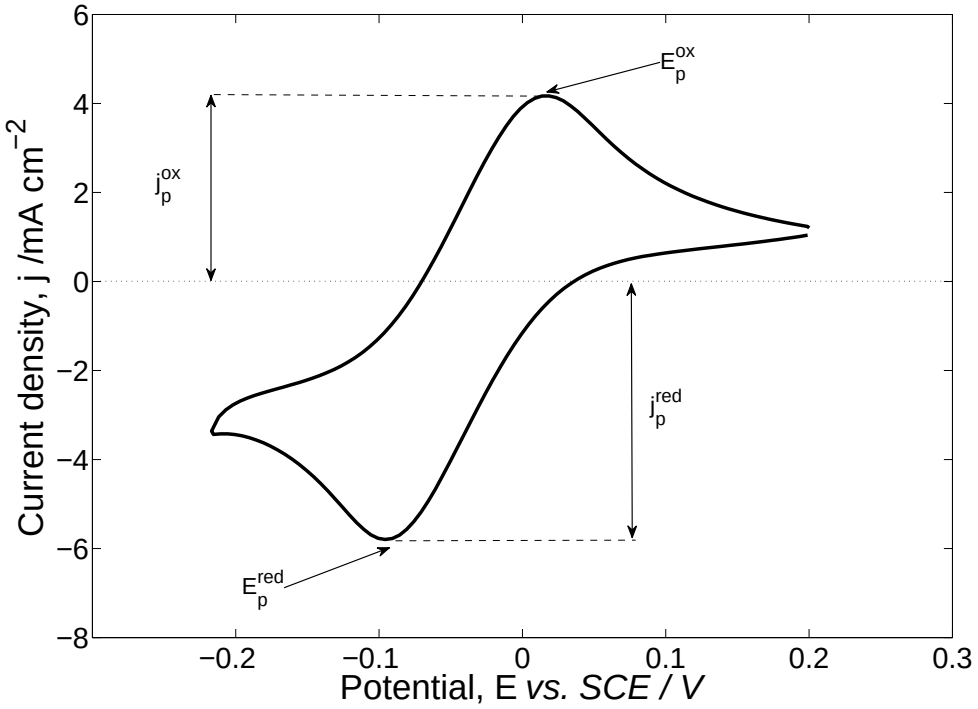

Figure 3.1: *Cyclic voltammogram used as a qualitative example. It corresponds to the voltammogram presented in figure 4.2(b) and page 62.*

potentials). Some of the important characteristics that are monitored in a cyclic voltammogram are the oxidation and reduction potentials (E_p^{ox} and E_p^{red}), and the oxidation and the reduction current density values (j_p^{ox} and j_p^{red}) which are marked in figure 3.1. Except of these, some characteristics which give equally important information about the electrochemical system under investigation are the shape of the peaks and any difference that is noticed after consecutive cycling [176].

For further information on this technique the reader is addressed to references [176], [178] and [175].

3.4 Microscopy

No pretreatment was carried out on the samples before the microscopy. The scanning electron microscope (SEM) was a JSM 6500F thermal emission scanning electron microscope with an accelerating voltage of 0.5-30 kV. The same instrument was used for the energy dispersion X-ray (EDX) analysis. The samples were mounted on the appropriate holder and they were attached on it by using double-sided adhesive tape. Photographic images were taken with a Leica M205C optical

microscope.

3.5 HPA redox activity experiments

3.5.1 Cyclic voltammetry

The electrochemical cell that was used during the investigation of HPA redox activity was a three-compartment cell (Figure 3.2).

A platinum mesh (1.5 cm^2) was used as the counter electrode and a saturated calomel electrode (SCE) was used as the reference electrode. The working electrode was a flat glass carbon disc electrode (GCE) with a diameter of 0.3 cm and a surface area of 0.07 cm^2. The working electrode was placed in the main compartment of the cell in a close distance from the end of the Luggin capillary which was connecting the part of the cell where the reference electrode was placed. The electrode was polished on a 1.00 μm and 0.05 μm Buehler microfibre polishing cloth with a water suspension of alumina (Aluminium oxide Al_2O_3).

The electrolytes that were used during the HPA solution based experiments were 5×10^{-2} M $H_3PMo_{12}O_{40}$ in 1.0 M H_2SO_4, 10×10^{-2} M $H_3PMo_{12}O_{40}$ in 1.0 M H_2SO_4, 5×10^{-2} M $H_3PW_{12}O_{40}$ in 1.0 M H_2SO_4, 5×10^{-2} M $H_3PMo_{12}O_{40}$ in 4.0 M KOH and 5×10^{-2} M $H_3PW_{12}O_{40}$ in 4.0 M KOH.

Additionally, CVs with $H_3PMo_{12}O_{40}$ and $H_3PW_{12}O_{40}$ immobilised on the GCE were performed. The HPA was immobilised on the electrode by first immersing the GCE in a solution of HPA with isopropyl-alcohol (IPA) and subsequently drying it with hot air. The electrolyte used during the measurements was 1.0 M H_2SO_4. The electrolyte solutions were saturated with nitrogen or oxygen for 20 minutes before each measurement. The scan rates of the measurements were 10, 50 and 100 mV sec^{-1}.

3.6 HPA gas diffusion electrodes

The preparation of the HPA gas diffusion electrodes was carried out in two different steps, first the catalyst ink was prepared following which, it was printed on a Toray® carbon gas diffusion layer (GDL) substrate.

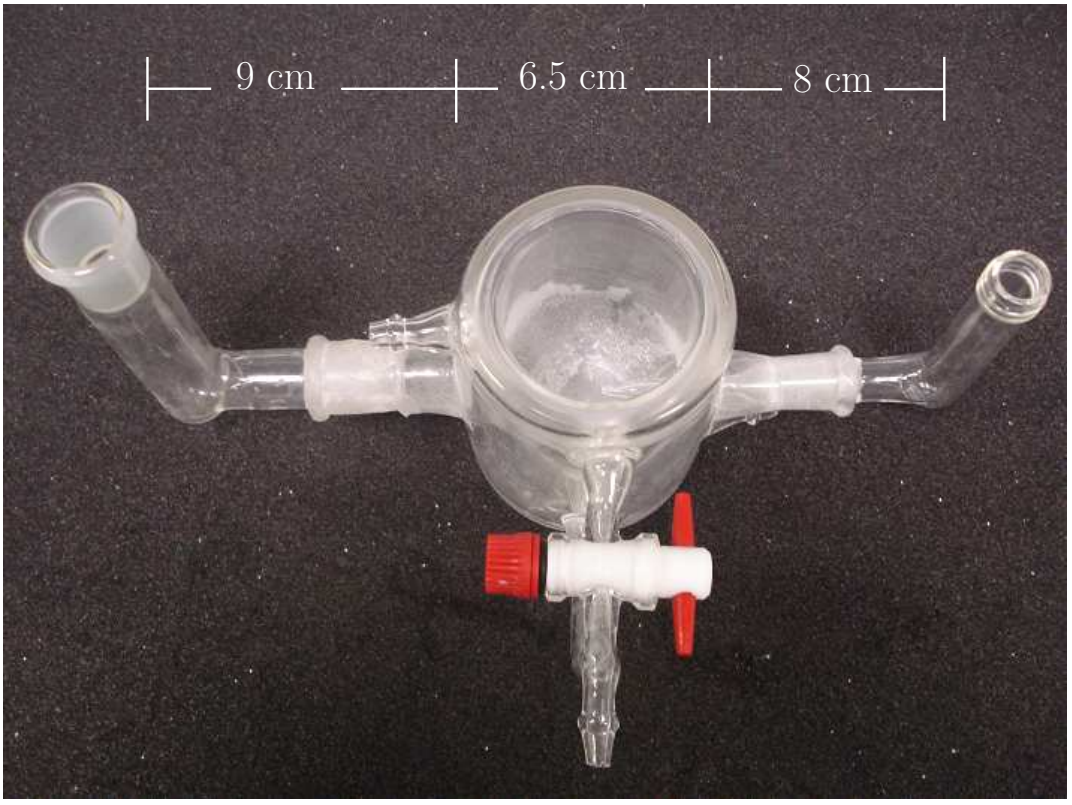

(a)

(b)

Figure 3.2: *The electrochemical cell used during the measurements of the HPA redox activity*

3.6.1 Catalyst ink preparation

The materials that were used for the formation of catalyst inks are nickel (Ni) nano-powder, nickel carbonate ($NiCo_3{\cdot}2Ni(OH)_2{\cdot}2H_2O$), nickel micro-powder, phosphomolybdic acid ($H_3PMo_{12}O_{40}$or PMA), phosphotungstic acid ($H_3PW_{12}O_{40}$ or PWA), molybdenum (Mo) and Nafion®.

Two types of catalyst inks were made, following slightly different methodologies:

1. Catalyst inks with no or low HPA loading ($\leq$ 0.64 mg cm^{-2})
2. Catalyst inks with high HPA loading ($\leq$ 9.35 mg cm^{-2})

For the first inks without HPA, nickel nano-powder or nickel micro-powder (from 0.5 gr to 9.0 gr) were distributed within perfluorinated sulphonic acid ionomer solution, Nafion® (7.5 gr-10 gr). The resulting solution with the nickel and the Nafion® ionomer was mixed to form a homogeneous ink in a high-shear Silverson mixer (L4RT) which was operated at 7,500 r.p.m.. The mixer was fitted with a 2.54 cm high shear tubular head assembly and the mixing time was approximately one hour.

The inks which included heteropolyacids, (from 0.5 gr to 5.0 gr of PMA and 1.55 gr of PWA) or molybdenum (0.95 gr) were created in two consecutive steps. After the solution which contained the nickel and the Nafion® was initially mixed, the additional additives (e.g. PMA, PWA, Mo) were included into the ink. The new solution was then mixed using the high-shear Silverson mixer at 3,000 r.p.m. for ten additional minutes.

A different procedure was followed for the formation of the catalyst inks with high HPA loading which were applied on the electrodes in chapter 6 (page 98). The procedure is the following, unless otherwise stated. The nickel powder (nickel micro-powder or nickel carbonate), the HPA (PMA or PWA) and 12 ml of Iso-propyl alcohol (IPA-C_3H_8O) were mixed with the high-shear Silverson mixer for one hour at 7,500 r.p.m.. The mixed solution was maintained at room temperature (20^{o}C) for four days in order to allow the evaporation of the IPA. After the IPA was evaporated, the Nafion® solution was added in the ink and the new solution was consecutively mixed for one hour with the high-shear Silverson mixer at 7500 r.p.m..

The amount of nickel micro-powder introduced in the inks was kept constant at 6 gr, while the amount of the HPAs was varying. The amount of phosphomolybdic

acid started from 6 gr to 20 gr while the amount of phosphotungstic acid varied from 9.47 gr to 40 gr. Additionally, the amount of nickel carbonate was approximately 4 gr, while the amount of the Nafion® solution varied between 10 to 16 gr.

3.6.2 Printing the electrodes

The electrodes were constructed following a procedure adapted from Wills et al. [179]. The carbon paper was pre-wetted with 50% v/v IPA aqueous solution in order to improve wetting of the ink and produce a catalyst layer with good adhesion and uniformity. The printing was either by screen-printing or by manually spreading the catalyst ink on the pre-wetted GDL with a glass rod. The electrode was then either left to dry at room temperature (20°C) for approximately 20-24 hours or it was placed in the oven at 50°C for 10 minutes.

3.6.3 Cyclic voltammetry

In order to monitor the performance of each HPA gas diffusion electrode a two compartment, three-electrode electrochemical galvanostatic cell made of glass was designed and constructed (Figure 3.3).

The cell was constructed to allow the electrolyte to contact the catalyst-printed face of the GDE, while a controlled gas (O_2 or air) supply was applied to the air-side of the GDE. Sections of the air-breathing electrodes were mounted between the air chamber and the electrolyte sections of the glass cell. A platinum mesh was placed on the air side of the electrode to provide electrical contact to the GDE.

The surface of the working electrode was 1.33 cm^2. During the experiments, the manufactured gas diffusion electrodes were used as the working electrode, platinum mesh (1.5 cm^2) was used as the counter electrode and a saturated calomel electrode (SCE) was used as the reference electrode. A Luggin capillary was incorporated into the cell in order to reduce IR drop between the working electrode and the reference electrode. The experiments were carried out in alkaline electrolyte (4.0 M KOH).

The scan rate during the CVs with the steady O_2 flow was 50 mV sec^{-1} and the scan rates during the CVs with the fixed air flow from the air pump were 50 mV sec^{-1} and 100 mV sec^{-1}. The voltammograms were recorded between different

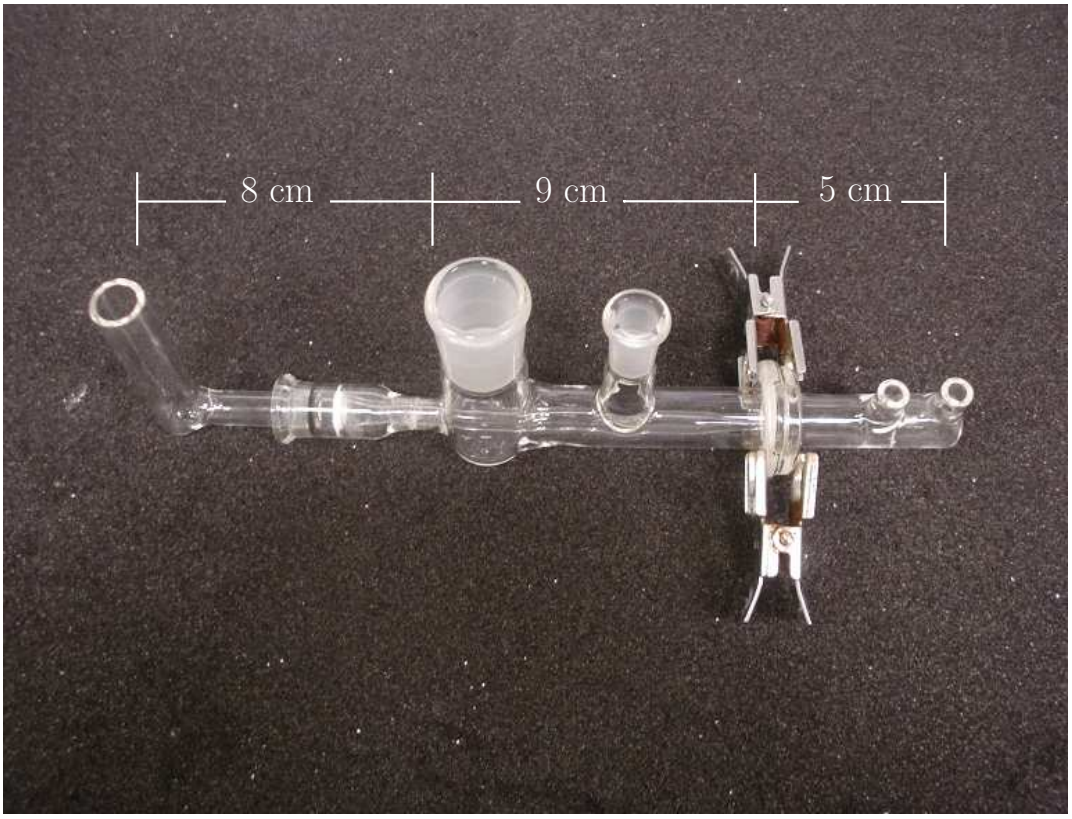

(a)

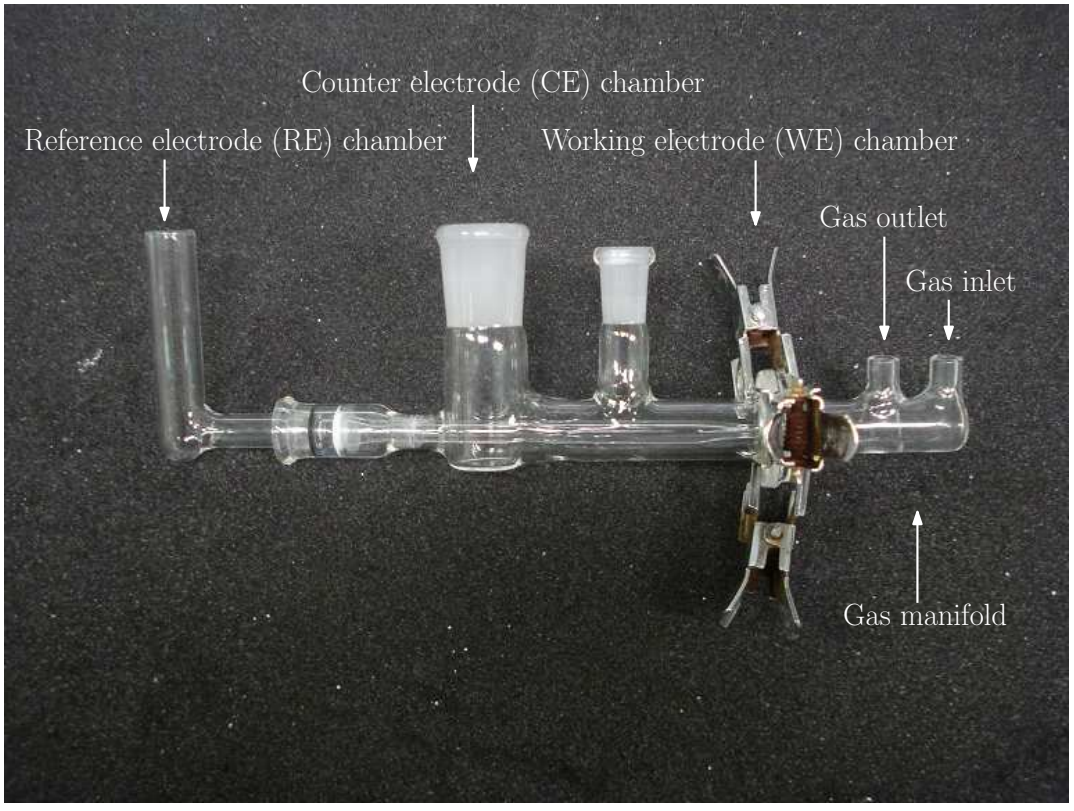

(b)

Figure 3.3: *The electrochemical cell used during the measurements with the HPA gas diffusion electrodes*

potential limits. The scanning during all the voltammetries started from zero potential towards positive potentials, it continued to negative potentials and then back to zero, unless otherwise stated.

3.6.4 Constant current potentiometry

The apparatus for the constant current potentiometry measurements was exactly the same as described in the cyclic voltammetry subsection (Figure 3.3). The electrolyte that was used was 4.0 M KOH and the cell potential was measured every 1 s (interval time $> 0.1s$).

During the potentiometry measurements with the fixed oxygen flow which are presented in chapter 5 (page 83), the applied current density was 44 mA cm^{-2}, the charging/discharging time was 300 sec and six consecutive cycles of charging and discharging were monitored. The applied current density during the experiments with the fixed air flow which are presented in the same chapter (pages 84 and 85) was 50 mA cm^{-2} and 100 mA cm^{-2} while the charging/discharging time was 7200 sec (2 hours) consequently until the electrodes were broken.

During the constant current measurements in chapter 6, the applied current density values varied from 5 mA cm^{-2} to 80 mA cm^{-2}. The duration of the OER/ORR time varied between 600 s and 3,600 s.

3.7 Magnéli phase electrodes

Two types of bulk Magnéli phase materials were electrochemically tested; fibres and tablets. The materials together with information about their characteristics are summarised in table 3.1.

Magnéli material	**Organic binder loading (% w.t.)**	**Diameter (mm)**
Fibres	2.5	0.125
Tablets	7.5	10.4
	10	
	12.5	
	20	
	50	

Table 3.1: *Details of bulk Magnéli electrode materials*

In order to characterise the Magnéli fibres an electrical contact was made using aluminium paste to silver wires. The fibres were afterwards dried at 120°C for 10 minutes and then fired at 710°C for 10 minutes.

After the electrical contact was created, the fibre was mounted in a plastic pipette, where subsequently Epoxy was added to insulate and stabilise the fibre. After the Epoxy has dried and the microelectrode was solid, the tip of the pipette was polished with two different emery papers (800 grit and 1200 grit) by using a polishing wheel in order to reveal the tip of the fibre and to create a uniform planar Magnéli electrode (Figure 3.4).

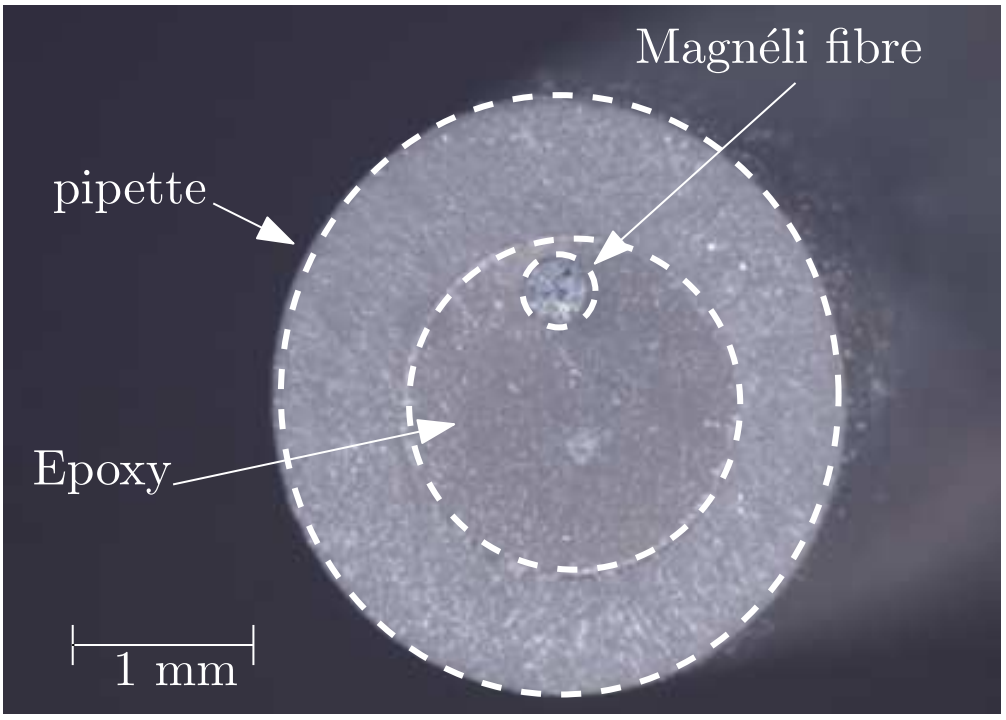

Figure 3.4: *An image of the microelectrode with the Magnéli fibre*

Magnéli tablets with varying porosity were also tested. During the manufacturing procedure for the Magnéli fibres, 2.5% w.t. organic binder (polyethylene glycol-PEG 8000) was used. In order to increase the porosity of the samples and limit the grain growth, the percentage of the organic binder which was involved was increased. The different percentages of binder loading that was used for the different tablets was: 7.5, 10, 12.5, 20 and 50 w.t.%, consecutively.

In order to characterise the Magnéli tablets they had to be converted into planar electrodes. Firstly, an electrical contact was made on the top surface of the tablet, by using silver paste and copper tinned wire. Silver paste was used instead of the aluminium paste because the aluminium paste requires a temperature treatment

after its application (120°C for 10 minutes and then 710°C for 10 minutes) which could possibly affect the porosity of the tablet.

The Magnéli tablet was then inserted into a plastic tube with a similar diameter size of the tablet that would only let its bottom surface being in contact with the electrolyte (Figure 3.5).

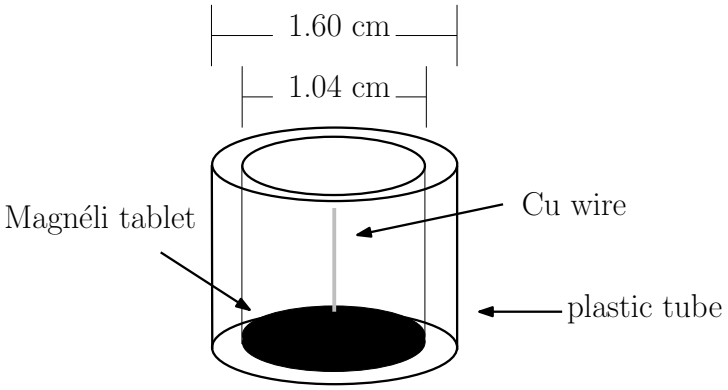

Figure 3.5: *The design of the electrode with the Magnéli tablet*

3.7.1 Cyclic voltammetry

For the cyclic voltammetries on the microelectrodes with the Magnéli fibres and on the electrodes with the Magnéli tablets, the electrochemical cell which is shown in figure 3.2 was used. The counter electrode was a platinum mesh (1.5 cm^2), the reference electrode was a saturated calomel electrode (SCE), while the Magnéli electrodes were the working electrodes. The working electrode area of the microelectrodes with the Magnéli fibres was 0.05 mm^2, while the working electrode area of the electrodes with the Magnéli tablets was 0.85 cm^2. The working electrode was placed in the main compartment of the cell in a close distance from the end of the Luggin capillary which was connecting the part of the cell where the reference electrode was placed. The Magnéli fibres in the pipettes were polished on a 1.00 μm and 0.05 μm Buehler microfibre polishing cloth with a water suspension of alumina (Aluminium oxide-Al_2O_3) and they were subsequently rinsed with distilled water before each measurement.

The electrolytes used were 10 μM $K_3Fe(CN)_6$ in 1.0 M KCl, 1.0 M H_2SO_4, 5×10^{-2} M PWA in 1.0 M H_2SO_4 and 5.0 mM $K_3Fe(CN)_6$ in 0.1 M KNO_3. The scan rates during the cyclic voltammetries were 20, 50 and 100 mV sec^{-1}. The solutions were de-oxygenated by using nitrogen for 20 minutes before the beginning

of the measurements, unless otherwise stated. The voltammograms were recorded between different potential limits.

3.8 APS & PVD coated substrates

Electrochemical characterisation measurements were conducted on different coated electrodes. The substrates were stainless steel, aluminium and carbon polymer substrates and they have been coated by using (i) atmospheric plasma spray (APS) application or (ii) physical vapour deposition (PVD). The coatings and substrates of the characterised samples are summarised in table 3.2.

Substrates	**Coating method**	**Materials**	**Particle size, (μm)**
Stainless steel	PVD	TiN	0.75
		ZrN	1.00
		CrN + C	($\approx$1.00)
		CrN	1.00
		TiN	1.30
		C	0.2-3.00
		Graphit_iC^{TM}	1.10
Aluminium	APS	Magnéli	N/A
Carbon polymer			

Table 3.2: *Details of the coatings that have been used on the different substrates*

Atmospheric plasma spray was used to coat stainless steel (0.5 cm and 0.5 mm thick), aluminium (1 mm thick) and carbon polymer substrates (4 mm thick) (table 3.2). The coating was made of a powder based on rutile TiO_2 and Magnéli phases (Ti_8O_{15} and Ti_9O_{17}) which was sprayed by using an APS A-3000S system with an F4 plasma torch (Sulzer Metco, Germany). The APS coated electrodes were prepared at the Thermal Spray Centre, CPT, University of Barcelona. It has to be noted that the conductive part of the APS coating is the Magnéli sub-oxide phases so in this thesis, the name used to refer to these electrodes is *APS Magnéli phase coated electrodes*.

More information about the particle sizes of the PVD coatings of TiN, TiN & C, ZrN, CrN, CrN & C and Graphit_iC^{TM} are summarised in table 3.2.

3.8.1 Cyclic voltammetry

The electrochemical cell that was used during the cyclic voltammetries on the APS Magnéli spray coated electrodes and the PVD coated electrodes is shown in figure 3.6. The surface of the working electrode in this cell is 1.13 cm^2. Each electrode was rinsed with distilled water before being used as a working electrode. The counter electrode was a platinum mesh (1.5 cm^2) and the reference electrode was a saturated calomel electrode (SCE). The experiments were carried out in aqueous solutions of 1.0 M H_2SO_4, 1.0 M KCl and 4.0 M KOH. The electrolytes were de-oxygenated by using nitrogen for 15 minutes before the beginning of each measurement. The scan rates were 50 mV sec^{-1} and 100 mV sec^{-1}. The voltammograms were recorded between different potential limits. The scanning during all the voltammetries started from zero potential towards positive potentials, it continued to negative potentials and then back to zero, unless otherwise stated.

(a)

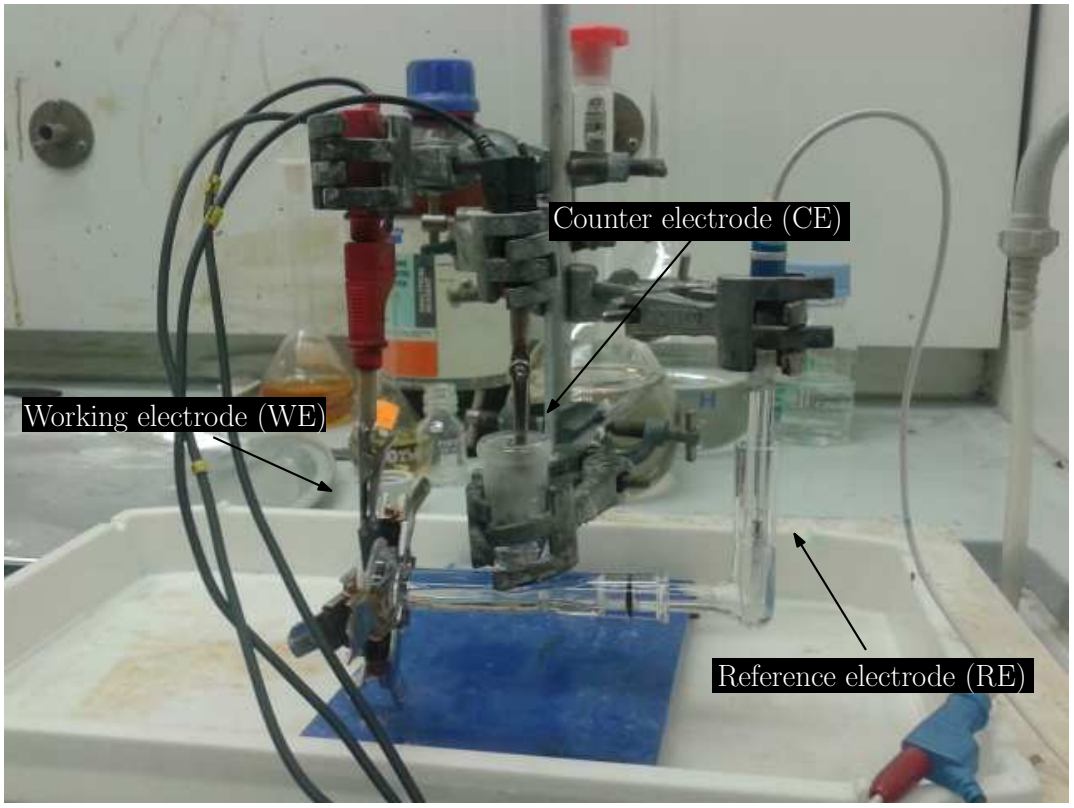

(b)

Figure 3.6: *The glass electrochemical cell used for the characterisation of the different coated electrodes*

Chapter 4

Investigation of the redox activity of HPAs

4.1 Introduction

The redox behaviour of the heteropolyacids was first observed in 1864 [180]. Different techniques, such as polarography [181, 182, 183], cyclic voltammetry [184, 185, 186, 187, 188, 189, 190, 191, 192], optical spectroscopy [193], UV-visible spectroscopy [194], nuclear magnetic resonance (NMR) [195, 196], scanning tunnelling microscopy (STM) [197], tunnelling spectroscopy (TS) [197], IR spectroscopy [33, 196, 183], electronic spectroscopy [195], X-ray diffraction [183], and more recently computational analytical methods (e.g. density functional theory/DFT)[198, 199] have been applied to characterise heteropolyacids.

It is known from the literature that Keggin type heteropolyacids are redox active with reversible one- and two-electron reactions [186]. The redox potential of the heteropolyacids depends mostly on the addenda atoms and secondary on the heteroatoms of the molecule, while the number of the electrons that are transferred during the redox reactions depends strongly on the charge of the heteropolyacid and on the pH and the nature of the electrolyte [33, 200, 201, 27, 190].

The electrochemical behaviour of the HPAs has previously been studied either by dissolving them in a supporting electrolyte or by immobilising them on an electrode surface, e.g. graphite, glassy carbon etc. [33, 188, 186].

The HPAs that are used in this project are phosphomolybdic acid ($H_3PMo_{12}O_{40}$) and phosphotungstic acid ($H_3PW_{12}O_{40}$). Both acids were chosen according to a

review of literature. It was shown that phosphomolybdic acid can act as a catalyst for the oxygen reduction reaction in acidic environments, while phosphotungstic acid has been readily applied as an additive in fuel cell membranes and electrodes whereas they both HPAs have exhibited steady and significant current densities in acidic media [19, 191, 107].

Despite these heteropolyacids have found application in energy conversion technologies as redox mediators and membrane additives, they have so far not been exploited directly either as energy storage active materials or in alkali environments. In this chapter, their electrochemical response when dissolved in acid (1.0 M H_2SO_4) and alkaline (4.0 M KOH) solutions along with their response when they are immobilised on an electrode surface are exploited.

4.2 Results and discussion

4.2.1 Cyclic voltammetries

4.2.1.1 Heteropolyacids dissolved in acidic solution

In figure 4.1, voltammograms of phosphomolybdic acid dissolved in sulphuric acid are shown. The two electrolytic solutions were 5×10^{-2} M PMA in 1.0 M H_2SO_4 and 10×10^{-2} M PMA in 1.0 M H_2SO_4, respectively. The electrolyte was de-oxygenated for 20 minutes before each measurement.

For the voltammetry of 5×10^{-2} M PMA in H_2SO_4, the potential was scanned from 0.6 V *vs.* SCE towards negative potentials. At -0.15 V *vs.* SCE the sweep direction was reversed and the potential returned to 0.6 V *vs.* SCE. The scanning during the voltammetry of 10×10^{-2} M PMA in H_2SO_4 started from 0.75 V *vs.* SCE towards negative potentials, it continued until -0.3 V *vs.* SCE and then back to 0.75 V *vs.* SCE.

A first ill-defined reduction peak in the voltammogram of 5×10^{-2} M PMA in the supporting electrolyte is observed at 0.45 V *vs.* SCE, a second well-defined reduction peak is observed at 0.35 V *vs.* SCE, a third well-defined reduction peak is observed at 0.17 V *vs.* SCE and a fourth well-defined reduction peak is observed at -0.04 V *vs.* SCE. In the same voltammogram, four oxidation peaks are observed at 0.03, 0.24, 0.41 and 0.49 V *vs.* SCE, respectively. The first, the second

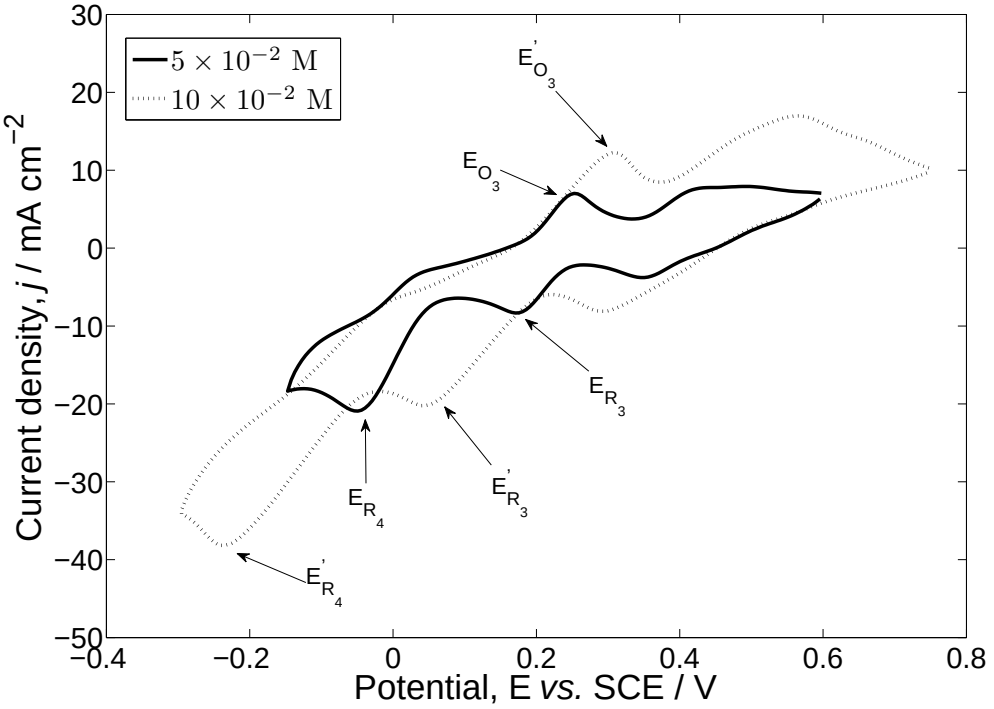

Figure 4.1: *Cyclic voltammograms of 5×10^{-2} M PMA (black line) and 10×10^{-2} M PMA (dotted line) dissolved in 1.0 M H_2SO_4. The electrolyte was saturated with nitrogen gas. The fourth cycle of each voltammogram is presented. The scan rate of the voltammogram was 100 mV sec^{-1} and the temperature was 20^{o}C. The working electrode area was 0.07 cm^2.*

and the fourth oxidation peaks are ill-defined while the third oxidation peak is a well-defined peak.

In the voltammogram of the more concentrated HPA solution (10×10^{-2} M PMA in 1.0 M H_2SO_4), the redox peaks are more broad when compared to the peaks of the voltammogram of 5×10^{-2} M PMA in H_2SO_4. Three well-defined reduction peaks are observed at 0.29, 0.04 and -0.23 V *vs.* SCE and an ill-defined reduction peak is observed at 0.54 V *vs.* SCE. Four oxidation peaks are observed at -0.01, 0.31, 0.57 and 0.65 V *vs.* SCE. Similarly, to the voltammogram of 5×10^{-2} M PMA, first, the second and the fourth oxidation peaks in the voltammogram of 10×10^{-2} M PMA are ill-defined peaks, while the third oxidation peak is a well-defined peak.

Additionally, the current density value observed at the fourth reduction peak (E'_{R_4}) of the voltammogram of the 10×10^{-2} M PMA is $j = -38.16$ mA cm^{-2}, which is two times higher than $j = -20.9$ mA cm^{-2} which is the current density value which is observed at the fourth reduction peak (E_{R_4}) of the voltammogram of 5×10^{-2} M PMA. Hence, it can be observed that the current density values which

were exhibited during the voltammograms depend on the concentration of PMA in the supporting electrolyte, since the solution with the double PMA concentration (10×10^{-2} M PMA) exhibited two times higher current density values.

For a fully reversible redox reaction, both oxidants and reactants have to be dissolved and stable in the electrolyte while the electron transfers have to be fast [176]. There are qualitative and quantitative methods that can be followed in order to judge whether a redox reaction is reversible or irreversible based on a cyclic voltammogram.

Qualitatively, the first test is with experience and by eye. Some very general rules describing the shape of a voltammogram of a reversible redox couple are that the potential difference between the oxidation and the reduction peak should be small and that the peaks should be high and steep [176].

From the shapes of the voltammograms in figure 4.1, it can be seen that neither voltammogram fulfils the above requirements, since the peaks are broad and there is great separation peak for the most of the redox couples.

However, it has to be noted that the concentration of the PMA (5×10^{-2} M PMA and 10×10^{-2} M PMA) in the supporting electrolyte is very high for voltammetry, since the concentration of a dissolved species in a supporting electrolyte is usually around 5×10^{-3} M. So, the irreversible shapes of the redox peaks of the voltammograms are possibly due to the high IR effect which results from the high PMA concentration.

There are a few diagnostic tests that help towards a more quantitative analysis on the reversibility of a redox reaction [176]. One of these diagnostic tests is based on the potential difference between the reduction and the oxidation peak potentials. According to Pletcher, for a reversible reaction it applies that [176]:

$$E_{O-R} = E_O - E_R = \frac{59}{n}mV \tag{4.1}$$

where E_{O-R} is the potential difference between the oxidation and the reduction peak, E_O is the oxidation peak potential, E_R is the reduction peak potential and n is the number of electrons which is transferred during the redox reaction.

However, if the potential difference is larger than that,

$$E_{O-R} = E_O - E_R > \frac{59}{n}mV \text{ and } f(k_s, v) \tag{4.2}$$

then the redox reaction is irreversible.

This reversibility test will be applied on the third redox couple of both voltammograms of 5×10^{-2} M PMA and 10×10^{-2} M PMA in 1.0 M H_2SO_4. These specific redox couples were chosen because they show the most well-defined peaks in each voltammogram which is an indication of reversibility, since the steeper the redox peaks are, the more reversible the redox reaction is [176].

These two redox couples, E_{R_3}/E_{O_3} and $E^{'}_{R_3}/E^{'}_{O_3}$, are labelled in figure 4.1. The third reduction peak of the voltammogram of 5×10^{-2} M PMA is E_{R_3} and the third oxidation peak is E_{O_3}, while the third reduction peak of the voltammogram of 10×10^{-2} M PMA is $E^{'}_{R_3}$ and the second oxidation peak is $E^{'}_{O_3}$.

The number of the electrons which are transferred during the second redox transfer are $n = 2$ and the potential difference between the oxidation and the reduction peak of the voltammogram of 5×10^{-2} M PMA in 1.0 M H_2SO_4 is :

$$\begin{aligned} E_{O_3-R_3} &= E_{O_3} - E_{R_3} \\ &= 0.24 - 0.17 \\ &= 0.07\,V \\ &= 70\,mV > \frac{59}{n}mV \qquad\qquad n = 2 \\ &= 70\,mV > 29.5\,mV \end{aligned}$$

While, the potential difference between the oxidation and the reduction peak of the voltammogram of 10×10^{-2} M PMA in 1.0 M H_2SO_4 is :

$$\begin{aligned} E^{'}_{O_3-R_3} &= E^{'}_{O_3} - E^{'}_{R_3} \\ &= 0.31 - 0.04 \\ &= 0.27\,V \\ &= 270\,mV > \frac{59}{n}mV \qquad\qquad n = 2 \\ &= 270\,mV > 29.5\,mV \end{aligned}$$

Based on the results from the reversibility diagnostic tests, it was shown that both redox reactions are irreversible. However, the potential difference between the E_{O_3} and the E_{R_3} is smaller (70 mV) when compared to the potential difference between $E^{'}_{O_3}$ and $E^{'}_{R_3}$ (270 mV). This difference shows that IR drop in the voltammogram of 5×10^{-2} M PMA in H_2SO_4 is less when compared with the IR drop which is

observed in the voltammogram of 10×10^{-2} M PMA in H_2SO_4.

That shows that the kinetics of the redox reactions are slower when the amount of the PMA in the supporting electrolyte is higher due to IR drop. However, the current density values that are shown in the voltammogram of 10×10^{-2} M PMA in 1.0 M H_2SO_4 are higher when compared to the current density values which are observed in the voltammogram of 5×10^{-2} M PMA in 1.0 M H_2SO_4, since for example, the current density at E_{O_2} is at 8 mA cm^{-2}, while the corresponding value at E'_{O_2} is at 12 mA cm^{-2}.

Hence, this initial characterisation of PMA in H_2SO_4 showed that its redox reactions are irreversible possibly due to high IR drop.

In figure 4.2, the voltammogram of 5×10^{-2} M PWA in 1.0 M H_2SO_4 is shown. The electrolyte was de-oxygenated for 20 minutes with nitrogen gas before each measurement.

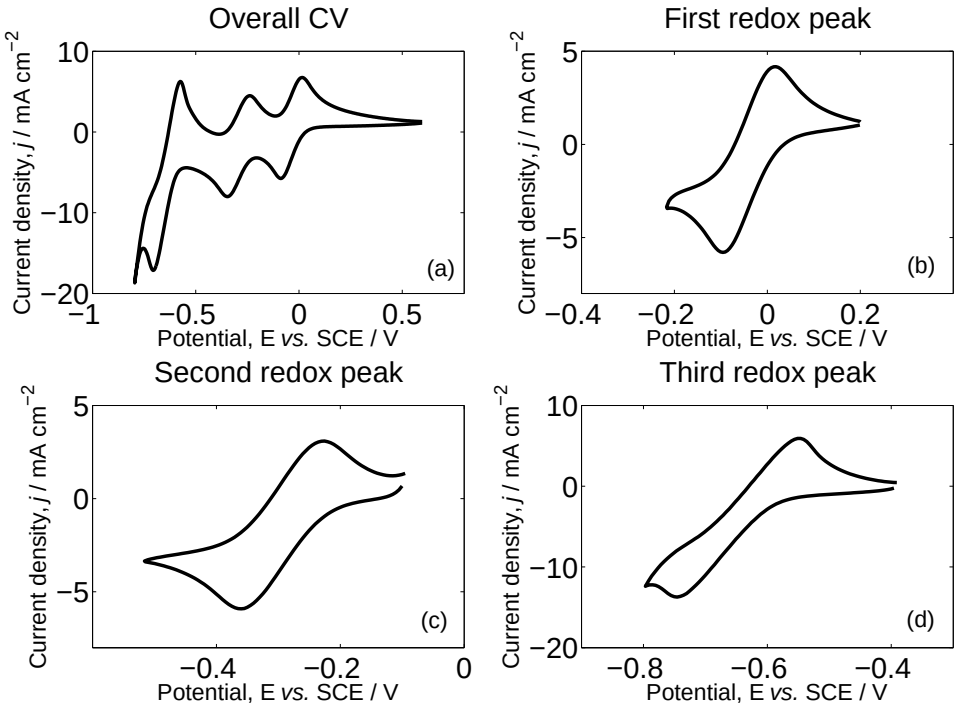

Figure 4.2: *Cyclic voltammograms of 5×10^{-2} M PWA dissolved in 1.0 M H_2SO_4; (a) is the overall voltammogram, (b) is the voltammogram of the first redox peak, (c) is the voltammogram of the second redox peak and (d) is the voltammogram of the third redox peak. The electrolyte was saturated with nitrogen gas. The second cycle of each voltammogram is presented. The scan rate of the voltammogram was 100 mV sec^{-1} and the temperature was 20^{o}C. The working electrode area was 0.07 cm^2.*

For the voltammetry in figure 4.2(a), the potential was scanned from 0.6 V *vs.*

SCE towards negative potentials. At -0.8 V *vs.* SCE the sweep direction was reversed and the potential returned to 0.6 V *vs.* SCE.

Three well-defined redox couples are observed in this voltammogram. These redox couples are shown separately in figures 4.2(b), 4.2(c) and 4.2(d). In these voltammograms, the scanning potential limits were adjusted accordingly, in order to include only one redox couple in each voltammogram.

The scanning during the voltammetry in figure 4.2(b) started from 0.2 V *vs.* SCE towards negative potentials, it continued until -0.22 V *vs.* SCE and then back to 0.2 V *vs.* SCE. For the voltammetry in figure 4.2(c), the potential was scanned from -0.095 V *vs.* SCE towards negative potentials. At -0.52 V *vs.* SCE the sweep direction was reversed and the potential returned to -0.095 V *vs.* SCE. The scanning during the voltammetry in figure 4.2(d) started from -0.39 V *vs.* SCE towards negative potentials, it continued until -0.8 V *vs.* SCE and then back to -0.39 V *vs.* SCE.

According to the literature, the redox reactions of PWA that are taking place in acidic aqueous solutions are the following [186]:

$$PW_{12}O_{40}{}^{3-} + e^- \longleftrightarrow PW_{12}O_{40}{}^{4-} \qquad (C\,4.1)$$

$$PW_{12}O_{40}{}^{4-} + e^- \longleftrightarrow PW_{12}O_{40}{}^{5-} \qquad (C\,4.2)$$

$$PW_{12}O_{40}{}^{5-} + 2\,e^- + H^+ \longleftrightarrow HPW_{12}O_{40}{}^{6-} \qquad (C\,4.3)$$

Hence, based on the literature and on the voltammetries in figure 4.2, the first two reduction peaks which are observed at -0.09 and -0.34 V *vs.* SCE correspond to two, one-electron reductions and the third reduction peak which is observed at -0.71 V *vs.* SCE corresponds to a two-electron reduction. It can be stated that this observation confirms the literature [186, 182, 202]. The three corresponding oxidation peaks are observed at -0.57, -0.24 and 0.02 V *vs.* SCE, respectively.

The voltammograms in figure 4.2 have well-defined redox peaks and the peak

separation is small, so it is possible to have reversible redox reactions. However, this has to be tested quantitatively, so in order to test the reversibility of the three redox reactions, the diagnostic test which was already used previously (equation 4.1) is applied.

For the first redox couple it is:

$$E_{(O-R)_1} = 110\,mV > 59\,mV$$

For the second redox couple it is:

$$E_{(O-R)_2} = 100\,mV > 59\,mV$$

And for the third redox couple it is:

$$E_{(O-R)_3} = 140\,mV > 29.5mV$$

From these results it is shown that the redox reactions that are observed are not fully reversible, since none of them satisfies the equation 4.1. However, the potential difference between the oxidation and the reduction peak of each redox couple is not much higher than the value (59 mV) which defines reversibility. Additionally, the redox couples can be easily isolated and identified.

In both figures 4.2 and 4.3, the results from the electrochemical characterisation of phosphotungstic acid (PWA) dissolved in H_2SO_4 are shown. The only difference in these two figures is that before the measurement in figure 4.2, the electrolyte was saturated with nitrogen gas while before the measurement in figure 4.3, the electrolyte was saturated with oxygen gas.

In figure 4.3, the electrolyte was oxygenated for 20 minutes before the measurement. The cycling during the voltammetry in figure 4.3(a) started from 1.2 V *vs.* SCE towards negative potentials, it continued until -1.2 V *vs.* SCE and then back to 1.2 V *vs.* SCE.

As with the de-oxygenated CVs in figure 4.2, three redox peaks are observed in the voltammogram in figure 4.3. In figures 4.3(b), 4.3(c) and 4.3(d), these three redox couples are separately presented. The cycling during the voltammetry in figure 4.3(b) started from 0.3 V *vs.* SCE towards negative potentials, it continued until -0.3 V *vs.* SCE and then back to 0.3 V *vs.* SCE. For the voltammogram

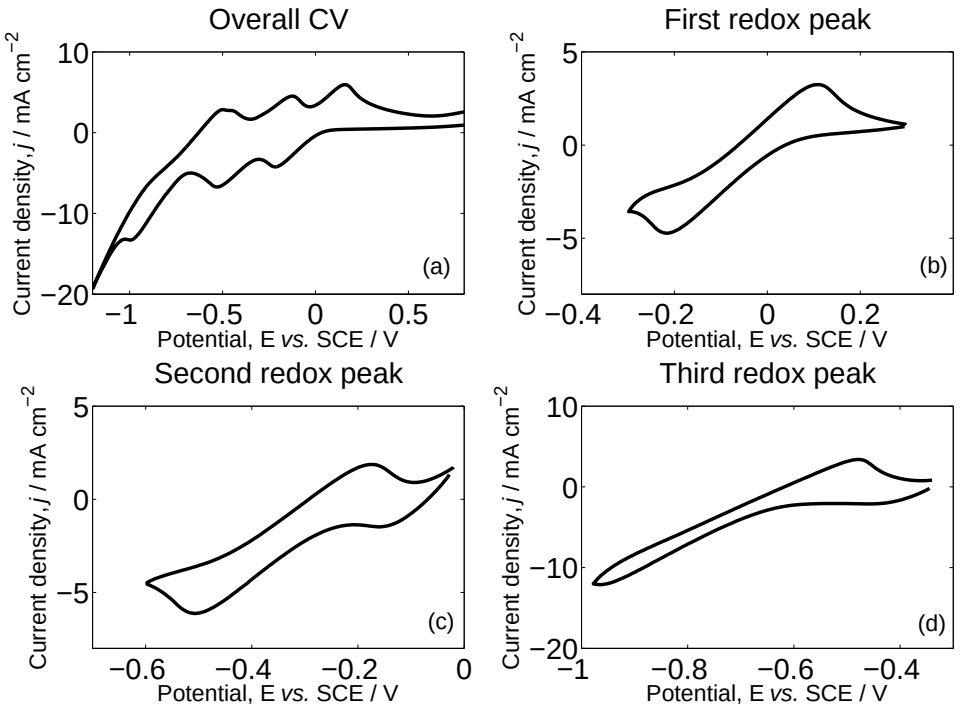

Figure 4.3: *Cyclic voltammograms of 5×10^{-2} M PWA in 1.0 M H_2SO_4; (a) is the overall voltammogram, (b) is the voltammogram of the first redox peak, (c) is the voltammogram of the second redox peak and (d) is the voltammogram of the third redox peak. The electrolyte was saturated with oxygen gas. The second cycle of each voltammogram is presented. The scan rate of the voltammogram was 100 mV sec^{-1} and the temperature was 20°C. The working electrode area was 0.07 cm^2.*

in figure 4.3(c) the potential was scanned from -0.02 V *vs.* SCE towards negative potentials. At -0.6 V *vs.* SCE the sweep direction was reversed and the potential returned to -0.02 V *vs.* SCE. The scanning during the voltammetry in figure 4.3(d) started from -0.34 V *vs.* SCE towards negative potentials, it continued until -0.98 V *vs.* SCE and then back to -0.34 V *vs.* SCE.

The reduction peaks are observed at -0.21, -0.51 and -0.96 V *vs.* SCE, while the three main oxidation peaks are shown at -0.48, -0.17 and 0.11 V *vs.* SCE.

The voltammograms in figure 4.3 show that the first and the second redox couples can be easily isolated. However, it is not as simple for the third redox couple since the third oxidation peak is at -0.5 V *vs.* SCE which is very close to the potential value were the second reduction peaks appears (-0.53 V *vs.* SCE). The first two redox couples are believed to be two one-electron reactions and the third redox couple is believed to be a two-electron reaction.

All three redox reactions show slow kinetics for the electron transfer since there is a high separation peak between the oxidation and the reduction peak of each

couple.

Hence, the same diagnostic test (equation 4.1) will be applied in figure 4.3, in order to test whether the the redox reactions are irreversible or not.

For the first redox couple it is:

$$E'_{(O-R)_1} = 320\,mV > 59\,mV$$

For the second redox couple it is:

$$E'_{(O-R)_2} = 680\,mV > 59\,mV$$

For the third redox couple it is:

$$E'_{(O-R)_3} = 480\,mV > 29.5\,mV$$

As already assumed from the shape of the voltammograms, the results from this diagnostic test confirmed that the redox reactions in figure 4.3 are irreversible, since the values of the potential difference between the oxidation and the reduction peaks were greater than the potential value which defines reversibility.

In general, taking into account the results from the quantitative test on the reversibility of both voltammograms, the potential difference between the oxidation and the reduction peaks at the voltammograms of figure 4.2 were smaller (110 mV, 100 mV and 140 mV) when compared to the same values at the voltammogram of figure 4.3 (320mV, 680mV and 480 mV). This shows that the redox couples are more reversible when the electrolyte is de-oxygenated with nitrogen gas which could mean that oxygen forms a film on the electrode which affects the redox reactions.

4.2.1.2 Heteropolyacids dissolved in alkaline solution

The redox behaviour of phosphomolybdic and phosphotungstic acids have been documented in acidic solutions [185, 189, 188] but they have not been investigated in alkaline solutions for OER and ORR.

Therefore, an initial electrochemical characterisation of phosphomolybdic and phosphotungstic acid in an alkaline electrolyte (4.0 M KOH) was conducted and

the results are presented in this section.

In figure 4.4, the voltammogram of 5×10^{-2} M PMA in 4.0 M KOH is shown. The electrolyte was de-oxygenated for 20 minutes with nitrogen gas before the cycling.

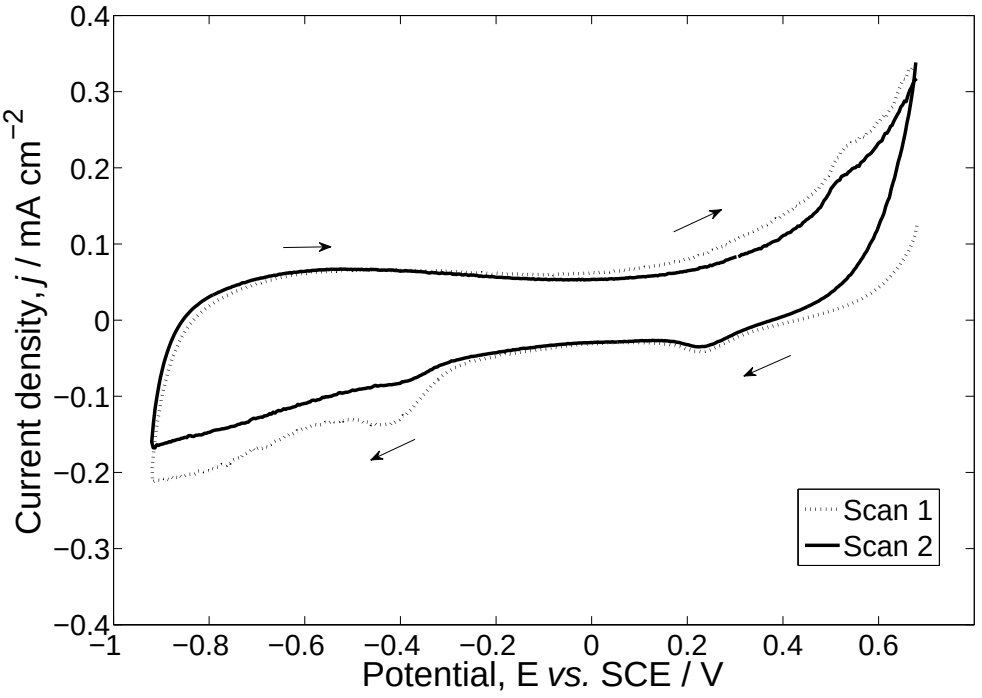

Figure 4.4: *Cyclic voltammograms of 5×10^{-2} M PMA in 4.0 M KOH. The electrolyte was saturated with nitrogen gas. The first cycle (dotted line) and the second cycle (black line) of the voltammogram are presented. The scan rate of the voltammogram was 100 mV sec^{-1} and the temperature was 20°C. The working electrode area was 0.07 cm^2.*

During the CV, the potential was scanned from 0.68 V *vs.* SCE towards negative potentials. At -0.92 V *vs.* SCE the sweep direction was reversed and the potential returned to 0.68 V *vs.* SCE.

Two small reduction peaks are observed at 0.23 and -0.40 V *vs.* SCE and an ill-defined oxidation peak is observed at 0.5 V *vs.* SCE. The redox activity of PMA decays quickly since during the second cycle, the second reduction peak has almost disappeared. Therefore, the voltammogram in figure 4.4 shows that phosphomolybdic acid does not show strong redox behaviour in alkaline solutions, since it is likely they decompose in this environment [203].

The voltammogram of 5×10^{-2} M PWA in 4.0 M KOH is presented in figure 4.5. The electrolyte was de-oxygenated for 20 minutes with nitrogen gas before the measurement. The scanning during the voltammetry of 5×10^{-2} M PWA in 4.0 M

KOH started from 1.3 V *vs.* SCE towards negative potentials, it continued until -1.8 V *vs.* SCE and then back to 1.3 V *vs.* SCE.

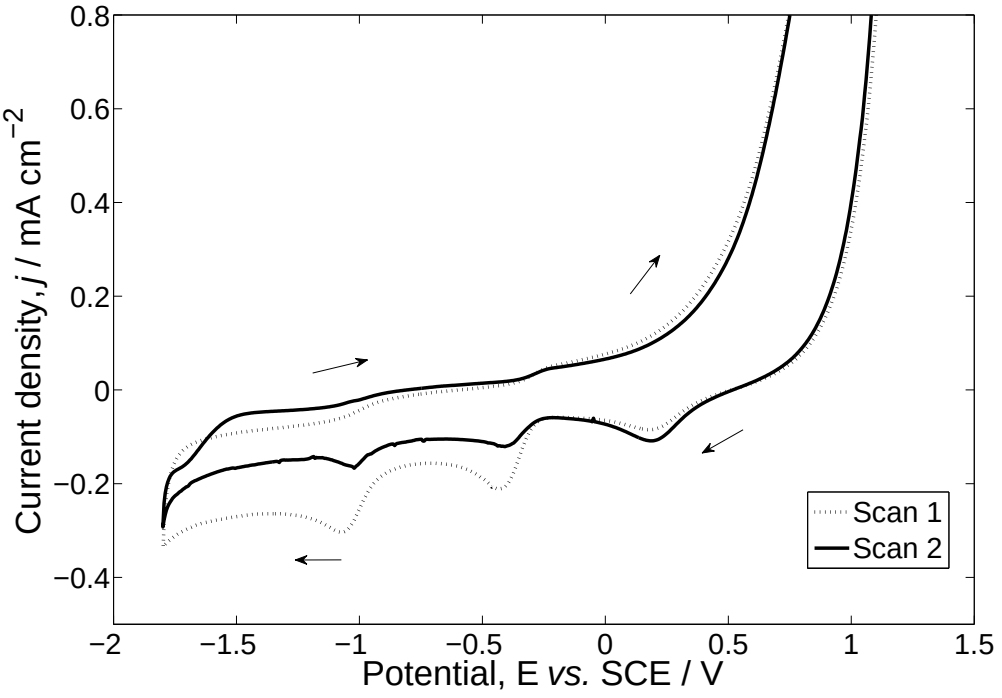

Figure 4.5: *Cyclic voltammograms of 5×10^{-2} M PWA in 4.0 M KOH. The electrolyte was saturated with nitrogen gas. The first cycle (dotted line) and the second cycle (black line) of the voltammogram are presented. The scan rate of the voltammogram was 100 mV sec^{-1} and the temperature was 20°C. The working electrode area was 0.07 cm^2.*

Three clear reduction peaks are observed at 0.2, -0.42 and -1.02 V *vs.* SCE while two limited oxidation peaks are observed at -1.5 and -0.88 V *vs.* SCE. The current density of the third reduction peak during the first cycle exhibits approximately -0.3 mA cm^{-2}, while the same reduction peak during the second cycle exhibits only -0.16 mA cm^{-2}. Thus, the results show that the phosphotungstic acid is not stable in aqueous, alkaline media since there is a big difference between the voltammograms obtained during the first and the second cycle of the measurement. Additionally, the electron reduction reactions are not reversible, since the oxidation peaks are too broad and small.

When comparing the voltammograms in figures 4.4 and 4.5, it can be said that both phosphomolybdic acid and phosphotungstic acid do not show reversible redox activity and stability, when being dissolved in alkaline media.

These results are consistent with the literature, since when heteropolyacids are dissolved in solution show more reversible and stable redox activity in acidic en-

vironment but limited stability and hence poor redox behaviour in alkali environment.

4.2.1.3 Glassy carbon electrode modified with heteropolyacids in acidic solution

Since the stability of the HPA dissolved in aqueous solutions is not satisfactory, heteropolyacids were immobilised on a glassy carbon electrode (GCE) and the results from the electrochemical characterisation of the HPA-modified electrode is presented in this section.

A simple and commonly used method to develop a mono-layer of HPA on an electrode's surface is to dip the electrode in an acidic solution which includes the HPA [186]. This method was followed for the modification of the GCE in this section and additional details about this procedure can be found in chapter 3 (page 45).

The voltammogram of a PMA-modified GCE in 1.0 M H_2SO_4 is presented in figure 4.6. The electrolyte was de-oxygenated with nitrogen gas for 20 minutes before the measurement.

The scanning during the cycling started from 0.58 V *vs.* SCE towards negative potentials, it continued until -0.52 V *vs.* SCE and then back to 0.58 V *vs.* SCE.

Four irreversible, well-defined reduction peaks are observed at 0.33, 0.18, -0.04 and -0.44 V *vs.* SCE, two additional weak reduction peaks are observed at -0.20 and -0.28 V *vs.* SCE, respectively and several ill-defined oxidation peaks can be observed at -0.31 -0.20, -0.08, -0.002 and 0.28 V *vs.* SCE during the first cycle of the voltammogram. However, during the fifth cycle of the voltammogram no redox peaks are observed.

The redox activity exhibited by the PMA-modified GCE during the first cycle of the voltammogram is similar to the redox activity exhibited when PMA was dissolved in H_2SO_4 which was presented in figure 4.1. The three reduction peaks in figure 4.1 are observed at 0.35, 0.17 and -0.04 V *vs.* SCE, which are approximately the same potential values where the first three reduction peaks are shown in figure 4.6 (0.33, 0.18 and -0.04 V *vs.* SCE).

In figure 4.7, the voltammogram of a PWA-modified GCE in 1.0 M H_2SO_4 is presented. The electrolyte was de-oxygenated for 20 minutes with nitrogen gas

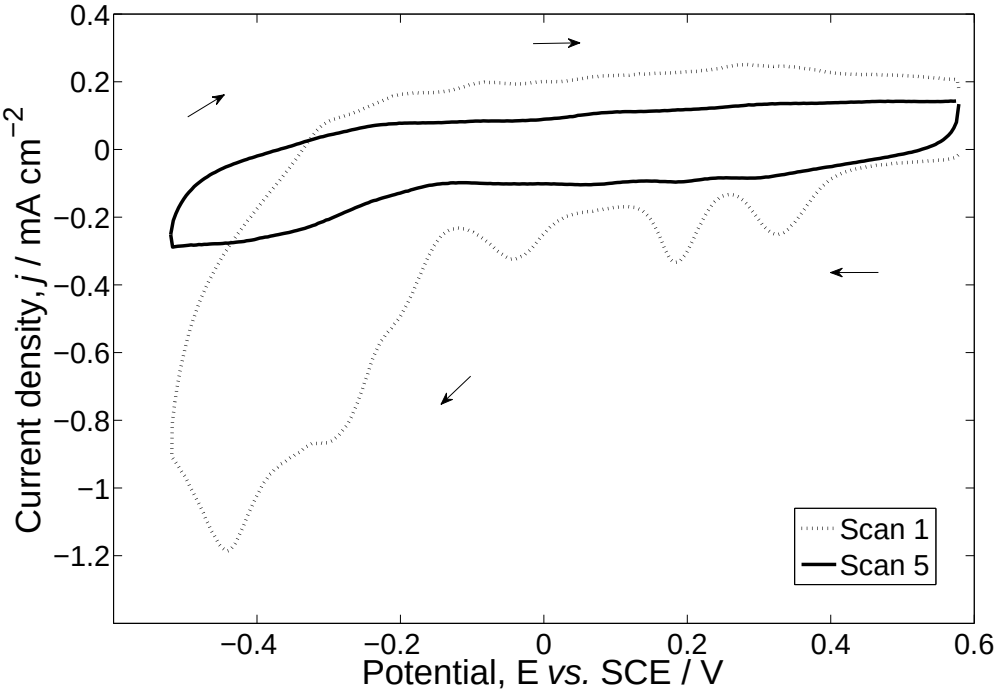

Figure 4.6: *Cyclic voltammograms of a PMA-modified GCE in 1.0 M H_2SO_4. The electrolyte was saturated with nitrogen gas. The first cycle (dotted line) and the fifth cycle (black line) of the voltammogram are presented. The scan rate of the voltammogram was 100 mV sec^{-1} and the temperature was 20°C. The working electrode area was 0.07 cm^2.*

before the measurement.

For the voltammetry in figure 4.7, the potential was scanned from 0.5 V *vs.* SCE towards negative potentials. At -0.75 V *vs.* SCE the sweep direction was reversed and the potential returned to 0.5 V *vs.* SCE.

Several reduction and oxidation peaks are observed in the voltammogram. One clear reduction peak is observed at -0.63 V *vs.* SCE and a clear oxidation peak is observed at -0.60 V *vs.* SCE. Some additional reduction peaks are observed at 0.33, -0.05, -0.41 V *vs.* SCE and extra oxidation peaks are shown at -0.52, -0.56 and 0.11 V *vs.* SCE.

From figure 4.7, it can be seen that the PWA is not well immobilised on the GCE since there is a drop of approximately 0.07 mA cm^{-2} in the current density value exhibited at the third reduction peak, between the first and the ninth cycle which shows low stability. Additionally, when comparing these results to the results from the voltammogram in 5×10^{-2} M PWA in 1.0 M H_2SO_4 (figure 4.2) it seems that the only well-defined redox couple observed at -0.63/-0.60 V *vs.* SCE in figure 4.7 is probably the two electron redox couple which was also observed in

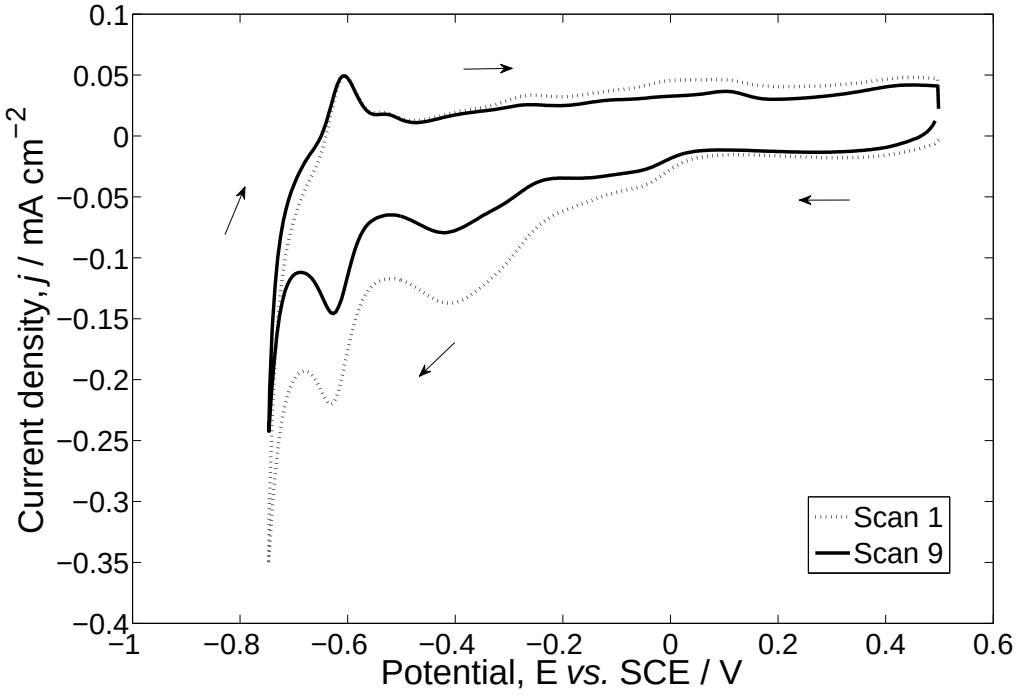

Figure 4.7: *Cyclic voltammograms of a PWA-modified GCE in 1.0 M H_2SO_4. The electrolyte was saturated with nitrogen gas. The first cycle (dotted line) and the ninth cycle (black line) of the voltammogram are presented. The scan rate of the voltammogram was 100 mV sec^{-1} and the temperature was 20°C. The working electrode area was 0.07 cm^2.*

the voltammogram in figure 4.2.

4.3 Conclusions and Further Work

Cyclic voltammetry measurements were performed in order to investigate the redox activity of heteropolyacids (phosphomolybdic and phosphotungstic acid) when dissolved in acidic and alkaline aqueous solutions. The results from these experiments have shown that both heteropolyacids undergo one- and two-electron redox reactions in acidic solutions. However, phosphotungstic acid gave better results when compared to the results obtained from the phosphomolybdic acid, since the voltammograms of the PWA showed less irreversible electron transfers and better-defined redox peaks.

The individual redox couples of PWA in H_2SO_4 can be isolated as separate, stable electrochemical reactions. This demonstrates their potential for energy storage applications, such as in redox active electrolytes of redox flow cells.

Two different CV measurements were made on PWA; one in a de-oxygenated and one in a oxygenated, acidic electrolyte solution. There was an obvious difference in the redox activity of the PWA between the two different voltammograms. It was shown that the redox reactions of PWA in acid were more reversible when the electrolyte was de-oxygenated. That behaviour implies that either PWA participates in the oxygen reactions and hence it is consumed during the cycling or that there is a background oxygen reduction on the surface of the glassy carbon electrode which causes the distortion of the voltammogram.

The second part of the CVs was based on HPAs in alkaline environment (4.0 M KOH). Heteropolyacids have been widely tested in acid but there is not a lot of research in HPAs in alkali. The results from these CVs showed that both heteropolyacids display poor redox activity and low stability when tested in aqueous, alkaline solutions.

Further cyclic voltammetries were made on phosphomolybdic and phosphotungstic acid immobilised on a glassy carbon electrode in acidic environment. The PWA-modified glassy carbon electrodes showed again better results when compared to the results obtained from the PMA-modified electrodes. The redox reactions were more reversible and the stability was higher for the PWA-modified GCE, however still not satisfactory.

The voltammograms when the heteropolyacids were dissolved in the acidic electrolyte showed many similarities with the voltammograms when the HPAs were immobilised on the GCE. It has been shown that both phosphomolybdic acid and phosphotungstic acid exhibit redox activity but more research has to based on their immobilisation on an electrode due to their poor stability issues. Hence, suitable immobilisation media need to be identified to develop incorporating HPA redox active electrodes.

The results show that the PMA and the PWA show poor performance towards redox activity when exposed to an alkali environment. A method of modifying them or protecting them from alkali conditions would therefore be requested if they were to be used in such applications.

Chapter 5

HPA gas diffusion electrodes

5.1 Introduction

In the previous chapter (Chapter 4), HPAs (PMA and PWA) showed satisfactory redox activity when characterised in acidic environment. However, when the heteropolyacids were tested in alkali environment the redox activity that they exhibited was inadequate. Additionally, PMA and PWA were deposited on a glassy carbon electrode and the results from the CVs of the HPA-modified GCE showed poor stability and redox activity.

In order to overcome the low stability issues, the HPAs had to be combined with a different material which would protect and stabilise them. As mentioned in the literature review (chapter 2, page 35), nickel is commonly used as a catalyst in positive electrodes of rechargeable alkaline batteries due to the reversibility of its redox couple and its stability in corrosion [145]. Hence, in this chapter, heteropolyacids are combined with nickel powder and Nafion® to form a catalyst ink which was subsequently applied on a gas diffusion layer (carbon Toray paper) to create an HPA gas diffusion electrode.

Cyclic voltammetry and constant current cycling between OER and ORR in alkaline environment were the two methods that were used to characterise the gas diffusion electrodes incorporating heteropolyacids. It is important to mention that the effect of the heteropolyacids on oxygen evolution and oxygen reduction under alkaline conditions has not been investigated before, as they are believed to be unstable in these environments. However, this chapter presents some initial results from the electrochemical characterisation of the HPA gas diffusion electrodes

which demonstrates that HPAs can be stabilised when combined with nickel metal.

Two different HPAs were used as additives in the catalyst ink; phosphomolybdic acid (PMA) and phosphotungstic acid (PWA). Molybdenum (Mo) was also used as an additive, in order to compare the performance of the electrode with nickel and molybdenum to the behaviour obtained by the nickel and phosphomolybdic acid electrode.

Additionally, microscopy tests were performed on the manufactured electrodes in order to monitor their structure before and after the cycling.

Finally, an HPA gas diffusion electrode was used as the positive electrode in a zinc-air flow cell. Charging/discharging measurements were performed on the battery to investigate the performance of the manufactured electrode in a real-time environment of a functional device.

5.2 Results and discussion

Table 5.1 summarises the nomenclature and the composition characteristics of the different catalyst inks that have been used in order to manufacture the HPA gas diffusion electrodes which are presented in this section.

The names of the manufactured GDEs are given to them after the name of the catalyst ink which was used for their formation. For example, electrode *Ni-nano PMA I* has been formed by printing a certain amount of the Ni-nano PMA I ink on a carbon Toray paper. Additional to the electrodes which were made with the inks from table 5.1, the *Nafion®* electrode had just Nafion® printed on its surface and the carbon electrode is a plain Toray paper.

5.2.1 Cyclic voltammetries

This section consists of the cyclic voltammetry results in alkaline electrolyte on the manufactured gas diffusion electrodes. The electrolyte that has been used during these experiments was 4.0 M KOH because it is commonly used in fuel cells and metal-air batteries which utilise alkali electrolytes.

The cyclic voltammograms of electrodes with different catalyst inks under fixed O_2 or fixed air flow are presented. All electrodes are air-breathing which means that the results give a true reflection of OER and ORR performance.

Nomenclature	Compounds	Quantity (gr)
Ni-nano	Nickel nano-powder Nafion®	5.0 15
Ni	Nickel micro-powder Nafion®	1.508 10.171
Ni-nano PMA I	Nickel nano-powder PMA Nafion®	5.0 5.0 15.0
Ni-nano PMA II	Nickel nano-powder PMA Nafion®	1.14 1.5 14.73
Ni PMA	Nickel micro-powder PMA Nafion®	1.537 1.513 10.107
Ni PWA	Nickel micro-powder PWA Nafion®	1.865 1.557 11.02
Ni Mo	Nickel micro-powder Mo Nafion®	1.5 0.948 10.129
Nafion® PMA	PMA Nafion®	1.8 8.98

Table 5.1: *Table of the catalyst inks*

In figure 5.1, the voltammograms of the *Nafion®*, *Nafion® PMA*, *carbon* and *Ni-nano* electrodes in 4.0 M KOH under fixed O_2 flow are shown. The voltammograms of the *Nafion®*, *Nafion® PMA* and *carbon* electrodes were recorded between -0.5 and 0.7 V *vs*. SCE. The voltammogram of the *Ni-nano* electrode was recorded between -0.7 and 0.7 V *vs*. SCE.

The *Nafion®* electrode had a Nafion® loading of 0.94 mg cm^{-2}. The HPA loading of the *Nafion® PMA* electrode is 1.05 mg cm^{-2}. The nickel loading of the *Ni-nano* electrode is 1.16 mg cm^{-2}.

The *Ni-nano* electrode exhibits the expected electrochemical activity. At the voltammogram of the *Ni-nano* electrode, (*peak (a)*) is because of the oxidation of $Ni(OH)_2$ to NiOOH and (*peak (c)*) is probably due to the oxidation of metallic Ni to NiO_x and $Ni(OH)_2$ [204]. The OER at the voltammogram of the *Ni-nano* electrode is observed at potentials more positive than 0.55 V *vs*. SCE. During the reverse scan, a reduction peak is observed (*peak (b)*) due to the reduction of NiOOH to $Ni(OH)_2$ and the ORR occurs at around -0.4 V *vs*. SCE.

It has to be mentioned that the *Nafion®*, *Nafion® PMA* and *carbon* electrodes

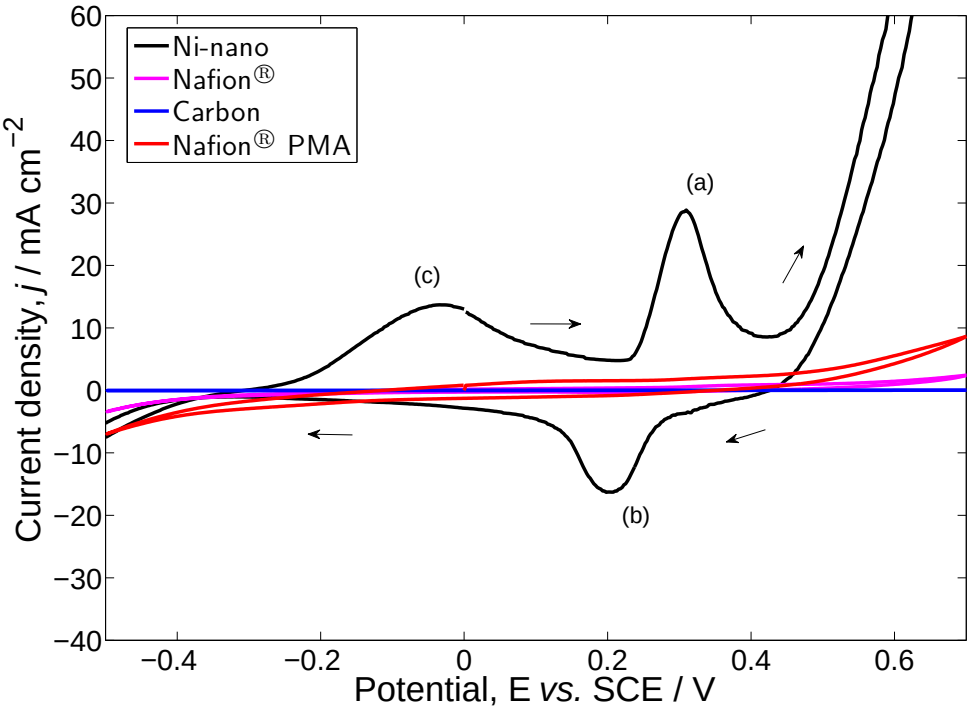

Figure 5.1: *Cyclic voltammograms of the Ni-nano (black line), Nafion® (pink line), carbon (blue line) and Nafion® PMA (red line) electrodes in 4.0 M KOH and fixed O_2 flow ($100\,cm^3\,min^{-1}$). The second cycle of each voltammogram is presented. The scan rate of the voltammograms was 50 mV sec^{-1} and the temperature was 20°C. The working electrode area was 1.33 cm^2.*

show very little electrochemistry in the potential range which is investigated, since no oxidation or reduction peaks are observed and the oxygen evolution and reduction reactions cannot be easily distinguished. These electrodes act as a base line, against which the effect of combining HPA and Ni can be measured.

The voltammograms in figure 5.2 were performed in order to investigate whether the anodic current which is observed at negative potentials in the CVs of the Ni HPA electrodes is due to the hydrogen evolution (HER) or the oxygen reduction reaction (ORR).

The same Ni PMA electrode was used in both measurements. The electrolyte which was used for the first voltammogram (solid line), has not gone through any pretreatment before the measurement and fixed air was fed into the cell during the voltammogram. While for the second voltammogram (dotted line), the electrolyte was saturated with nitrogen gas for 20 minutes before the measurement and nitrogen gas was fed into the cell during the measurement. Hence, during the second voltammogram the oxygen was removed from the electrolyte.

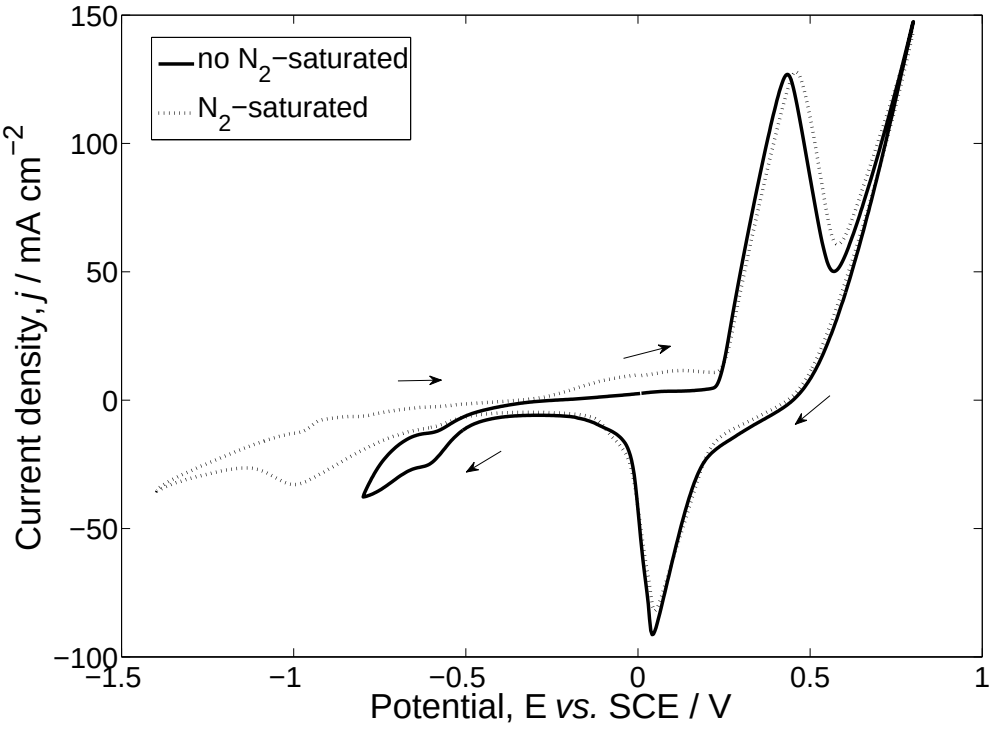

Figure 5.2: *Cyclic voltammograms of a Ni PMA electrode in 4.0 M KOH. The electrolyte was not saturated and air was fed into the cell (solid line) while the electrolyte was saturated with nitrogen gas before the measurement and nitrogen gas was fed into the cell (dotted line) The second cycle of each voltammogram is presented. The scan rate of the voltammograms was 50 mV sec^{-1} and the temperature was 20^{o}C. The working electrode area was 1.33 cm^2.*

The scanning potential limits during the voltammogram of the Ni PMA in the electrolyte with oxygen present were between +0.8 V *vs.* SCE and -0.8 V *vs.* SCE while the potential limits of the measurement in the de-oxygenated electrolyte were between +0.8 V *vs.* SCE and -1.4 V *vs.* SCE.

In both voltammograms, a well-defined reduction peak and a well-defined oxidation peak are observed. At the voltammogram of the Ni PMA electrode with oxygen being present in the electrolyte, the reduction peak was observed at approximately 0.04 V *vs.* SCE, the oxidation peak was shown at around 0.43 V *vs.* SCE and oxygen started evolving at approximately 0.57 V *vs.* SCE towards more positive potentials.

The reduction peak of the voltammogram of the Ni PMA electrode in the de-oxygenated electrolyte was observed at around 0.05 V *vs.* SCE, the oxidation peak of the same voltammogram is shown at approximately 0.46 V *vs.* SCE, while oxygen evolution began at 0.58 V *vs.* SCE towards more positive potentials

Towards negative potentials a anodic current is observed at both voltammograms. However, when comparing the potential values where the anodic current of the two voltammograms occurred, it is observed that the anodic current of the voltammogram with oxygen present in the electrolyte started at more positive potential values compared to the potential values of the anodic current of the voltammogram when oxygen is absent.

More specifically, at -0.55 V *vs.* SCE the current density of the voltammogram with oxygen present in the electrolyte is j=-17.49 mA cm^{-2}, while at the same potential value the current density of the voltammogram with the de-oxygenated electrolyte is j=-8.74 mA cm^{-2}. This difference in the current density values shows that when oxygen is present in the electrolyte, the anodic current appears faster, hence the reaction which takes place at negative potential values is related to oxygen rather than to hydrogen which shows that it is not due to hydrogen evolution.*

The cyclic voltammograms of the *Ni-nano* and *Ni-nano PMA I* electrodes in 4.0 M KOH are shown in figure 5.3. Both voltammograms were recorded between -0.7 and 0.7 V *vs*. SCE. The measurement was taken under fixed O_2 flow and the voltammograms are normalised to the nickel loading of each electrode, assuming that the catalyst ink has a uniform consistency and that it has been printed uniformally on the carbon paper.

The *Ni-nano* electrode's nickel loading is 1.16 mg cm^{-2}. For the *Ni-nano PMA I* electrode, both the nickel loading and the HPA loading are 0.64 mg cm^{-2}.

The enhancement by PMA in the OER activity of nickel is clearly shown in this plot. The onset potential value for ORR at the *Ni-nano PMA I* electrode is similar to the value exhibited by the *Ni-nano* electrode (around -0.4 V *vs*. SCE). However, at higher potential values the *Ni-nano PMA I* electrode exhibits increased current density when compared to the *Ni-nano* electrode. It can be seen that the *Ni-nano PMA I* electrode shows enhanced behaviour towards the oxygen evolution reaction, since the OER begins at 0.4 V *vs*. SCE against 0.55 V *vs*. SCE which is the potential value where OER occurs for the *Ni-nano* electrode.

For both electrodes, the $Ni(OH)_2$ to NiOOH oxidation peak is observed at 0.31

* The electrode which was used in these measurements is one of the *Ni PMA* electrodes which is presented in the next chapter (chapter 6 and page 98), the *Ni PMA IV*. However, it is more suitable to include these voltammograms in this chapter in order to demonstrate that the reaction that takes place at negative potentials is the ORR. It can be seen, that a small poor defined reduction and a small poor defined oxidation peak are also observed in the voltammograms. These peaks are possibly due to the high HPA loading that the *Ni PMA IV* electrode includes.

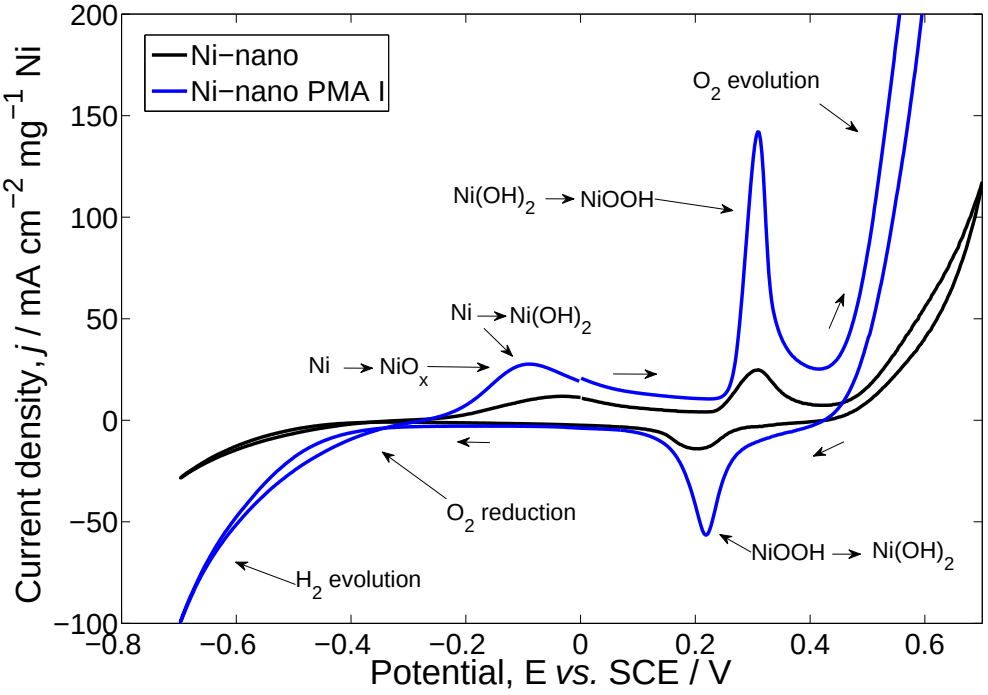

Figure 5.3: *Cyclic voltammograms of the Ni-nano (black line) and Ni-nano PMA I (blue line) electrodes in 4.0 M KOH and fixed O_2 flow ($100\,cm^3\,min^{-1}$). The second cycle of each voltammogram is presented. The scan rate of the voltammograms was 50 mV sec^{-1} and the temperature was 20°C. The working electrode area was 1.33 cm^2.*

V *vs*. SCE. The reduction peak due to the reduction of NiOOH to $Ni(OH)_2$ is present at 0.22 V *vs*. SCE for the *Ni-nano PMA I* electrode, whereas for the *Ni-nano* electrode the reduction peak is observed at 0.20 V *vs*. SCE. Generally, the features of the voltammogram of the *Ni-nano PMA I* are sharper and they exhibit higher peak current density values when compared to the voltammogram of the *Ni-nano* electrode. A current density of 100 mA cm^{-2} is achieved at 0.29 V *vs*. SCE for the *Ni-nano PMA I* electrode versus 0.68 V *vs*. SCE for the *Ni-nano* electrode. Thus, HPA enhances the activity of nickel's electrochemistry and reduces the overpotential for the OER.

In figure 5.4, the cyclic voltammetries of *Ni PMA* and *Ni PWA* electrodes in 4.0 M KOH under fixed air flow are shown. The scanning potential values were between -0.7 V *vs*. SCE and 0.6 V *vs*. SCE.

The nickel loading for the *Ni PMA* electrode is 0.41 mg cm^{-2} and for the *Ni PWA* electrode is 0.54 mg cm^{-2}. The HPA loading is 0.40 mg cm^{-2} for the *Ni PMA* electrode and 0.45 mg cm^{-2} for the *Ni PWA* electrode. The voltammograms are normalised by the nickel loading in each electrode.

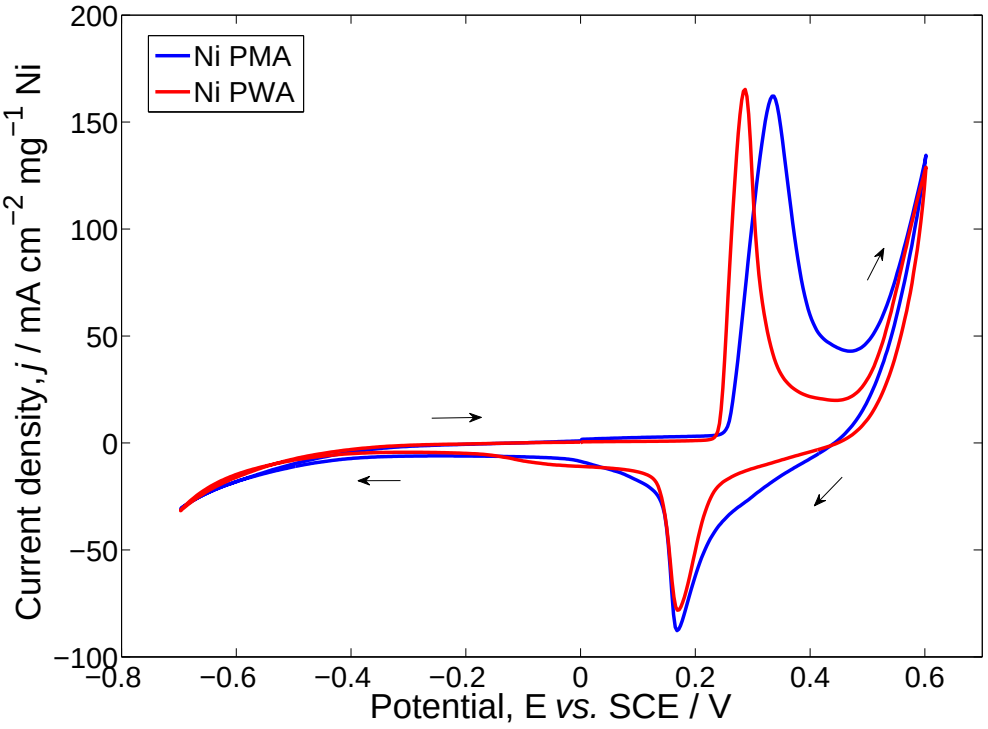

Figure 5.4: *Cyclic voltammograms of the Ni PMA (blue line) and Ni PWA (red line) electrodes in 4.0 M KOH and fixed air flow. The second cycle of each voltammogram is presented. The scan rate of the voltammograms was 50 mV sec^{-1} and the temperature was 20^{o}C. The working electrode area was 1.33 cm^2.*

One can see that the voltammograms of the electrodes which incorporate the two different HPAs are very similar. Two redox peaks can be easily distinguished in both voltammograms. The electrode with the PMA shows OER activity at approximately 0.46 V *vs*. SCE towards more positive potentials and the electrode with the PWA at roughly 0.45 V *vs*. SCE towards more positive potentials. At the voltammogram of the *Ni PMA* electrode, the oxidation peak is observed at 0.33 V *vs*. SCE and the reduction peak is shown at 0.17 V *vs*. SCE. The oxidation peak of the *Ni PWA* voltammogram is observed at 0.28 V *vs*. SCE and the reduction peak appears at 0.17 V *vs*. SCE. In conclusion, the cyclic voltammetries of the *Ni PMA* and *Ni PWA* electrodes showed similar results, however, the oxidation peak of the electrode with PWA was slightly shifted towards more negative potentials.

It has to be mentioned that in figure 5.3, a second oxidation peak is observed at the voltammogram of the *Ni PMA* electrode (at circa -0.09 V *vs*. SCE), however there is not such an oxidation peak in the voltammograms in figure 5.4. It is believed that this peak appears due to two reasons. The first one is the different impact that nickel nano-powder and nickel micro-powder have on the electrochemistry of

the gas diffusion electrode, since the electrodes in figure 5.3 are made of an ink that includes nickel nano-powder while nickel micro-powder has been added in the ink which was used for the electrodes in figure 5.4. The second reason is that during the voltammetries that are presented in figure 5.3, O_2 was supplied in the cell, whereas unprocessed air was being fed into the cell during the CVs which are shown in figure 5.4.

As already mentioned, HPAs are not known for their stability in alkaline media. It was therefore important to establish whether it was the presence of molybdenum (Mo) in combination with the nickel powder that resulted in the enhanced activity results or the combination of HPA with Ni. In order to investigate this aspect, an electrode with nickel powder and molybdenum has been manufactured and tested by cyclic voltammetry in alkaline environment.

In figure 5.5, the voltammogram of the *Ni*, *Ni PMA* and *Ni Mo* electrodes in 4.0 M KOH and under fixed air flow are presented. The scanning potential varied between -0.6 V *vs*. SCE and 0.6 V *vs*. SCE.

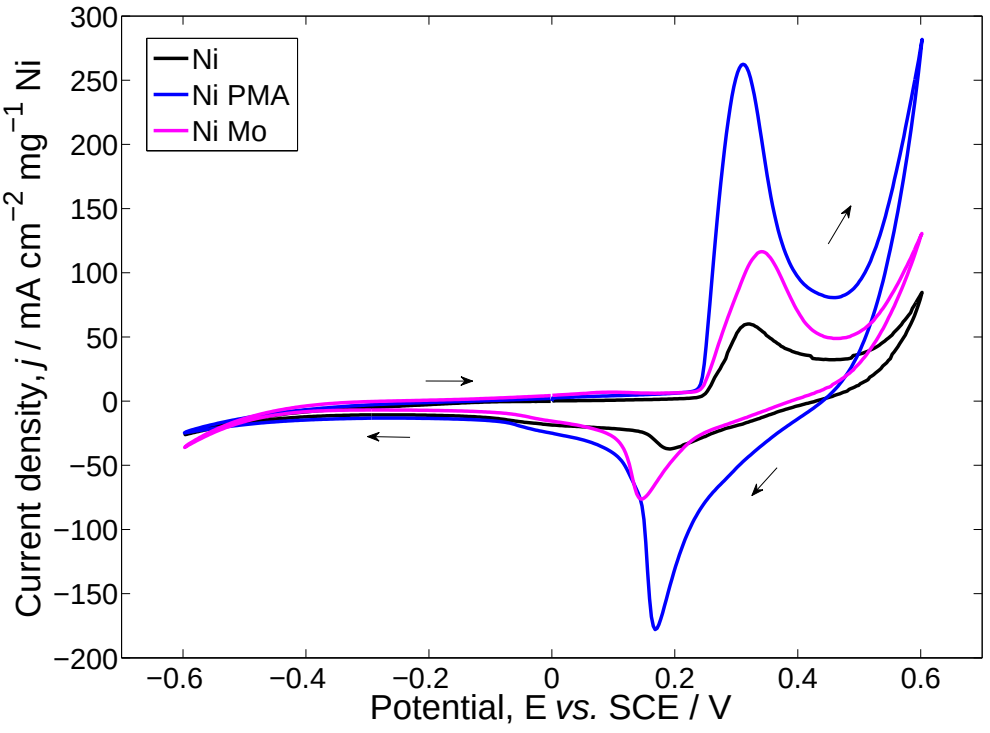

Figure 5.5: *Cyclic voltammograms of the Ni (black line), Ni PMA (blue line) and Ni Mo (pink line) electrodes in 4.0 M KOH and fixed air flow. The second cycle of each voltammogram is presented. The scan rate of the voltammograms was 100 mV sec^{-1} and the temperature was 20^{o}C. The working electrode area was 1.33 cm^2.*

The nickel loading of the *Ni* electrode is 0.17 mg cm^{-2}, while for the *Ni Mo* electrode

is 0.46 mg cm^{-2}. For the *Ni PMA*, the nickel loading and the HPA loading are both 0.43 mg cm^{-2}. All the voltammograms are normalised to the nickel loading of each electrode.

It can be seen that the addition of molybdenum shifts the oxidation peak to more positive potentials, since it was observed at 0.34 V *vs*. SCE at the voltammogram of the *Ni Mo* electrode and at 0.32 V *vs*. SCE at the voltammograms of the *Ni* and the *Ni PMA* electrode. The reduction peak is shifted towards more negative potentials with the addition of Mo, since it is shown at 0.15 V *vs*. SCE at the voltammogram of the *Ni Mo* electrode, at 0.19 V *vs*. SCE at the voltammogram of the *Ni* electrode and at 0.17 *vs*. SCE at the voltammogram of the *Ni PMA* electrode. The starting potentials for OER (0.46 V *vs*. SCE) and ORR (-0.43 V *vs*. SCE) are similar for all the electrodes.

It is observed that at higher overpotentials, the *Ni PMA* electrode exhibits higher current density values when compared to the *Ni Mo* and the *Ni* electrodes. Additionally, the voltammogram of the *Ni PMA* electrode showed higher and sharper current peaks compared to both the voltammograms of the *Ni* and the *Ni Mo* electrodes. Hence, it has been shown that molybdenum does not contribute towards the enhanced activity of the electrode for OER and ORR and that the enhancement is purely due to the presence of the PMA.

5.2.2 Constant current potentiometry

Since, the HPA gas diffusion electrodes are targeted at applications such as regenerative fuel cell and metal-air batteries, stability under repeated OER and ORR conditions is essential.

In figure 5.6, six consecutive cycles between ORR and OER at the *Ni-nano PMA II* in 4.0 M KOH are shown. The measurements were under fixed O_2 flow and each cycle lasted for 600 sec (300 sec followed by 300 sec ORR). The applied current density was 44 mA cm^{-2}. The electrode's nickel loading is 0.45 mg cm^{-2} and its HPA loading is 0.60 mg cm^{-2}.

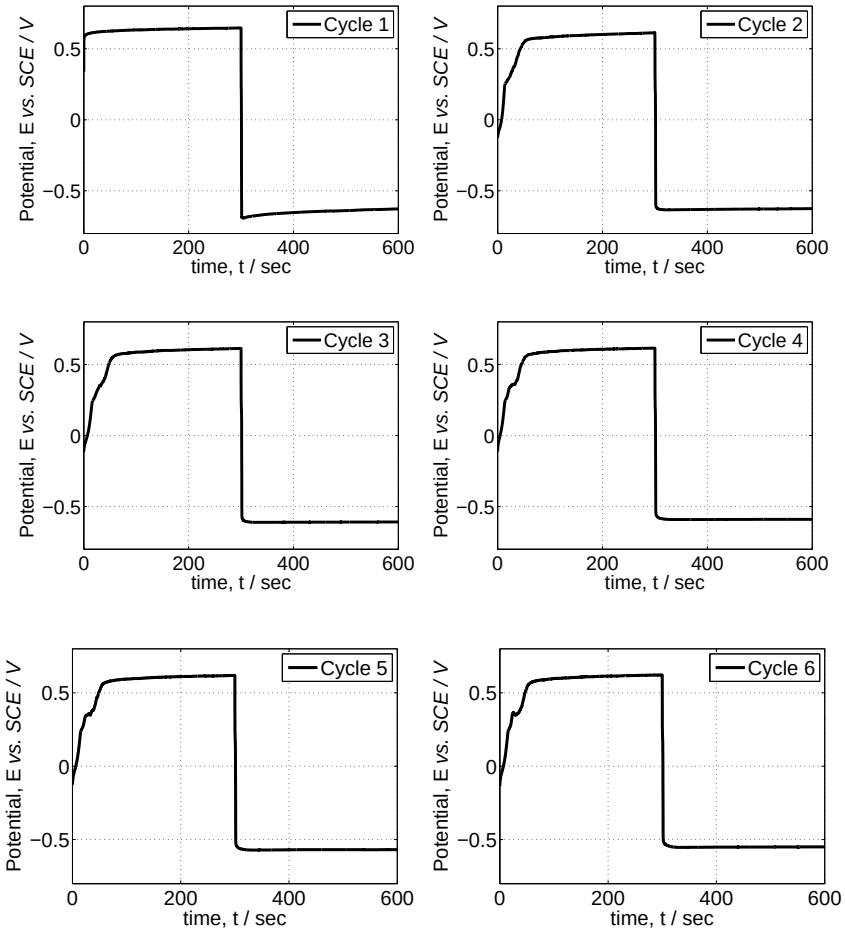

Figure 5.6: *Constant current measurements between OER and ORR at the Ni PMA electrode in 4.0 M KOH and fixed O_2 flow ($100\,cm^3\,min^{-1}$) at a current density of 44 mA cm^{-2}. The temperature was 20°C and the working electrode area was 1.33 cm^2.*

It is observed that during all the cycles the potential values for each reaction are the same, since the potential was at +0.6 V *vs.* SCE during OER and at -0.6 V *vs.* SCE during ORR. Therefore, the electrode potential remains stable in a period

of time (3600 sec) under OER and ORR conditions. From the second circle and until the sixth circle, a second peak at around 0.2 V can be observed and it is believed that it occurs due to oxidation of Ni to $Ni(OH)_2$ and its further oxidation to NiOOH [52].

In figure 5.7, the constant current measurements between OER and ORR of the *Ni* electrode, the *Ni PMA* electrode and the *Ni PWA* electrode are presented.

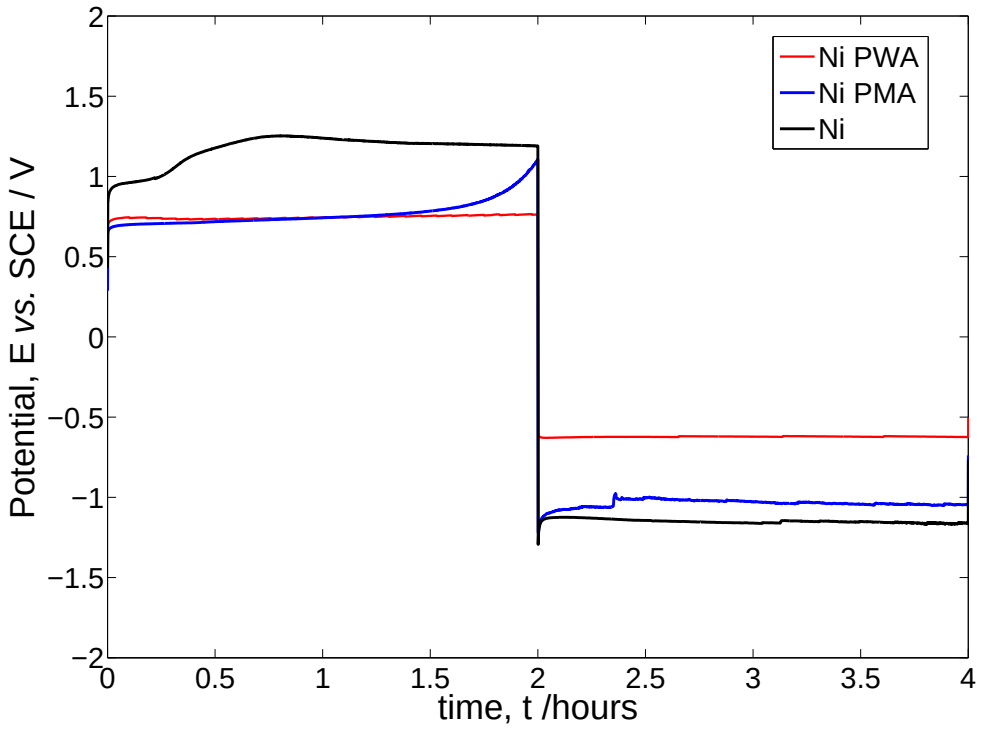

Figure 5.7: *Constant current measurements between OER and ORR at the Ni (black line), Ni PMA (blue line) and Ni PWA (red line) electrodes in 4.0 M KOH, fixed air flow and current density* 50 *mA* cm^{-2}. *The temperature was 20°C and the working electrode area was 1.33* cm^2.

Oxygen evolution and oxygen reduction lasts for two hours each. A current density of 50 mA cm^{-2} was applied throughout and the measurement took place under a fixed air flow.

The nickel loading of the *Ni PWA* electrode is 0.54 mg cm^{-2} and its HPA loading is 0.45 mg cm^{-2}. The *Ni* and the *Ni PMA* electrodes which have been used in this constant current measurement have been also used in the cyclic voltammetry measurement shown in figure 5.5. Hence, their structural characteristics have already been presented.

The potential values that were obtained from the cycling on the *Ni PWA* electrode

were much more favourable when compared to the potential values exhibited by the *Ni* and *Ni PMA* electrodes. The *Ni PWA* electrode shows lower potential difference between the value obtained during OER and the value obtained during ORR ($E_{OER} - E_{ORR} = 1.35$ V) when it is compared to the potential difference obtained from the measurements on the *Ni* electrode ($E_{OER} - E_{ORR} = 2.4$ V) and on the *Ni PMA* electrode ($E_{OER} - E_{ORR} = 1.77$ V).

After the first two hours, the *Ni PMA* electrode and the *Ni* electrode started to degrade and they failed after four and six hours, respectively. This may be because of degradation, due to HPA loss or due to catalyst layer delamination. The *Ni PWA* electrode though, gives stable results for a much longer period of time.

Additionally, it has to be mentioned that both the *Ni PMA* and the *Ni* electrodes exhibited very negative potential values during the ORR in figure 5.7 and it is likely that H_2 evolution is occurring rather than O_2 reduction.

In figure 5.8, the constant current cycling between OER and ORR on the *Ni PWA* electrode in 4.0 M KOH is shown. The current density which was applied during the measurement was 50 mA cm^{-2} and fixed air flow was fed into the cell.

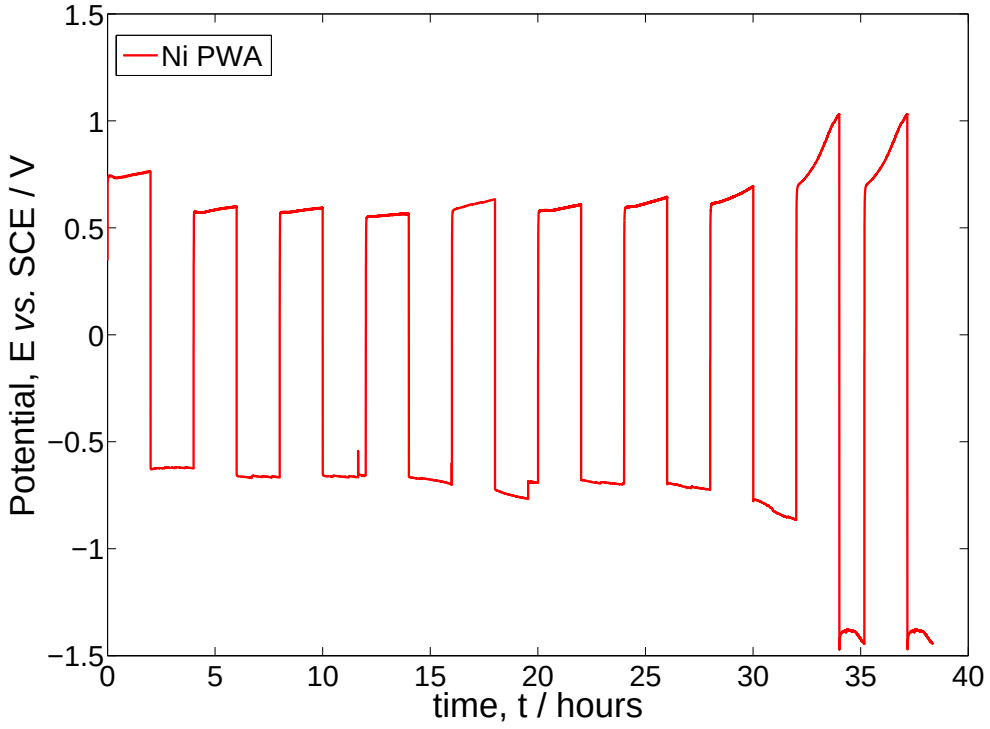

Figure 5.8: *Constant current measurements between OER and ORR at the Ni PWA electrode in 4.0 M KOH, fixed air flow and current density 50 mA cm^{-2}. The temperature was 20°C and the working electrode area was 1.33 cm^2.*

The results from the constant current cycling shows that the *Ni PWA* electrode can be stable during OER and during ORR at 50 mA cm^{-2} for approximately 14 hours.

The electrode started to degrade after more than 30 hours. After the end of the experiment, the degraded electrode had cracks and its colour has changed. A visual observation revealed that delamination of the catalyst layer was the likely cause of the reduced activity, rather than dissolution or degradation of the catalyst itself.

5.2.3 Microscopy

The results from the constant current cycling between OER and ORR on the HPA gas diffusion electrodes which were presented in section 5.2.2 showed that the electrodes fail after consecutive cycling. In order to investigate the reason behind this deficiency, SEM imaging and EDX screening were performed on the electrodes' surface to monitor the changes before and after cyclic voltammetry measurements.

An image taken with SEM on a fresh *Ni PMA* electrode is shown in figure 5.9.

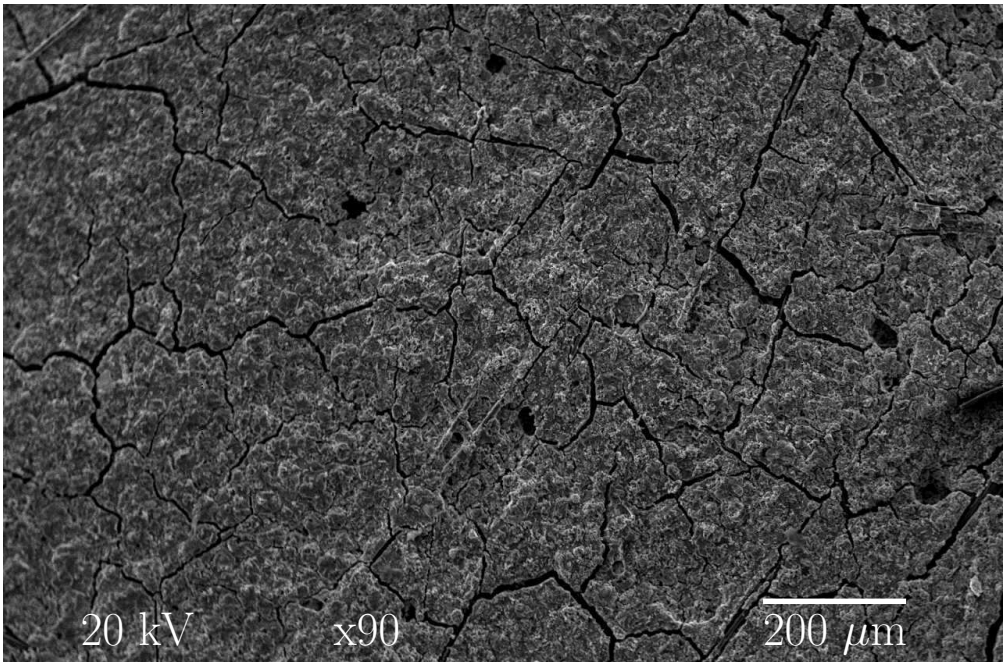

Figure 5.9: *SEM picture of a fresh Ni PMA electrode*

One can see from the SEM image that there is a uniform distribution of the catalyst on the carbon substrate and only some minor agglomerates and cracks can be observed.

The image which is presented in figure 5.10 is an SEM image taken on the same *Ni PMA* electrode but after it was subjected to cyclic voltammetry in 4.0 M KOH. Based on the image, it can be observed that there is loss of the catalyst layer of the *Ni PMA* electrode after the cycling since in certain areas the carbon substrate has been revealed.

The SEM results can be further confirmed by the EDX screening that it was performed on the same *Ni PMA* electrode before and after the cyclic voltammetries (table 5.2).

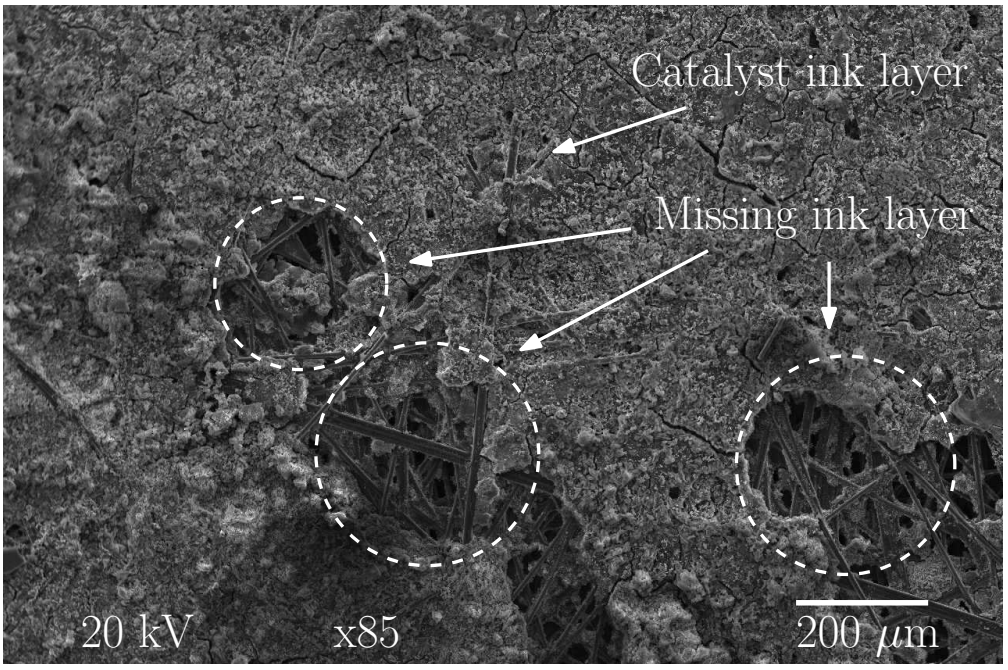

Figure 5.10: *SEM picture of a used Ni PMA electrode after it has undergone consecutive cycling (both CV and constant current potentiometry) in alkaline environment (4.0 M KOH).*

Before the cycling, the electrode's surface had a high amount of PMA (42.32% molybdenum), while after the cycling the amount was reduced to 16.24 %. Additionally, during the EDX on the fresh electrode, carbon was not detected and there was 39.13% of carbon observed on the same electrode after the cycling.

Element	**Unused Ni PMA electrode**		**Used Ni PMA electrode**	
	Weight %	**Atomic %**	**Weight %**	**Atomic %**
Carbon	N/A	N/A	39.13	64.23
Oxygen	20.57	47.62	12.13	14.94
Fluoride	4.72	9.20	7.15	7.42
Potassium	20.20	19.14	9.27	4.67
Nickel	12.21	7.70	16.08	5.40
Molybdenum	42.32	16.34	16.24	3.34

Table 5.2: *Table of EDX results on a Ni PMA electrode before and after testing.*

Hence, based on the SEM images and the results from the EDX measurements on the *Ni PMA* electrode, it is shown that the catalyst layer of the *Ni HPA* electrodes degrades after consecutive cycling.

5.2.4 Charge / discharge in a battery

A zinc-air flow cell was used to demonstrate proof-of-concept operation of the HPA gas diffusion electrodes in a functional device. C-Tech Innovation Ltd. provided a parallel plate flow cell for this demonstration, which was operated with guidance from Scott Gorman (University of Southampton). The cell is shown in figures 5.11 and 5.12 and comprises:

- a brass current collector for the negative electrode;
- carbon/polymer electrode onto which zinc deposition and stripping occurs;
- a polypropylene flow chamber through which an electrolyte containing zincate can be circulated;
- the HPA gas diffusion electrode (*Ni-nano PMA II*);
- a nickel coated brass flow field plate to act as the positive current collector and supply air to the reverse of the HPA GDE.

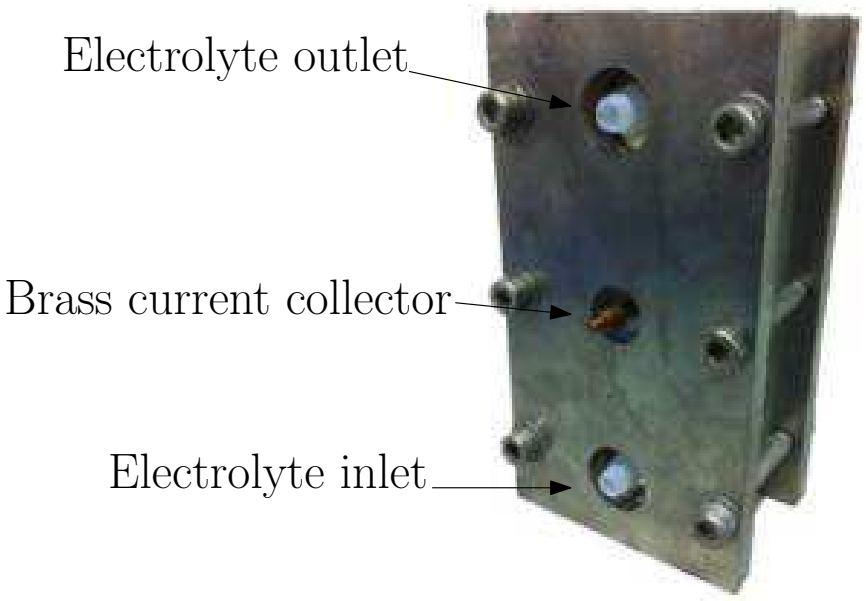

Figure 5.11: *A front view image of the flow cell provided by C-Tech Innovation Ltd.*

During charge, zinc is deposited at the negative electrode and oxygen is evolved at the positive electrode (HPA GDE). On discharge, the zinc is dissolved back into the electrolyte as zincate, while oxygen is reduced at the positive electrode. The reactions are given below:

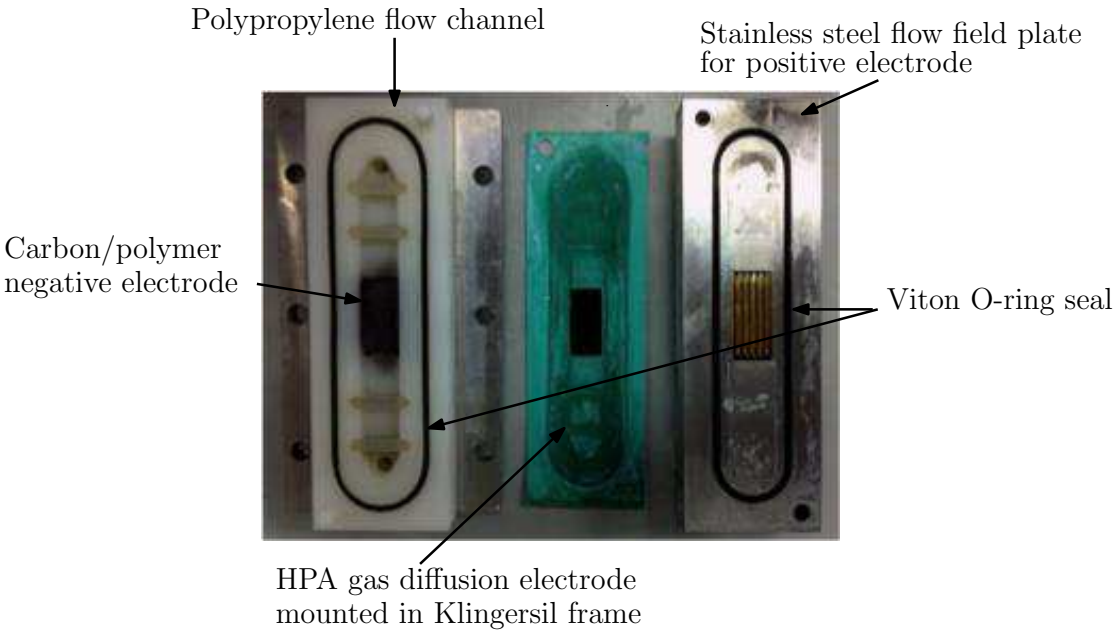

Figure 5.12: *A plan view image of the flow cell provided by C-Tech Innovation Ltd.*

Negative electrode reaction

$$Zn(OH)_4^{2-} + 2e^- \underset{discharge}{\overset{charge}{\Longleftrightarrow}} Zn + 4OH^- \tag{5.1}$$

Positive electrode reaction

$$4OH^- + 4e^- \underset{discharge}{\overset{charge}{\Longleftrightarrow}} O_2 + 2H_2O \tag{5.2}$$

Cell reaction

$$Zn(OH)_4^{2-} \underset{discharge}{\overset{charge}{\Longleftrightarrow}} Zn + \frac{1}{2}O_2 + 2OH^- + H_2O \tag{5.3}$$

The flow cell had an inter-electrode gap of 1.2 cm and was operated at 20°C. A *Ni-nano PMA II* electrode with dimensions 2 cm × 4 cm (8 cm^2) was fitted into the cell. Air was supplied to the rear face of the positive electrode at 200 cm^3 per minute. The cell was then supplied from a reservoir containing 500 cm^3 of an electrolyte initially consisting of 0.5 M ZnO in 8.0 M KOH flowing with a linear velocity of 2 cm sec^{-1}.

The cell was subjected to a series of charge/discharge cycles. During charging, the cell was charged for 30 minutes at a constant current of 10 mA cm^{-2}, followed by a discharge period at the same current density, which was ended when the cell

voltage dropped below 0.4 V. A saturated calomel electrode (SCE) was fitted into the flow circuit to monitor the air electrode potential separately to the cell voltage. The experiment was run for 30 consecutive cycles.

In order to compare the performance of the cell throughout this series of experiments the following parameters are used :

Voltage efficiency: $n_V = \frac{V_{discharge}}{V_{charge}}$

Charge efficiency: $n_C = \frac{Q_{discharge}}{Q_{charge}}$

Energy efficiency: $n_E = \frac{E_{discharge}}{E_{charge}}$

Table 5.3 summarises the charge voltage, the discharge voltage, the voltage efficiency, the charge efficiency and the energy efficiency values which have been obtained from the 1st, the 3rd, the 23rd and the 30th cycles from the charging/discharging measurement.

Cycle	**Charge voltage**	**Discharge voltage**	**Voltage efficiency, %**	**Charge efficiency, %**	**Energy efficiency, %**
1	2.13	0.86	40	80	32
3	2.09	0.90	43	88	38
23	2.00	0.95	47	86	40
30	2.00	1.00	50	93	46

Table 5.3: *Table of the charge voltage, the discharge voltage, the voltage efficiency, the charge efficiency and the energy efficiency for the 1st, the 3rd, the 23rd and the 30th cycles from the charging/discharging cycling of the zinc-air battery which incorporated the HPA gas diffusion electrode as the positive electrode.*

The voltage efficiency during the 1st cycle is 40% and the same parameter during the 30th improved to 50%. The value of the charge efficiency at the beginning of the cycling is 80% and reached 93% at the end of the measurement. Additionally, the energy efficiency of the cell started at 32% and improved to 46% at the 30th cycle.

Hence, it can be seen from table 5.3 that the voltage efficiency, the charge efficiency and the energy efficiency values improve as the measurement proceeds.

Figure 5.13 presents the cell voltage *vs.* time response cycles 23 to 30. The 23rd cycle shows the voltage during charge was approximately 2.0 V, while on discharge the voltage was approximately 0.95 V. The voltage during discharge remained steady until the zinc layer formed during charge had been consumed

and the voltage rapidly dropped, at which point the next charge/discharge cycle started. Over the consecutive cycles the discharge voltage slowly improved to approximately 1.0 V.

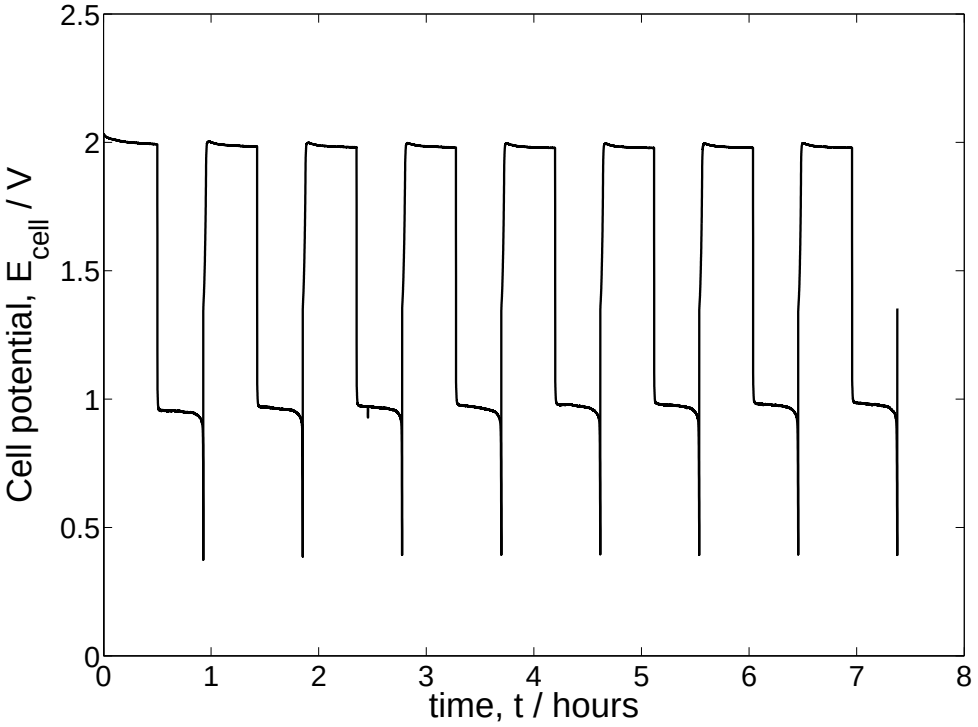

Figure 5.13: *Charge-discharge cycles obtained from C-Tech Innovation Ltd. 8 cm^2 laboratory flow cell at a current density of 10 mA cm^{-2}. The air electrode was the Ni-nano PMA II electrode. The cycles presented are from the 23^{rd} to the 30^{th} cycle. The temperature was 20^oC.*

The negative electrode and the efficiency of the zinc deposition and stripping processes show the charge efficiency. However, the positive electrode dominates the voltage efficiency.

Figure 5.14 shows the individual potential for the *Ni-nano PMA II* electrode over the first 8 cycles. It can be seen that the potential values it exhibits are 0.37 V *vs.* SCE during charging and between -0.70 and -0.57 V *vs.* SCE during discharging.

The voltage difference between charge and discharge during the first cycle is 1.07 V, which lowers to 0.94 V during subsequent cycling. The result is a voltage efficiency of 50 % for the overall cell.

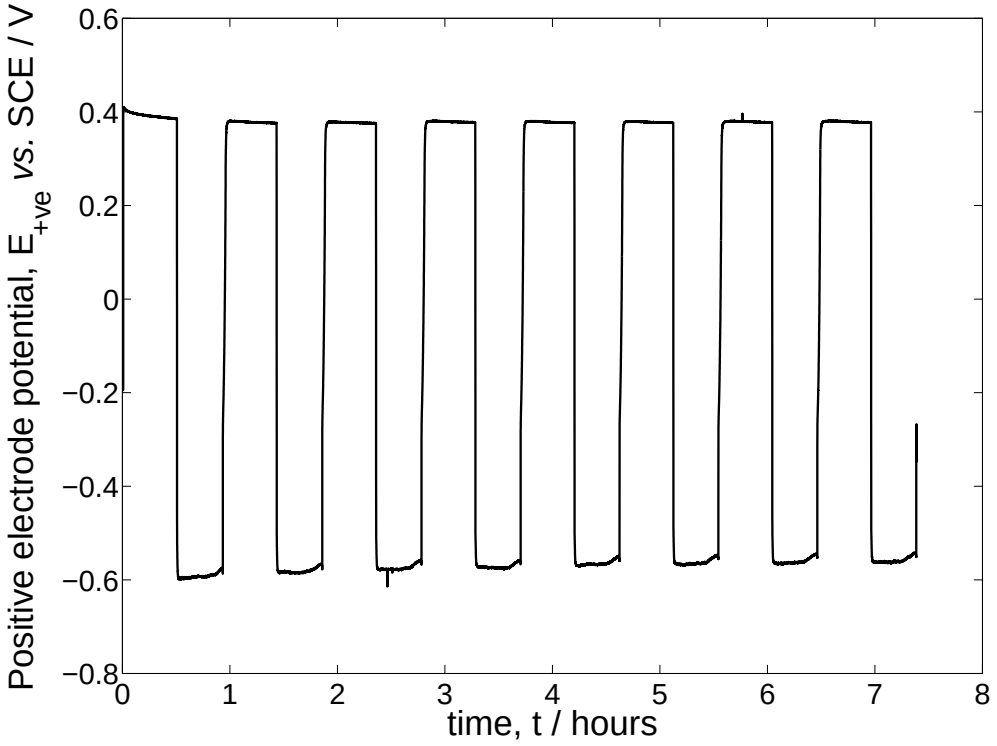

Figure 5.14: *The positive electrode potential results versus time during charge-discharge cycles obtained from C-Tech Innovation Ltd. 8 cm^2 laboratory flow cell at a current density of 10 mA cm^{-2}. The positive electrode was the Ni-nano PMA II electrode. The cycles presented are from the 23^{rd} to the 30^{th} cycle. The temperature was 20°C.*

5.3 Conclusions and Further Work

Novel bifunctional electrodes incorporating HPAs to improve OER and ORR overpotentials have been constructed and tested in an alkaline electrolyte. The bifunctional electrodes incorporated nickel, heteropolyacids (phosphomolybdic and phosphotungstic acid) and Nafion® in their catalyst ink and a Toray carbon paper was used as the gas diffusion substrate.

The manufactured gas diffusion electrodes have been tested with cyclic voltammetry and constant current measurements between ORR and OER. From the literature and chapter 4, the characterisation of heteropolyacids in alkaline has shown that the HPAs have low stability and low redox activity in high pH values. However, the incorporation of HPAs in the catalyst ink of these bifunctional electrodes in conjunction with nickel nano-powder and nickel micro-powder has shown stable and enhancing results towards OER and ORR.

The results from the cyclic voltammetry measurements are similar for the elec-

trodes that incorporated PMA and PWA and they confirm that the enhancing effect is due to the addition of HPA in nickel and not just the HPA or any other component (e.g. Mo, Nafion® etc.). Hence, it was shown that the enhanced activity is likely not due to HPA decomposition to a Mo/Ni catalyst. Further investigation has to be performed in order to distinguish whether there is a difference in the behaviour of the two different heteropolyacids.

In order to investigate whether the anodic current which is observed at negative potentials is due to ORR, an HPA gas diffusion electrode incorporating PMA was characterised by cyclic voltammetry in two different KOH solutions, a solution that included oxygen and a solution that has been de-oxygenated. Comparing the two voltammograms, it was shown that when oxygen was present in the electrolyte, the anodic current occurred at a certain potential, while when the solution was de-oxygenated the anodic current was observed at lower potentials. Hence, it was shown that the anodic current was due to an oxygen related reaction, hence the oxygen reduction reaction.

The constant current cycling between OER and ORR on the manufactured GDEs showed that the electrode which incorporated PWA performs better. However, the potential difference between OER and ORR are still too high for fuel cell and battery applications.

Additionally, based on the constant current cycling results and the results from the SEM and the EDX on an HPA gas diffusion electrode before and after some testing, it was noticed that the catalyst layer of the electrode degrades after consecutive cycling. Hence, improved robustness of the catalyst layer and/or different GDL support material are required. Therefore, more focus has to be set on the different effect that different catalyst loadings, nickel loading and HPA loadings may show. Additionally, alternative gas diffusion substrates have to be tested in order to investigate whether the carbon Toray paper is a suitable choice.

Finally, the results from the charging/discharging measurements obtained from a zinc-air flow cell with an HPA GDE acting as the positive electrode provided evidence that the Ni HPA gas diffusion electrodes could be used in devices that require oxygen evolution (e.g. water electrolysers), oxygen reduction (e.g. fuel cells) or bifunctional oxygen reduction and evolution (e.g. air batteries). No such electrodes are currently commercially available and furthermore, most air electrodes for fuel cells utilise precious metals, which these HPA electrodes do not.

Further development of the HPA gas diffusion electrodes will be undertaken in the

following chapter to provide more characterisation data with the aim of improving performance. The results from the research that has been made on this topic is analysed and discussed in the following chapters.

Chapter 6

Further investigation on HPA gas diffusion electrodes

6.1 Introduction

Chapter 5 showed proof of concept for an HPA-based OER/ORR gas diffusion electrode. However, in order to have a uniform and reliable gas diffusion electrode, further attention had to be paid to the formulation of the catalyst ink. The HPA content in the ink and the ink loading on the substrates were the initial focus.

After suitable characteristics for the catalyst ink were found, a number of electrodes were prepared with the corresponding ink. Each electrode had a different ink solid loading in order to investigate how the ink solid loading of the HPA electrodes affects their electrochemical performance.

It is suspected that HPA forms a salt with nickel [205]. As such, Ni carbonate was used to first prepare a Ni-HPA salt which was then used in place of a nickel powder/HPA combination in the gas diffusion electrodes.

6.2 Results and discussion

6.2.1 Cyclic voltammetries

6.2.1.1 Electrodes with varying HPA content

The initial step towards improving the HPA GDEs was focused on the composition of the catalyst inks. The inks consist of nickel cabonyl, HPA and Nafion®. Inks containing PMA and or PWA were created.

The amount of the nickel micro-powder in each ink was kept constant (6 grams) while the amount of the HPA (PMA or PWA) was gradually increased. In table 6.1 the amount of HPA which was added in the different catalyst inks are summarised. These inks were used to print the HPA gas diffusion electrodes.

Nomenclature	HPA content (gr)	HPA weight:ink solid weight ratio
Ni PMA I	6.01	0.46
Ni PMA II	11.99	0.63
Ni PMA III	16.01	0.70
Ni PMA IV	18.03	0.72
Ni PMA V	20.01	0.74
Ni PMA VI	31.60	0.82
Ni PWA I	9.47	0.57
Ni PWA II	18.94	0.73
Ni PWA III	25.24	0.78
Ni PWA IV	28.46	0.80
Ni PWA V	31.57	0.82
Ni PWA VI	40.00	0.85

Table 6.1: *Table of the manufactured catalyst inks with varying HPA content and constant Ni content (6 grams per ink)*

As described in the previous chapter, the addition of HPA in the catalyst layer of the gas diffusion electrode enhances the performance of the electrode towards the OER and increases the exhibited current. Hence, it is expected that while the amount of HPA in the catalyst ink is increasing, the performance of the corresponding HPA electrode is going to be improving accordingly. However, it is likely that high concentrations of HPA in the ink may result on adverse effect, particularly on poor catalyst layer stability, as the ratio of the Nafion® binder decreases. Hence, the amount of HPA in the ink increased until the point where the performance of the HPA electrodes started decreasing.

In order to monitor the performance of the HPA gas diffusion electrodes, they were electrochemically characterised using cyclic voltammetry. In order to facilitate the comparison between the HPA GDEs, some characteristic potential values were monitored in every CV. Figure 6.1 is added as a reference CV to highlight these potential values.

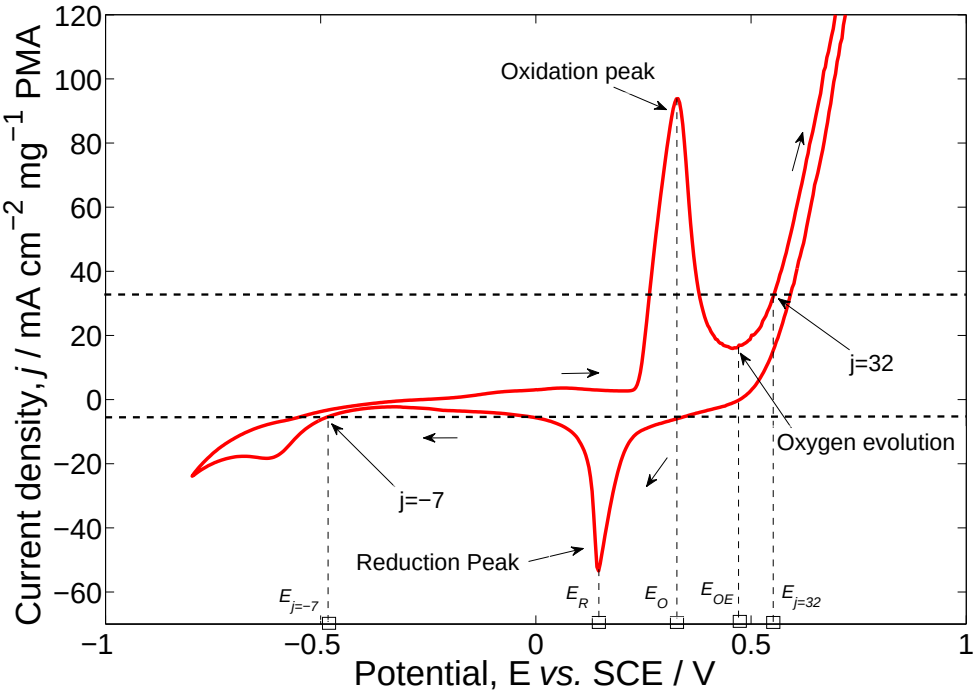

Figure 6.1: *Cyclic voltammograms of a Ni PMA electrode in 4.0 M KOH and fixed O_2 flow ($300\,cm^3\,min^{-1}$). The third cycle of the voltammogram is presented. The scan rate of the voltammograms was 50 mV sec^{-1} and the temperature was 20°C. The working electrode area was 1.33 cm^2.*

In all the voltammograms, an oxidation peak due to the oxidation of $Ni(OH)_2$ to NiOOH and a reduction peak due to the reduction of NiOOH back to $Ni(OH)_2$ were observed. The potential of the oxidation peak is described as E_O and the potential of the reduction peak as E_R. A method to measure the reversibility of the electrode reaction is by monitoring the potential difference between E_O and E_R ($E_O - E_R$) [206].

The oxygen evolution potential (E_{OE}) is an important characteristic that can be used for the evaluation of the electrode's performance. The oxygen evolution potential was taken as the potential after the oxidation peak where the current starts increasing.

Another two potential values have been chosen as a way to compare the performance of the electrodes, the potential value at j=32 mA cm^{-2} mg^{-1} HPA ($E_{j=32}$)

and the potential value at j=-7 mA cm^{-2} mg^{-1} HPA ($E_{j=-7}$). $E_{j=32}$ was taken at the potential where j equals to 32 mA cm^{-2} mg^{-1} HPA for the first time after the oxidation peak and the $E_{j=-7}$ was taken at the potential where j equals to -7 mA cm^{-2} mg^{-1} HPA for the first time after the reduction peak (6.1)

The lower these potential values are, the more efficient the electrode is at evolving O_2. Hence, the best performing electrode is defined to be the electrode which exhibits the lowest values for $E_O - E_R$, E_{OE}, $E_{j=32}$ and $E_{j=-7}$.

6.2.1.1.1 Electrodes with varying PMA:Ni ratio

The cyclic voltammetries on the Ni PMA electrodes were taken in 4.0 M KOH and under fixed O_2 flow ($300\,cm^3\,min^{-1}$). The voltage limits were between +0.8 V *vs.* SCE and -0.8 V *vs.* SCE. Four consecutive cycles were performed on each electrode to ensure reproducible data, since after the third scan the voltammograms were stable. The voltammograms are normalised by the HPA loading.

As mentioned before, the best performing electrode is the electrode which exhibits the lowest potential values for $E_O - E_R$, E_{OE}, $E_{j=32}$ and $E_{j=-7}$.

From table 6.2 and figure 6.2, it can be seen that the $E_O - E_R$ values are similar for the *Ni PMA I* and the *Ni PMA II* electrodes but they are lower for the *Ni PMA III*, the *Ni PMA IV* and the *Ni PMA V* electrodes. The lowest value for the $E_O - E_R$ is obtained by the CV of the *Ni PMA V* electrode and it is at 184.6 mV *vs.* SCE.

Electrodes	**PMA:Ni ratio**	**HPA loading (mg cm^{-2})**	**E_O-E_R (mV)**	**E_{OE} (mV *vs.* SCE)**	**$E_{j=32}$ (mV *vs.* SCE)**	**$E_{j=-7}$ (mV *vs.* SCE)**
Ni PMA I	1.0	1.92	438	618	654	−544
Ni PMA II	2.0	2.80	435	648	735	−550
Ni PMA III	2.7	2.99	373	551	639	−523
Ni PMA IV	3.0	2.79	284	544	627	−529
Ni PMA V	3.3	3.26	185	458	551	−510
Ni PMA VI	5.3	4.90	208	470	627	−558

Table 6.2: *Structural details of the Ni PMA electrodes and characteristic potential values obtained from the cyclic voltammetries on the Ni PMA electrodes. E_O−E_R is the difference between the oxidation peak potential and the reduction peak potential, E_{OE} is the oxygen evolution potential, $E_{y=32}$ is the potential value at j=32 mA cm^{-2} mg^{-1} HPA and abs($E_{y=-7}$) is the absolute value of the potential at j=-7 mA cm^{-2} mg^{-1} HPA.*

One would expect that the E_{OE} values would show similar trend to the one observed for the $E_O - E_R$ values. On the contrary, there is a fluctuation with the *Ni PMA II* exhibiting a higher E_{OE} value compared to the value obtained from the CV of the *Ni PMA I* electrode. Additionally, the *Ni PMA II* electrode showed a higher E_{OE} value than the value exhibited by the *Ni PMA III* electrode. In general, the lowest E_{OE} value corresponds to the value exhibited by the *Ni PMA V* electrode (478 mV *vs.* SCE).

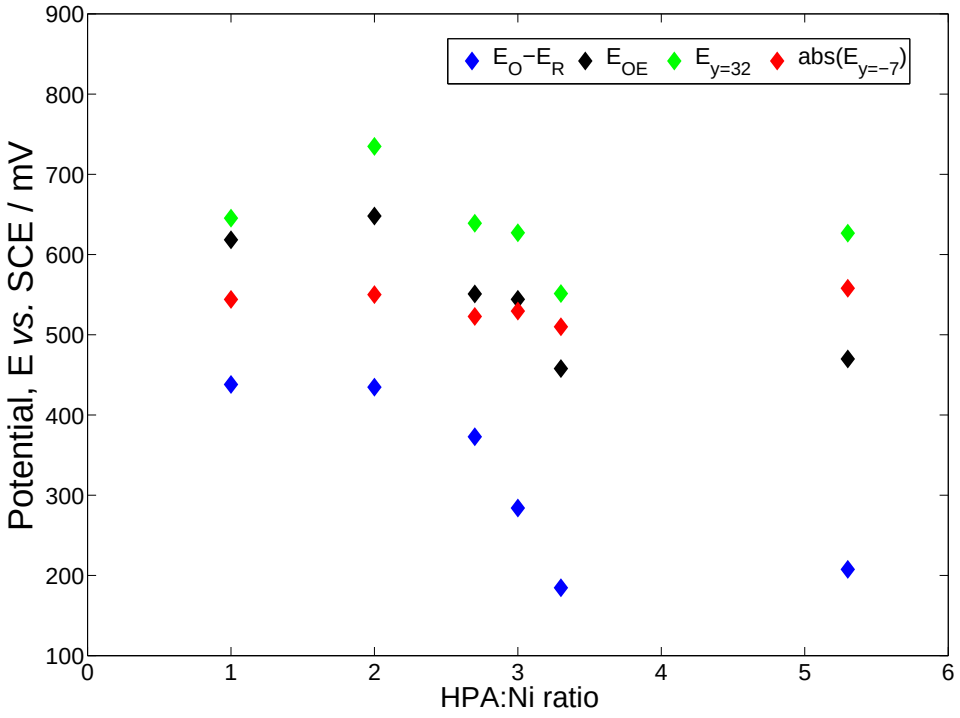

Figure 6.2: *Characteristic potential values of the Ni PMA electrodes with different HPA:Ni ratio obtained from their cyclic voltammograms in 4.0 M KOH and fixed O_2 flow ($300\,cm^3\,min^{-1}$). E_O−E_R is the difference between the oxidation peak potential and the reduction peak potential (blue points), E_{OE} is the oxygen evolution potential (black points), $E_{y=32}$ is the potential value at j=32 mA cm^{-2} mg^{-1} HPA (green points) and abs($E_{y=-7}$) is the absolute value of the potential at j=-7 mA cm^{-2} mg^{-1} HPA (red points).*

The values for the $E_{j=32}$ exhibited by the *Ni PMA II* and the *Ni PMA IV* electrodes were higher when compared to the values exhibited by the *Ni PMA I* and the *Ni PMA III* electrodes, respectively. However, similarly to the previous observations, the lowest value for the $E_{j=32}$ value (551.3 mV *vs.* SCE) is exhibited by the *Ni PMA V* electrode.

Finally, the differences in the $E_{j=-7}$ values that were obtained by the Ni PMA electrodes (*Ni PMA I -Ni PMA VI*) are not as profound as they were for the rest

of the potential values that are included in figure 6.2. Nevertheless, the lowest value for the $E_{j=-7}$ is from the CV of the *Ni PMA V* electrode (-510 mV *vs.* SCE).

Hence, the electrode that shows the lowest values for the $E_O - E_R$, E_{OE}, $E_{j=32}$ and $E_{j=-7}$ is the *Ni PMA V* electrode which means that the *Ni PMA V* is rated as the best electrode compared to the rest of the Ni PMA electrodes.

The observations based on the results summarised in table 6.2 and figure 6.2 about the potential values which were exhibited by the Ni PMA electrodes can be also confirmed by the CVs that are included in figure 6.3.

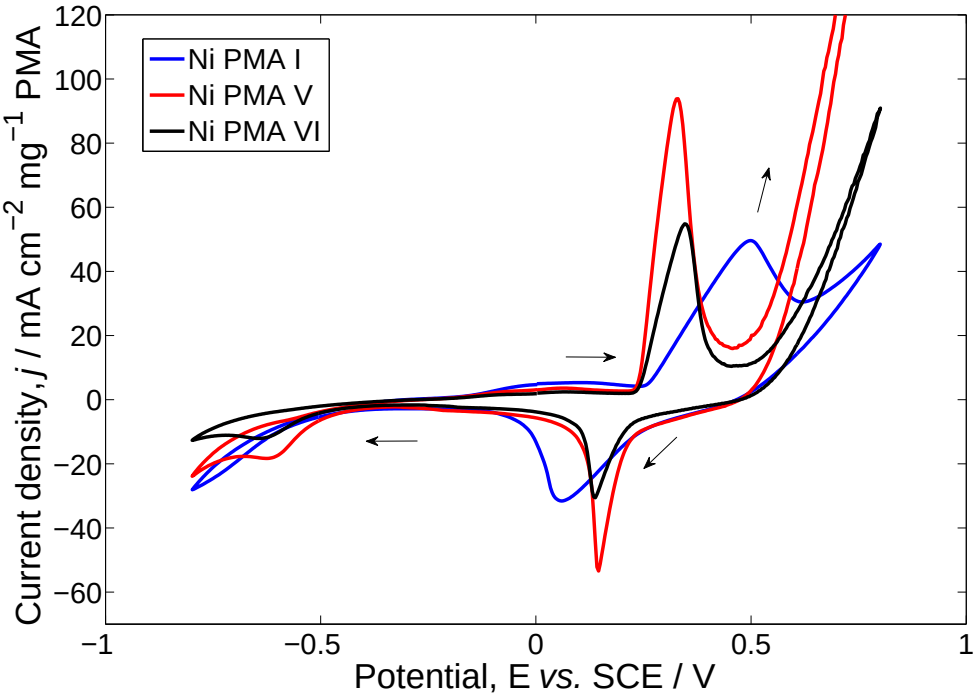

Figure 6.3: *Cyclic voltammograms of the Ni PMA I (blue line), Ni PMA V (red line) and Ni PMA VI (black line) electrodes in 4.0 M KOH and fixed O_2 flow (300 $cm^3\ min^{-1}$). The third cycle of each voltammogram is presented. The scan rate of the voltammograms was 50 mV sec^{-1} and the temperature was 20°C. The working electrode area was 1.33 cm^2.*

In this figure, the cyclic voltammetries of three Ni PMA electrodes are presented. The electrodes were chosen to represent one electrode with low (*Ni PMA I*), one electrode with medium (*Ni PMA V*) and one electrode with high (*Ni PMA VI*) HPA:Ni ratio.

From figure 6.3, it can be seen that the *Ni PMA I* electrode which had the lowest PMA:Ni ratio (1.0) showed very poor results, since the $E_O - E_R$ was equal to 438

mV, the E_{OE} was equal to 618 mV *vs.* SCE, the $E_{j=32}$ was equal to 654 mV *vs.* SCE and the $E_{j=-7}$ was equal to -544 mV *vs.* SCE which were all higher to the potential values obtained when the HPA:Ni ratio of the electrodes was increased.

When the PMA:Ni ratio in the electrode was 3.3 the results from the CVs of the related electrode (*Ni PMA V*) were noticeably better with the $E_O - E_R$ being equal to 185 mV, the E_{OE} was equal to 458 mV *vs.* SCE, the $E_{j=32}$ was equal to 551 mV *vs.* SCE and the $E_{j=-7}$ was equal to -510 mV *vs.* SCE.

However, when the HPA:Ni ratio on the electrode reached 5.3 (*Ni PMA VI*), the CV of the *Ni PMA VI* electrode showed that the $E_O - E_R$ was equal to 207 mV, the E_{OE} was equal to 470 mV *vs.* SCE, the $E_{j=32}$ was equal to 627 mV *vs.* SCE and the $E_{j=-7}$ was equal to -558 mV *vs.* SCE which were higher to the potential values which were exhibited by the *Ni PMA V* electrode.

From these CVs, it is confirmed again that the electrode with the best performance is the *Ni PMA V* electrode.

6.2.1.1.2 Electrodes with varying PWA:Ni ratio

The same experimental procedure was followed in order to discover the optimum amount of PWA that should be included in the catalyst ink. A series of CVs were taken on the *Ni PWA* electrodes under 4.0 M KOH and fixed O_2 flow ($300\,cm^3\,min^{-1}$). The voltage limits were between +0.8 V *vs.* SCE and -0.8 V *vs.* SCE. Four consecutive cycles were performed on each electrode to ensure reproducible data, since after the third scan the received results were stable. The voltammograms are normalised by the HPA loading.

In table 6.3 and in figure 6.4, the values of $E_O - E_R$, E_{OE}, $E_{j=32}$ and $E_{j=-7}$ which were obtained from the CVs of the *Ni PWA* electrodes are summarised.

It can be seen that it is slightly more complicated to distinguish the electrode which gives the lowest values for $E_O - E_R$, E_{OE}, $E_{j=32}$ and $E_{j=-7}$ among the *Ni PWA* electrodes when compared to the results of the Ni PMA electrodes (fig. 6.2). In figure 6.2 there is a descending effect in the potential values as the HPA:Ni ratio is increasing which makes it easier to identify the electrode with the lowest potential values but there is not a similar effect observed in figure 6.4.

If the values obtained from the *Ni PWA III* electrode are excluded, the values for $E_O - E_R$, E_{OE}, $E_{j=32}$ and $E_{j=-7}$ of the *Ni PWA I* to the *Ni PWA IV* electrodes are

Electrodes	**PWA:Ni ratio**	**HPA loading (mg cm^{-2})**	**E_O-E_R (mV)**	**E_{OE} (mV *vs.* SCE)**	**$E_{j=32}$ (mV *vs.* SCE)**	**$E_{j=-7}$ (mV *vs.* SCE)**
Ni PWA I	1.6	2.31	310	553	644	−587
Ni PWA II	3.2	2.88	322	546	621	−540
Ni PWA III	4.2	5.77	413	578	678	−623
Ni PWA IV	4.7	3.93	262	476	576	−563
Ni PWA V	5.3	4.03	261	486	588	−574
Ni PWA VI	6.7	9.35	354	565	754	−648

Table 6.3: *Structural details of the Ni PWA electrodes and characteristic potential values obtained from the cyclic voltammetries on the Ni PWA electrodes. $E_O - E_R$ is the difference between the oxidation peak potential and the reduction peak potential, E_{OE} is the oxygen evolution potential, $E_{y=32}$ is the potential value at j=32 mA cm^{-2} mg^{-1} HPA and abs($E_{y=-7}$) is the absolute value of the potential at j=-7 mA cm^{-2} mg^{-1} HPA.*

decreasing as the PWA content is increasing. The lowest values for E_{OE}, $E_{j=32}$ and $E_{j=-7}$ correspond to the values obtained by the CVs of *Ni PWA IV* since the values exhibited by the *Ni PWA V* and the *Ni PWA VI* electrodes are both higher.

However, the $E_O - E_R$ value exhibited by *Ni PWA IV* electrode is 262 mV *vs.* SCE whereas the value which is exhibited by the *Ni PWA V* electrode is 261 mV *vs.* SCE. The voltage difference between these two values is only one millivolt and taking into account the low potential values of E_{OE}, $E_{j=32}$ and $E_{j=-7}$ which were exhibited by the *Ni PWA IV* electrode, it can be still supported that the *Ni PWA IV* electrode performs better than the rest of the *Ni PWA* electrodes.

As for the *Ni PWA III* electrode, considering its HPA:Ni ratio, the potential values for the E_{OE}, $E_{j=32}$ and $E_{j=-7}$ were high when compared to the rest of the electrodes. This result could possibly be due the high HPA loading (5.77 mg cm^{-2}) of the electrode when compared to the 2.88 mg cm^{-2} HPA loading of the *Ni PWA II* electrode and the 3.93 mg cm^{-2} HPA loading of the *Ni PWA IV* electrode.

Hence, it is observed that the ink solid loading affects the electrochemical performance of the electrode which probably also shows that the ratio of Ni:Nafion®:HPA is equally important to the HPA:Ni ratio. This initial observation on the effect of the ink solid loading on the electrochemical performance of the electrode is going to be further investigated later on in this chapter, however the importance of the Ni:Nafion®:HPA has to be examined in the future.

In figure 6.5, the CVs of an electrode with low (*Ni PWA I*), medium (*Ni PWA*

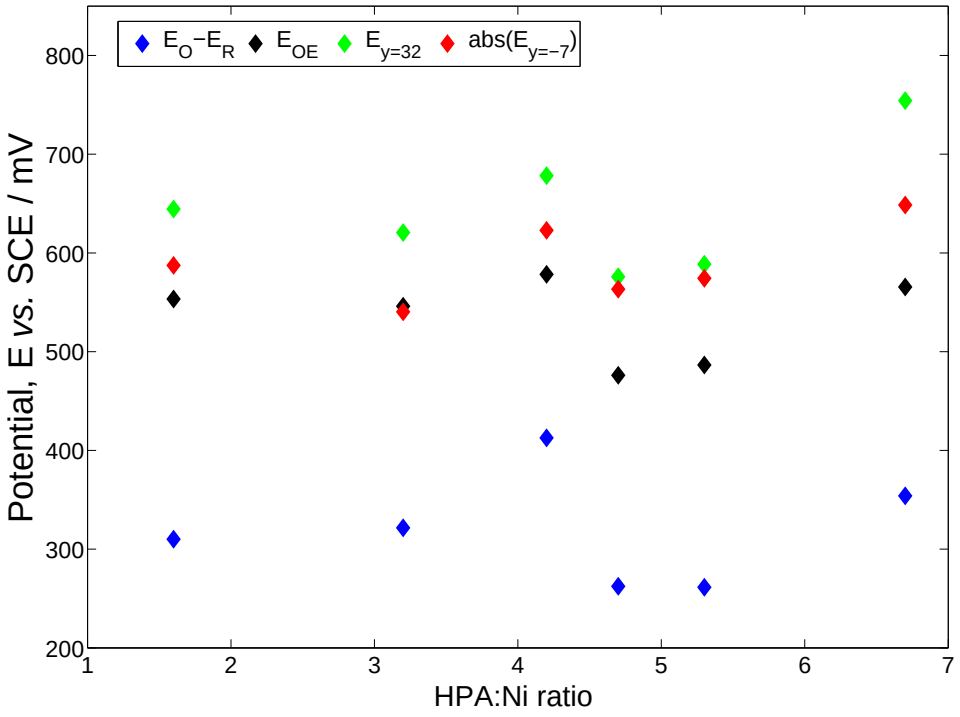

Figure 6.4: *Characteristic potential values obtained from the cyclic voltammograms of the Ni PWA electrodes with different HPA:Ni ratio in 4.0 M KOH and fixed O_2 flow (300 $cm^3\,min^{-1}$). E_O-E_R is the difference between the oxidation peak potential and the reduction peak potential (blue points), E_{OE} is the oxygen evolution potential (black points), $E_{y=32}$ is the potential value at j=32 mA cm^{-2} mg^{-1} HPA (green points) and abs($E_{y=-7}$) is the absolute value of the potential at j=-7 mA cm^{-2} mg^{-1} HPA (red points).*

IV) and high (*Ni PWA VI*) HPA:Ni ratio are presented.

Generally, it can be observed that the *Ni PWA I* electrode exhibits the lowest performance of these three electrodes, since the $E_O - E_R$ was 310 mV, the E_{OE} was 553 mV *vs.* SCE, the $E_{j=32}$ was equal to 644 mV *vs.* SCE and the $E_{j=-7}$ was -587 mV *vs.* SCE. The *Ni PWA IV* electrode with 4.7 HPA:Ni ratio has an improved performance with the $E_O - E_R$ equal to 262 mV, the E_{OE} equal to 476 mV *vs.* SCE, the $E_{j=32}$ equal to 576 mV *vs.* SCE and the $E_{j=-7}$ equal to -563 mV *vs.* SCE. Finally, the potential values exhibited by the *Ni PWA VI* electrode (HPA:Ni ratio=6.7) were 354 mV for the $E_O - E_R$, 565 mV *vs.* SCE for the E_{OE}, 754 mV *vs.* SCE for the $E_{j=32}$ and -648 mV *vs.* SCE for the $E_{j=-7}$ which showed that the *Ni PWA VI* electrode had a decreased performance since the potential values exhibited were higher than the values exhibited by the *Ni PWA IV* electrode.

The *Ni PWA IV* electrode exhibited higher current density values, the potential

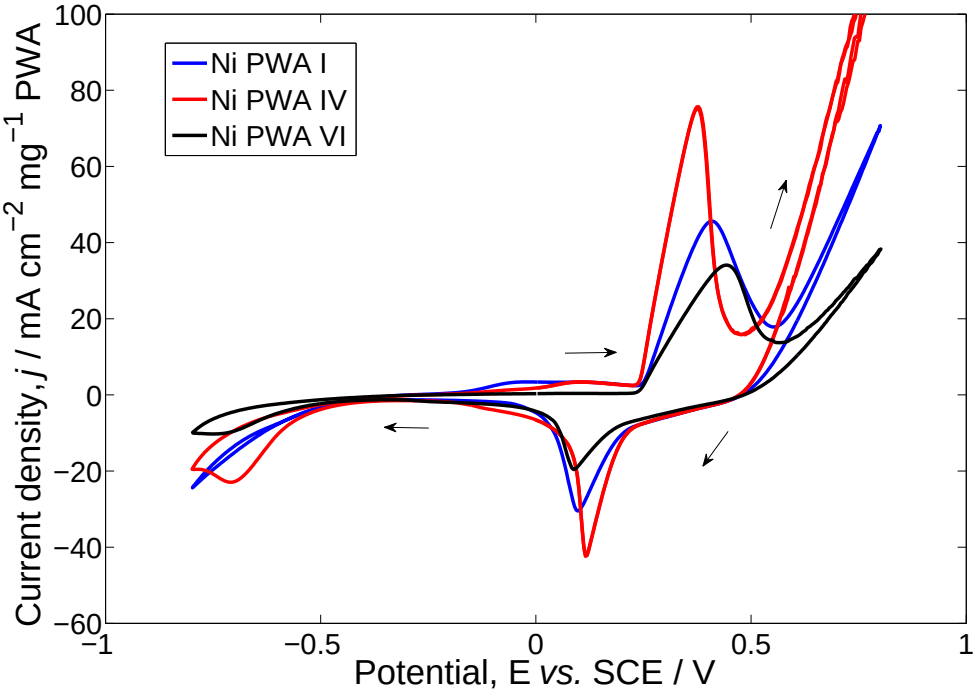

Figure 6.5: *Cyclic voltammograms of the Ni PWA I (blue line), Ni PWA IV (red line) and Ni PWA VI (black line) electrodes in 4.0 M KOH and fixed O_2 flow (300 $cm^3\ min^{-1}$). The third cycle of each voltammogram is presented. The scan rate of the voltammograms was 50 mV sec^{-1} and the temperature was 20°C. The working electrode area was 1.33 cm^2.*

difference between the oxidation and the reduction peak was lower and the over-potential related to the OER was smaller when compared to the CV of both *Ni PWA I* and *Ni PWA VI* electrodes.

Hence, from figures 6.5, 6.4 and table 6.3, the *Ni PWA IV* electrode, whose HPA:Ni ratio was equal to 4.7, has the best electrochemical performance. In general, this supports the initial idea that as the HPA:Ni ratio increases, the performance of the related electrode improves until a point where the additional increase on the HPA:Ni ratio results to a lower performance by the related electrode.

6.2.1.1.3 Comparison between the best performing Ni PMA *vs.* the best performing Ni PWA electrode

The next question that has to be answered is whether the addition of PWA or the addition of PMA contributes towards a better electrode. For that reason, the results from the CVs of the *Ni PMA V* electrode which had the most enhanced

behaviour among the Ni PMA electrodes and the *Ni PWA IV* electrode which showed the best results among the *Ni PWA* electrodes are compared.

From table 6.4, the $E_O - E_R$ for the *Ni PWA IV* electrode is 262 mV *vs.* SCE versus 185 mV *vs.* SCE for the *Ni PMA V* electrode and the E_{OE} value is 476 mV *vs.* SCE for the *Ni PWA IV* electrode versus 458 mV *vs.* SCE for the *Ni PMA V* electrode. The value of $E_{j=32}$ which was exhibited by the *Ni PWA IV* electrode is 576 mV *vs.* SCE against 551 mV *vs.* SCE which was exhibited by the *Ni PMA V* and the $E_{j=-7}$ for the *Ni PWA IV* electrode is -563 mV *vs.* SCE against -510 mV *vs.* SCE for the *Ni PMA V* electrode.

Electrodes	**HPA:Ni ratio**	**HPA loading (mg cm^{-2})**	**E_O-E_R (mV)**	**E_{OE} (mV *vs.* SCE)**	**$E_{j=32}$ (mV *vs.* SCE)**	**$E_{j=-7}$ (mV *vs.* SCE)**
Ni PMA V	3.3	3.26	185	458	551	−510
Ni PWA IV	4.7	3.93	262	476	576	−563

Table 6.4: *Characteristics of the Ni PMA V and Ni PWA IV electrodes*

Hence, the values of $E_O - E_R$, E_{OE}, $E_{j=32}$ and $E_{j=-7}$ are lower for the *Ni PMA V* electrode. So, the addition of PMA in the catalyst ink gives better results when compared to the results from the incorporation of PWA in the catalyst ink. This is an initial remark and more details have to be taken into account (e.g. ink solid loading, HPA loading etc) in order to come up to a definite conclusion.

6.2.1.2 Nickel carbonate instead of nickel micro-powder

Since it was concluded in 6.2.1.1 that the Ni PMA electrode gives favourable results when compared to the Ni PWA electrode, the following experiments focus further on the investigation of the composition of the Ni PMA inks. Hence, the results from the research on whether the substitution of nickel micro-powder with nickel carbonate in the catalyst inks improves the resulting electrode's electrochemical performance are presented.

Combining metallic nickel with HPA is likely to result in a system where the HPA is complexed to the outer surface of the nickel, i.e. a metallic substrate to which the HPA binds. On the contrary, the combination of nickel carbonate with PMA forms a Ni-PMA salt ($Ni_3(PMo_{12}O_{40})_2$) where three atoms of nickel are surrounded by two molecules of HPA [205]. Hence, it was investigated whether the presence of

the Ni-HPA salt in the catalyst ink enhances further the performance of the Ni PMA electrodes.

Therefore, two additional Ni PMA inks were prepared, ink *Ni PMA A* and *Ni PMA B* and details about these two inks can be found in table 6.5.

Nomenclature	Compounds	Quantity (gr)
Ni PMA A	Nickel carbonate	3.98
	PMA	49.24
	Nafion®	16.54
Ni PMA B	Nickel carbonate	3.976
	PMA	49.03
	Nickel micro-powder	3.10
	Nafion®	16.47

Table 6.5: *Table of details of the manufactured catalyst inks with nickel carbonate and PMA*

The *Ni PMA A* ink consists of Ni-PMA salt and Nafion® while the *Ni PMA B* ink consists of nickel micro-powder, the Ni-PMA salt and Nafion®.

Both the *Ni PMA A* and the *Ni PMA B* electrodes were electrochemically characterised by cyclic voltammetry in 4.0 M KOH and under fixed O_2 flow ($300\,cm^3\,min^{-1}$). The total cycles were four and the voltage limits were between +0.8 V *vs.* SCE and -0.8 V *vs.* SCE. The voltammograms are normalised by the HPA loading.

The characteristic potential values from the voltammograms of *Ni PMA A* and *Ni PMA B* electrodes in addition to the results from voltammogram of the *Ni PMA V* electrode, which was introduced in 6.2.1.1, are presented table 6.6 and the voltammograms in figure 6.6. It has to be noted that in these voltammograms the potential value that was chosen was the $E_{j=-4}$.

Electrodes	E_O-E_R (mV)	E_{OE} (mV *vs.* SCE)	$E_{j=20}$ (mV *vs.* SCE)	$E_{j=-4}$ (mV *vs.* SCE)
Ni PMA A	127	473	643	−510
Ni PMA B	135	496	625	−492
Ni PMA V	185	458	201	−449

Table 6.6: *Characteristic potential values obtained from the cyclic voltammetries of the Ni PMA A, Ni PMA B and Ni PMA V electrodes. $E_O - E_R$ is the difference between the oxidation peak potential and the reduction peak potential, E_{OE} is the oxygen evolution potential, $E_{y=32}$ is the potential value at j=32 mA cm^{-2} mg^{-1} HPA and abs($E_{y=-7}$) is the absolute value of the potential at j=-7 mA cm^{-2} mg^{-1} HPA.*

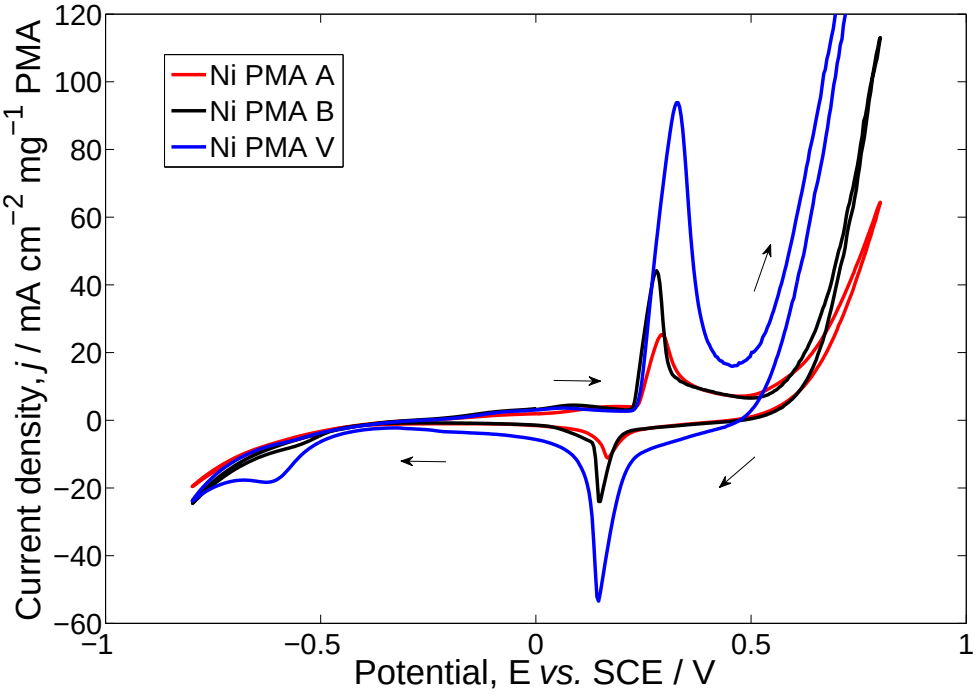

Figure 6.6: *Cyclic voltammograms of the Ni PMA A (red line), Ni PMA B (black line) and Ni PMA V (blue line) electrodes. The electrolyte is 4.0 M KOH and the experiment is under fixed O_2 flow ($300\,cm^3\,min^{-1}$). The third cycle of each voltammogram is presented. The scan rate of the voltammograms was 50 mV sec^{-1} and the temperature was 20^{o}C. The working electrode area was 1.33 cm^2.*

From table 6.6 and figure 6.6, it can be seen that the electrodes with the nickel carbonate have lower potential difference between the E_O and the E_R when compared to the results from the CV of the *Ni PMA V* electrode. This shows that the kinetics of the redox reaction between Ni^{2+} and Ni^{3+} are faster when the Ni-PMA salt is present.

Both *Ni PMA A* and *Ni PMA B* electrodes gave low current density values with the *Ni PMA A* electrode exhibiting the lowest values. Additionally, with the aid of table 6.6 it can be seen that the *Ni PMA A* electrode has the largest values for the E_{OE}, the $E_{j=20}$ and the $E_{j=-4}$. The related values exhibited by the *Ni PMA B* electrode were lower when compared to the values exhibited by *Ni PMA A* but higher when compared to the values from the CV of the *Ni PMA V* electrode. Therefore, the Ni PMA V electrode still shows the best electrochemical activity when compared to the *Ni PMA A* and the *Ni PMA B* electrodes.

From these results it was shown that the electrodes which were formed by the ink with the Ni-HPA salt are stable and they operate under alkaline environment. The active species in these electrodes are believed to be the Ni-HPA salt

$Ni_3(PMo_{12})_{40})_2$. However, the Ni:HPA ratio and the nickel surface area are two very important characteristics of the electrodes and from figure 6.6 it can be seen that when the CV is normalised by the electrode's PMA loading, the electrodes with nickel micro-powder and HPA work better. The reason behind this enhanced performance of the electrodes with nickel micro-powder and PMA is not yet fully explored but an initial speculation is that it is due to the metallic nickel's higher electron conductivity which exists in the nickel micro-powder.

6.2.1.3 Ink solid loading effect

Electrodes were made using the same Ni PMA ink but with varying the ink's solid loading. The Ni PMA ink which was used it incorporated 20.01 grams of PMA and it was the ink that has been used to print the *Ni PMA V* electrode which has shown the best results in 6.2.1.1 and 6.2.1.2. The ink solid loading and the HPA loading values of these new electrodes can be found in table 6.7.

Electrodes	**Ink solid loading (mg cm^{-2})**	**HPA loading (mg cm^{-2})**	**E_O-E_R (mV)**	**E_{OE} (mV *vs.* SCE)**
Ni PMA V_1	5.78	4.27	310	521
Ni PMA V_2	7.61	5.62	295	514
Ni PMA V_3	8.50	6.28	200	469

Table 6.7: *Details about the ink solid loading and the HPA loading of the Ni PMA V_1, Ni PMA V_2 and Ni PMA V_3 electrodes*

These electrodes were characterised by cyclic voltammetry in 4.0 M KOH and under fixed O_2 flow ($300\,cm^3\,min^{-1}$). The total cycles were four and the voltage limits were between +0.8 V *vs.* SCE and -0.8 V *vs.* SCE.

From table 6.7 and figure 6.7, it is shown that the *Ni PMA V_3* electrode exhibits the lowest values for the $E_O - E_R$ (200 mV) and the E_{OE} (469 mV *vs.* SCE).

The $E_O - E_R$ value for the *Ni PMA V_2* is 295 mV *vs.* SCE, while for the *Ni PMA V_1* is 310 mV *vs.* SCE. The E_{OE} for the *Ni PMA V_2* started at 514 mV *vs.* SCE towards positive potentials and for the *Ni PMA V_1* electrode it began at 521 mV *vs.* SCE towards positive potentials. Comparing the results from the voltammograms of these three electrodes it can be seen that the *Ni PMA V_1* electrode exhibits the highest values and hence was the worst electrochemical performance.

The CVs on these three electrodes are shown in figure 6.8.

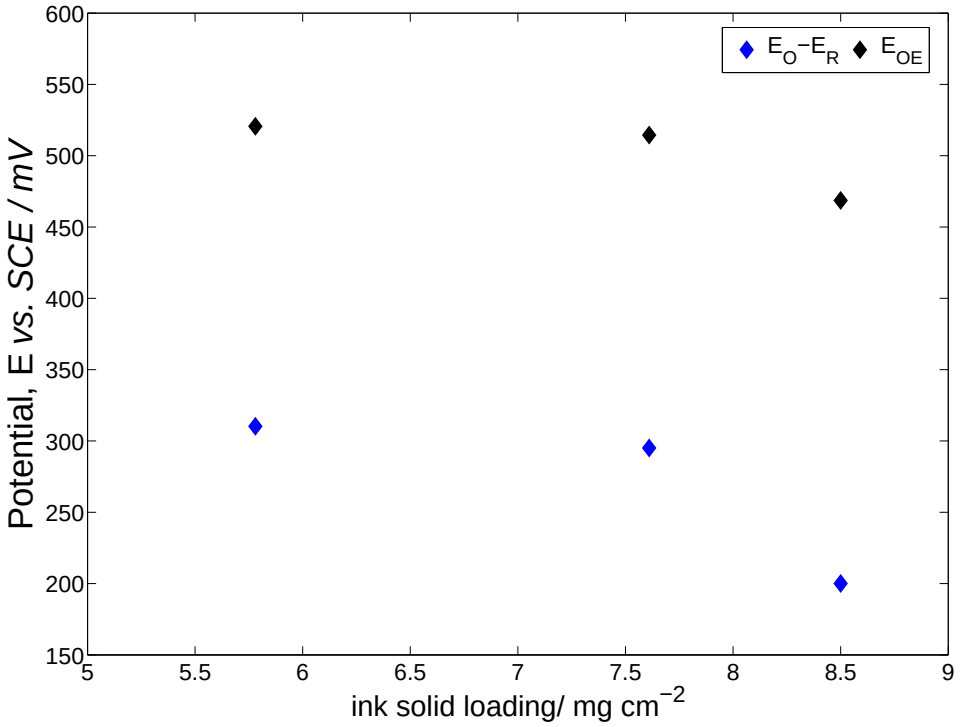

Figure 6.7: *Characteristic potential values of the Ni PMA electrodes with different ink solid loading obtained from their cyclic voltammograms in 4.0 M KOH and fixed O_2 flow ($300\,cm^3\,min^{-1}$). E_O-E_R is the difference between the oxidation peak potential and the reduction peak potential (blue points) and E_{OE} is the oxygen evolution potential (black points)*

In figure 6.8a, it is shown that there is a slight difference between the three different voltammograms on the three different *Ni PMA* electrodes but it is not much distinct. It is shown that the *Ni PMA* V_3 with 8.50 mg cm^{-2} ink solid loading shows the best performance since it has the lowest overpotential for oxygen evolution and the lowest difference between the oxidation and the reduction peak. While the electrode with the lowest ink solid loading (5.78 mg cm^{-2} for *Ni PMA* V_1) gave the most poor performance.

In terms of the current density values which were exhibited by the three *Ni PMA* electrodes in figure 6.8a, the electrode with the 7.61 mg cm^{-2} ink solid loading (*Ni PMA* V_1) showed the highest current density values at the oxidation and the reduction peaks of the voltammogram but the electrode with the highest ink solid loading, 8.50 mg cm^{-2} exhibited higher current density values during the OER.

The CVs in figure 6.8b are the same CVs as those presented in figure 6.8a but they are normalised by the PMA loading. In figure 6.8b, it is shown that the *Ni PMA* V_1 electrode with 5.78 mg cm^{-2} ink solid loading exhibited the highest

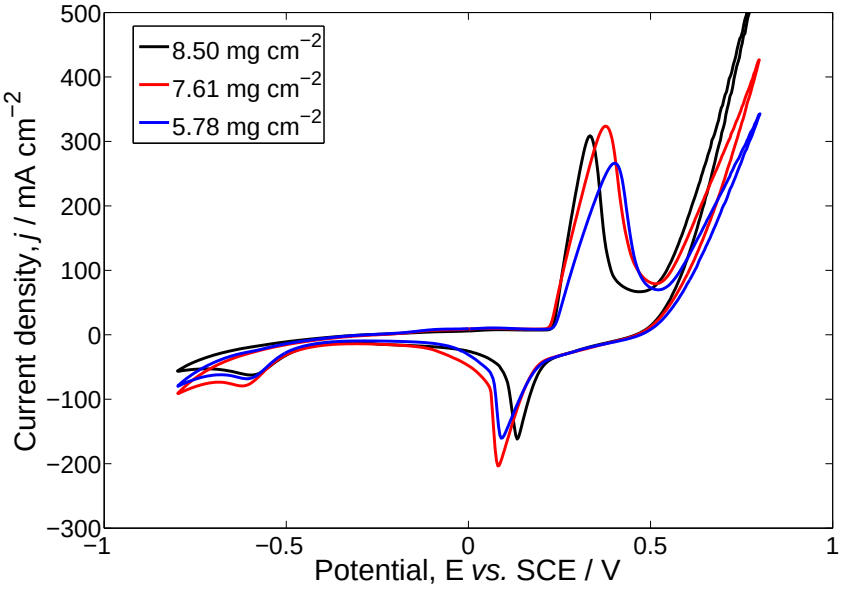

(a)

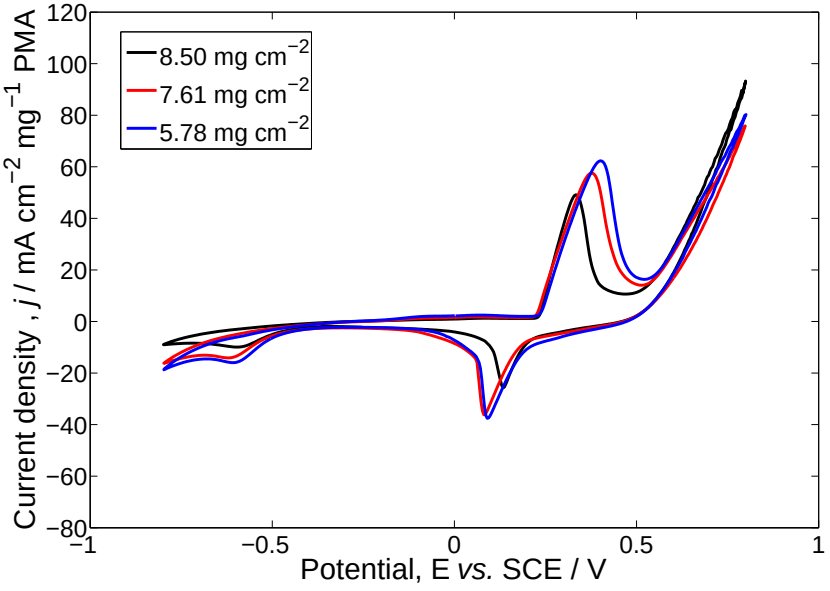

(b)

Figure 6.8: *Cyclic voltammograms of the Ni PMA electrodes with different ink solid loading; 8.50 mg cm^{-2} (black line), 5.78 mg cm^{-2} (blue line) and 7.61 mg cm^{-2} (red line). The measurements are under 4.0 M KOH and fixed O_2 flow ($300\,cm^3\,min^{-1}$). The third cycle of each voltammogram is presented. The scan rate of the voltammograms was 50 mV sec^{-1} and the temperature was 20°C. The working electrode area was 1.33 cm^2.*

current density values but the *Ni PMA V_3* electrode with 8.50 mg cm^{-2} ink solid loading showed that the difference between E_O and E_R and the E_{OE} value are the lowest when compared to the other two electrodes.

Hence, the kinetics of the electron transfer reactions on the electrodes were fast when the ink solid loading was the highest. However, when the voltammograms were normalised by the PMA loading, it was observed that the current density values that the electrode with the lowest ink solid loading exhibited were the highest. So, it can be concluded that high ink solid loading promotes the electron transfer reactions but does not enhance high current density values on the electrode's surface.

6.2.2 Constant current potentiometry

The results from the constant current measurements between OER and ORR on the Ni PMA electrodes are presented in this section. The first set of measurements focuses on the investigation of the effect that the ink solid loading of the *Ni HPA* electrodes potentially has on the electrode's performance.

In figure 6.9, one cycle of ORR and OER at the electrodes *Ni PMA* V_1, *Ni PMA* V_2 and *Ni PMA* V_3 are shown. These electrodes have been previously tested by using cyclic voltammetry in figures 6.2.1.1 and 6.2.1.3.

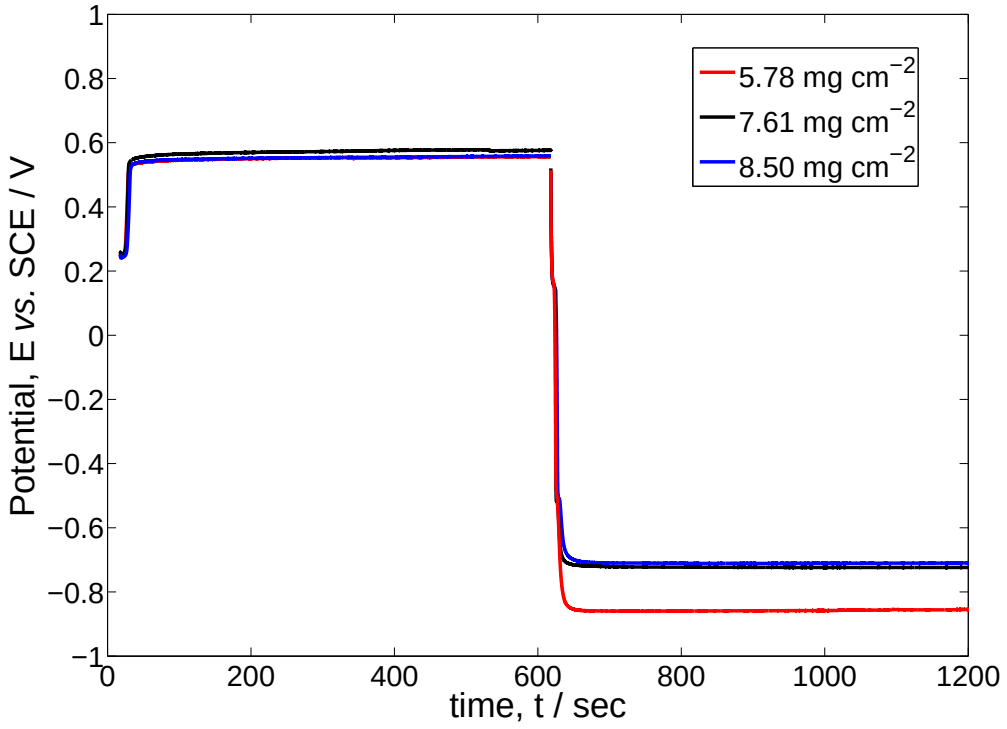

Figure 6.9: *Constant current measurements Ni PMA electrodes with different ink solid loading; 5.78 mg cm^{-2} (red line), 7.61 mg cm^{-2} (black line) and 8.50 mg cm^{-2} (blue line). The measurements were under 4.0M KOH, O_2 flow (300 $cm^3\,min^{-1}$) and current density* 50 *mA cm^{-2}. The temperature was 20^{o}C and the working electrode area was 1.33 cm^2.*

The electrolyte was 4.0 M KOH and the O_2 flow was 300 $cm^3\,min^{-1}$ during the measurement. Each cycle lasted for 1200 sec since the OER lasted for 600 seconds followed by 600 seconds of ORR. The current density which was applied during the OER was +50 mA cm^{-2} and -50 mA cm^{-2} during the ORR. All the electrodes seem stable in alkaline environment during the OER and ORR measurements.

The potential difference between OER and ORR for the electrode with the highest

ink solid loading (*Ni PMA V$_3$*) is close to 1.26 V. For the *Ni PMA V$_2$* with 7.61 mg cm^{-2} ink solid loading the potential difference between OER and ORR is approximately 1.29 V and for the electrode with the lowest ink solid loading (*Ni PMA V$_1$*) the potential difference is 1.41 V. The lowest potential difference between the OER and the ORR is observed for the *Ni PMA V$_3$* electrode. Therefore the results from the constant current cycling confirm the results obtained from the cyclic voltammetries on these electrodes (figures 6.2.1.1 and 6.2.1.3) and shows that the electrode with the highest solid ink loading exhibited the best results.

In figure 6.10, the average potential during the constant current measurements versus the applied current density is presented.

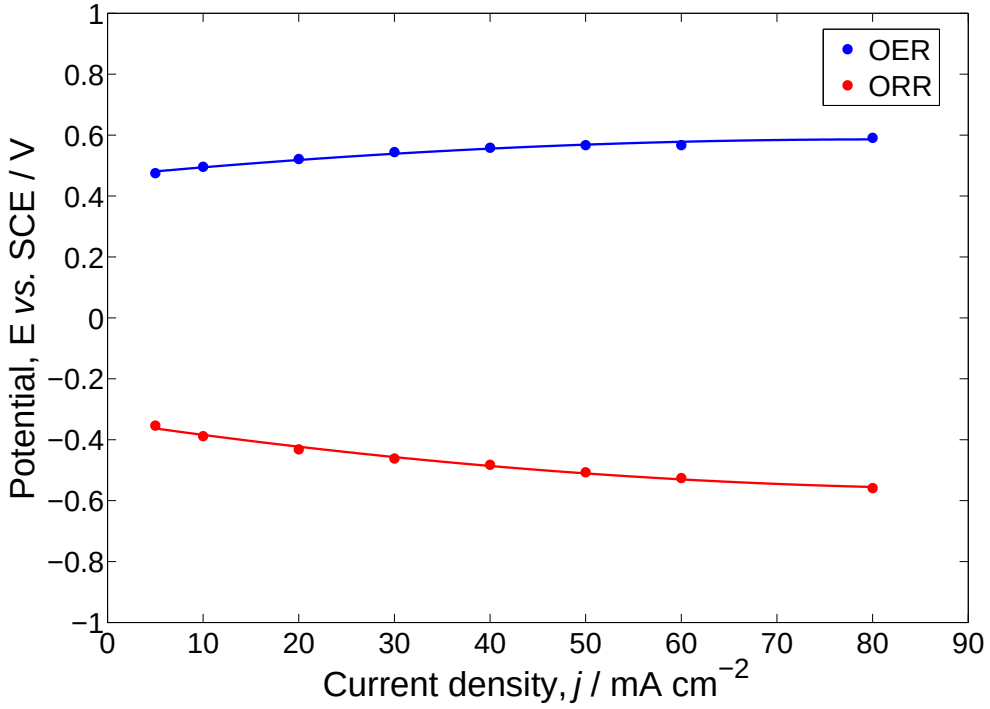

Figure 6.10: *Representation of the average potential values exhibited during the constant current measurements on the Ni PMA V electrode. The measurements took place in 4.0M KOH and O_2 flow (300 $cm^3\,min^{-1}$). The applied current density values varied from 5 mA cm^{-2} to 50 mA cm^{-2}. The temperature was 20^{o}C and the working electrode area was 1.33 cm^2.*

Since the majority of the experiments which were presented in this chapter have shown that the *Ni PMA V* electrode has the best electrochemical performance, the last experiment was performed in order to monitor the electrode's behaviour during the OER and the ORR under different applied current density values. Each cycle lasted for 20 minutes (10 minutes of charging and 10 minutes of discharging). The applied current density values are different for each cycle and they varied from

5 to 80 mA cm^{-2}.

It has to be mentioned that the current density values which were applied during these measurements were low when compared to the values that are used in fuel cells or water electrolysers. However, the applied current density did not exceed 80 mA cm^{-2} because when the applied current density was higher than that, the oxygen which was evolving during OER was blocking the working electrode's surface area and hence it was not possible to receive consistent results.

It can be seen that the potential difference was increasing in parallel to the current density. The potential difference between OER and ORR varied from 0.84 V at 5 mA cm^{-2} to 1.14 V at 80 mA cm^{-2}.

6.3 Conclusions and Further work

Further investigation based on the structural characteristics of the HPA gas diffusion electrodes has been made. A variety of catalyst inks with nickel and phosphomolybdic acid as well as with nickel and phosphotungstic acid were manufactured where the nickel content was kept constant while the HPA content was varying.

The HPA GDEs were all characterised by cyclic voltammetry in an alkaline solution and they all showed stable results. The characterisation of the electrodes showed that as the HPA content was being increased, the performance of the HPA electrodes was being improved. However, it was observed that after a threshold point the addition of more HPA in the catalyst ink contributed towards the decrease in the electrode's performance. In the comparison between the best performing Ni PMA and Ni PWA electrode it was shown that the Ni PMA electrode gave the best results.

Additional investigation was made in order to distinguish whether the substitution of nickel micro-powder with nickel carbonate in the catalyst Ni PMA inks enhances the performance of the electrodes. Nickel carbonate with HPA form Ni-HPA salts ($Ni_3(PMo_{12}O_{40})_2$). Electrodes with the Ni-HPA salt were manufactured and tested with cyclic voltammetry. The results showed that the electrodes were stable under the alkaline environment during the measurements and that the Ni-HPA salts probably act as the active species in the electrode. However, this investigation showed that the nickel micro-powder is more suitable nickel source for the Ni PMA catalyst inks when compared to nickel carbonate.

The effect of the ink solid loading of the electrode in the Ni PMA electrode's performance was examined. Ni PMA electrodes were manufactured by using the same catalyst ink but varying their ink solid loading. The electrodes were tested with cyclic voltammetry and constant current cycling between OER and ORR. The results from their characterisation showed that the variation on the ink solid loading of the electrode does affect the performance of the electrode.

The next step on the optimisation of the HPA gas diffusion electrodes after the research on their catalyst layer is the investigation on alternative materials to carbon Toray paper substrates to be used as the electrode's substrate.

Chapter 7

Alternative materials as electrode substrates

7.1 Introduction

Chapter 6 (page 38) was based on understanding the catalyst layer of the HPA gas diffusion electrodes. The next step for their further development is focused on the electrode substrate. The literature review (2.2.2) highlighted that alternative materials to carbon are needed to be used as electrode substrates for bifunctional air electrodes. Additionally, constant current measurements on the HPA electrodes which were presented in chapter 5, showed that the HPA gas diffusion electrodes are failing after around 10 hours of cycling. This could possibly be due to their carbon Toray paper substrate since carbon substrates degrade after long-term application due to the carbon oxidation during water electrolysis [13]. So, alternative materials to carbon for their application as electrode substrates are investigated in this section.

The work presented in this chapter investigates:

- bulk Magnéli phase materials;
- Magnéli phase coated electrodes;
- further non-carbon, non-metallic coated electrodes.

In chapter 2 it was mentioned that Magnéli phase materials exhibit high electrical conductivity and are electrochemically stable [172]. Furthermore, Magnéli phase

materials have been widely used in fuel cells and batteries as catalyst supports or additives to active materials [168, 171, 207]. Due to these reasons, bulk Magnéli phase materials were electrochemically investigated. The results from their electrochemical characterisation are presented in this chapter.

Except of Magnéli phase materials, a great variety of additional materials have been used as electrode substrates in bifunctional electrodes such as oxidation resistant alloys (aluminium alloys), ceramic materials, carbon-based materials and metallic materials, (i.e. stainless steel) [208, 209, 168, 13, 142, 210, 211, 212, 213, 214]. Despite metals have high electrical conductivity, high mechanical strength, low cost and are easier to manufacture, they fail due to corrosion under the acidic or alkaline environment of the electrolyte and the potential values under which the electrochemical devices operate [215, 13]. In order to protect the substrates from corrosion and also improve their porosity and their electrical conductivity, coatings with conductive and corrosion resistant materials are usually applied on the metallic substrates [210, 209].

Electrodes with different coatings on stainless steel, aluminium and carbon polymer substrates have been electrochemically characterised in order to monitor their performance as potential electrode substrates. The requirements for a potential substrate is to have (i) limited electrochemical activity and (ii) high electrochemical stability within the potential values and under the electrolyte environment where the electrode operates.

Experiments were carried out in order to monitor the substrates' performance between OER and ORR so their potential window of operation can be monitored. According to the results in chapters 5 and 6, the potential window of operation for the Ni HPA electrodes is approximately between -0.5 V *vs.* SCE and +0.6 V *vs.* SCE. The results from the characterisation of the coated substrates are presented and discussed in this chapter.

7.2 Results and discussion

7.2.1 Studies on Magnéli phase materials

This section aims at demonstrating that as well as being electrochemically stable, the Magnéli phase materials can support electron transfer redox reactions in order to test their performance as an electrode substrate. Two different forms of

Magnéli phase materials have been used; dense fibres and porous tablets. Both Magnéli dense fibres and Magnéli porous tablets have been converted into suitable electrodes and the procedure has been described in detail in chapter 3 (pages 50 and 52).

7.2.1.1 Microelectrodes with Magnéli dense fibres

In this section, microelectrodes that incorporate Magnéli dense fibres have been tested by cyclic voltammetry.

In figure 7.1, a voltammogram of the Magnéli microelectrode in 10 μM $K_3Fe(CN)_6$ in 1.0 M KCl is shown. The scan rate of the voltammogram was 100 mV sec^{-1}. The scanning started from 1.0 V *vs.* SCE towards negative potentials, it continued until -0.8 V *vs.* SCE and then back to 1.0 V *vs.* SCE.

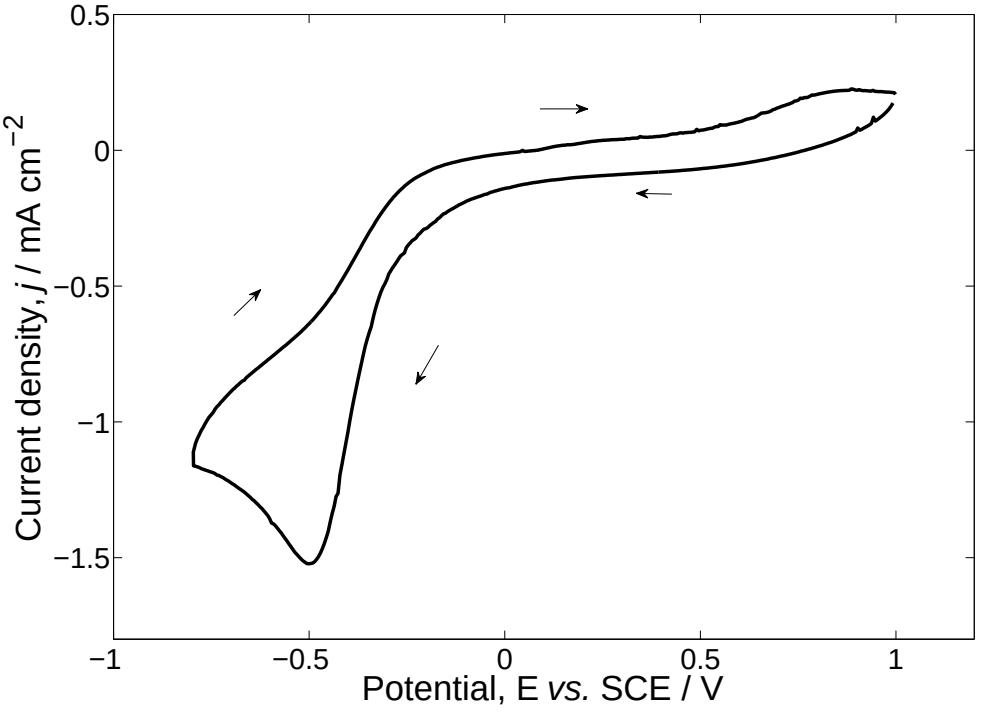

Figure 7.1: *Cyclic voltammograms of Magnéli microelectrodes in 10 μM $K_3Fe(CN)_6$ in 1.0 M KCl. The fourth cycle of the voltammogram is presented. The scan rate of the voltammogram was 100 mV sec^{-1} and the temperature was 20°C. The working electrode area was 0.05 mm^2.*

The electrolyte was potassium ferricyanide ($K_3Fe(CN)_6$) in potassium chloride (KCl) because the ferrocyanide/ferricyanide ($Fe(CN)_6^{3-}$ /$Fe(CN)_6^{4-}$) couple is a

standard redox couple that has been widely used in electrochemistry in order to monitor electron transfer redox reactions.

From figure 7.1, it can be seen that the voltammogram gives consistent results to the ones expected from the literature [216, 171]. One quasi-reversible reduction peak at circa -0.5 V *vs.* SCE and one limited oxidation peak at approximately 0.8 V *vs.* SCE are observed. It can be seen that the voltage difference between the oxidation and the reduction peak is high (1.3 V) which means that the kinetics of the redox reaction of the ferro-ferricyanide couple are not very fast on the Magnéli microelectrode. Hence, it can be seen that the Magnéli phase materials can support electron redox reactions but their reaction kinetics need to be enhanced.

In figure 7.2, cyclic voltammetries of a Magnéli microelectrode and a glassy carbon electrode in 5.0 μM $K_3Fe(CN)_6$ in 0.1 M KNO_3 are shown. The electrolyte was de-oxygenated by nitrogen for 20 minutes and the scan rate was 50 mV sec^{-1}.

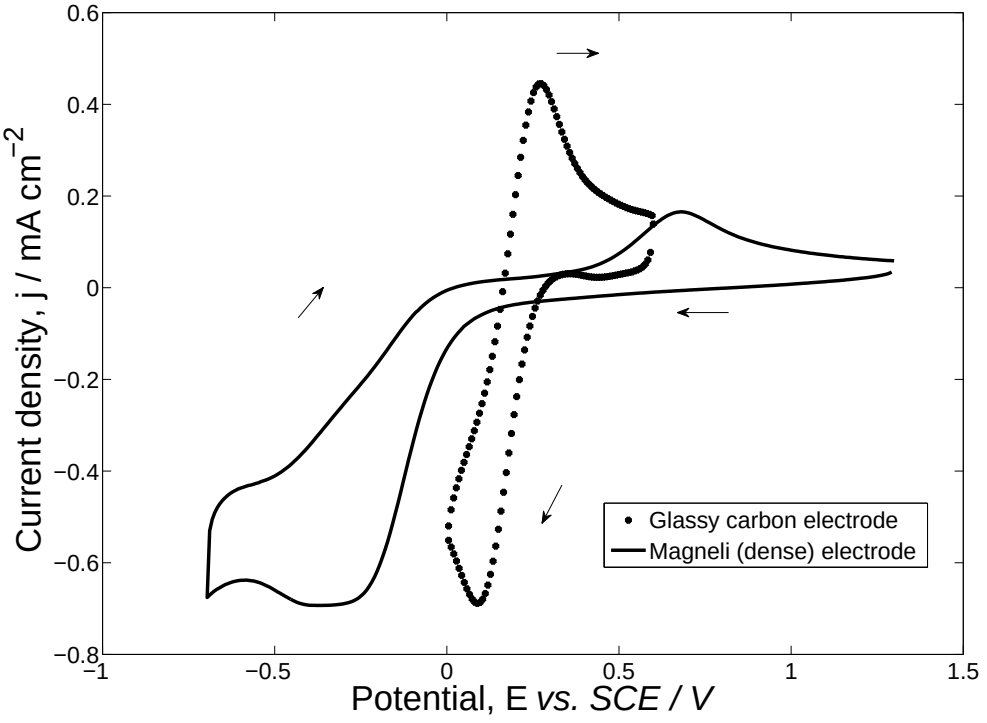

Figure 7.2: *Cyclic voltammograms of Magnéli fibre microelectrode (black line) and glassy carbon electrode (dotted line) in 5.0 μM $K_3Fe(CN)_6$ in 0.1 M KNO_3. The third cycle of each voltammogram is presented. The scan rate of the voltammograms was 50 mV sec^{-1} and the temperature was 20°C.*

The scanning of the measurement on the glassy carbon electrode started at 0.6 V *vs.* SCE towards negative potentials. At 0 V *vs.* SCE the sweep direction was reversed and the potential returned to 0.6 V *vs.* SCE.

For the measurement on the Magnéli microelectrode, the potential was scanned from 1.3 V *vs.* SCE towards negative potentials, it continued until -0.7 V *vs.* SCE and then it was scanned back to 1.3 V *vs.* SCE. The limits of each measurement had to be adjusted so both the oxidation and the reduction peak of each voltammogram are included.

In both voltammograms an oxidation and a reduction peak are observed. The oxidation peak at the CV of the glassy carbon electrode is at 0.27 V *vs.* SCE and the reduction peak is at 0.09 V *vs.* SCE. In the voltammogram of the Magnéli microelectrode, the oxidation peak is observed at approximately 0.68 V *vs.* while the reduction peak is shown at -0.33 V *vs.* SCE. Additionally, the current density values exhibited at the reduction peaks in both CVs are approximately the same (-0.7 mA cm^{-2}) but the current density values of the oxidation peaks exhibited by the two different electrodes are not equal. In the voltammogram of the glassy carbon electrode, a current density of 0.44 mA cm^{-2} is observed at the oxidation peak whereas in the voltammogram of the Magnéli microelectrode the current density at its oxidation peak is approximately 0.16 mA cm^{-2}. This is probably observed because the redox species diffuse away from the Magnéli surface due to the longer cycling when compared to the cycling of the glassy carbon electrode and also due to IR drop.

The potential difference between the oxidation and the reduction peak which was observed at the voltammogram of the glassy carbon electrode is much lower (0.18 V) when compared to the peak potential difference exhibited by the Magnéli microelectrode (1.01 V). This large separation peak at the voltammogram of the Magnéli microelectrode demonstrates that the electrode exhibits slow kinetics and so a larger overpotential for the redox electron transfer. The different reaction kinetics between the two electrodes is due to the different electron conduction mechanisms that these two electrodes have, since the carbon electrode has a metallic conductivity while the Magnéli materials show conductivity on their surface. Hence, when the surface of the Magnéli electrode is getting oxidised the rate of oxidation of ferrocyanide is reduced and so the overpotential of the redox reactions is increased [216].

Since the Magnéli phase materials can support redox transfer reactions, PWA dissolved in 1.0 M H_2SO_4 was used during the next measurement in order to monitor the performance of the materials for the HPA redox reactions. Thus, in figure 7.3, the cyclic voltammograms of a Magnéli microelectrode in 5×10^{-2} M of PWA in 1.0 M H_2SO_4 and a Magnéli microelectrode in 1.0 M H_2SO_4 are shown.

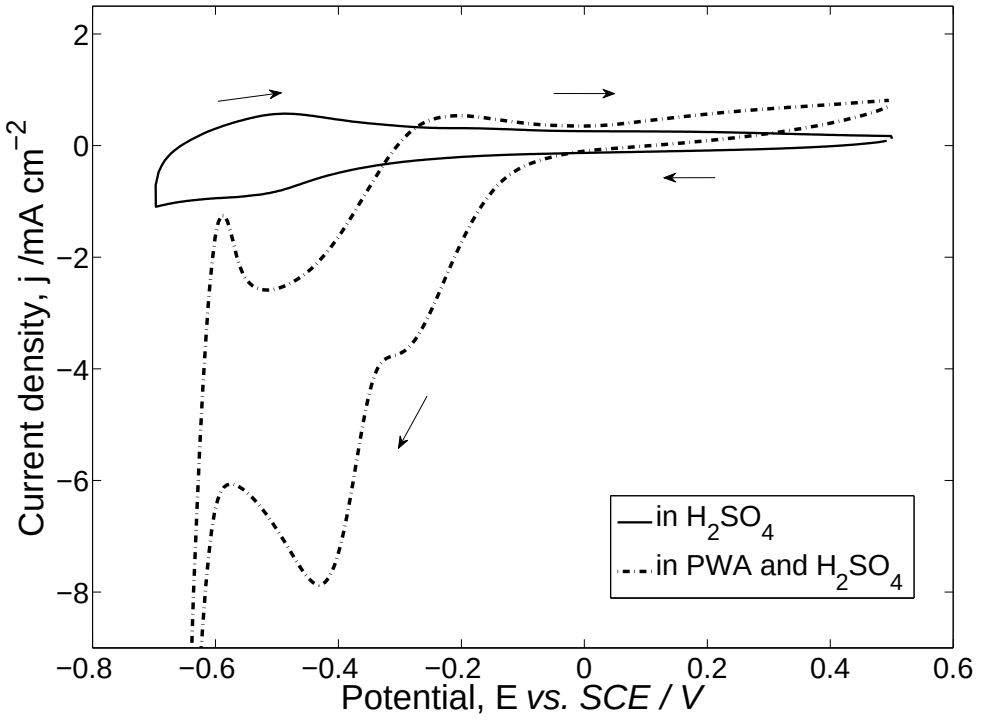

Figure 7.3: *Cyclic voltammograms of Magnéli microelectrodes in* 5×10^{-2} *M of PWA in 1.0 M* H_2SO_4 *(dotted line), in 1.0 M* H_2SO_4 *(black line). The electrolyte was saturated with nitrogen gas. The second cycle of the voltammogram is presented. The scan rate of the voltammogram was 100 mV sec*$^{-1}$ *and the temperature was 20°C. The working electrode area was 0.05 mm*^{2}*.*

The electrolyte has been de-oxygenated with nitrogen gas for 20 minutes before each measurement. The scan rate of the voltammograms was 100 mV sec^{-1}. The scanning of the measurement on the Magnéli microelectrode in 5×10^{-2} M PWA in 1.0 M H_2SO_4 started from 0.5 V *vs.* SCE towards negative potentials, it continued until -0.65 V *vs.* SCE and then back to 0.5 V *vs.* SCE. For the measurement on the Magnéli microelectrode in 1.0 M H_2SO_4, the potential was scanned from 0.5 V *vs.* SCE towards negative potentials. At -0.7 V *vs.* SCE the sweep direction was reversed and the potential returned to 0.5 V *vs.* SCE.

The results from the cyclic voltammetry of the Magnéli microelectrode in plain H_2SO_4 are consistent with the results that are found in literature [171]. An ill-defined reduction peak is shown at circa -0.52 V *vs.* SCE and an ill-defined oxidation peak is shown at -0.49 V *vs.* SCE. According to literature, the oxidation and reduction peaks are due to the changes in the oxidation state of the titanium at the surface of the electrode [216]. Hydrogen evolution occurs after -0.7 V *vs.* SCE while OER is not observed within the potential limits of the voltammogram.

A few reduction and oxidation peaks are observed in the voltammogram of the Magnéli microelectrode in 5 mM of PWA in 1.0 M H_2SO_4 in figure 7.3. The first reduction peak is a limited peak which is observed at circa -0.28 V *vs.* SCE and the second reduction peak is a well-defined, quasi-reversible, reduction peak which is observed at -0.43 V *vs.* SCE. Accordingly to the two reduction peaks, two oxidation peaks are also shown in the voltammogram of the Magnéli microelectrode in 5×10^{-2} M of PWA in 1.0 M H_2SO_4. The first oxidation peak is a clear oxidation peak at -0.59 V *vs.* SCE and the second oxidation peak is a limited oxidation peak at approximately -0.23 V *vs.* SCE. HER starts after -0.6 V *vs.* SCE towards more negative potentials and oxygen evolution does not occur within the scanning potential limits of the measurement.

From both figures 7.1 and 7.3, it can be seen that the Magnéli phase materials can support the HPA redox reactions which makes them a potential choice for an electrode substrate in a HPA redox flow system.

Additionally, according to the literature the Magnéli phase materials are suitable candidates as a substrate for metal layers since when metals are electroplated on Magnélis they demonstrate high quality substrates [216, 217]. So, in order to overcome the large overpotential that Magnéli phase materials demonstrate for electron redox reactions, a way to combine the heteropolyacids and the Magnéli phase materials would be to immobilise the HPAs on a Magnéli phase substrate.

7.2.1.2 Electrodes with Magnéli porous tablets

The Magnéli fibres that have been used in both figures 7.1 and 7.3 are dense fibres with limited porosity. According to the literature, the porosity of the Magnéli materials influences their electrochemical behaviour and it has been shown that between a sample of Magnéli material with many large pores and a sample which has a small number of small pores, the most enhanced electrochemical behaviour is observed by the sample with the large pores [171]. Hence, some initial results from the electrochemical characterisation on Magnéli phase materials with higher porosity are presented in this section.

The Magnéli phase materials in this section are Magnéli phase porous tablets. In order to increase the porosity of the samples, the percentage of the organic binder which was incorporated during their manufacturing procedure was increased. Details about the different electrodes that have been tested and the percentage of the organic binder which has been added to each of them, are shown in table 7.1.

Nomenclature	wt% binder
Magnéli-7.5	7.5
Magnéli-10	10
Magnéli-12.5	12.5
Magnéli-20	20
Magnéli-50	50

Table 7.1: *Table of nomenclature for the porous Magnéli samples*

In figure 7.4, voltammograms of the Magnéli porous electrodes are presented. The porosity of the electrodes varied since the binder content that was added during the manufacture of the tablets varied (7.5, 10, 12, 20 and 50 w.t. % binder). The electrolyte was 5.0 mM $K_3F(CN)_6$ in 0.1 M KNO_3 and it was de-oxygenated with nitrogen for 20 minutes before each measurement.

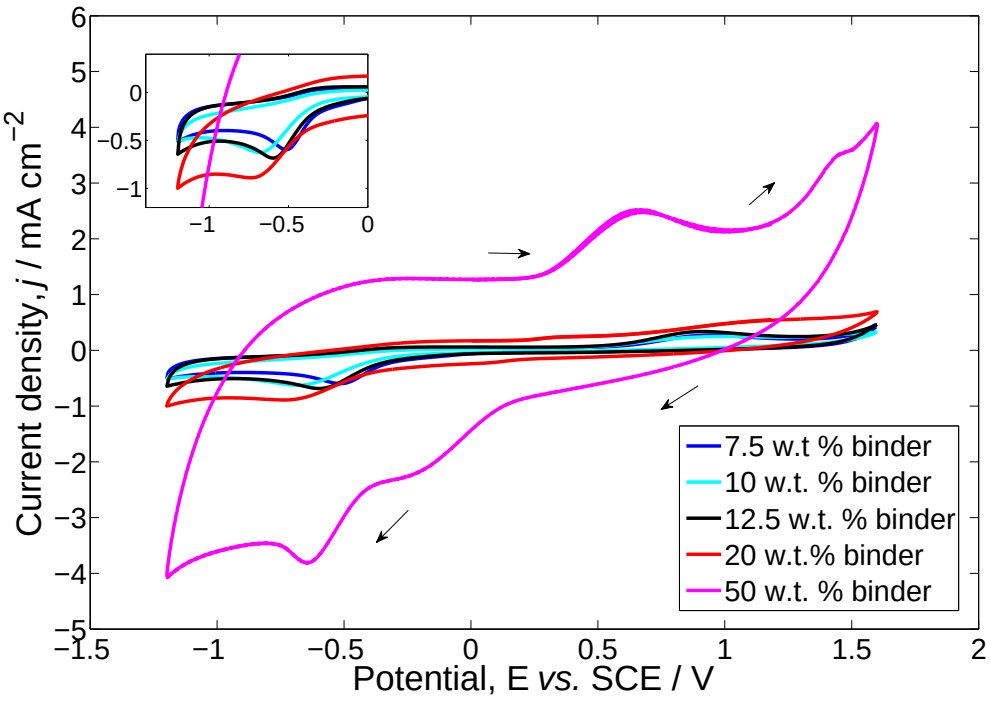

Figure 7.4: *Cyclic voltammograms of Magnéli electrodes with different binder contents;7.5 w.t.% binder (blue line), 10 w.t.% binder (cyan line), 12.5 w.t. % binder (black line), 20 w.t. % binder (red line) and 50 w.t. % binder (pink line) in $K_3F(CN)_6$ in 0.1 M KNO_3. The electrolyte was saturated with nitrogen gas. The third cycle of each voltammogram is presented. The scan rate of the voltammogram was 50 mV sec^{-1} and the temperature was 20°C. The working electrode area was 0.85 cm^2.*

The scanning during the measurements for the *Magnéli-7.5*, *Magnéli-10* and *Magnéli-12.5* electrodes started from 0.5 V *vs.* SCE towards negative potentials, it continued until -0.65 V *vs.* SCE and then back to 0.5 V *vs.* SCE . The scanning during

the measurements for the *Magnéli-20*, and *Magnéli-50* electrodes started from 0 V *vs.* SCE towards positive potentials until 1.6 V *vs.* SCE, it continued to negative potentials until -1.2 V *vs.* SCE and then back to 0 V *vs.* SCE.

In figure 7.4, one clear oxidation and one clear reduction peak are observed at the voltammograms of the *Magnéli-7.5*, *Magnéli-10* and *Magnéli-12.5* electrodes. The reduction peak of the voltammogram of the *Magnéli-7.5* electrode is at -0.5 V *vs.* SCE and the oxidation peak is at 0.94 V *vs.* SCE. In the voltammogram of the *Magnéli-10* electrode, the reduction peak is at -0.68 V *vs.* SCE and the oxidation peak is at 1.05 V *vs.* SCE, while in the voltammogram of the *Magnéli-12.5* electrode the reduction peak is observed at -0.59 V *vs.* SCE and the oxidation peak is observed at 0.90 V *vs.* SCE.

The *Magnéli-20* electrode showed a reduction peak at -0.71 V *vs.* SCE but no oxidation peak. The *Magnéli-50* electrode showed two reduction and two oxidation peaks, from which one of the oxidation and one of the reduction peaks are clear peaks and the other two were limited peaks. The clear oxidation peak was at 0.65 V *vs.* SCE, the clear reduction peak was at -0.65 V *vs.* SCE, the limited oxidation peak was at 1.44 V *vs.* SCE and the limited reduction peak was at -0.18 V *vs.* SCE. Hence, different electrochemical behaviour is observed at the voltammograms of the *Magnéli-50* electrode when compared to the rest of the electrodes also due to the high IR drop which is observed at its.

In order to compare the performance of the porous Magnéli electrodes the peak height of their main reduction peak at circa -0.6 V *vs.* is monitored. The current density values of the peaks *vs.* their w.t% binder content are plotted in figure 7.5.

In figure 7.5, it is shown that as the organic binder content increases, the current density values of the samples increase as well. The *Magnéli-7.5* electrode had the lowest reduction peak height (-0.59 mA cm^{-2}) while the *Magnéli-10* and the *Magnéli-20* electrodes exhibited slightly higher current density values (-0.61 and -0.68 mA cm^{-2} respectively).

The current density value of the reduction peak in the voltammogram of the *Magnéli-20* electrode was -0.89 mA cm^{-2} which was higher than the current density values that were exhibited by the three previous electrodes (*Magnéli-7.5,Magnéli-10,Magnéli-12.5*). The highest peak height was observed in the voltammogram of the *Magnéli-50* electrode and it was equal to -3.82 mA cm^{-2}.

As a result, it was shown that when the porosity of the Magnéli phase materials is increased, the current density values that they display during their CVs are

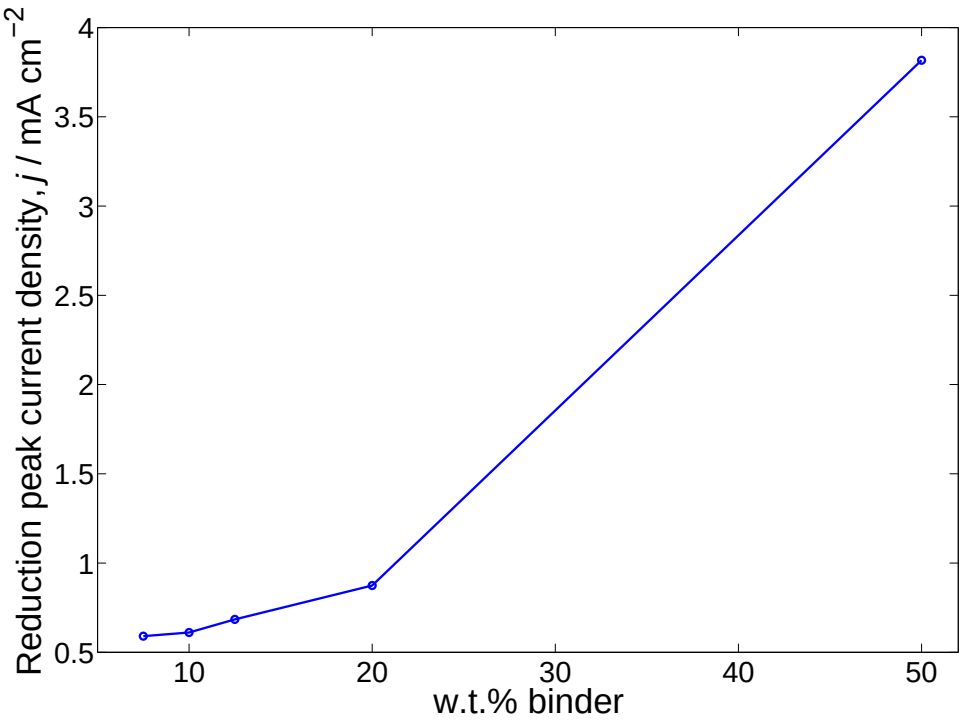

Figure 7.5: *Reduction peak current density values vs. the w.t.% of binder of each Magnéli porous electrode. Data are obtained from the cyclic voltammetries of Magnéli microelectrodes with different binder content (fig. 7.4).*

higher, as well.

7.2.2 Electrodes with APS Magnéli coating

It was shown that together with the increasing porosity of the Magnéli porous tablets, the IR drop was increasing accordingly. Hence, the aim of the further investigation on Magnéli phase materials is to achieve maintaining their high porosity while their IR drop is decreased. A possible solution to this problem is to obtain a fine, uniform, thin and porous Magnéli phase coating that could be applied on any selected material. Hence, in this section, Magnéli phase coated electrodes by a novel coating technique are electrochemically characterised.

The coating technique was a thermal spray technique called Atmospheric Plasma Spray (APS) coating technique. This technique has been previously used in order to develop passive surfaces which prevent wear and corrosion and it was shown that it is also possible to create functional active surfaces by using the same coating technique [218].

The APS was containing a powder based on rutile TiO_2 and Magnéli phases (Ti_8O_{15} and Ti_9O_{17}). It has to be noted that the electrically conductive and active factor of the APS coating is the Magnéli phase part, so it is justified to refer to the electrodes as *APS Magnéli phase coated* electrodes.

Stainless steel, aluminium and carbon polymer have been used as substrates in the APS coated electrodes. Some important characteristics of these materials are summarised in table 7.2 [209, 208, 219, 220, 221]:

Substrates	**Density (g m^{-3})**	**Electrical conductivity (S m^{-1})**
Stainless steel	7.93	1.33×10^6
Aluminium	2.7	37.7×10^6
Carbon composite	2.1	5×10^3

Table 7.2: *Table of property values of the substrates used for the APS Magnéli phase coated electrodes at 20°C*

Each material has been chosen for a different reason. Stainless steel has high chemical stability and high electrical conductivity (1.33×10^6 S m^{-1}) but low corrosion resistivity, while aluminium is low cost and low weight but has lower mechanical strength and corrosion resistivity when compared to stainless steel [209, 208]. Additionally, carbon-polymer materials have lower cost, lower weight, higher corrosion resistivity but lower electrical conductivity and mechanical strength when compared to metallic materials [209, 222]

7.2.2.1 APS Magnéli phase coated electrodes with stainless steel substrates

In figure 7.6, the cyclic voltammograms of an electrode with APS Magnéli phase coating on a stainless steel substrate and an uncoated stainless steel substrate in 1.0 M H_2SO_4 are presented. The electrolyte was de-oxygenated with nitrogen gas for 15 minutes before each measurement. The scan rate of the voltammograms was 50 mV sec^{-1}. The scanning during the measurements was between 2.3 V *vs.* SCE and -1.3 V *vs.* SCE.

It can be seen that for the uncoated electrode, a non-reversible oxidation wave occurs probably due to the oxidation of Fe^{II} to Fe^{III} on the stainless steel surface. At potentials more positive than 1.0 V *vs*. SCE oxygen evolution takes place, while at potentials more negative than -0.75 V *vs*. SCE, hydrogen evolution occurs. The voltammogram of the coated electrode shows that there is limited electrochemistry

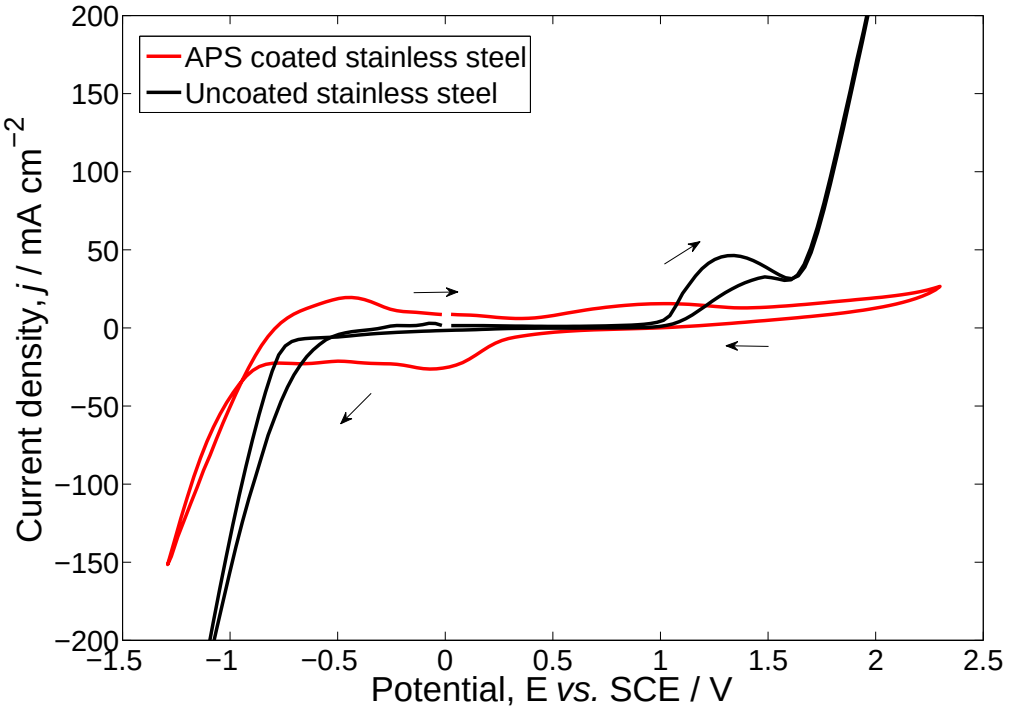

Figure 7.6: *Cyclic voltammograms of stainless steel substrate (black line) and APS Magnéli phase coated stainless steel substrate (red line) in 1.0 M H_2SO_4. The electrolyte was saturated with nitrogen gas. The fourth cycle of each voltammogram is presented. The scan rate of the voltammogram was 50 mV sec^{-1} and the temperature was 20°C. The working electrode area was 1.13 cm^2.*

at positive potentials before the oxygen evolution starts at potentials more positive than 2.4 V *vs.* SCE. The first reduction peak is observed at -0.01 V *vs.* SCE and the second reduction peak is observed at -0.07 V *vs.* SCE. Two oxidation peaks are also seen at -0.46 and at 0.98 V *vs.* SCE. Hydrogen evolution occurs at potentials more negative than -1.0 V *vs.* SCE which is consistent with CVs of Magnéli materials presented in literature [168]. The electrochemistry is reversible and stable which shows that there is no material degradation observed with the successive CVs. Additionally, there is no Fe^{II}/Fe^{III} oxidation peak observed which shows that the APS Magnéli coating protects the stainless steel substrate from oxidation.

Comparing the electrochemical performance of the APS Magnéli coated electrode with the performance of the bulk Magnéli electrodes it can be observed that the APS Magnéli coated electrode exhibits higher current density values in lower over-potentials. For example, in figure 7.6, the APS Magnéli coated electrode exhibits -22.78 mA cm^{-2} at -0.7 V *vs.* SCE, while in figure 7.3 the Magnéli microelectrode gives only -1.08 mA cm^{-2} at the same potential. Hence, it is shown that the APS

Magnéli coating has lower resistance and demonstrates higher electron transfer kinetics on its surface when compared to the bulk Magnéli samples.

In figure 7.7, the voltammograms of the APS Magnéli phase coated and uncoated stainless steel electrode in 4.0 M KOH are presented. The electrolyte was deoxygenated with nitrogen gas for 15 minutes before each measurement. The scan rate of the voltammograms was 50 mV sec^{-1}. The scanning during the measurements was between 1.5 V *vs.* SCE and -1.7 V *vs.* SCE.

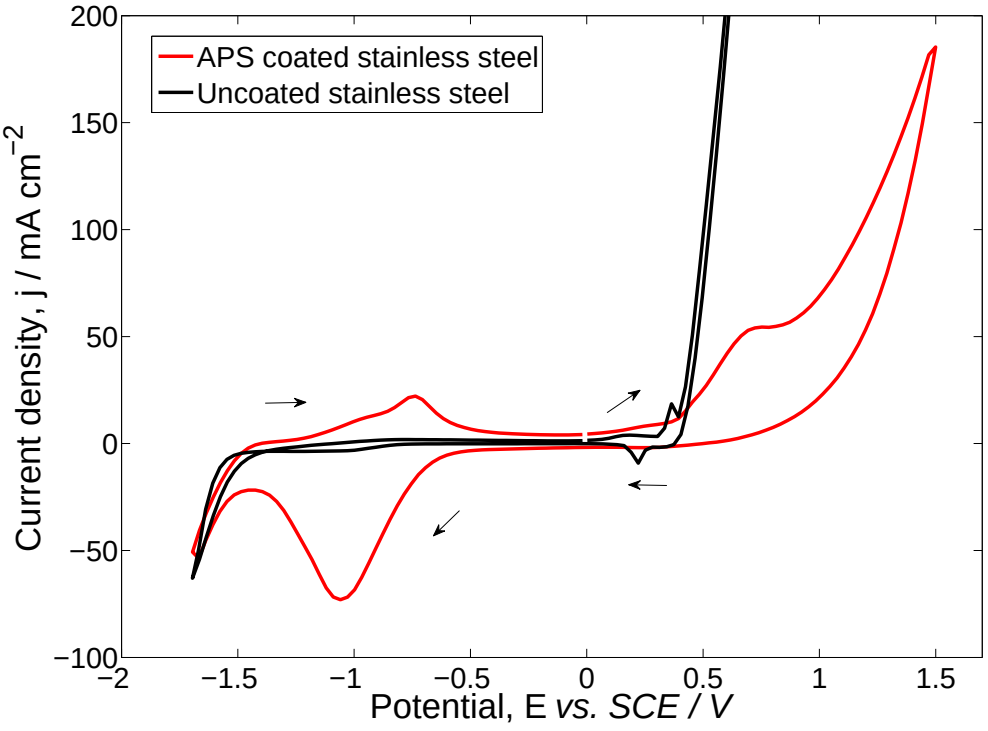

Figure 7.7: *Cyclic voltammograms of stainless steel substrate (black line) and APS Magnéli phase coated stainless street substrate (red line) in 4.0 M KOH. The electrolyte was saturated with nitrogen gas. The fourth cycle of each voltammogram is presented. The scan rate of the voltammogram was 50 mV sec^{-1} and the temperature was 20°C. The working electrode area was 1.13 cm^2.*

The uncoated electrode shows a significant oxidation at potentials more positive than 0.4 V *vs*. SCE, while at potentials more negative than -1.4 V *vs*. SCE hydrogen evolution occurs. Additionally, an oxidation peak is observed at 0.36 V *vs.* SCE and a reduction peak is shown at 0.22 V *vs.* probably due to the Fe^{II}/Fe^{III} redox couple.

The voltammogram of the coated stainless steel electrode shows a well-defined, quasi-reversible reduction peak at -1.06 V *vs*. SCE and hydrogen evolution takes place at potentials more negative than -1.48 V *vs*. SCE. An oxidation peak is

observed at -0.74 V *vs*. SCE and another oxidation peak at 0.7 V *vs.* SCE. Oxygen evolution occurs at potentials more positive than 0.9 V *vs*. SCE. Similarly to the CVs in figure 7.6, the APS coating prevents the oxidation of the stainless steel substrate since no Fe^{II}/Fe^{III} redox peaks are observed.*

* As already explained in the experimental details section, two different APS Magnéli coated electrodes which have a stainless steel substrate with different thickness have initially been tested. The results from the cyclic voltammetry measurements of both electrodes were the same and for that reason only the cyclic voltammograms of the electrode with the thick stainless steel substrate were chosen to be shown (figures 7.6 and 7.7).

7.2.2.2 APS Magnéli phase coated electrodes with aluminium substrates

Cyclic voltammetries took place to characterise the APS Magnéli phase coated aluminium substrates in 1.0 M H_2SO_4 and 4.0 M KOH solutions. An uncoated aluminium substrate has been also tested in order be able to compare the enhancement after the application of the APS Magnéli phase coating.

In figure 7.8, two different voltammograms are shown; a voltammogram of an APS Magnéli phase coated aluminium substrate (figure 7.8a) and a voltammogram of an uncoated aluminium substrate (figure 7.8b), both in 1.0 M H_2SO_4. The electrolyte was de-oxygenated with nitrogen gas for 15 minutes before each measurement. The scan rate of the voltammograms was 50 mV sec^{-1}. The scanning during the measurements was between 2.3 V *vs.* SCE and -1.3 V *vs.* SCE.

In figure 7.8b, the CV of the uncoated aluminium electrode shows no electrochemistry at positive potentials before 1.8 V *vs*. SCE, when oxygen evolution begins. At potentials more negative than -1.3 V *vs*. SCE hydrogen evolution occurs. In figure 7.8a, at the voltammogram of the coated aluminium electrode, oxygen evolution starts at around 1.8 V *vs*. SCE and hydrogen evolution occurs at potentials more negative than -0.8 V *vs*. SCE. Two oxidation peaks are observed at -0.46 V *vs*. SCE and -0.10 V *vs*. SCE and a reduction peak is observed at -0.6 V *vs*. SCE. It has to be noted that higher current density values are observed at the CV of the coated electrode when compared to the uncoated electrode. A current density of 3.87 mA cm^{-2} is achieved at 1.79 V *vs.* SCE for the APS Magnéli phase coated electrode while for the uncoated electrode the current density at 1.79 V *vs.* SCE is 0.59 mA cm^{-2}.

The voltammograms of an APS Magnéli phase coated and an uncoated aluminium electrode in 4.0 M KOH are shown in figure 7.9. The electrolyte was de-oxygenated with nitrogen gas for 15 minutes before each measurement. The scan rate of the voltammograms was 50 mV sec^{-1}. The scanning during the measurements was between 2.0 V *vs.* SCE and -1.8 V *vs.* SCE.

At potentials more positive than approximately -1.75 V *vs*. SCE the uncoated aluminium substrate dissolved anodically (fig. 7.9b). The electrode with the APS coating does not dissolve during the measurement. According to the cyclic voltammogram (fig. 7.9a), oxygen evolution occurs at potentials more positive than 1.0 V *vs*. SCE and hydrogen evolution occurs at potentials more negative than 1.5 V *vs*. SCE. An irreversible reduction peak is observed at approximately -1.7 V *vs*.

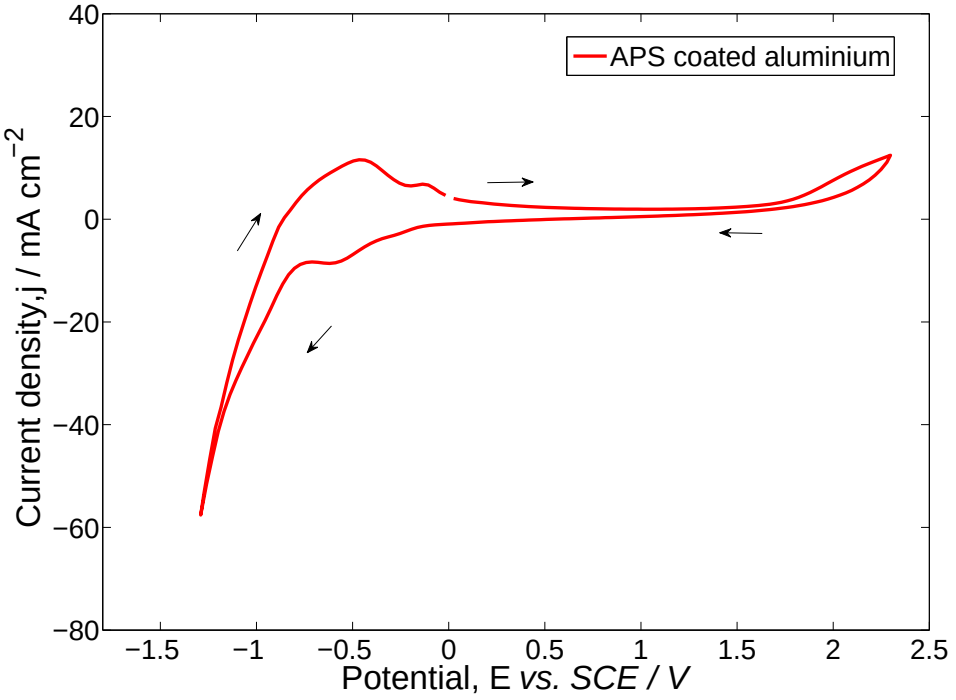

(a)

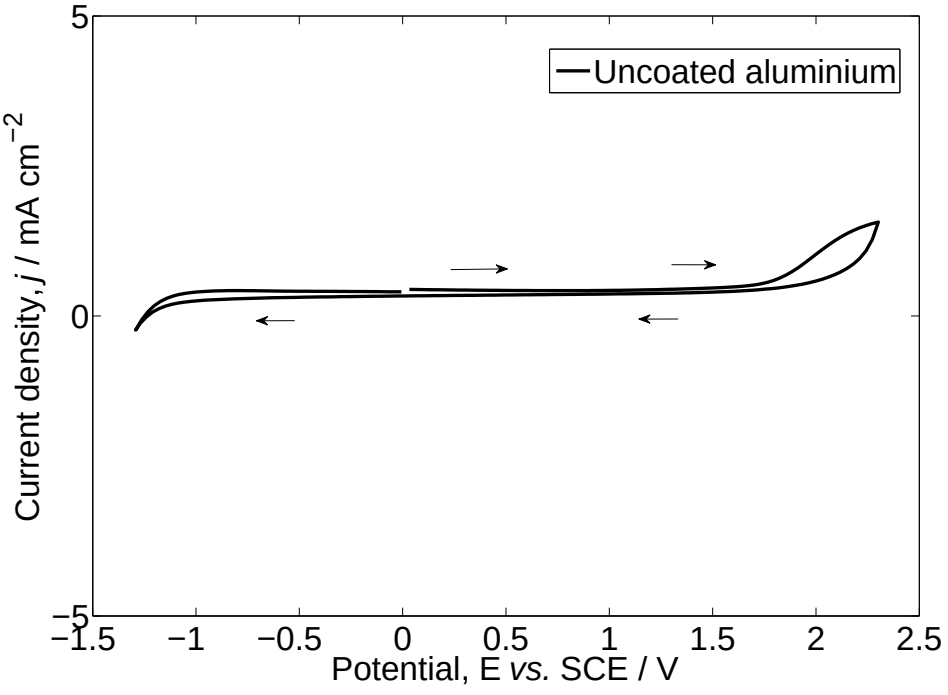

(b)

Figure 7.8: *Cyclic voltammograms of (a) APS Magnéli phase coated aluminium substrate (b) uncoated aluminium substrate in 1.0 M H_2SO_4. The electrolyte was saturated with nitrogen gas. The fourth cycle of each voltammogram is presented. The scan rate of the voltammogram was 50 mV sec^{-1} and the temperature was 20°C. The working electrode area was 1.13 cm^2.*

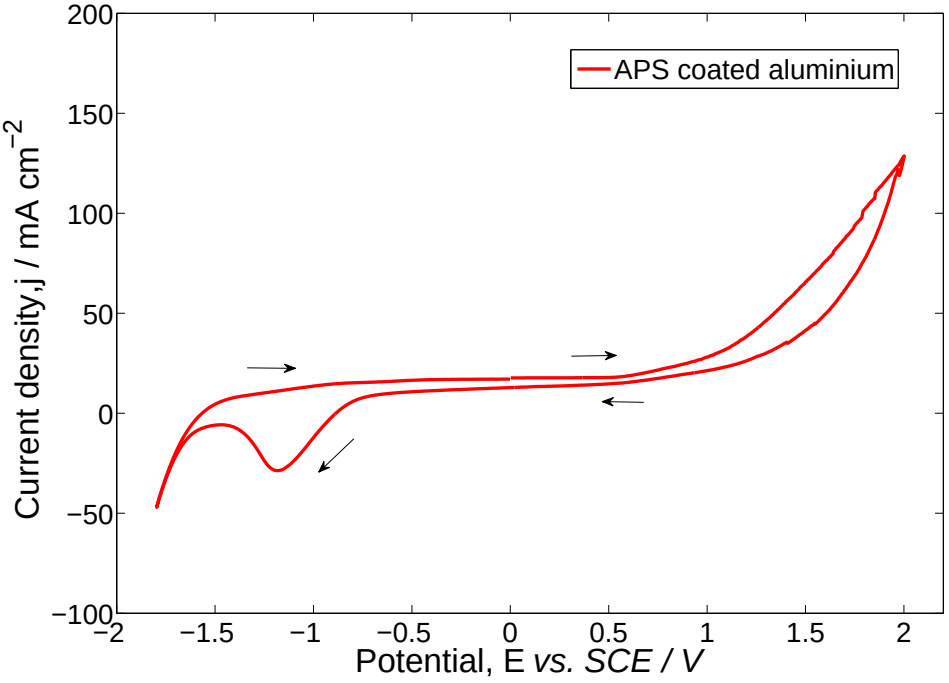

(a)

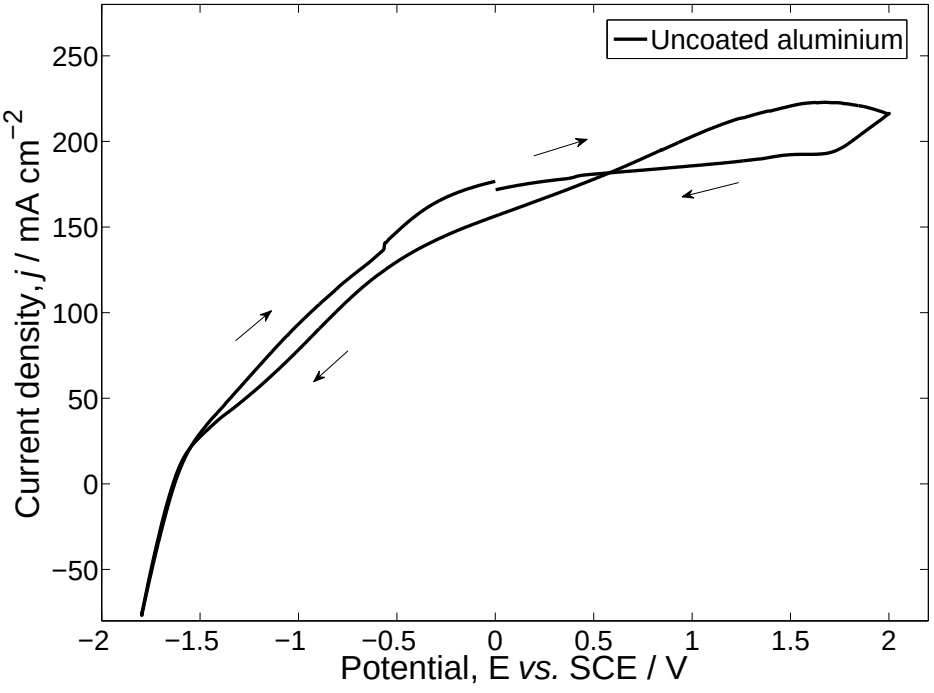

(b)

Figure 7.9: *Cyclic voltammograms of (a) APS Magnéli phase coated and (b) uncoated aluminium substrate in 4.0 M KOH. The electrolyte was saturated with nitrogen gas. The fourth cycle of each voltammogram is presented. The scan rate of the voltammogram was 50 mV sec^{-1} and the temperature was 20^{o}C. The working electrode area was 1.13 cm^{2}.*

SCE.

It is clearly shown that the Magnéli phase coating protects the aluminium substrate from dissolving in the alkaline electrolyte. Hence, a Magnéli phase coated aluminium substrate could be a good candidate as a light weight corrosion resistant electrode since aluminium has a really low density (table 7.2).

7.2.2.3 APS Magnéli phase coated electrodes with carbon polymer substrates

The cyclic voltammetries of the APS Magnéli phase coated and uncoated carbon polymer substrates took place under acidic (1.0 M H_2SO_4), alkaline (4.0 M KOH) and neutral (1.0 M KCl) electrolytic environment.

In figure 7.10, the voltammograms of an APS Magnéli phase coated carbon polymer substrate in 1.0 M H_2SO_4 (figure 7.10a) and 4.0 M KOH (figure 7.10b) are shown. The electrolyte was de-oxygenated with nitrogen gas for 15 minutes before each measurement. The scan rate of the voltammograms was 50 mV sec^{-1}. The scanning during the measurements in H_2SO_4 was between 2.3 V *vs.* SCE and -1.3 V *vs.* SCE, while the scanning during the measurements in KOH was between 1.5 V *vs.* SCE and -1.8 V *vs.* SCE.

In figure 7.10a, oxygen evolution takes place at potentials more positive than 1.5 V *vs*. SCE. Two reduction peaks are observed at circa 1.0 V *vs*. SCE and 0.7 V *vs*. SCE and a third reduction peak is shown at approximately -0.6 V *vs*. SCE. Hydrogen evolution starts at -0.8 V *vs*. SCE towards more negative potentials. Additionally, two oxidation peaks occur at -0.45 V *vs*. SCE and -0.1 V *vs*. SCE.

In figure 7.10b, the CV shows that oxygen evolution occurs at potentials more positive than 0.5 V *vs*. SCE. During the reverse scan, three non-reversible reduction peaks are shown at 0.2 V *vs*. SCE, -0.47 V *vs*. SCE and -1.14 V *vs*. SCE. Hydrogen evolution takes place at potentials more negative than -1.5 V *vs*. SCE.

In figure 7.11, the CV of the APS Magnéli phase coated polymer electrode in 1.0 M KCl is shown. The electrolyte was de-oxygenated with nitrogen gas for 15 minutes before each measurement. The scan rate of the voltammograms was 50 mV sec^{-1}. The scanning during the measurements was between 2.3 V *vs.* SCE and -1.3 V *vs.* SCE.

Oxygen evolution occurs at potentials more positive than 1.16 V *vs*. SCE while two irreversible reduction peaks are observed at 0.47 V *vs*. SCE and at -0.6 V *vs*. SCE, respectively. Hydrogen evolution takes place at potentials more negative than -1.2 V *vs*. SCE.

In all the voltammograms of the APS Magnéli phase coated polymer electrodes, many reduction peaks are observed. The electrolytes in figures 7.10 and 7.11 vary (H_2SO_4, KOH and KCl), so it is unlike to get the observed redox peaks due to a contaminant. A first attempt to explain this trend could be that there is an

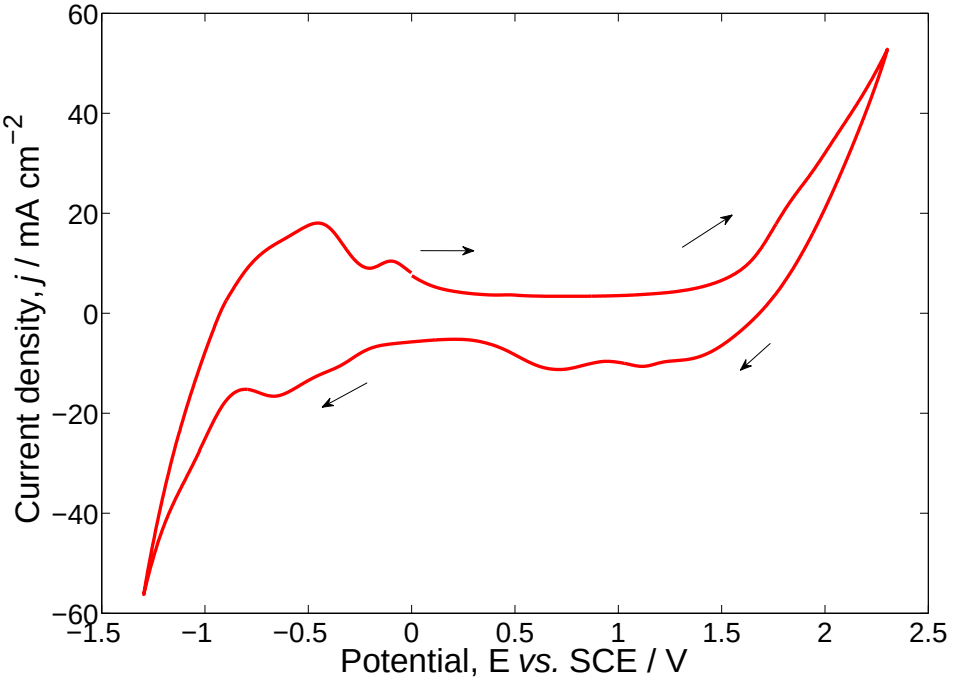

(a)

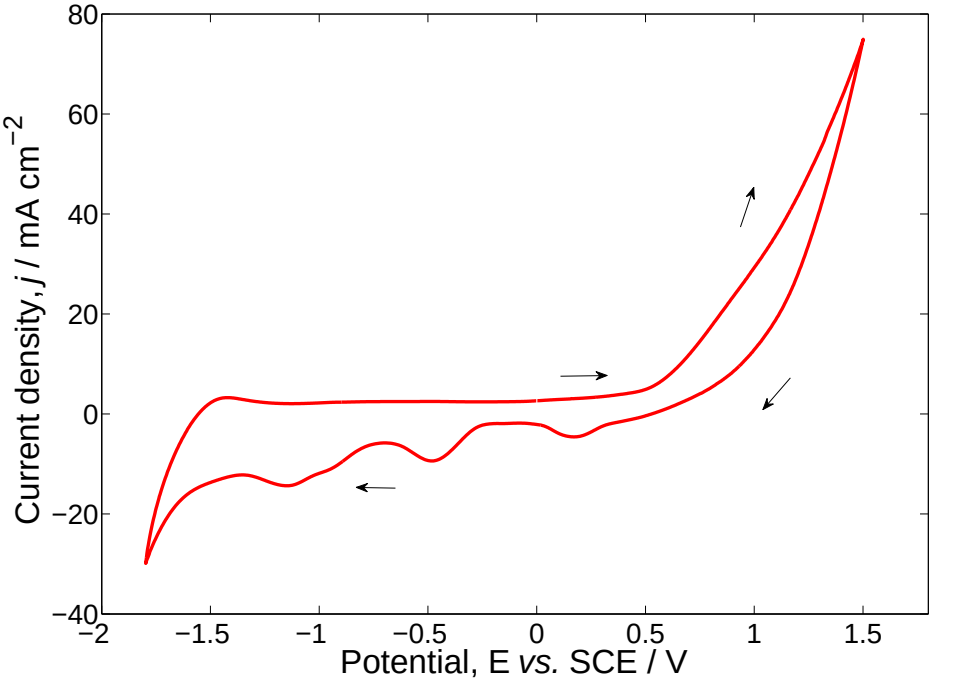

(b)

Figure 7.10: *Cyclic voltammograms in of APS Magnéli phase coated polymer substrate (a) 1.0 M H_2SO_4 and (b) 4.0 M KOH. All the electrolyte solutions were saturated with nitrogen gas. The fourth cycle of each voltammogram is presented. The scan rate of the voltammograms was 50 mV sec^{-1} and the temperature was 20°C. The working electrode area was 1.13 cm^2.*

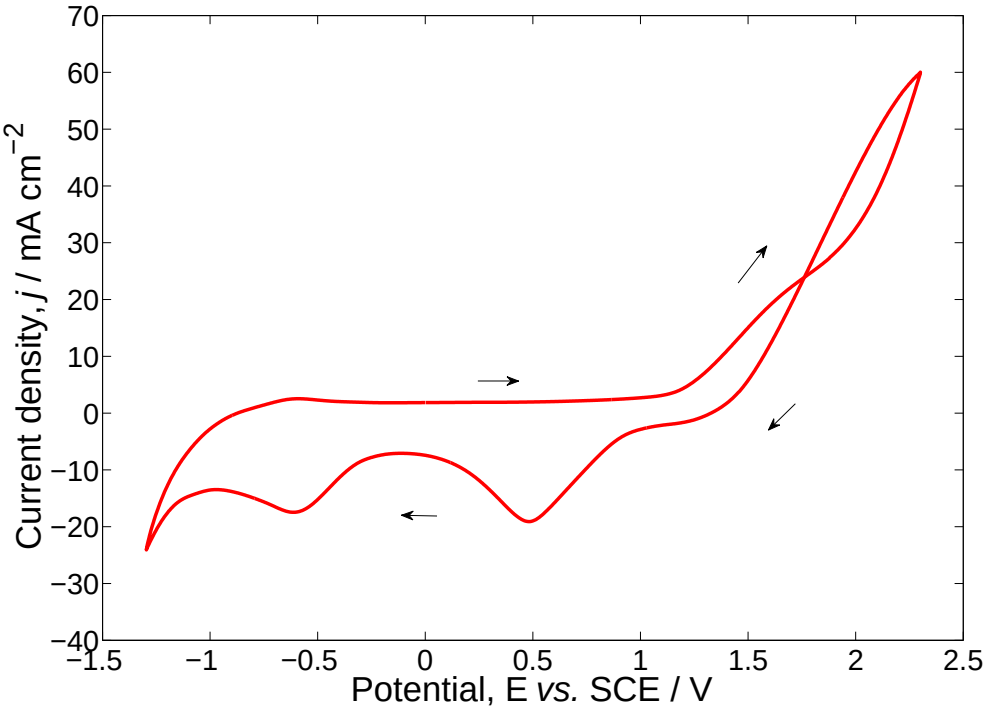

Figure 7.11: *Cyclic voltammogram of APS Magnéli phase coated polymer substrate in 1.0 M KCl. The electrolyte was saturated with nitrogen gas. The fourth cycle of each voltammogram is presented. The scan rate of the voltammogram was 50 mV sec^{-1} and the temperature was 20°C. The working electrode area was 1.13 cm^2.*

interaction between the Magnéli phase coating and the carbon polymer substrate that leads to a functionalised carbon polymer.

According to literature, during the cyclic voltammetries of Magnéli phase materials transitions from lower to higher oxidation states of the TiO_x and transitions back to the lower oxidation state take place. So since there are different stoichiometries of the Magnéli phase materials, it is not simple to detect the origin of each different reduction and oxidation peak in figures 7.10 and 7.11 [223, 171, 170, 216].

7.2.3 Electrodes with PVD coating

The characterisation of APS Magnéli phase coatings on different materials has shown that the coating is electrically conductive and chemically insulating, since it protected the various substrate materials from corrosion and improved their electrical conductivity. As already mentioned, the APS coating technique is a novel technique and hence it is rather complicated and time consuming to obtain a thin and uniform coating at the moment. Additionally, Magnéli phase materials have large overpotential in redox reactions due to their conductivity mechanism. So it is important to investigate more materials to the Magnéli phase materials as potential coatings on electrode substrates.

A more common and simple coating technique, the Physical Vapour Deposition (PVD) technique, was chosen in order to coat a stainless steel substrate with a selection of different materials. By using PVD instead of APS it was easier to manufacture and therefore, test many different coatings. The target after the investigation on the PVD coated electrodes is to select the best performing materials and create APS coatings that will include these specific materials.

The materials that have been used as coatings were: titanium nitride (TiN), titanium nitride with carbon (TiN/C), zirconium nitride (ZrN), chromium nitride (CrN), chromium nitride with carbon (CrN/C) and Graphit_iC^{TM}. The selection of these materials has been based on the literature since all of them, except Graphit_iC^{TM}, have been used as coatings on bipolar plates in PEMFCs [224, 225, 226, 227, 228, 229, 230, 231, 232, 233, 234].

Titanium nitride is a ceramic with high, metal-like electrical conductivity, high corrosion resistance and high chemical inertness, while when titanium nitride combined with carbon (TiN/C) was applied in a bipolar plate it gave 14 times higher output power when compared to the bipolar plate that had only titanium nitride [224, 230, 231, 232, 225, 235]. Zirconium nitride (ZrN) shows high corrosion resistance when used as a bipolar plate at both the anode and the cathode of a PEMFC and satisfies the DOE target [226]. Chromium nitride (CrN) and chromium nitride with carbon (CrN/C) show low interfacial contact resistance (ICR) values and high corrosion resistivity [228, 227, 233, 234].

In table 7.3, all the materials and some representative references from their previous applications are presented.

Graphit_iC^{TM}, is a coating which has been developed and patented by Teer Coat-

Materials	Applications	References
TiN	Coating on metallic bipolar plates in PEMFCs	[224, 230, 231, 232]
TiN/C		[225]
ZrN		[226]
CrN		[227]
CrN/C		[228, 233, 234]
Graphit_iC^{TM}	Wear resistant applications	[229]

Table 7.3: *Table of the materials chosen as PVD coatings*

ings and according to the official description "it is a conducting carbon based coating with a graphitic microcrystalline structure" [236]. It has previously been used as a wear resistant coating in various applications and it was decided to test it as a potential coating in electrodes of electrochemical devices [229].

Initial cyclic voltammetry measurements were taken on the electrodes with the PVD coated stainless steel substrates in 1.0 M H_2SO_4 and 4.0 M KOH. The potential limits from the measurements on each coated substrate for both the CVs in 1.0 M H_2SO_4 and 4.0 M KOH are summarised in table 7.4.

Coatings	Potential limits (V *vs.* SCE)				Stable window (V *vs.* SCE)			
	1.0 M H_2SO_4		4.0 M KOH		1.0 M H_2SO_4		4.0 M KOH	
	From	To	From	To	From	To	From	To
TiN/C	-1.4	2.0	-1.0	1.0	-0.06	0.84	-0.42	0.25
TiN	-0.8	1.2	-1.8	0.7	-0.35	0.08	-1.20	0.40
ZrN	-0.8	1.6	-1.8	0.7	-0.68	1.02	-1.51	0.42
Graphit_iC^{TM}	-1.0	1.9	-1.9	1.0	0.57	0.75	N/A	N/A
CrN	-0.85	1.1	-1.6	0.45	-0.48	0.36	N/A	N/A
CrN/C	-0.8	1.3	-1.6	1.0	-0.02	1.08	N/A	N/A

Table 7.4: *Table of the scanning potential limits and the stable potential window from the voltammograms of the PVD coated electrodes in 1.0 M H_2SO_4 and 4.0 M KOH*

In figure 7.12, the cyclic voltammograms of the different PVD coated electrodes in 1.0 M H_2SO_4 are shown. The electrolyte was saturated with nitrogen gas for 15 minutes before each measurement. The scan rate of the voltammograms was 50 mV sec^{-1}.

In figure 7.12a, the electrode with the TiN/C coating shows the smallest potential window of operation (-0.06 to 0.84 V *vs.* SCE). After 0.84 V *vs.* SCE and towards more positive potentials, there is a broad oxidation wave leading to either OER or oxidation of the TiN/C coating. At potentials lower than approximately -0.06 V *vs.* SCE hydrogen evolution takes place. The electrode with the TiN coating

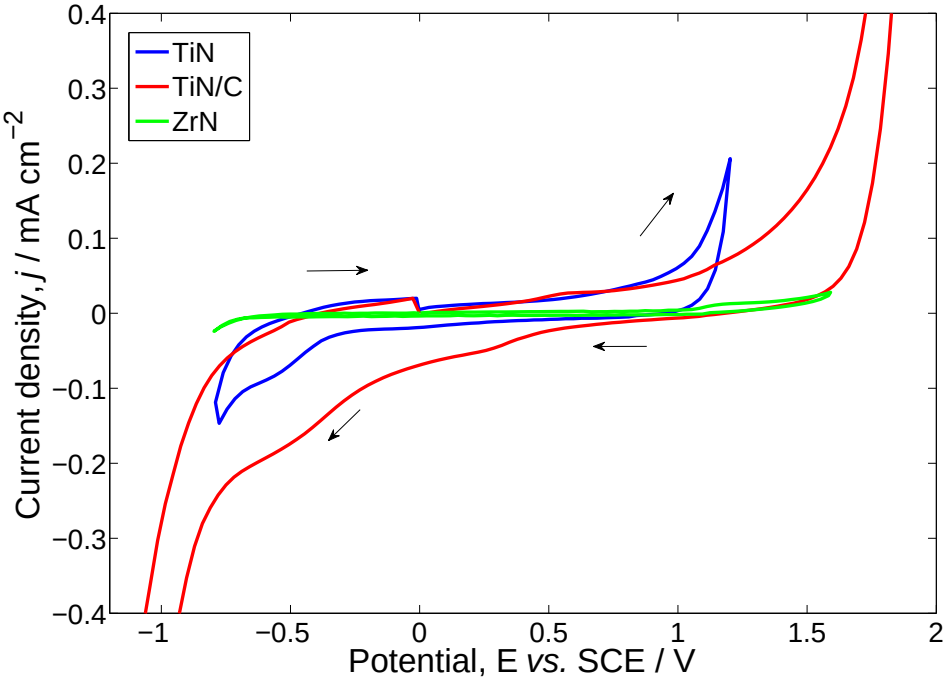

(a)

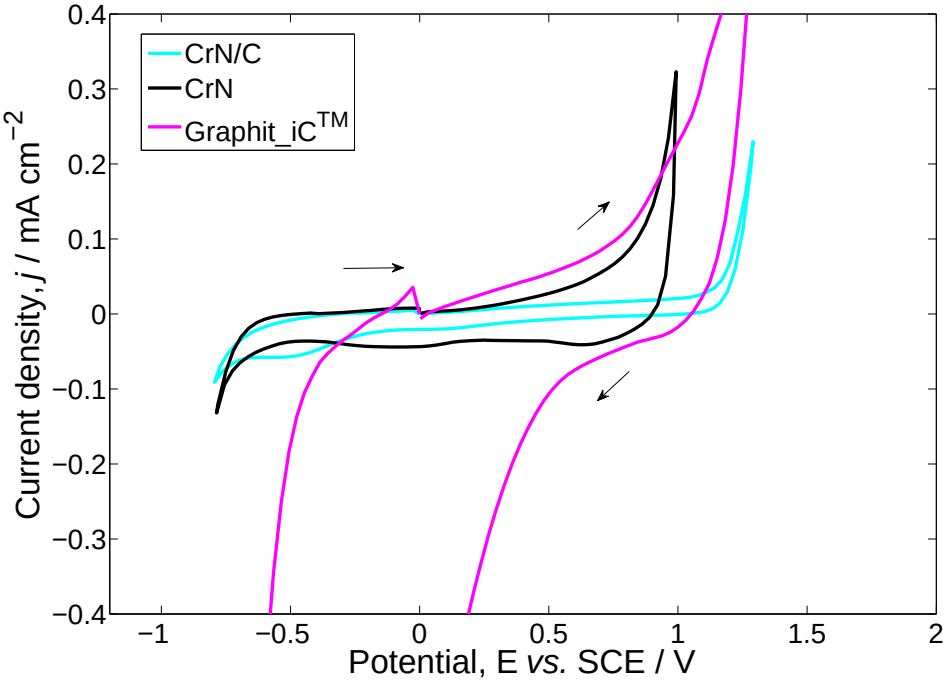

(b)

Figure 7.12: *Cyclic voltammograms of electrodes with various different coatings: (a) TiN (blue line), TiN /C (red line), ZrN (green line), (b) CrN/C (cyan line), CrN (black line) and Graphit_iC™ (pink line) in 1.0 M H_2SO_4. The electrolyte was saturated with nitrogen gas. The first cycle of each voltammogram is presented. The scan rate of the voltammograms was 50 mV sec^{-1} and the temperature was 20°C. The working electrode area was 1.13 cm^2.*

operates over a wider potential range (-0.35 to 0.8 V *vs.* SCE) when compared to the electrode with the TiN/C coating. The electrode with the TiN coating exhibits an oxidation wave at potentials more positive than 0.8 V *vs.* SCE while hydrogen evolution starts at potentials lower than -0.35 V *vs.* SCE. The electrode that had the ZrN coating shows the best potential window of operation (between -0.68 V *vs.* SCE and 1.02 V *vs*. SCE).

In figure 7.12b, the electrode with the Graphit_iC^{TM} coating gives the smallest potential window (0.57 to 0.75 V *vs.* SCE) when compared to the rest of the PVD coated electrodes. High oxidation currents are observed at potentials more positive than 0.75 V *vs* SCE towards more positive potentials and hydrogen evolution starts at approximately 0.57 V *vs.* SCE at the graphite voltammogram. The voltammogram of the electrode with CrN coating shows a reduction peak at 0.65 V *vs.* SCE and a second reduction peak at around -0.1 V *vs.* SCE. Oxygen evolution reaction or oxidation of the CrN coating starts at around 0.36 V *vs.* SCE towards more positive potentials and hydrogen evolution begins at -0.48 V *vs.* SCE towards more negative potentials. Finally, the electrode with the CrN/C coating shows the widest potential window of operation among the electrodes in figure 7.12b. An oxidation wave is observed at 1.08 V *vs.* SCE towards more positive potentials and hydrogen evolution at -0.02 V *vs.* SCE towards negative potentials while one reduction peak is observed at 0.06 V *vs.* SCE and a second reduction peak is observed at -0.5 V *vs.* SCE.

In figure 7.13, the cyclic voltammograms of the PVD coated electrodes in 4.0 M KOH are presented. The electrolyte was saturated with nitrogen gas for 15 minutes before each measurement. The scan rate of the voltammograms was 50 mV sec^{-1}.

In figure 7.13a, the smallest potential window of operation (-0.42 to 0.25 V *vs.* SCE) is shown at the voltammogram of the electrode with the TiN/C coating. Hydrogen evolution at the CV of the TiN/C coated electrode starts at -0.42 V *vs.* SCE toward more negative potentials, while a broad oxidation wave leading towards either OER or oxidation of the coating is observed at potentials more positive than 0.25 V *vs.* SCE. At the voltammogram of the TiN coated electrode, oxygen evolution or oxidation of the TiN coating is observed at 0.4 V *vs.* SCE towards more positive potentials, while hydrogen evolution starts at approximately -1.2 V *vs.* SCE towards more negative potentials. OER or the oxidation of the coating of the ZrN coated electrode starts at 0.42 V *vs.* SCE towards more positive potentials. Hydrogen evolution takes place at potentials more negative than -1.51

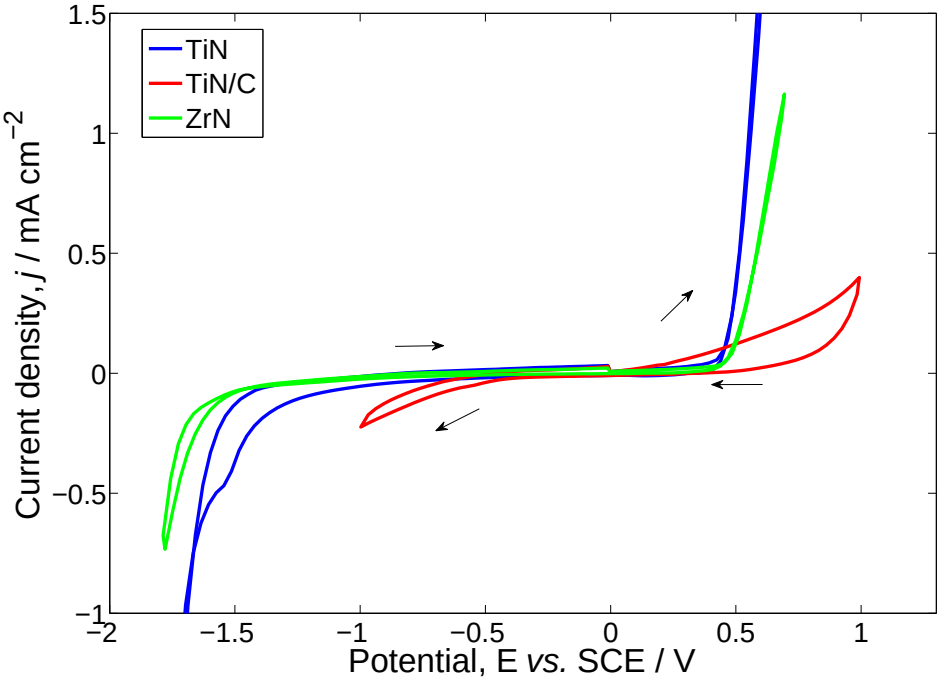

(a)

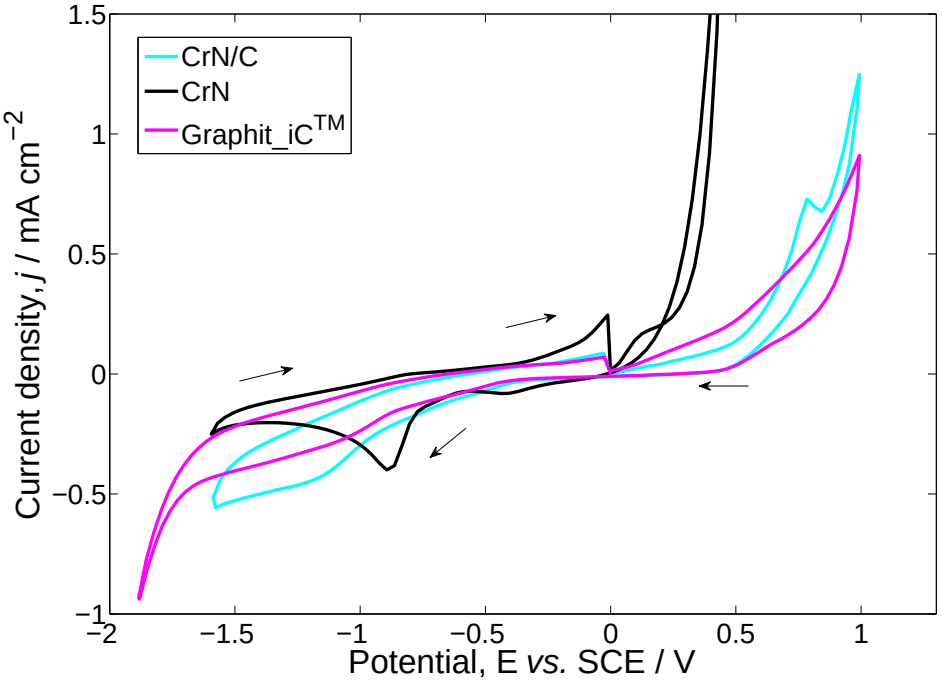

(b)

Figure 7.13: *Cyclic voltammograms of electrodes with various different coatings: (a) TiN (blue line), TiN /C (red line), ZrN (green line), (b) CrN/C (cyan line), CrN (black line) and Graphit_iC^{TM} (pink line) in 4.0 M KOH. The electrolyte was saturated with nitrogen gas. The first cycle of each voltammogram is presented. The scan rate of the voltammograms was 50 mV sec^{-1} and the temperature was 20°C. The working electrode area was 1.13 cm^2.*

V *vs.* SCE. The electrodes with the TiN and the ZrN coatings show similar behaviour.

In figure 7.13b, the CVs of the electrodes with CrN, CrN/C and Graphit_ic^{TM} are presented. All three electrodes seem to corrode really fast in alkaline environment.

The PVD coated electrodes failed after some cycles (figures 7.12 and 7.13) and the CVs that are presented are the cycles that showed the most stable results. The reason why the electrodes fail after consecutive cycling can be explained by looking the photographs in figures 7.14 and 7.15, which show the PVD coated electrodes after consecutive cycling in 1.0 M H_2SO_4 and 4.0 M KOH, respectively. It can be seen that there is an evidence of surface degradation observed as discolouring, pitting and raised corrosion products in both figures with some electrodes showing more severe corrosion than others. In figure 7.14, it can be seen that the most affected electrode is possibly the electrode with the ZrN coating and in figure 7.15 the mostly affected is the electrode with the TiN coating.

Hence, even if the ZrN coated electrode had shown the widest potential window of operation amongst all the electrodes both in 1.0 M H_2SO_4 (-0.68 to 1.02 V *vs.* SCE) and in 4.0 M KOH (-1.51 to 0.42 V *vs.* SCE), the electrode's surface is affected with successive cyclic voltammetry showing surface degradation based on the photographs in figures 7.14 and 7.15.

This can be verified by the voltammogram in figure 7.16 where the voltammogram of the ZrN coated electrode in 1.0 M H_2SO_4 before and after some consecutive cycling is presented. The electrolyte was de-oxygenated with nitrogen gas for 15 minutes and the scan rate of the voltammograms was 50 mV sec^{-1}. It can be seen from the voltammogram in figure 7.16 that the performance of the ZrN coated electrode drops after long cycling since the voltammogram of the eight cycle of the measurement shows that the electrode is not stable and its potential window of operation decreases from -0.68 to 1.2 V *vs.* SCE to 0.44 to 0.76 V *vs.* SCE.

Additionally, it can be seen that generally the PVD coated stainless steel substrates get oxidised at positive potentials which makes them inadequate candidates for potential electrode substrates in a bifunctional O_2/air electrode

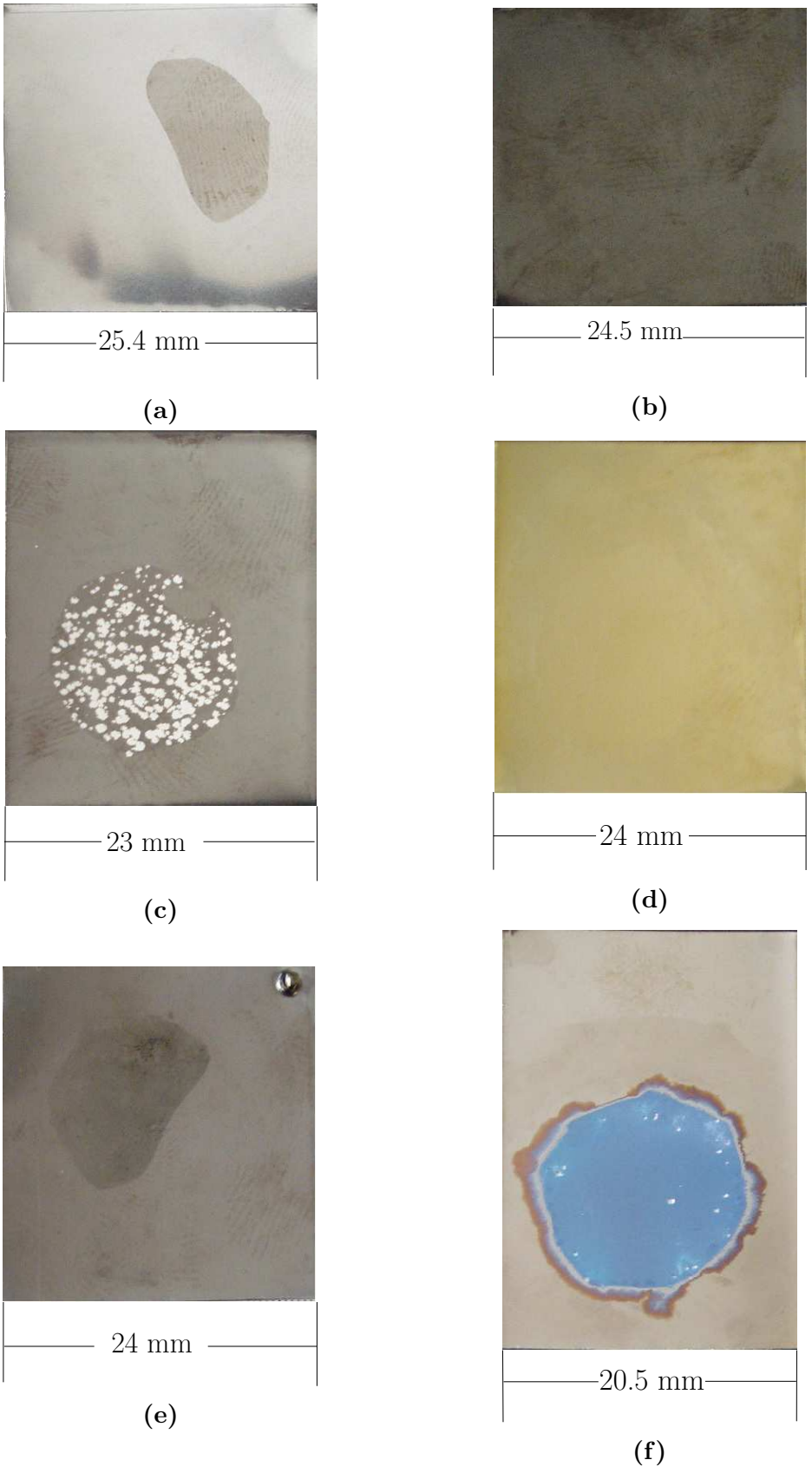

Figure 7.14: *Photographs of the electrodes after cycling in 1.0 M H_2SO_4: (a) CrN, (b) CrN/C (c) Graphit_iC^{TM}, (d)TiN, (e)TiN/C and (f) ZrN*

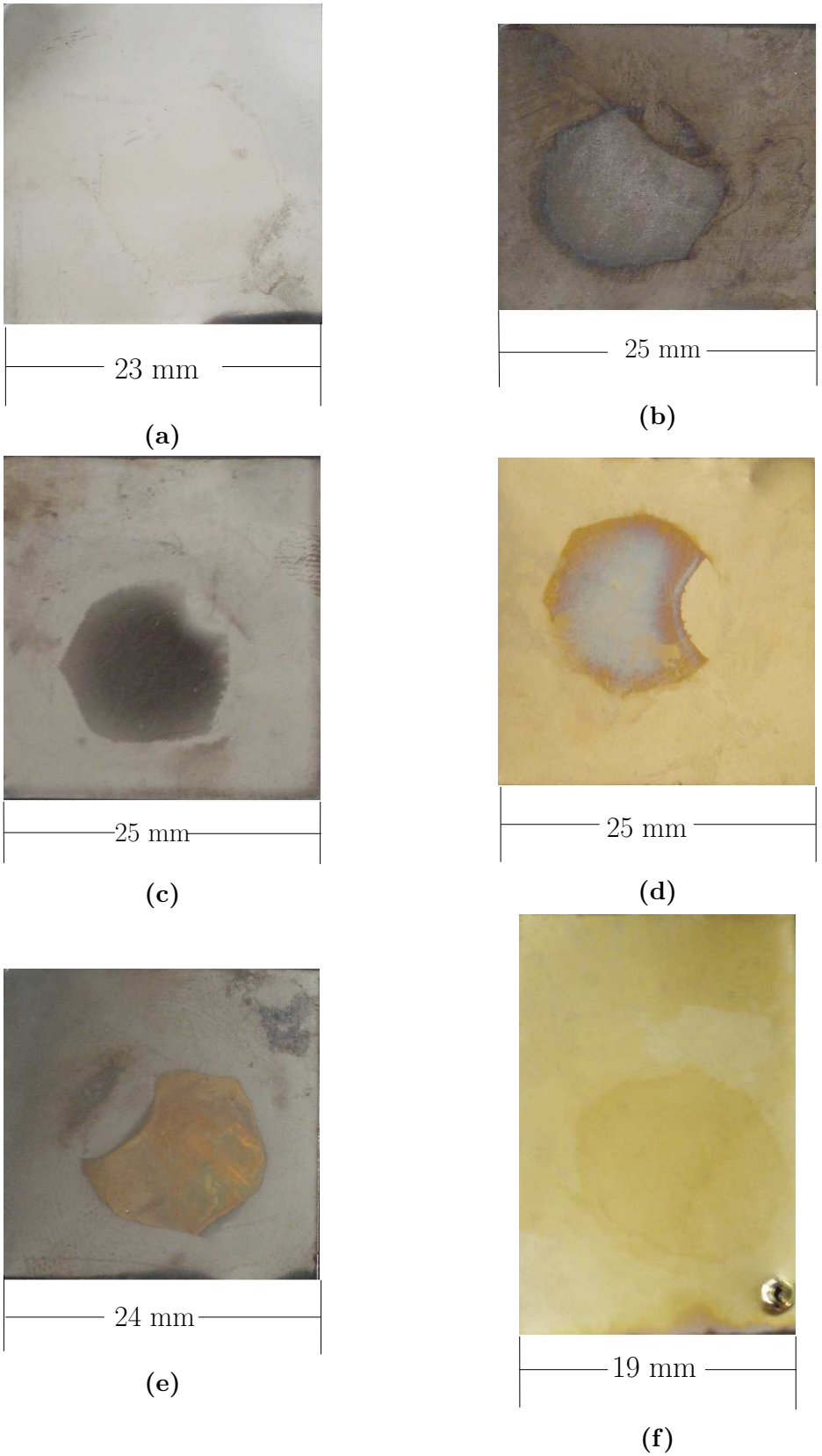

Figure 7.15: *Photographs of the electrodes after cycling in 4.0 M KOH: (a) CrN, (b) CrN/C (c) Graphit_iC^{TM}, (d)TiN, (e)TiN/C and (f) ZrN*

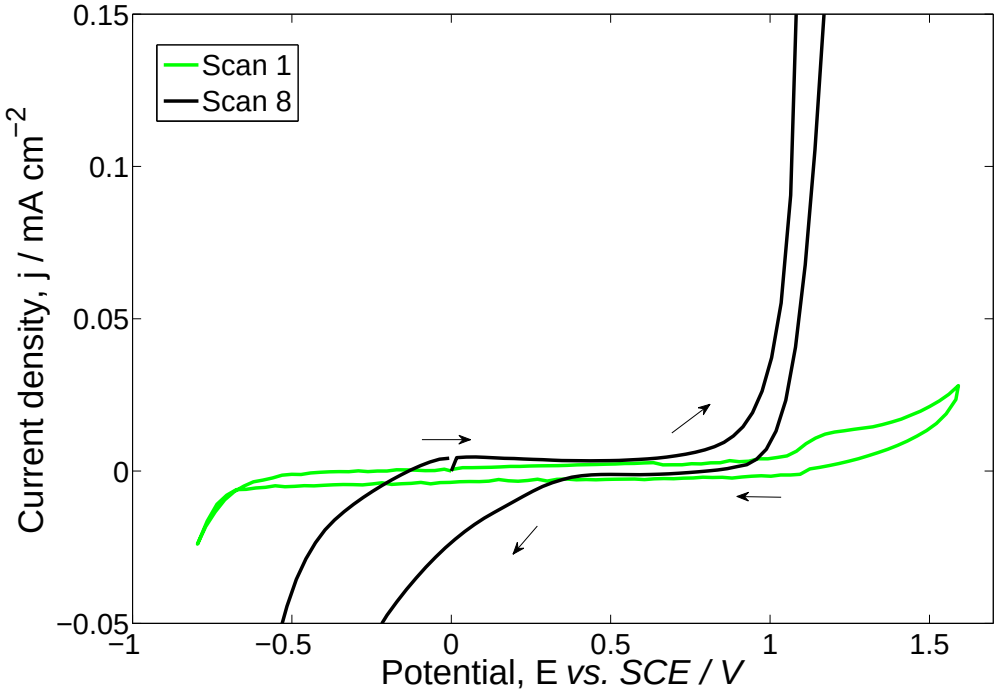

Figure 7.16: *Cyclic voltammograms of the ZrN coated stainless steel electrode in 1.0 M H_2SO_4. The electrolyte was saturated with nitrogen gas. The first cycle (green line) and the eighth cycle (black line) of the voltammogram are presented. The scan rate of the voltammogram was 50 mV sec^{-1} and the temperature was 20°C. The working electrode area was 1.13 cm^2*

7.3 Conclusions and Further Work

The results from the electrochemical characterisation on Magnéli phase bulk materials showed that they can support redox electron transfer reactions. Additionally, Magnéli materials with various porosities were tested and the results from these measurements can support the idea that the higher the porosity of the Magnéli phase materials, the higher current density values the materials displays. Hence, it is shown that porous Magnéli materials can be used as high surface area electrodes or electrode supports and gas diffusion layers. However, the porous Magnéli phase materials had high electrical resistance and low electron transfer kinetics so they were applied as thin coatings on a variety of different substrates to eliminate this two disadvantages.

Hence, a variety of APS Magnéli phase coated stainless steel, aluminium and carbon polymer substrates have been electrochemically tested. The CVs on these electrodes showed that the coating protects the substrates from oxidation and improves the conductivity of the electrodes. Furthermore, the electrochemistry

of the APS Magnéli phase electrodes was reversible and stable, since no material degradation was observed with successive CVs. It was shown that the APS Magnéli coating protects the substrates in aggressive electrolytes, over the potential region of the OER and ORR reactions and therefore may offer a good surface for the HPA gas diffusion electrodes. Also, based on the high overpotential requirements that the Magnéli phase materials demonstrated, their combination with HPAs could overcome this poor electron kinetics drawback. Hence, it offers an electrode type that is light weight and highly conductive which could be useful in many applications, such as flow batteries, fuel cells, etc.

Stainless steel substrates have been coated with CrN, CrN/C, Graphit_iC^{TM}, TiN, TiN/C and ZrN by using PVD as the coating technique. The PVD coatings were not stable after successive cycling, however the electrodes with the ZrN coating showed high overpotentials for hydrogen and oxygen evolution. The potential window of operation of the electrode with the ZrN coating was from -0.68 to 1.02 V *vs.* SCE in acidic environment (1.0 M H_2SO_4) and from -1.51 to 0.42 V *vs.* SCE in alkaline environment (4.0 M KOH). Hence, ZrN could be suitable to be used in an APS coating.

The operational potential window of the APS Magnéli coated stainless steel electrode was between -0.75 and 2.4 V *vs.* SCE in 1.0 M H_2SO_4 while the stainless steel substrate without the coating was operating without oxidation between -0.55 and 1.01 V *vs.* SCE in the same acidic environment. In 4.0 M KOH, the APS Magnéli coated stainless steel substrate was stable between -1.48 and 0.9 V *vs.* SCE and the uncoated stainless steel substrate was giving stable results from -1.4 to 0.39 V *vs* SCE. Hence, it was shown that the APS Magnéli phase coating protects the stainless steel substrate and shifts hydrogen evolution to more negative potentials and oxygen evolution to more positive potentials, creating a wider potential window when compared to the potential values that stainless steel and the PVD coated stainless steel substrates could operate without getting oxidised.

Additionally, the APS Magnéli coating improved the conductivity of the stainless steel substrate since the current density values exhibited by them were approximately three orders of magnitude higher than the values exhibited by the PVD coated stainless steel electrodes, both in acidic and alkaline environment

Chapter 8

Conclusions and Further work

8.1 Conclusions

This thesis presented the work from the investigation of the redox activity of two heteropolyacids (phosphomolybdic acid and phosphotungstic acid) dissolved in acidic and alkaline environment, the incorporation of these two HPAS into the catalyst layer of bifunctional HPA gas diffusion electrodes for OER and ORR and their characterisation in an alkaline aqueous electrolyte (4.0 M KOH). Additionally, a variety of non-carbon electrode materials has been presented and characterised as alternative choices to the commonly used carbon substrates.

Initially, the heteropolyacids have been electrochemically characterised with cyclic voltammetry while being dissolved in acidic (1.0 M H_2SO_4) and alkaline (4.0 M KOH) electrolytes which were either de-oxygenated or saturated with oxygen. The characterisation of phosphomolybdic acid and phosphotungstic acid in the de-oxygenated acidic electrolyte showed that they both exhibit significant redox activity which was non-reversible, while the phosphotungstic acid demonstrated more reversible results.

Additionally, the redox activity of the phosphotungstic acid in an oxygen saturated H_2SO_4 solution was monitored. Comparing the results of the dissolved PWA in the oxygenated and the de-oxygenated electrolyte a difference in the reversibility of their redox reactions can be monitored. It was observed that the voltammograms of the PWA in the de-oxygenated solution demonstrated higher reversibility.

Furthermore, both PMA and PWA exhibited poor redox activity and low stability when they were tested in the de-oxygenated alkaline electrolyte (4.0 M KOH).

Consequently, the HPAs were further characterised while being immobilised on a glassy carbon electrode. Cyclic voltammetry measurements in 1.0 M H_2SO_4 and 4.0 M KOH were performed on the HPA-modified electrodes. The results from these voltammograms showed that both heteropolyacids demonstrate low stability and that they were dissolved in the electrolyte after just a few cycles. However, the glassy carbon electrode which was modified with the phosphotungstic acid exhibited slightly better redox activity and stability when compared to the results obtained from the PMA-modified electrode.

In order to improve the poor stability issues that the heteropolyacids showed in alkaline environment, they had to be further immobilised. Hence, the heteropolyacids were combined with nickel and Nafion® in order to protect them from the alkaline electrolyte. Phosphomolybdic acid and phosphotungstic acid in combination with nickel (nickel nano-powder and nickel carbonly powder) and Nafion® formed catalyst inks which were consequently printed on a Toray carbon paper in order to create novel bifunctional electrodes which incorporate HPAs.

The electrochemical performance of the manufactured electrodes in 4.0 M KOH was investigated by using cyclic voltammetry and constant current measurements. A general remark raised from the most of the electrochemical measurements taken, is that the addition of HPA in nickel, enhances the activity of nickel towards the oxygen evolution reaction. The overpotential for OER when HPA is mixed with nickel in the catalyst ink is reduced when compared to the catalyst ink that includes only nickel. A slight reduction at the electrode potential for oxygen reduction reaction can be observed when HPA is added, comparing to the electrode potential for ORR at nickel. Additionally, by incorporating the heteropolyacids in the catalyst link of the electrode it was reported for the first time that HPAs can show stability in an alkaline aqueous solution.

However, the reduction is not high enough for commercial purposes, since the voltage difference between oxygen evolution and oxygen reduction for nickel with HPA electrodes is still high. A possible application though could be at electrodes of water electrolysers, since oxygen reduction does not happen in these devices [52].

Molybdenum(Mo) was also combined with nickel and Nafion® to form a catalyst ink which was used to create a Ni Mo electrode. The results from the cyclic voltammetry on this electrode showed that the incorporation of molybdenum had no effect on the nickel performance since it did not show enhancing results similar to the results observed with the Ni HPA electrodes. Hence, it was shown that the

performance of the electrode was not improved due to a possible decomposition of the HPA to a nickel-molybdenum complex which could have acted as a catalyst.

According to the results which are presented in chapter 5, the heteropolyacids with the tungsten showed higher enhancement to the nickel performance when compared to the enhancement by the heteropolyacids with the molybdenum. However, the difference between the CVs of the HPA gas diffusion electrodes that included PMA and PWA were not sufficiently distinct, hence further investigation was made in order to discover more about their different enhancing effects.

During the constant current experiments for OER and ORR, the electrodes with nickel and HPA showed stable results for a satisfying amount of time. A lower overpotential was observed during the cycling of the electrode with nickel and PWA. The results from the cycling of the electrode with nickel and PMA were rather interesting and they required further investigation. During the first 1.5 hours of charging, the potential values that it exhibited were similar to the ones observed with the electrode which incorporated PWA. After that point, the potential shifted to higher potentials and reached the potential value exhibited by the nickel electrode.

Based on the results from the constant current cycling and the additional microscopy measurements on the HPA gas diffusion electrodes it was shown that after some hours of testing, the catalyst layer deteriorates. In order to avoid the degradation of the catalyst layer and hence the failure of the electrode, more investigation on the properties of the catalyst layer and the alternative materials to the carbon Toray paper choice was required.

Further investigation on the catalyst ink composition, i.e. catalyst ink solid loading, choice of a different nickel etc., was performed in order to optimise the performance of the bifunctional HPA gas diffusion electrodes. The first step in this series of experiments was based on the variation of the amount of heteropolyacids which was added in the catalyst ink, while the nickel content was kept constant.

The electrodes which incorporated these catalyst inks were all electrochemically characterised in 4.0 M KOH with cyclic voltammetry. The results from their characterisation showed that while the amount of the heteropolyacid in the ink was increasing, the performance of the electrode was improving. However, it was observed that after a specific amount of HPA, when the added HPAs was increasing further, the performance of the electrode which incorporated the catalyst ink was deteriorating.

The best performing electrode with PMA and the best performing electrode which included PWA were found. When the performance of these two electrodes was compared, it was observed that the electrode with the phosphomolybdic acid exhibited slightly more enhancing results. Hence, the rest of the investigation on the HPA gas diffusion electrodes was focused on the electrodes that incorporated phosphomolybdic acid.

Subsequently, electrodes with phosphomolybdic acid and two different types of nickel (nickel micro-powder and nickel carbonate) were manufactured. It is reported in literature that the combination of nickel carbonate with heteropolyacids forms a nickel-HPA complex. Hence, it was investigated whether the substitution of nickel carbonyl with the salt that is formed when PMA and nickel carbonate are combined ($Ni_3(PMo_{12}O_{40})$ improves the performance of the HPA gas diffusion electrodes. When the results from the electrochemical characterisation of the electrodes with the Ni-PMA salt were compared to the results obtained from the electrodes with nickel carbonyl and PMA it was shown that even if both types of electrodes give stable results in alkaline environment, the most suitable type of nickel for the HPA gas diffusion electrodes is the nickel carbonyl.

Finally, the effect of the catalyst ink solid loading on the electrode was investigated. Three electrodes with different ink solid loading but the same catalyst ink which included nickel and phosphomolybdic acid were manufactured. Their electrochemical characterisation by cyclic voltammetry and constant current cycling in 4.0 M KOH showed that the ink solid loading influences the performance of the HPA gas diffusion electrode. However, this aspect has to be further explored since the electrode with the highest ink solid loading demonstrated fast electron transfer kinetics and small potential difference between OER and ORR but the electrode with the lowest ink solid loading exhibited higher current density values.

Due to the failing of the HPA electrode after consecutive cycling, attention was drawn to different materials for the electrode's support rather than the carbon Toray paper. Initial electrochemical characterisation in acidic, alkaline and neutral electrolytes was obtained on Magnéli spray coated electrodes with different substrates.

A number of materials has been investigated as alternatives to the carbon electrode support:

- Magnéli phase bulk materials;

- APS Magnéli phase spray coated electrodes;
- PVD coatings with various materials on a stainless steel substrate.

Looking at those non-carbon materials as candidates for alternative electrode substrates it could be concluded that Magnéli phase materials show promising results as both coating and bulk materials. However, Magnéli phase bulk materials exhibited high electrical resistance and poor electron transfer kinetics.

In order to overcome these drawbacks, thin coatings of Magnéli and other non-carbon materials were investigated. From the results received, the Magnéli coating is protecting the different substrates from corroding or dissolving in the electrolyte. Additionally, in the case of the stainless steel substrate, the APS Magnéli phase coating widens the potential operation window and facilitates redox electrochemistry. However, the electrodes with the PVD coating that include ZrN showed stable results in the different electrolytes under a wide potential window.

8.2 Further Work

8.2.1 HPA solution-based redox activity

The results from the investigation on the HPAs dissolved in acidic and alkaline environment showed that heteropolyacids demonstrate a redox activity when dissolved in these aqueous electrolytes. A potential application of heteropolyacids dissolved in a aqueous solution could be their incorporation in a redox flow battery as the electrolyte. However, the reversibility of the redox reactions was poor and more research could be focused on improving the reversibility of these reactions. The high concentration of the HPAs could explain the low reversibility due to high IR drop. So, an investigation on how the kinetics of the redox reactions of the heteropolyacids change while the concentration of the HPA in the solution vary, could be assessed.

It was shown that the reversibility of the redox reactions of PWA in a de-oxygenated acidic aqueous electrolyte was enhanced when compared to the results from the measurements in a solution that contained oxygen. Hence, after the concentration of the dissolved acid is going to be optimised, phosphotungstic acid could be used in a redox flow battery where the electrolyte will not include oxygen.

8.2.2 Bifunctional HPA gas diffusion electrodes

Even though the work on bifunctional HPA gas diffusion electrodes in chapters 5 and 6 showed that the addition of HPA in the catalyst ink reduces the potential between OER and ORR, the reduction due to the HPA is not big enough for commercial purposes. Since the voltage difference between oxygen evolution and oxygen reduction for nickel with HPA electrodes is still high a possible application though could be at electrodes of water electrolysers, since oxygen reduction does not happen in these devices [52].

It was proved for the first time that HPAs, when incorporated in the catalyst layer of a bifunctional oxygen/air electrode, can be stable in alkaline environment. However, when the electrodes were used in long term, some stability issues were observed. Hence, further investigation on catalyst ink composition, i.e. choice of a different binder etc., and the whole manufacturing process, i.e. uniform printing, monitor the effect of time on the electrodes performance etc., is required to optimise their performance. Additionally, further analysis based on the electrode's failure mechanism is required.

Finally, further investigation needs to be focused on the mechanism that metallic Ni and HPA combine in order to understand the reason behind the enhancement during the OER and ORR due to the addition of the heteropolyacids. An initial assumption is based on the idea that the result of their combination is a complex with HPA surrounding the metallic nickel. It is believed that the electronic conductivity is attributed to the nickel while enhanced proton conductivity could be due to the HPA.

8.2.3 Alternative materials as electrode substrates

According to the electrochemical characterisation on a variety of different materials as electrode substrates which is presented in chapter 7 and the literature review, APS coatings of Magnéli phase materials could be suitable coatings for high-weight, low resistance and low cost electrode materials. Additionally, it was shown that Magnéli phase materials display poor electron kinetics and their combination with HPAs could potentially improve their high overpotentials.

Furthermore, among the PVD coated substrates, the electrode which was coated by ZrN demonstrated a wide potential window however it was not stable after long

term cycling. So, if ZrN's low stability issues could be solved then an APS coating materials incorporating ZrN could be used created.

Appendix A - HPAs as additives in electrolyte membranes in fuel cells

Table 1: *HPAs as additives in electrolyte membranes in fuel cells*

Membrane	Additives	Proton conductivity	Comments	Authors
Nafion®	$H_4SiW_{12}O_{40}$, $H_3PW_{12}O_{40}$, $H_3PMo_{12}O_{40}$	$(1.5-9.5)\times10^{-2}$ S cm^{-1} at 100°C and 100% RH	Increased up to 95% water uptake with $H_3PMo_{12}O_{40}$ and the highest proton conductivity with $H_4SiW_{12}O_{40}$	[60]
	$H_4SiW_{12}O_{40}$ with and without thiophene	10.0×10^{-2} S cm^{-1} at 25°C and 100% RH	Good mechanical stability and strength after long term period	[61]
	$H_4SiW_{12}O_{40}$	1.7×10^{-2}S cm^{-1} at 110°C	High thermal stability and improved current density	[62]
	$H_3PW_{12}O_{40}$, $H_4SiW_{12}O_{40}$, $H_3PMo_{12}O_{40}$ and $H_4SiMo_{12}O_{40}$	1.5×10^{-2} S cm^{-1} at 120°C and 35% RH	Low crossover (1 mA/cm^2) & electrochemically unstable membranes with $H_3PMo_{12}O_{40}$ and $H_4SiMo_{12}O_{40}$	[63]

Continued on next page

Table 1 – *Continued from previous page*

Membrane	Additives	Proton conductivity	Comments	Authors
	$H_3PW_{12}O_{40}$ with larger cations (such as Cs^+,NH_4^+, Rb^+ & Tl^+)	1.6×10^{-2} S cm^{-1} at 120°C and 35% RH	Low hydrogen crossover currents	[58]
	$Cs_{2.5}H_{0.5}PW_{12}O_{40}$	1.42×10^{-2} S cm^{-1} at 80°C and 100% RH	Better results than that of Nafion	[64]
	$H_3PW_{12}O_{40}$ on SiO_2	2.67×10^{-2} S cm^{-1} at 110°C and 70% RH	Higher water uptake and higher proton conductivities at low relative humidity values	[65]
	$H_3PW_{12}O_{40}$ on SiO_2	2.51×10^{-3} S cm^{-1} at 90°C and 40% RH	82 mA cm^{-2} at 0.6 V at 90°C and 40% RH	[66]
Nafion®	$H_3PW_{12}O_{40}$ with SiO_2, ZrO_2 and TiO_2	1.5×10^{-2} S cm^{-1} at 120°C and 35% RH	Low hydrogen crossover currents	[67]
	$H_3PW_{12}O_{40}$ on meso-SiO_2	7.0×10^{-2} S cm^{-1} at RT and 25% RH and 11.0×10^{-2} S cm^{-1} at RT and 100% RH	Elevated temperature of 120°C, low humidity of 25 RH% the Nafion-$H_3PW_{12}O_{40}$/meso-SiO_2 composite membrane showed a steady performance	[68]
	$H_3PW_{12}O_{40}$ on SiO_2	2.67×10^{-2} S cm^{-1} at 110°C and 70% RH	540 mA cm^{-2} at 0.4 V 110°C and at 70% RH condition vs. 95 mA cm^{-2} for Nafion®	[69]
	$H_3PMo_{12}O_{40}$	3.5×10^{-2}S cm^{-1} at 80 °C & 100%RH	Decreased methanol permeation rate	[84]

Continued on next page

Table 1 – *Continued from previous page*

Membrane	Additives	Proton conductivity	Comments	Authors
Nafion®	$Cs_{2.5}H_{0.5}PW_{12}O_{40}$	N/A	1.1 W cm^{-2} at 70 °C	[82]
	$Cs_{2.5}H_{0.5}PW_{12}O_{40}$	3.6×10^{-2} S cm^{-1}	Low methanol diffusion coefficient& maximum power density 26% higher	[85]
	$H_3PMo_{12}O_{40}$ and PPO	3.41×10^{-2} S cm^{-1} at 20 °C	Reduced methanol crossover	[57]
	$H_3PW_{12}O_{40}$ and SiO_2	2.2×10^{-2} S cm^{-1} at 80°C and 100% RH	Higher open circuit voltage and maximum power	[81]
	$H_3PW_{12}O_{40}$ on ZrO_2	6×10^{-3} S cm^{-1} at 120°C and 25% RH	Good electrochemical stability more than 150 cycles at 90°C	[56]
	$H_3PW_{12}O_{40}$ on SiO_2	0.12 S cm^{-1} at 50°C and 100% RH and 0.16 S cm^{-1} at 75°C and 100% RH	50 – 80% reduced methanol cross-over	[83]
PFSA	$H_3PW_{12}O_{40}$, $H_4SiW_{12}O_{40}$	1.13×10^{-1} S cm^{-1} at 100°C and 80% RH	N/A	[237]
MCM 41	$H_3PW_{12}O_{40}$	0.08 S cm^{-1}	Better overall cell performance	[238]
	$H_3PW_{12}O_{40}$ or $H_3PMo_{12}O_{40}$	10^{-2} S cm^{-1} at RT	High thermal and structural stability	[239]
	$H_3PW_{12}O_{40}$	4.5×10^{-2} S cm^{-1} at 150°C	N/A	[240]
PVA	$H_4GeW_{12}O_{40}$	2.11×10^{-2} S cm^{-1} at 20°C with 80% of $H_4GeW_{12}O_{40}$	N/A	[70]

Continued on next page

Table 1 – *Continued from previous page*

Membrane	Additives	Proton conductivity	Comments	Authors
PVA	$H_4SiW_{12}O_{40}$	8.31×10^{-3} S cm^{-1} at 100°C and 100% RH	N/A	[71]
	$H_3PMo_{12}O_{40}$, glutaraldehyde & 3-aminopropyl-triethoxydilane	10^{-3}-10^{-1} S cm^{-1} at 20°C - 140°C and 30-90% RH	Stable up to 300°C	[72]
	$H_3PW_{12}O_{40}$	6.27×10^{-3} S cm^{-1} at 20°C	Methanol permeability 1.28×10^{-7} - 4.54×10^{-7} cm^2 s^{-1}	[86]
	$H_3PW_{12}O_{40}$	5.18×10^{-4} S cm^{-1} at 20°C	Lower methanol permeability and increased proton conductivity	[88]
	$H_5GeW_{10}MoVO_{40}$	1.22×10^{-2} S cm^{-1} at 20°C	N/A	[241]
	$H_3PW_{12}O_{40}$ on SiO_2	1.7×10^{-2} S cm^{-1} at 20°C	Methanol permeability 10^{-7} - 10^{-8} cm^2 s^{-1}	[87]
	$H_4SiW_{12}O_{40}$ and zirconium phosphate	10^{-2} S cm^{-1} at 60% RH	Reduced methanol crossover	[90]
	PAM with $Cs_{2.5}H_{0.5}PW_{12}O_{40}$ and $Cs_{2.5}H_{0.5}PMo_{12}O_{40}$	1.8×10^{-3} - 3.7×10^{-3} S cm^{-1} at 20°C and 50% RH	Excellent swelling, thermal, oxidative and additive stability	[89]

Continued on next page

Table 1 – *Continued from previous page*

Membrane	Additives	Proton conductivity	Comments	Authors
PVA	$Cs_1H_3SiW_{12}O_{40}$, $Cs_2H_2SiW_{12}O_{40}$ and zirconium phosphate	10^{-3} to 10^{-2} S cm^{-1} at 50% RH	Reduced methanol crossover	[91]
	$H_3PW_{12}O_{40}$ and DTPA	10^{-3} S cm^{-1}	Increased proton conductivity with the addition of HPA	[242]
	$H_3PW_{12}O_{40}$ and PES	N/A	Improved thermal stability Decreased water intake Improved ion exchange capacity Improved proton and methanol permeability	[92]
SPEEK	$H_3PW_{12}O_{40}$, $H_3PMo_{12}O_{40}$ and $Na_2HPW_{12}O_{40}$	More than 10^{-2} S cm^{-1} at 20°C and 1.1×10^{-1} S cm^{-1} at 120°C and 55% RH	N/A	[73]
	$CsH_2PW_{12}O_{40}$ and $CsH_3SiW_{12}O_{40}$	2.25×10^{-3} S cm^{-1} at 80°C under 80% RH	Maximum power density values (245 mW cm^{-2} and 247 mW cm^{-2})	[74]
	$Cs_{2.5}H_{0.5}PW_{12}O_{40}$ on Pt	5.3×10^{-2}S cm^{-1}at 60°C and 100% RH	Improved stability	[75]
	$Cs_{2.5}H_{0.5}PW_{12}O_{40}$ on Pt& $H_4SiW_{12}O_{40}$	6.82×10^{-2} S cm^{-1}	Higher conductivity than Nafion 117	[76]
	$H_3PW_{12}O_{40}$ on SiO_2	6.2×10^{-3} S cm^{-1} at 100°C and 90% RH	Double proton conductivity values than plain SPEEK's values	[77]

Continued on next page

Table 1 – *Continued from previous page*

Membrane	Additives	Proton conductivity	Comments	Authors
SPEEK	$H_3PW_{12}O_{40}$ and MCM 41	2.75×10^{-3} S cm^{-1} at 20°C	Higher selectivity and thermal stability	[78]
	$H_4SiW_{12}O_{40}$ on SiO_2,Al_2O_3	6.1×10^{-2} S cm^{-1} at RT and 100% RH	Low methanol permeability	[93]
	γ-$K_9SiW_{10}O_{36}$	2.9×10^{-2} S cm^{-1} at 90°C and 100%RH	Low methanol crossover and higher stability	[94]
	$Cs_{2.5}H_{0.5}PW_{12}O_{40}$	1.3×10^{-1} S cm^{-1} at 80°C and 100%RH	Methanol permeability (4.7×10^{-7} cm^2 s^{-1}) Improved hydrolytic stability	[95]
PBI	$H_3PW_{12}O_{40}$ and $H_4SiW_{12}O_{40}$	7.0×10^{-2}S cm^{-1} at 100°C and 5% RH	N/A	[243]
	$CsH_2PW_{12}O_{40}$ and $CsH_3SiW_{12}O_{40}$	1.91×10^{-2}S cm^{-1} at 160°C and 0% RH	N/A	[244]
	$Cs_{2.5}H_{0.5}PMo_{12}O_{40}$ and H_3PO_4	2.3×10^{-1}S cm^{-1} at 160°C and 8.4% RH	Generally higher proton conductivities than plain PBI Good thermal stability	[245]
	$H_3PW_{12}O_{40}$ on SiO_2	1.2×10^{-3} S cm^{-1} at 160°C and 100% RH	Mechanically stable	[246]
	$H_3PW_{12}O_{40}$ on SiO_2	3×10^{-3} S cm^{-1} at 100°C and 100% RH (1.4-1.5) $\times$ 10^{-3} S cm^{-1} between 90°-150°C at 100% RH	Chemically and thermally stable membranes	[247]

Continued on next page

Table 1 – *Continued from previous page*

Membrane	**Additives**	**Proton conductivity**	**Comments**	**Authors**
PBI	$H_3PW_{12}O_{40}$	10^{-6} S cm^{-1}	Very low values due to low interaction of the $H_3PW_{12}O_{40}$ and the polymer	[248]
PEG	$H_4SiW_{12}O_{40}$	N/A	Ion-exchange capacities twice of Nafion 117, but the cell perfomance is poor	[249]
PVdf	$H_3PW_{12}O_{40}$ and Al_2O_3	1.96×10^{-3} S cm^{-1} at 25^oC	Good thermal stability up to 240°C but lower conductivites than the HPA alone	[250]
PVdf/HFP	$H_3PW_{12}O_{40}$, $H_3PW_{12}O_{40}$, a-$H_3P_2W_{18}O_{62}$, $H_6P_2W_{21}O_{71}$ and $H_6As_2W_{21}O_{69}$	N/A	Good currents at RT but stability issues	[251]
SPI	$H_3PW_{12}O_{40}$	2.18×10^{-1} S cm^{-1} at 90°C	Decreased water permeability	[252]
SPSF	$H_3PW_{12}O_{40}$	1.4×10^{-1} S cm^{-1} at 120°C and 100% RH	Improved mechanical strength and low water uptake	[253]
SPES-C	$H_3PW_{12}O_{40}$	4.5×10^{-2}S cm^{-1} at 90°C and 100% RH 6.7×10^{-2}S cm^{-1} at 110°C and 100% RH	Thermally stable up to 200°C	[82]
SPEEK/SPS-co-PPSS	$H_3PW_{12}O_{40}$	6.29×10^{-2} S cm^{-1} at 80°C	N/A	[254]

Continued on next page

Table 1 – *Continued from previous page*

Membrane	**Additives**	**Proton conductivity**	**Comments**	**Authors**
s-PEK	$H_3PW_{12}O_{40}$, $H_3PMo_{12}O_{40}$ on SiO_2 or ZrO_2	8.6×10^{-2} S cm^{-1} at 20°C and 100% RH	Leaking of HPA	[255]
SPAES	$H_3PW_{12}O_{40}$	1.5×10^{-1} S cm^{-1} at 130°C and 100% RH	High water retention at elevated temperature (100-280°C)	[256]
SPAEK-C	$H_3PW_{12}O_{40}$ and PANI	9.3×10^{-2}S cm^{-1} at 25°C and 100% RH 0.24S cm^{-1} at 80°C and 100% RH	Reduced methanol permeability Higher conductivities than Nafion or pristine SPAEK-C	[257]
Chitosan	$H_3PW_{12}O_{40}$	2.4×10^{-2} S cm^{-1} at 80°C and 100% RH	Good swelling properties and low methanol permeability	[258]
	$H_3PW_{12}O_{40}$, $H_3PMo_{12}O_{40}$ & $H_4SiW_{12}O_{40}$	1.5×10^{-2} S cm^{-1} at 25^oC	Low methanol permeability 2.7×10^{-7} cm^2/s Comparatively high proton conductivity	[259]
SPAEK-COOH	$H_3PW_{12}O_{40}$ and Chitosan	8.6×10^{-2} S cm^{-1} at 25^oC and 100% RH	Low water swelling ration and methanol permeability	[260]
Y-zeolite	$H_3PMo_{12}O_{40}$ & $H_3PW_{12}O_{40}$	1.1×10^{-2} S cm^{-1} at RT and 100% RH	N/A	[261]
P_2O_5 - SiO_2 glass	$H_3PW_{12}O_{40}$	9.1×10^{-2} S cm^{-1} at 90°C and 30% RH	Good mechanical and thermal stability	[262]
P_2O_2 - SiO_2	$H_3PW_{12}O_{40}$ and ZrO_2	N/A	43 mW cm^{-2} was obtained at 27°C and 30%	[263]

Continued on next page

Table 1 – *Continued from previous page*

Membrane	**Additives**	**Proton conductivity**	**Comments**	**Authors**
P_2O_5-SiO_2/TiO_2 (Sol-gel)	$H_3PW_{12}O_{40}$and TiO_2	2.9×10^{-2} S cm^{-1} at 30°C and 85% RH	Good thermal stability	[264]
Organically modified silicate (Sol-gel)	$H_3PW_{12}O_{40}$ and $H_4SiW_{12}O_{40}$	10^{-3} S cm^{-1} at RT	High open circuit voltage	[265]
GPTMS	$H_3PW_{12}O_{40}$	1.0×10^{-2}S cm^{-1} at 80°C and 100% RH	Maximum power density 45 mW cm^{-2} Current density 175 mA cm^{-2} at 0.2V at 90° and 100% RH	[266]
Zirconia bridged hydrocarbon	$H_3PW_{12}O_{40}$	4×10^{-3} S cm^{-1} at 150°C and 100% RH	High thermal stability	[267]
PVACO	$H_3PMo_{12}O_{40}$	2.68×10^{-3}S cm^{-1} at RT	Lower proton conductivity Better resistance to methanol permeability than Nafion 117 under similar measurement conditions	[268]
PEO	$H_4SiW_{12}O_{40}$	6.3×10^{-2}S cm^{-1} at RT	$H_4SiW_{12}O_{40}$ is complexed with PEO and it forms a new compound	[269]
	$H_3PW_{12}O_{40}$ on SiO_2	5.0×10^{-3} S cm^{-1} at 80°C and 100% RH	Thermally stable at high temperature	[270]

Continued on next page

Table 1 – *Continued from previous page*

Membrane	**Additives**	**Proton conductivity**	**Comments**	**Authors**
Organic/ inorganic nanohybrid macro-molecules (Sol-gel)	$H_3PW_{12}O_{40}$	3×10^{-2} S cm^{-1} at 140°C and 0% RH	Fast ionic transport through the hybrid membrane Thermally stable	[271]
SPAENK	$H_3PW_{12}O_{40}$	1.5×10^{-1} S cm^{-1} at 90°C and 100% RH	Comparable conductivities with those of Nafion 117 Not really good results	[272]
Poly(styrene -co-methacrulate) - silica	$H_3PW_{12}O_{40}$	1.1 S cm^{-1} at 120°C and 100% RH 6×10^{-2} S cm^{-1} at 80°C and 60% RH	N/A	[273]
SPEEK-WC	$H_3PW_{12}O_{40}$, $H_3PMo_{12}O_{40}$ and $H_4SiW_{12}O_{40}$	(0.08-0.1) S cm^{-1} at RT	Proton conductivity of the SPEEK-WC membranes is more stable at high temperature than commercial Nafion 117	[274]
ABPI	$H_3PMo_{12}O_{40}$	3×10^{-2} S cm^{-1} at 185°C and 0% RH	Stable up to 200°C	[99]
	$H_3PMo_{12}O_{40}$	3.5×10^{-2} S cm^{-1} at 185°C and 0% RH	Stable up to 200°C	[275]
Sepoxy	$H_3PW_{12}O_{40}$	2.32×10^{-5} S cm^{-1} at 80°C and 0% RH 1.31×10^{-5} S cm^{-1} at 200°C and 0% RH	Membranes with $H_3PW_{12}O_{40}$ functioned to 200°C	[276]

References

[1] I. V. Kozhevnikov, "Advances in Catalysis by Heteropolyacids," *Russian Chemical Reviews*, vol. 56, no. 9, p. 811, 1987.

[2] G. Maksimov, E. Paukshtis, A. Budneva, R. Maksimovskaya, and V. Likholobov, "Acidity of heteropoly acids with various structures and compositions studied by IR spectroscopy of the pyridinium salts," *Russian Chemical Bulletin*, vol. 50, no. 4, pp. 587–590, 2001.

[3] R. A. Huggins, *Energy Storage*. New York: Springer, 2010.

[4] E. Council, "2030 Framework for Climate and Energy," 2014. Available at *http* : $//ec.europa.eu/energy/2030_en.htm$.

[5] S. S. Sandhu, G. W. Brutchen, and J. P. Fellner, "Lithium/air cell: Preliminary mathematical formulation and analysis," *Journal of Power Sources*, vol. 170, no. 1, pp. 196–209, 2007.

[6] H. M. A. Amin, H. Baltruschat, D. Wittmaier, and K. A. Friedrich, "A Highly Efficient Bifunctional Catalyst for Alkaline Air-Electrodes Based on a Ag and Co_3O_4 Hybrid: RRDE and Online DEMS Insights," *Electrochimica Acta*, vol. 151, no. 0, pp. 332–339, 2015.

[7] S. A. Grigoriev, P. Millet, K. A. Dzhus, H. Middleton, T. O. Saetre, and V. N. Fateev, "Design and characterization of bi-functional electrocatalytic layers for application in PEM unitized regenerative fuel cells," *International Journal of Hydrogen Energy*, vol. 35, no. 10, pp. 5070–5076, 2010.

[8] P. Millet, R. Ngameni, S. A. Grigoriev, and V. N. Fateev, "Scientific and engineering issues related to PEM technology: Water electrolysers, fuel cells and unitized regenerative systems," *International Journal of Hydrogen Energy*, vol. 36, no. 6, pp. 4156–4163, 2011.

[9] M. Maja, C. Orecchia, M. Strano, P. Tosco, and M. Vanni, "Effect of structure of the electrical performance of gas diffusion electrodes for metal air batteries," *Electrochimica Acta*, vol. 46, no. 23, pp. 423–432, 2000.

[10] L. Jörissen, "Bifunctional oxygen/air electrodes," *Journal of Power Sources*, vol. 155, no. 1, pp. 23–32, 2006.

[11] D. Linden and T. B. Reddy, *Handbook of batteries*. McGraw-Hill handbooks, New York: McGraw-Hill, 4th ed., 2011.

[12] V. Neburchilov, H. Wang, J. J. Martin, and W. Qu, "A review on air cathodes for zinc-air fuel cells," *Journal of Power Sources*, vol. 195, no. 5, pp. 1271–1291, 2010.

[13] J. Pettersson, B. Ramsey, and D. Harrison, "A review of the latest developments in electrodes for unitised regenerative polymer electrolyte fuel cells," *Journal of Power Sources*, vol. 157, no. 1, pp. 28–34, 2006.

[14] M. Ni, M. K. H. Leung, and D. Y. C. Leung, "Theoretical analysis of reversible solid oxide fuel cell based on proton-conducting electrolyte," *Journal of Power Sources*, vol. 177, no. 2, pp. 369–375, 2008.

[15] T. Burchardt, "An evaluation of electrocatalytic activity and stability for air electrodes," *Journal of Power Sources*, vol. 135, no. 12, pp. 192–197, 2004.

[16] V. Nikolova, P. Iliev, K. Petrov, T. Vitanov, E. Zhecheva, R. Stoyanova, I. Valov, and D. Stoychev, "Electrocatalysts for bifunctional oxygen/air electrodes," *Journal of Power Sources*, vol. 185, no. 2, pp. 727–733, 2008.

[17] M. Carmo, D. L. Fritz, J. Mergel, and D. Stolten, "A comprehensive review on PEM water electrolysis," *International Journal of Hydrogen Energy*, vol. 38, no. 12, pp. 4901–4934, 2013.

[18] T. Smolinka, "FUELS HYDROGEN PRODUCTION — Water Electrolysis," in *Encyclopedia of Electrochemical Power Sources* (J. Garche, ed.), pp. 394–413, Amsterdam: Elsevier, 2009.

[19] M. Kourasi, R. G. A. Wills, A. A. Shah, and F. C. Walsh, "Heteropolyacids for fuel cell applications," *Electrochimica Acta*, vol. 127, no. 0, pp. 454–466, 2014.

[20] J. B. Moffat, "Metal-oxygen clusters the surface and catalytic properties of heteropoly oxometalates." Kluwer Academic/Plenum Publishers, 2001.

[21] L. C. W. Baker and D. C. Glick, "Present General Status of Understanding of Heteropoly Electrolytes and a Tracing of Some Major Highlights in the History of Their Elucidation," *Chemical Reviews*, vol. 98, no. 1, pp. 3–50, 1998.

[22] L. Pauling, "The molecular structure of the tungstosilicates and related compounds," *Journal of the American Chemical Society*, vol. 51, no. 10, pp. 2868–2880, 1929.

[23] A. F. Wells, *Structural inorganic chemistry*. Oxford: Clarendon Press, 5th ed., 1984.

[24] D. E. Katsoulis, "A Survey of Applications of Polyoxometalates," *Chemical Reviews*, vol. 98, pp. 359–388, 1998.

[25] C. L. Hill and C. M. Prosser-McCartha, "Homogeneous catalysis by transition metal oxygen anion clusters," *Coordination Chemistry Reviews*, vol. 143, no. 0, pp. 407–455, 1995.

[26] C. L. Hill, "Introduction: PolyoxometalatesMulticomponent Molecular Vehicles To Probe Fundamental Issues and Practical Problems," *Chemical Reviews*, vol. 98, pp. 1–2, 1998.

[27] M. T. Pope and A. Mller, "Polyoxometalate Chemistry: An Old Field with New Dimensions in Several Disciplines," *Angewandte Chemie International Edition in English*, vol. 30, no. 1, pp. 34–48, 1991.

[28] M. Pope, "Polyoxo Anions: Synthesis and Structure," in *Comprehensive coordination chemistry II : from biology to nanotechnology* (J. A. McCleverty and T. J. Meyer, eds.), vol. 4, pp. 635–678, Amsterdam London: Elsevier Pergamon, 2nd ed., 2004.

[29] C. L. Hill, "Polyoxometalates: Reactivity," in *Comprehensive coordination chemistry II : from biology to nanotechnology* (J. A. McCleverty and T. J. Meyer, eds.), vol. 4, Amsterdam London: Elsevier Pergamon, 2nd ed., 2004.

[30] I. V. Kozhevnikov, "Catalysis by Heteropoly Acids and Multicomponent Polyoxometalates in Liquid-Phase Reactions," *Chemical Reviews*, vol. 98, no. 1, pp. 171–198, 1998.

[31] N. N. Greenwood and A. Earnshaw, *Chemistry of the Elements*. Oxford: Butterworth Heinemann, 2nd edition ed., 1997.

[32] R. Jansen, H. van Veldhuizen, M. Schwegler, and H. van Bekkum, "Recent (1987-1993) developments in heteropolyacid catalysts in acid catalyzed reactions and oxidation catalysis," *Recueil des Travaux Chimiques des Pays-Bas*, vol. 113, no. 3, pp. 115–135, 1994.

[33] I. K. Song and M. A. Barteau, "Redox properties of Keggin-type heteropolyacid (HPA) catalysts: effect of counter-cation, heteroatom, and polyatom substitution," *Journal of Molecular Catalysis A: Chemical*, vol. 212, no. 12, pp. 229–236, 2004.

[34] J. Wang, C. Hu, M. Jian, J. Zhang, and G. Li, "Catalytic oxidation performance of the α-Keggin-type vanadium-substituted heteropolymolybdates: A density functional theory study on $[PV_nMo_{12-n}O_{40}]^{(3+n)^-}$ (n=0-3)," *Journal of Catalysis*, vol. 240, no. 1, pp. 23–30, 2006.

[35] M. Misono, "Recent progress in the practical applications of heteropolyacid and perovskite catalysts: Catalytic technology for the sustainable society," *Catalysis Today*, vol. 144, no. 34, pp. 285–291, 2009.

[36] M. Misono, I. Ono, G. Koyano, and A. Aoshima, "Heteropolyacids. Versatile green catalysts usable in a variety of reaction media," *Pure and Applied Chemistry*, vol. 72, no. 7, pp. 1305–1311, 2000.

[37] M. Misono and N. Nojiri, "Recent progress in catalytic technology in Japan," *Appl. Catal.*, vol. 64, pp. 1–30, 1990.

[38] M. T. Pope, *Heteropoly and isopoly oxometalates*. Inorganic chemistry concepts ;, Berlin: Springer, 1983.

[39] M. Jeliki-Stankov, S. Uskokovi-Markovi, I. Holclajtner-Antunovi, M. Todorovi, and P. Djurdjevi, "Compounds of Mo, V and W in biochemistry and their biomedical activity," *Journal of Trace Elements in Medicine and Biology*, vol. 21, no. 1, pp. 8–16, 2007.

[40] D. C. Crans, "Enzyme Interactions with Labile Oxovanadates and Other Polyoxometalates," *Comments on Inorganic Chemistry*, vol. 16, no. 1-2, pp. 35–76, 1994.

[41] J. T. Rhule, C. L. Hill, D. A. Judd, and R. F. Schinazi, "Polyoxometalates in Medicine," *Chemical Reviews*, vol. 98, no. 1, pp. 327–358, 1998.

[42] U. B. Mioc, V. S. Kuntic, Z. P. Nedic, I. M. Filipovic, and S. B. Jelic, "Anticoagulant effect of tungstophosphoric acid salt studied by IR spectroscopy," *J. Serb. Chem. Soc.*, vol. 61, pp. 767–771, 1996.

[43] A. P. S. Chouhan and A. K. Sarma, "Modern heterogeneous catalysts for biodiesel production: A comprehensive review," *Renewable and Sustainable Energy Reviews*, vol. 15, no. 9, pp. 4378–4399, 2011.

[44] S. Li, Y. Wang, S. Dong, Y. Chen, F. Cao, F. Chai, and X. Wang, "Biodiesel production from Eruca Sativa Gars vegetable oil and motor, emissions properties," *Renewable Energy*, vol. 34, no. 7, pp. 1871–1876, 2009.

[45] S. Zhang, Y.-G. Zu, Y.-J. Fu, M. Luo, D.-Y. Zhang, and T. Efferth, "Rapid microwave-assisted transesterification of yellow horn oil to biodiesel using a heteropolyacid solid catalyst," *Bioresour Technol*, vol. 101, pp. 931–6, 2010.

[46] H.-C. Sheu and J.-S. Shih, "Organic ammonium ion selective electrodes based on 18-crown-6-phosphotungstic acid precipitates," *Anal. Chim. Acta*, vol. 324, pp. 125–134, 1996.

[47] C. Eppelsheim and N. Hampp, "Potentiometric thick-film sensor for the determination of the neurotransmitter acetylcholine," *Analyst*, vol. 119, pp. 2167–71, 1994.

[48] A. J. Polak and A. J. Beuhler, "Gas detection with an electrolyte membrane and solid internal reference." UOP Inc., USA ., 1985.

[49] O. Nakamura, T. Kodama, I. Ogino, and Y. Miyake, "Purification of hydrogen with a hydrogen ion-conductive solid separator." Agency of Industrial Sciences and Technology, Japan ., 1976.

[50] O. Savadogo, "Chemically and electrochemically deposited thin films for solar energy materials," *Solar Energy Materials and Solar Cells*, vol. 52, no. 34, pp. 361–388, 1998.

[51] S. Sachdeva, J. A. Turner, J. L. Horan, and A. M. Herring, "The use of heteropoly acids in proton exchange fuel cells," *Struct. Bonding (Berlin, Ger.)*, vol. 141, pp. 115–168, 2011.

[52] R. G. A. Wills, M. Kourasi, A. A. Shah, and F. C. Walsh, "Molybdophosphoric acid based nickel catalysts as bifunctional oxygen electrodes in alkaline media," *Electrochemistry Communications*, vol. 22, no. 0, pp. 174–176, 2012.

[53] O. Nakamura, T. Kodama, I. Ogino, and Y. Miyake, "High-conductivity solid proton conductors: dodecamolybdophosphoric acid and dodecatungstophosphoric acid crystals," *Chem. Lett.*, pp. 17–18, 1979.

[54] S. Bose, T. Kuila, T. X. H. Nguyen, N. H. Kim, K.-t. Lau, and J. H. Lee, "Polymer membranes for high temperature proton exchange membrane fuel cell: Recent advances and challenges," *Progress in Polymer Science*, vol. 36, no. 6, pp. 813–843, 2011.

[55] L. Zhang, S.-R. Chae, Z. Hendren, J.-S. Park, and M. R. Wiesner, "Recent advances in proton exchange membranes for fuel cell applications," *Chemical Engineering Journal*, vol. 204206, no. 0, pp. 87–97, 2012.

[56] A. Sacca, A. Carbone, R. Pedicini, M. Marrony, R. Barrera, M. Elomaa, and E. Passalacqua, "Phosphotungstic Acid Supported on a Nanopowdered ZrO_2 as a Filler in Nafion-Based Membranes for Polymer Electrolyte Fuel Cells," *Fuel Cells*, vol. 8, no. 3-4, pp. 225–235, 2008.

[57] J. Sauk, J. Byun, and H. Kim, "Composite Nafion/polyphenylene oxide (PPO) membranes with phosphomolybdic acid (PMA) for direct methanol fuel cells," *Journal of Power Sources*, vol. 143, no. 12, pp. 136–141, 2005.

[58] V. Ramani, H. R. Kunz, and J. M. Fenton, "Stabilized composite membranes and membrane electrode assemblies for elevated temperature/low relative humidity PEFC operation," *Journal of Power Sources*, vol. 152, no. 0, pp. 182–188, 2005.

[59] V. S. Bagotsky, *Fuel cells : problems and solutions*. The Electrochemical Society series, Hoboken, N.J.: Wiley, 2009.

[60] B. Tazi and O. Savadogo, "Effect of various heteropolyacids (HPAs) on the characteristics of Nafion - HPAS membranes and their H_2/O_2 polymer electrolyte fuel cell parameters," *Journal of New Materials for Electrochemical Systems*, vol. 4, pp. 187–196, 2001.

[61] B. Tazi and O. Savadogo, "Parameters of PEM fuel-cells based on new membranes fabricated from Nafion, silicotungstic acid and thiophene," *Electrochimica Acta*, vol. 45, no. 2526, pp. 4329–4339, 2000.

[62] H. Tian and O. Savadogo, "Silicotungstic Acid Nafion Composite membrane for proton-exchange membrane fuel cell operation at high temperature," *Journal of New Materials for Electrochemical Systems*, vol. 9, no. 1, pp. 61–71, 2006.

[63] V. Ramani, H. R. Kunz, and J. M. Fenton, "Investigation of Nafion/HPA composite membranes for high temperature/low relative humidity PEMFC operation," *Journal of Membrane Science*, vol. 232, no. 12, pp. 31–44, 2004.

[64] M. Amirinejad, S. S. Madaeni, M. A. Navarra, E. Rafiee, and B. Scrosati, "Preparation and characterization of phosphotungstic acid-derived salt/Nafion nanocomposite membranes for proton exchange membrane fuel cells," *Journal of Power Sources*, vol. 196, no. 3, pp. 988–998, 2011.

[65] Z.-G. Shao, P. Joghee, and I. M. Hsing, "Preparation and characterization of hybrid Nafion-silica membrane doped with phosphotungstic acid for high temperature operation of proton exchange membrane fuel cells," *Journal of Membrane Science*, vol. 229, no. 12, pp. 43–51, 2004.

[66] A. Mahreni, A. B. Mohamad, A. A. H. Kadhum, W. R. W. Daud, and S. E. Iyuke, "Nafion/silicon oxide/phosphotungstic acid nanocomposite membrane with enhanced proton conductivity," *Journal of Membrane Science*, vol. 327, no. 12, pp. 32–40, 2009.

[67] V. Ramani, H. R. Kunz, and J. M. Fenton, "Metal dioxide supported heteropolyacid/Nafion composite membranes for elevated temperature/low relative humidity PEFC operation," *Journal of Membrane Science*, vol. 279, no. 12, pp. 506–512, 2006.

[68] X.-M. Yan, P. Mei, Y. Mi, L. Gao, and S. Qin, "Proton exchange membrane with hydrophilic capillaries for elevated temperature PEM fuel cells," *Electrochemistry Communications*, vol. 11, no. 1, pp. 71–74, 2009.

[69] Z.-G. Shao, H. Xu, M. Li, and I. M. Hsing, "Hybrid Nafioninorganic oxides membrane doped with heteropolyacids for high temperature operation of proton exchange membrane fuel cell," *Solid State Ionics*, vol. 177, no. 78, pp. 779–785, 2006.

[70] Q. Wu, H. Wang, C. Yin, and G. Meng, "Preparation and performance of PVA films composited with 12-tungstogermanic heteropoly acid," *Materials Letters*, vol. 50, pp. 61–65, 2001.

[71] S. Shanmugam, B. Viswanathan, and T. K. Varadarajan, "Synthesis and characterization of silico-tungstic acid based organic-inorganic nanocomposite membrane," *Journal of Membrane Science*, vol. 275, pp. 105–109, 2006.

[72] U. Thanganathan, S. Kumar, A. Kishimoto, and K. Kimura, "Synthesis of organic/inorganic hybrid composite membranes and their structural and conductivity properties," *Materials Letters*, vol. 72, no. 0, pp. 81–87, 2012.

[73] S. M. J. Zaidi, S. D. Mikhailenko, G. P. Robertson, M. D. Guiver, and S. Kaliaguine, "Proton conducting composite membranes from polyether ether ketone and heteropolyacids for fuel cell applications," *Journal of Membrane Science*, vol. 173, no. 1, pp. 17–34, 2000.

[74] S. Y. Oh, T. Yoshida, G. Kawamura, H. Muto, M. Sakai, and A. Matsuda, "Proton conductivity and fuel cell property of composite electrolyte consisting of Cs-substituted heteropoly acids and sulfonated poly(etherether ketone)," *Journal of Power Sources*, vol. 195, no. 18, pp. 5822–5828, 2010.

[75] Y. Zhang, H. Zhang, C. Bi, and X. Zhu, "An inorganic/organic self-humidifying composite membranes for proton exchange membrane fuel cell application," *Electrochimica Acta*, vol. 53, no. 12, pp. 4096–4103, 2008.

[76] S. J. Peighambardoust, S. Rowshanzamir, M. G. Hosseini, and M. Yazdanpour, "Self-humidifying nanocomposite membranes based on sulfonated poly(ether ether ketone) and heteropolyacid supported Pt catalyst for fuel cells," *International Journal of Hydrogen Energy*, vol. 36, no. 17, pp. 10940–10957, 2011.

[77] I. Colicchio, F. Wen, H. Keul, U. Simon, and M. Moeller, "Sulfonated poly(ether ether ketone)silica membranes doped with phosphotungstic acid. Morphology and proton conductivity," *Journal of Membrane Science*, vol. 326, no. 1, pp. 45–57, 2009.

[78] M. Bello, S. M. J. Zaidi, and S. U. Rahman, "Proton and methanol transport behavior of SPEEK/TPA/MCM-41 composite membranes for fuel cell application," *Journal of Membrane Science*, vol. 322, no. 1, pp. 218–224, 2008.

[79] K. Scott, W. Taama, and J. Cruickshank, "Performance and modelling of a direct methanol solid polymer electrolyte fuel cell," *Journal of Power Sources*, vol. 65, no. 12, pp. 159–171, 1997.

[80] J. Larminie and A. Dicks, *Fuel cell systems explained*. Chichester: Wiley, 2nd ed., 2003.

[81] W. Xu, T. Lu, C. Liu, and W. Xing, "Low methanol permeable composite Nafion/silica/PWA membranes for low temperature direct methanol fuel cells," *Electrochimica Acta*, vol. 50, pp. 3280–3285, 2005.

[82] L. Li and Y. Wang, "Proton conducting composite membranes from sulfonated polyethersulfone Cardo and phosphotungstic acid for fuel cell application," *Journal of Power Sources*, vol. 162, no. 1, pp. 541–546, 2006.

[83] H. Kim and H. Chang, "Organic/inorganic hybrid membranes for direct methanol fuel cells," *Journal of Membrane Science*, vol. 288, pp. 188–194, 2007.

[84] P. Dimitrova, K. A. Friedrich, U. Stimming, and B. Vogt, "Modified Nafion-based membranes for use in direct methanol fuel cells," *Solid State Ionics*, vol. 150, pp. 115–122, 2002.

[85] Y. Xiang, M. Yang, J. Zhang, F. Lan, and S. Lu, "Phosphotungstic acid (HPW) molecules anchored in the bulk of Nafion as methanol-blocking membrane for direct methanol fuel cells," *Journal of Membrane Science*, vol. 368, no. 12, pp. 241–245, 2011.

[86] L. Li, L. Xu, and Y. Wang, "Novel proton conducting composite membranes for direct methanol fuel cell," *Materials Letters*, vol. 57, pp. 1406–1410, 2003.

[87] W. Xu, C. Liu, X. Xue, Y. Su, Y. Lu, W. Xing, and T. Lu, "New proton exchange membranes based on poly (vinyl alcohol) for DMFCs," *Solid State Ionics*, vol. 171, pp. 121–127, 2004.

[88] C. W. Lin, R. Thangamuthu, and C. J. Yang, "Proton-conducting membranes with high selectivity from phosphotungstic acid-doped poly(vinyl alcohol) for DMFC applications," *Journal of Membrane Science*, vol. 253, pp. 23–31, 2005.

[89] M. Helen, B. Viswanathan, and S. S. Murthy, "Poly(vinyl alcohol)-polyacrylamide blends with cesium salts of heteropolyacid as a polymer electrolyte for direct methanol fuel cell applications," *Journal of Applied Polymer Science*, vol. 116, pp. 3437–3447, 2010.

[90] M. Helen, B. Viswanathan, and S. S. Murthy, "Synthesis and characterization of composite membranes based on -zirconium phosphate and silicotungstic acid," *Journal of Membrane Science*, vol. 292, pp. 98–105, 2007.

[91] M. Helen, B. Viswanathan, and S. Srinivasa Murthy, "Fabrication and properties of hybrid membranes based on salts of heteropolyacid, zirconium phosphate and polyvinyl alcohol," *Journal of Power Sources*, vol. 163, no. 1, pp. 433–439, 2006.

[92] S. S. Madaeni, S. Amirinejad, and M. Amirinejad, "Phosphotungstic acid doped poly(vinyl alcohol)/poly(ether sulfone) blend composite membranes for direct methanol fuel cells," *Journal of Membrane Science*, vol. 380, no. 12, pp. 132–137, 2011.

[93] A. F. Ismail, N. H. Othman, and A. Mustafa, "Sulfonated polyether ether ketone composite membrane using tungstosilicic acid supported on silicaaluminium oxide for direct methanol fuel cell (DMFC)," *Journal of Membrane Science*, vol. 329, no. 12, pp. 18–29, 2009.

[94] M. L. Ponce, L. A. S. de A. Prado, V. Silva, and S. P. Nunes, "Membranes for direct methanol fuel cell based on modified heteropolyacids," *Desalination*, vol. 162, no. 0, pp. 383–391, 2004.

[95] H. Doğan, T. Y. Inan, E. Unveren, and M. Kaya, "Effect of cesium salt of tungstophosphoric acid (Cs-TPA) on the properties of sulfonated polyether ether ketone (SPEEK) composite membranes for fuel cell applications," *International Journal of Hydrogen Energy*, vol. 35, no. 15, pp. 7784–7795, 2010.

[96] M. Chojak, A. Kolary-Zurowska, R. Wlodarczyk, K. Miecznikowski, K. Karnicka, B. Palys, R. Marassi, and P. J. Kulesza, "Modification of Pt nanoparticles with polyoxometallate monolayers: Competition between activation and blocking of reactive sites for the electrocatalytic oxygen reduction," *Electrochimica Acta*, vol. 52, no. 18, pp. 5574–5581, 2007.

[97] A. A. Gewirth and M. S. Thorum, "Electroreduction of Dioxygen for Fuel-Cell Applications: Materials and Challenges," *Inorganic Chemistry*, vol. 49, no. 8, pp. 3557–3566, 2010.

[98] H. A. Gasteiger, S. S. Kocha, B. Sompalli, and F. T. Wagner, "Activity benchmarks and requirements for Pt, Pt-alloy, and non-Pt oxygen reduction catalysts for PEMFCs," *Applied Catalysis B: Environmental*, vol. 56, no. 12, pp. 9–35, 2005.

[99] P. Gómez-Romero, J. A. Asensio, and S. Borrós, "Hybrid proton-conducting membranes for polymer electrolyte fuel cells: Phosphomolybdic acid doped poly(2,5-benzimidazole)-(ABPBI-$H_3PMo_{12}O_{40}$)," *Electrochimica Acta*, vol. 50, no. 24, pp. 4715–4720, 2005.

[100] A. A. Shah, T. R. Ralph, and F. C. Walsh, "Modeling and Simulation of the Degradation of Perfluorinated Ion-Exchange Membranes in PEM Fuel Cells," *Journal of the Electrochemical Society*, vol. 156, no. 4, pp. B465–B484, 2009.

[101] R. Wlodarczyk, M. Chojak, K. Miecznikowski, A. Kolary, P. J. Kulesza, and R. Marassi, "Electroreduction of oxygen at polyoxometallate-modified glassy carbon-supported Pt nanoparticles," *Journal of Power Sources*, vol. 159, no. 2, pp. 802–809, 2006.

[102] R. Wlodarczyk, A. Kolary-Zurowska, R. Marassi, M. Chojak, and P. J. Kulesza, "Enhancement of oxygen reduction by incorporation of heteropolytungstate into the electrocatalytic ink of carbon supported platinum nanoparticles," *Electrochimica Acta*, vol. 52, no. 12, pp. 3958–3964, 2007.

[103] M. I. Borzenko, M. Chojak, P. J. Kulesza, G. A. Tsirlina, and O. A. Petrii, "Platinization assisted by Keggin-type heteropolytungstates," *Electrochimica Acta*, vol. 48, no. 2526, pp. 3797–3804, 2003.

[104] A. Damjanovic, M. A. Genshaw, and J. O. Bockris, "Distinction between Intermediates Produced in Main and Side Electrodic Reactions," *The Journal of Chemical Physics*, vol. 45, no. 11, pp. 4057–4059, 1966.

[105] H. S. Wroblowa, P. Yen Chi, and G. Razumney, "Electroreduction of oxygen: A new mechanistic criterion," *Journal of Electroanalytical Chemistry and Interfacial Electrochemistry*, vol. 69, no. 2, pp. 195–201, 1976.

[106] A. J. Appleby, "Electrocatalysis and fuel cells," *Catalysis Reviews*, vol. 4, no. 1, pp. 221–244, 1971.

[107] R. J. Stanis, M.-C. Kuo, A. J. Rickett, J. A. Turner, and A. M. Herring, "Investigation into the activity of heteropolyacids towards the oxygen reduction reaction on PEMFC cathodes," *Electrochimica Acta*, vol. 53, no. 28, pp. 8277–8286, 2008.

[108] R. P. Brooker, P. Baker, H. R. Kunz, L. J. Bonville, and R. Parnas, "Effects of Silicotungstic Acid Addition to the Electrodes of Polymer Electrolyte Membrane Fuel Cells," *Journal of the Electrochemical Society*, vol. 156, no. 11, pp. B1317–B1321, 2009.

[109] S. Dsoke, A. Kolary-Zurowska, A. Zurowski, P. Mignini, P. J. Kulesza, and R. Marassi, "Rotating disk electrode study of $Cs_{2.5}H_{0.5}PW_{12}O_{40}$ as mesoporous support for Pt nanoparticles for PEM fuel cells electrodes," *Journal of Power Sources*, vol. 196, no. 24, pp. 10591–10600, 2011.

[110] M.-C. Kuo, B. R. Limoges, R. J. Stanis, J. A. Turner, and A. M. Herring, "The use of the heteropoly acids,$H_5PMo_{10}V_2O_{40}$, $H_7[P_2W_{17}O_{61}(Fe^{III} \cdot OH_2)]$ or $H_{12}[(P_2W_{15}O_{56})_2Fe_4^{III}(H_2O)_2]$, in the anode catalyst layer of a proton exchange membrane fuel cell," *Journal of Power Sources*, vol. 171, no. 2, pp. 517–523, 2007.

[111] I. Gatto, A. Saccà, A. Carbone, R. Pedicini, F. Urbani, and E. Passalacqua, "CO-tolerant electrodes developed with PhosphoMolybdic Acid for Polymer Electrolyte Fuel Cell (PEFCs) application," *Journal of Power Sources*, vol. 171, no. 2, pp. 540–545, 2007.

[112] R. J. Stanis, M.-C. Kuo, J. A. Turner, and A. M. Herring, "Use of W, Mo, and V Substituted Heteropolyacids for CO Mitigation in PEMFCs," *Journal of the Electrochemical Society*, vol. 155, no. 2, pp. B155–B162, 2008.

[113] E. G. Zhizhina, L. I. Kuznetsova, R. I. Maksimovskaya, S. N. Pavlova, and K. I. Matveev, "Oxidation of CO to CO_2 by heteropolyacids in the presence of palladium," *Journal of Molecular Catalysis*, vol. 38, no. 3, pp. 345–353, 1986.

[114] W. B. Kim, T. Voitl, G. J. Rodriguez-Rivera, S. T. Evans, and J. A. Dumesic, "Preferential Oxidation of CO in H_2 by Aqueous Polyoxometalates over Metal Catalysts," *Angewandte Chemie International Edition*, vol. 44, no. 5, pp. 778–782, 2005.

[115] B. R. Limoges, R. J. Stanis, J. A. Turner, and A. M. Herring, "Electrocatalyst materials for fuel cells based on the polyoxometalates," *Electrochimica Acta*, vol. 50, no. 5, pp. 1169–1179, 2005.

[116] A. Creeth, "Pt-free PEM cathode technology with fundamental durability benefits: FlowCath," *Fuel Cells Bulletin*, vol. 2011, no. 4, pp. 12–15, 2011.

[117] R. Singh, A. A. Shah, A. Potter, B. Clarkson, A. Creeth, C. Downs, and F. C. Walsh, "Performance and analysis of a novel polymer electrolyte membrane fuel cell using a solution based redox mediator," *Journal of Power Sources*, vol. 201, no. 0, pp. 159–163, 2012.

[118] T. Maiyalagan, "Silicotungstic acid stabilized PtRu nanoparticles supported on carbon nanofibers electrodes for methanol oxidation," *International Journal of Hydrogen Energy*, vol. 34, no. 7, pp. 2874–2879, 2009.

[119] A. Zurowski, A. Kolary-Zurowska, S. Dsoke, P. J. Barczuk, R. Marassi, and P. J. Kulesza, "Activation of carbon-supported platinum nanoparticles by zeolite-type cesium salts of polyoxometallates of molybdenum and tungsten towards more efficient electrocatalytic oxidation of methanol and ethanol," *Journal of Electroanalytical Chemistry*, vol. 649, no. 12, pp. 238–247, 2010.

[120] A. A. Shah, P. C. Sui, G. S. Kim, and S. Ye, "A transient PEMFC model with CO poisoning and mitigation by O_2 bleeding and Ru-containing catalyst," *Journal of Power Sources*, vol. 166, no. 1, pp. 1–21, 2007.

[121] J. S. Spendelow, P. K. Babu, and A. Wieckowski, "Electrocatalytic oxidation of carbon monoxide and methanol on platinum surfaces decorated with ruthenium," *Current Opinion in Solid State and Materials Science*, vol. 9, no. 12, pp. 37–48, 2005.

[122] M. J. Pollard, B. A. Weinstock, T. E. Bitterwolf, P. R. Griffiths, A. Piers Newbery, and J. B. Paine Iii, "A mechanistic study of the low-temperature conversion of carbon monoxide to carbon dioxide over a cobalt oxide catalyst," *Journal of Catalysis*, vol. 254, no. 2, pp. 218–225, 2008.

[123] Z. Cui, W. Xing, C. Liu, D. Tian, and H. Zhang, "Synthesis and characterization of $H_5PMo_{10}V_2O_{40}$ deposited Pt/C nanocatalysts for methanol electrooxidation," *Journal of Power Sources*, vol. 195, no. 6, pp. 1619–1623, 2010.

[124] L. Feng, Q. Lv, X. Sun, S. Yao, C. Liu, and W. Xing, "Enhanced activity of molybdovanadophosphoric acid modified Pt electrode for the electrooxidation of methanol," *Journal of Electroanalytical Chemistry*, vol. 664, no. 0, pp. 14–19, 2012.

[125] J. R. Ferrell III, M.-C. Kuo, J. A. Turner, and A. M. Herring, "The use of the heteropoly acids, $H_3PMo_{12}O_{40}$ and $H_3PW_{12}O_{40}$, for the enhanced electrochemical oxidation of methanol for direct methanol fuel cells," *Electrochimica Acta*, vol. 53, no. 14, pp. 4927–4933, 2008.

[126] K.-Y. Chan, J. Ding, J. Ren, S. Cheng, and K. Y. Tsang, "Supported mixed metal nanoparticles as electrocatalysts in low temperature fuel cells," *J. Mater. Chem.*, vol. 14, pp. 505–516, 2004.

[127] H. Li, X. Zhang, H. Pang, C. Huang, and J. Chen, "PMo_{12}-functionalized graphene nanosheet-supported PtRu nanocatalysts for methanol electro-oxidation," *J. Solid State Electrochem.*, vol. 14, pp. 2267–2274, 2010.

[128] S. Li, X. Yu, G. Zhang, Y. Ma, J. Yao, and P. de Oliveira, "Green synthesis of a Pt nanoparticle/polyoxometalate/carbon nanotube tri-component hybrid and its activity in the electrocatalysis of methanol oxidation," *Carbon*, vol. 49, no. 6, pp. 1906–1911, 2011.

[129] D. Pan, J. Chen, W. Tao, L. Nie, and S. Yao, "Polyoxometalate-Modified Carbon Nanotubes: New Catalyst Support for Methanol Electro-oxidation," *Langmuir*, vol. 22, no. 13, pp. 5872–5876, 2006.

[130] M. H. Seo, S. M. Choi, H. J. Kim, J. H. Kim, B. K. Cho, and W. B. Kim, "A polyoxometalate-deposited Pt/CNT electrocatalyst via chemical synthesis for methanol electrooxidation," *Journal of Power Sources*, vol. 179, no. 1, pp. 81–86, 2008.

[131] X. Jin, B. He, J. Miao, J. yuan, Q. Zhang, and L. Niu, "Stabilization and dispersion of PtRu and Pt nanoparticles on multiwalled carbon nanotubes using phosphomolybdic acid, and the use of the resulting materials in a direct methanol fuel cell," *Carbon*, vol. 50, no. 8, pp. 3083–3091, 2012.

[132] S. Guo, S. Dong, and E. Wang, "Constructing Carbon Nanotube/Pt Nanoparticle Hybrids Using an Imidazolium-Salt-Based Ionic Liquid as a Linker," *Advanced Materials*, vol. 22, no. 11, pp. 1269–1272, 2010.

[133] X. Hu, T. Wang, L. Wang, S. Guo, and S. Dong, "A General Route to Prepare One- and Three-Dimensional Carbon Nanotube/Metal Nanoparticle Composite Nanostructures," *Langmuir*, vol. 23, pp. 6352–6357, 2007.

[134] P. J. Barczuk, A. Lewera, K. Miecznikowski, A. Zurowski, and P. J. Kulesza, "Enhancement of catalytic activity of platinum-based nanoparticles towards electrooxidation of ethanol through interfacial modification with heteropolymolybdates," *Journal of Power Sources*, vol. 195, no. 9, pp. 2507–2513, 2010.

[135] J. R. Ferrell Iii, M.-C. Kuo, and A. M. Herring, "Direct dimethyl-ether proton exchange membrane fuel cells and the use of heteropolyacids in the anode catalyst layer for enhanced dimethyl ether oxidation," *Journal of Power Sources*, vol. 195, no. 1, pp. 39–45, 2010.

[136] J. Wu, X. Z. Yuan, J. J. Martin, H. Wang, J. Zhang, J. Shen, S. Wu, and W. Merida, "A review of PEM fuel cell durability: Degradation mechanisms and mitigation strategies," *Journal of Power Sources*, vol. 184, no. 1, pp. 104–119, 2008.

[137] J. O. Bockris and T. Otagawa, "The Electrocatalysis of Oxygen Evolution on Perovskites," *Journal of the Electrochemical Society*, vol. 131, no. 2, pp. 290–302, 1984. 10.1149/1.2115565.

[138] J. O. Bockris, T. Otagawa, and V. Young, "Solid state surface studies of the electrocatalysis of oxygen evolution on perovskites," *Journal of Electroanalytical Chemistry and Interfacial Electrochemistry*, vol. 150, no. 12, pp. 633–643, 1983.

[139] R. Othman, A. L. Dicks, and Z. Zhu, "Non precious metal catalysts for the PEM fuel cell cathode," *International Journal of Hydrogen Energy*, vol. 37, no. 1, pp. 357–372, 2012.

[140] L. L. Swette, A. B. LaConti, and S. A. McCatty, "Proton-exchange membrane regenerative fuel cells," *Journal of Power Sources*, vol. 47, no. 3, pp. 343–351, 1994.

[141] T. Ioroi, T. Oku, K. Yasuda, N. Kumagai, and Y. Miyazaki, "Influence of PTFE coating on gas diffusion backing for unitized regenerative polymer electrolyte fuel cells," *J. Power Sources*, vol. 124, pp. 385–389, 2003.

[142] A. Cisar, O. J. Murphy, and B. Clarke, "Bifunctional catalytic electrode," 01 2005. Patent US 6,838,205 B2.

[143] S. Altmann, T. Kaz, and K. A. Friedrich, "Bifunctional electrodes for unitized regenerative fuel cells," *Electrochim. Acta*, vol. 56, pp. 4287–4293, 2011.

[144] G. Chen, D. A. Delafuente, S. Sarangapani, and T. E. Mallouk, "Combinatorial discovery of bifunctional oxygen reduction water oxidation electrocatalysts for regenerative fuel cells," *Catalysis Today*, vol. 67, no. 4, pp. 341–355, 2001.

[145] J. Garche, *Encyclopedia of electrochemical power sources Vol. 1.* Amsterdam [u.a.]: Elsevier, 2009. ed.-in-chief Jrgen Garche ... Ill., graph. Darst. Literaturangaben.

[146] A. Seghiouer, J. Chevalet, A. Barhoun, and F. Lantelme, "Electrochemical oxidation of nickel in alkaline solutions: a voltammetric study and modelling," *Journal of Electroanalytical Chemistry*, vol. 442, no. 12, pp. 113–123, 1998.

[147] L. Swette, N. Kackley, and S. A. McCatty, "Oxygen electrodes for rechargeable alkaline fuel cells. III," *Journal of Power Sources*, vol. 36, no. 3, pp. 323–339, 1991.

[148] Y. Zhan, C. Xu, M. Lu, Z. Liu, and J. Y. Lee, "Mn and Co co-substituted Fe_3O_4 nanoparticles on nitrogen-doped reduced graphene oxide for oxygen electrocatalysis in alkaline solution," *Journal of Materials Chemistry A*, vol. 2, no. 38, pp. 16217–16223, 2014.

[149] H. Arai, S. Mller, and O. Haas, "AC Impedance Analysis of Bifunctional Air Electrodes for Metal-Air Batteries," *Journal of the Electrochemical Society*, vol. 147, no. 10, pp. 3584–3591, 2000. 10.1149/1.1393943.

[150] A. K. Shukla, A. M. Kannan, M. S. Hegde, and J. Gopalakrishnan, "Effect of counter cations on electrocatalytic activity of oxide pyrochlores towards oxygen reduction/evolution in alkaline medium: an electrochemical and spectroscopic study," *Journal of Power Sources*, vol. 35, no. 2, pp. 163–173, 1991.

[151] J. Prakash, D. A. Tryk, W. Aldred, and E. B. Yeager, "Investigations of ruthenium pyrochlores as bifunctional oxygen electrodes," *Journal of Applied Electrochemistry*, vol. 29, no. 12, pp. 1463–1469, 1999.

[152] F. Švegl, B. Orel, I. Grabec-Švegl, and V. Kaučič, "Characterization of spinel Co_3O_4 and Li-doped Co_3O_4 thin film electrocatalysts prepared by the solgel route," *Electrochimica Acta*, vol. 45, no. 2526, pp. 4359–4371, 2000.

[153] C. K. Lee, K. A. Striebel, F. R. McLarnon, and E. J. Cairns, "Thermal Treatment of La0.6Ca0.4CoO3 Perovskites for Bifunctional Air Electrodes," *Journal of the Electrochemical Society*, vol. 144, no. 11, pp. 3801–3806, 1997.

[154] C. Davidson, G. Kissel, and S. Srinivasan, "Electrode kinetics of the oxygen evolution reaction at $NiCo_2O_4$ from 30% KOH.: Dependence on temperature," *Journal of Electroanalytical Chemistry and Interfacial Electrochemistry*, vol. 132, no. 0, pp. 129–135, 1982.

[155] Y. Shao-Horn, W. Sheng, S. Chen, P. Ferreira, E. Holby, and D. Morgan, "Instability of Supported Platinum Nanoparticles in Low-Temperature Fuel Cells," *Topics in Catalysis*, vol. 46, no. 3, pp. 285–305, 2007.

[156] Y.-J. Wang, D. P. Wilkinson, and J. Zhang, "Noncarbon Support Materials for Polymer Electrolyte Membrane Fuel Cell Electrocatalysts," *Chemical Reviews*, vol. 111, no. 12, pp. 7625–7651, 2011.

[157] S. Velraj and J. H. Zhu, "Cycle life limit of carbon-based electrodes for rechargeable metalair battery application," *Journal of Electroanalytical Chemistry*, vol. 736, no. 0, pp. 76–82, 2015.

[158] N. Staud and P. N. Ross, "The Corrosion of Carbon Black Anodes in Alkaline Electrolyte: II . Acetylene Black and the Effect of Oxygen Evolution Catalysts on Corrosion," *Journal of the Electrochemical Society*, vol. 133, no. 6, pp. 1079–1084, 1986.

[159] P. N. Ross and M. Sattler, "The Corrosion of Carbon Black Anodes in Alkaline Electrolyte: III . The Effect of Graphitization on the Corrosion Resistance of Furnace Blacks," *Journal of the Electrochemical Society*, vol. 135, no. 6, pp. 1464–1470, 1988.

[160] N. Staud, H. Sokol, and P. N. Ross, "The Corrosion of Carbon Black Anodes in Alkaline Electrolyte: IV . Current Efficiencies for Oxygen Evolution from Metal OxideImpregnated Graphitized Furnace Blacks," *Journal of the Electrochemical Society*, vol. 136, no. 12, pp. 3570–3576, 1989. 10.1149/1.2096511.

[161] S. Müller, F. Holzer, H. Arai, and O. Haas, "A study of carbon-catalyst interaction in bifunctional air electrodes for zinc-air batteries," *Journal of New Materials for Electrochemical Systems*, vol. 2, no. 4, pp. 227–232, 1999.

[162] E. Antolini and E. R. Gonzalez, "Ceramic materials as supports for low-temperature fuel cell catalysts," *Solid State Ionics*, vol. 180, no. 910, pp. 746–763, 2009.

[163] P. N. Ross and H. Sokol, "The Corrosion of Carbon Black Anodes in Alkaline Electrolyte: I . Acetylene Black and the Effect of Cobalt Catalyzation," *Journal of the Electrochemical Society*, vol. 131, no. 8, pp. 1742–1750, 1984.

[164] S. W. T. Price, S. J. Thompson, X. Li, S. F. Gorman, D. Pletcher, A. E. Russell, F. C. Walsh, and R. G. A. Wills, "The fabrication of a bifunctional oxygen electrode without carbon components for alkaline secondary batteries," *Journal of Power Sources*, vol. 259, no. 0, pp. 43–49, 2014.

[165] X. Li, A. L. Zhu, W. Qu, H. Wang, R. Hui, L. Zhang, and J. Zhang, "Magnéli phase Ti_4O_7 electrode for oxygen reduction reaction and its implication for zinc-air rechargeable batteries," *Electrochimica Acta*, vol. 55, no. 20, pp. 5891–5898, 2010.

[166] G. Chen, S. R. Bare, and T. E. Mallouk, "Development of Supported Bifunctional Electrocatalysts for Unitized Regenerative Fuel Cells," *Journal of the Electrochemical Society*, vol. 149, no. 8, pp. A1092–A1099, 2002.

[167] E. E. Farndon and D. Pletcher, "Studies of platinized Ebonex electrodes," *Electrochimica Acta*, vol. 42, no. 8, pp. 1281–1285, 1997.

[168] F. C. Walsh and R. G. A. Wills, "The continuing development of Magnéli phase titanium sub-oxides and Ebonex electrodes," *Electrochimica Acta*, vol. 55, no. 22, pp. 6342–6351, 2010.

[169] V. Rashkova, S. Kitova, and T. Vitanov, "Electrocatalytic behavior of thin CoTeO films in oxygen evolution and reduction reactions," *Electrochimica Acta*, vol. 52, no. 11, pp. 3794–3803, 2007.

[170] P. Paunović, O. Popovski, E. Fidanevska, B. Ranguelov, D. Stoevska Gogovska, A. T. Dimitrov, and S. Hadi Jordanov, "Co-Magnéli phases electrocatalysts for hydrogen/oxygen evolution," *International Journal of Hydrogen Energy*, vol. 35, no. 19, pp. 10073–10080, 2010.

[171] J. R. Smith, F. C. Walsh, and R. L. Clarke, "Electrodes based on Magnéli phase titanium oxides: the properties and applications of Ebonex® materials," *Journal of Applied Electrochemistry*, vol. 28, no. 10, pp. 1021–1033, 1998.

[172] L. Vračar, S. Gojković, N. Elezović, V. Radmilović, M. Jakšić, and N. Krstajić, "Magnéli Phase Titanium Oxides as Catalyst Support - Electrochemical Behavior of Ebonex/Pt Catalysts," *Journal of New Materials for Electrochemical Systems*, vol. 9, pp. 99–106, 2006.

[173] B. May and D. Hodgson, "Fuel cells and fuel cell plates," 2004. Patent US 6,790,554B4.

[174] A. at: *http* : *//www.atraverda.com/*. Last accessed on 2nd of June 2013.

[175] A. J. Bard and L. R. Faulkner, *Electrochemical methods : fundamentals and applications*. New York ; Chichester: John Wiley, 2nd ed., 2001. 00038210 GBA18197 Allen J. Bard, Larry R. Faulkner. ill. ; 26 cm. Previous ed.: New York : Wiley, 1980. Includes bibliographical references and index.

[176] D. Pletcher, *A first course in electrode processes*. Cambridge: Royal Society of Chemistry, 2nd ed., 2009.

[177] C. M. A. B. A. M. O. Brett, *Electrochemistry. Principles, Methods and Applications*. Oxford University Press, 1993.

[178] R. S. Nicholson, "Theory and Application of Cyclic Voltammetry for Measurement of Electrode Reaction Kinetics.," *Analytical Chemistry*, vol. 37, no. 11, pp. 1351–1355, 1965.

[179] R. G. A. Wills, M. J. Watt-Smith, and F. C. Walsh, "The Use of Fluorocarbon Surfactants to Improve the Manufacture of PEM Fuel Cell Electrodes," *Fuel Cells*, vol. 9, no. 2, pp. 148–156, 2009.

[180] M. Marignac, "Recherches sur les acides silicotungstiques et note sur la constitution de l'acide tungstique," *Annales De Chimie et de Physique*, vol. 3, pp. 1–74, 1864.

[181] K. Eguchi, T. Seiyama, N. Yamazoe, S. Katsuki, and H. Taketa, "Electronic structures of $XMo_{12}O_{40}$ heteropolyanions (X = P, As, Si, and Ge) and their reduction behavior," *Journal of Catalysis*, vol. 111, no. 2, pp. 336–344, 1988.

[182] M. T. Pope and G. M. Varga, "Heteropoly Blues. I. Reduction Stoichiometries and Reduction Potentials of Some 12-Tungstates," *Inorganic Chemistry*, vol. 5, no. 7, pp. 1249–1254, 1966.

[183] C. Rocchiccioli-Deltcheff, A. Aouissi, M. M. Bettahar, S. Launay, and M. Fournier, "Catalysis by 12-Molybdophosphates: 1. Catalytic Reactivity of 12-Molybdophosphoric Acid Related to Its Thermal Behavior Investigated through IR, Raman, Polarographic, and X-ray Diffraction Studies: A Comparison with 12-Molybdosilicic Acid," *Journal of Catalysis*, vol. 164, no. 1, pp. 16–27, 1996.

[184] B. Keta and L. Nadjo, "Activation of electrode surfaces: Application to the lectrocatalysis of the hydrogen evolution reaction," *Journal of Electroanalytical Chemistry and Interfacial Electrochemistry*, vol. 191, no. 2, pp. 441–448, 1985.

[185] J. H. Choi, T. H. Kang, J. H. Song, Y. Bang, and I. K. Song, "Redox behavior and oxidation catalysis of $H_nXW_{12}O_{40}$ (X=Co^{2+},B^{3+},Si^{4+}, and P^{5+}) Keggin heteropolyacid catalysts," *Catalysis Communications*, vol. 43, no. 0, pp. 155–158, 2014.

[186] M. Sadakane and E. Steckhan, "Electrochemical Properties of Polyoxometalates as Electrocatalysts," *Chemical Reviews*, vol. 98, no. 1, pp. 219–238, 1998.

[187] F. A. R. S. Couto, A. M. V. Cavaleiro, J. D. Pedrosa de Jesus, and J. E. J. Simo, "Study of polyoxotungstates with the Keggin structure by cyclic voltammetry," *Inorganica Chimica Acta*, vol. 281, no. 2, pp. 225–228, 1998.

[188] B. Keita and L. Nadjo, "New aspects of the electrochemistry of Heteropolyacids. Part II. Coupled electron and proton transfers in the reduction of silicotungstic species," *Journal of Electroanalytical Chemistry*, vol. 217, pp. 287–304, 1987.

[189] C. Rong and F. C. Anson, "Spontaneous adsorption of heteropolytungstates and heteropolymolybdates on the surfaces of solid electrodes and the electrocatalytic activity of the adsorbed anions," *Inorganica Chimica Acta*, vol. 242, no. 12, pp. 11–16, 1996.

[190] S. Himeno, T. Osakai, and A. Saito, "Voltammetric Characterization of α- and β-Dodecamolybdophosphates in Aqueous Organic Solutions," *Bulletin of the Chemical Society of Japan*, vol. 62, no. 4, pp. 1335–1337, 1989.

[191] B. Keita and L. Nadjo, "Surface modifications with heteropoly and isopoly oxometalates: Part V. Electrocatalysis of the HER in alkaline solution," *Journal of Electroanalytical Chemistry and Interfacial Electrochemistry*, vol. 287, no. 1, pp. 149–157, 1990.

[192] S. Himeno, M. Takamoto, and T. Ueda, "Cation effects on the voltammetric behavior of α-Keggin-type $[SiMo_{12}O_{40}]_4$ and $[PMo_{12}O_{40}]_3$ complexes in CH_3COCH_3 and CH_3CN," *Journal of Electroanalytical Chemistry*, vol. 485, no. 1, pp. 49–54, 2000.

[193] J. J. Altenau, M. T. Pope, R. A. Prados, and H. So, "Models for heteropoly blues. Degrees of valence trapping in Vanadium(IV)- and Molybdenum(V)-substituted Keggin anions," *Inorganic Chemistry*, vol. 14, no. 2, pp. 417–421, 1975.

[194] D. R. Park, J. H. Song, S. H. Lee, S. H. Song, H. Kim, J. C. Jung, and I. K. Song, "Redox properties of $H_3PMo_xW_{12x}O_{40}$ and $H_6P_2Mo_xW_{18x}O_{62}$ heteropolyacid catalysts and their catalytic activity for benzyl alcohol oxidation," *Applied Catalysis A: General*, vol. 349, no. 12, pp. 222–228, 2008.

[195] J. N. Barrows and M. T. Pope, "Intramolecular Electron Transfer and Electron Delocalization in Molybdophosphate Heteropoly Anions," in *Electron Transfer in Biology and the Solid State*, vol. 226 of *Advances in Chemistry*, ch. 21, pp. 403–417, American Chemical Society, 1989.

[196] G. McGarvey and J. B. Moffat, "A study of solution species generated during the formation of 12-heteropoly oxometalate catalysts," *Journal of Molecular Catalysis*, vol. 69, pp. 137–155, 1991.

[197] I. K. Song and M. A. Barteau, "Bulk redox properties of heteropolyacids determined from surface properties of nanostructured heteropolyacid monolayers," *Journal of Molecular Catalysis A: Chemical*, vol. 182183, no. 0, pp. 185–193, 2002.

[198] X. Lopez, J. J. Carbo, C. Bo, and J. M. Poblet, "Structure, properties and reactivity of polyoxometalates: a theoretical perspective," *Chemical Society Reviews*, vol. 41, no. 22, pp. 7537–7571, 2012.

[199] X. Lopez, J. A. Fernandez, and J. M. Poblet, "Redox properties of polyoxometalates: new insights on the anion charge effect," *Dalton Transactions*, vol. 9, pp. 1162–1167, 2006.

[200] J. C. Védrine and J.-M. M. Millet, "Heteropolyoxometallate Catalysts for Partial Oxidation," in *Metal Oxide Catalysis*, pp. 561–594, Wiley-VCH Verlag GmbH & Co. KGaA, 2009.

[201] I. V. Kozhevnikov, *Catalysis by Polyoxometalates*, vol. 2 of *Catalysts for Fine Chemical Synthesis*. Chichester: John Wiley & Sons Ltd, 2002.

[202] B. Keita and L. Nadjo, "New aspects of the electrochemistry of heteropolyacids. Part IV. Acidity dependent cyclic voltammetric behaviour of phosphotungstic and silicotungstic heteropolyanions in water and N,N-dimenthylformamide," *Journal of Electroanalytical Chemistry*, vol. 227, pp. 77–98, 1987.

[203] A. A. Grinberg, *An Introduction to the Chemistry of Complex Compounds*. Leipzig: Pergamon Press, 1962.

[204] D. Hall, C. Bock, and B. MacDougall, "The Electrochemistry of Metallic Nickel: Oxides. Hydroxides, Hydrides and Alkaline Hydrogen Evolution," *Journal of The Electrochemical Society*, vol. 160, no. 3, pp. F235–F243, 2013.

[205] G. A. Tsigdinos, "Preparation and Characterization of 12-Molybdophosphoric and 12-Molybdosilicic Acids and Their Metal Salts," *Industrial and Engineering Chemistry Product Research and Development*, vol. 13, no. 4, pp. 267–274, 1974.

[206] K. Provazi, M. J. Giz, L. H. Dall'Antonia, and S. I. Crdoba de Torresi, "The effect of Cd, Co, and Zn as additives on nickel hydroxide opto-electrochemical behavior," *Journal of Power Sources*, vol. 102, no. 12, pp. 224–232, 2001.

[207] T. Ioroi, T. Akita, M. Asahi, S.-i. Yamazaki, Z. Siroma, N. Fujiwara, and K. Yasuda, "Platinum-titanium alloy catalysts on a Magnéli-phase titanium oxide support for improved durability in Polymer Electrolyte Fuel Cells," *Journal of Power Sources*, vol. 223, no. 0, pp. 183–189, 2013.

[208] S. S. Dihrab, K. Sopian, M. A. Alghoul, and M. Y. Sulaiman, "Review of the membrane and bipolar plates materials for conventional and unitized regenerative fuel cells," *Renewable and Sustainable Energy Reviews*, vol. 13, no. 67, pp. 1663–1668, 2009.

[209] R. Taherian, "A review of composite and metallic bipolar plates in proton exchange membrane fuel cell: Materials, fabrication, and material selection," *Journal of Power Sources*, vol. 265, no. 0, pp. 370–390, 2014.

[210] J. Andrews and A. K. Doddathimmaiah, "9 - Regenerative fuel cells," in *Materials for Fuel Cells* (M. Gasik, ed.), pp. 344–385, Woodhead Publishing, 2008.

[211] V. V. Nikam and R. G. Reddy, "Corrugated bipolar sheets as fuel distributors in PEMFC," *International Journal of Hydrogen Energy*, vol. 31, no. 13, pp. 1863–1873, 2006.

[212] S. Joseph, J. C. McClure, R. Chianelli, P. Pich, and P. J. Sebastian, "Conducting polymer-coated stainless steel bipolar plates for proton exchange membrane fuel cells (PEMFC)," *International Journal of Hydrogen Energy*, vol. 30, no. 12, pp. 1339–1344, 2005.

[213] H. Wang, G. Teeter, and J. Turner, "Investigation of a Duplex Stainless Steel as Polymer Electrolyte Membrane Fuel Cell Bipolar Plate Material," *Journal of the Electrochemical Society*, vol. 152, no. 3, pp. B99–B104, 2005.

[214] H. Wang and J. A. Turner, "Ferritic stainless steels as bipolar plate material for polymer electrolyte membrane fuel cells," *Journal of Power Sources*, vol. 128, no. 2, pp. 193–200, 2004.

[215] M. Gardon, S. Dosta, J. M. Guilemany, M. Kourasi, B. Mellor, and R. Wills, "Improved, high conductivity titanium sub-oxide coated electrodes obtained by Atmospheric Plasma Spray," *Journal of Power Sources*, vol. 238, no. 0, pp. 430–434, 2013.

[216] J. E. Graves, D. Pletcher, R. L. Clarke, and F. C. Walsh, "The electrochemistry of Magnéli phase titanium oxide ceramic electrodes Part I. The deposition and properties of metal coatings," *Journal of Applied Electrochemistry*, vol. 21, no. 10, pp. 848–857, 1991.

[217] M. Amjad and D. Pletcher, "Simple redox processes at tungsten bronze electrodes," *Journal of Electroanalytical Chemistry and Interfacial Electrochemistry*, vol. 59, no. 1, pp. 61–67, 1975.

[218] M. Gardon and J. M. Guilemany, "A review on fabrication, sensing mechanisms and performance of metal oxide gas sensors," *Journal of Materials Science: Materials in Electronics*, vol. 24, no. 5, pp. 1410–1421, 2013.

[219] J. R. Calvert and R. A. Farrar, *An engineering data book*. Basingstoke: Palgrave Macmillan, 3rd ed., 2008.

[220] G. Nikiforidis, L. Berlouis, D. Hall, and D. Hodgson, "Impact of electrolyte composition on the performance of the zinccerium redox flow battery system," *Journal of Power Sources*, vol. 243, no. 0, pp. 691–698, 2013.

[221] Entegris®, "Cell stack plates." Available at *http* : *//www.entegris.com/Resources/assets/*6002 − 2153 − 0312*.pdf* Last accessed 8th of December.

[222] L.-g. Xia, A.-j. Li, W.-q. Wang, Q. Yin, H. Lin, and Y.-b. Zhao, "Effects of resin content and preparing conditions on the properties of polyphenylene sulfide resin/graphite composite for bipolar plate," *Journal of Power Sources*, vol. 178, no. 1, pp. 363–367, 2008.

[223] J. E. Graves, D. Pletcher, R. L. Clarke, and F. C. Walsh, "The electrochemistry of Magnéli phase titanium oxide ceramic electrodes Part II: Ozone generation at Ebonex and Ebonex/lead dioxide anodes," *Journal of Applied Electrochemistry*, vol. 22, no. 3, pp. 200–203, 1992.

[224] D. Zhang, L. Duan, L. Guo, and W.-H. Tuan, "Corrosion behavior of TiN-coated stainless steel as bipolar plate for proton exchange membrane fuel cell," *International Journal of Hydrogen Energy*, vol. 35, no. 8, pp. 3721–3726, 2010.

[225] Y. Show, "Electrically conductive amorphous carbon coating on metal bipolar plates for PEFC," *Surface and Coatings Technology*, vol. 202, no. 47, pp. 1252–1255, 2007.

[226] W. Yoon, X. Huang, P. Fazzino, K. L. Reifsnider, and M. A. Akkaoui, "Evaluation of coated metallic bipolar plates for polymer electrolyte membrane fuel cells," *Journal of Power Sources*, vol. 179, no. 1, pp. 265–273, 2008.

[227] A. Pozio, F. Zaza, A. Masci, and R. F. Silva, "Bipolar plate materials for PEMFCs: A conductivity and stability study," *Journal of Power Sources*, vol. 179, no. 2, pp. 631–639, 2008.

[228] P. Yi, L. Peng, T. Zhou, J. Huang, and X. Lai, "Composition optimization of multilayered chromium-nitridecarbon film on 316L stainless steel as bipolar plates for proton exchange membrane fuel cells," *Journal of Power Sources*, vol. 236, no. 0, pp. 47–53, 2013.

[229] D. Camino, A. H. S. Jones, D. Mercs, and D. G. Teer, "High performance sputtered carbon coatings for wear resistant applications," *Vacuum*, vol. 52, no. 12, pp. 125–131, 1999.

[230] M. Li, S. Luo, C. Zeng, J. Shen, H. Lin, and C. Cao, "Corrosion behavior of TiN coated type 316 stainless steel in simulated PEMFC environments," *Corrosion Science*, vol. 46, no. 6, pp. 1369–1380, 2004.

[231] E. A. Cho, U. S. Jeon, S. A. Hong, I. H. Oh, and S. G. Kang, "Performance of a 1 kW-class PEMFC stack using TiN-coated 316 stainless steel bipolar plates," *Journal of Power Sources*, vol. 142, no. 12, pp. 177–183, 2005.

[232] Y. Wang and D. O. Northwood, "Effect of substrate material on the corrosion of TiN-coated stainless steels in simulated anode and cathode environments of proton exchange membrane fuel cells," *Journal of Power Sources*, vol. 191, no. 2, pp. 483–488, 2009.

[233] P. Yi, L. Peng, T. Zhou, H. Wu, and X. Lai, "CrNC multilayer film on 316L stainless steel as bipolar plates for proton exchange membrane fuel cells using closed field unbalanced magnetron sputter ion plating," *International Journal of Hydrogen Energy*, vol. 38, no. 3, pp. 1535–1543, 2013.

[234] K. Feng, Z. Li, H. Sun, L. Yu, X. Cai, Y. Wu, and P. K. Chu, "C/CrN multilayer coating for polymer electrolyte membrane fuel cell metallic bipolar plates," *Journal of Power Sources*, vol. 222, no. 0, pp. 351–358, 2013.

[235] K. Feng, Z. Li, F. Lu, J. Huang, X. Cai, and Y. Wu, "Corrosion resistance and electrical properties of carbon/chromium-titanium-nitride multilayer coatings on stainless steel," *Journal of Power Sources*, vol. 249, no. 0, pp. 299–305, 2014.

[236] D. G. Teer, "Magnetron sputter ion plating," 1997. International Patent EP0521045 B1.

[237] F. Meng, N. V. Aieta, S. F. Dec, J. L. Horan, D. Williamson, M. H. Frey, P. Pham, J. A. Turner, M. A. Yandrasits, S. J. Hamrock, and A. M. Herring, "Structural and transport effects of doping perfluorosulfonic acid polymers with the heteropoly acids, $H_3PW_{12}O_{40}$ or $H_4SiW_{12}O_{40}$," *Electrochimica Acta*, vol. 53, no. 3, pp. 1372–1378, 2007.

[238] Y. C. Kim, J. Y. Jeong, J. Y. Hwang, S. D. Kim, S. C. Yi, and W. J. Kim, "Incorporation of heteropoly acid, tungstophosphoric acid within MCM-41 via impregnation and direct synthesis methods for the fabrication of composite membrane of DMFC," *Journal of Membrane Science*, vol. 325, pp. 252–261, 2008.

[239] M. I. Ahmad, S. M. J. Zaidi, and S. Ahmed, "Proton conducting composites of heteropoly-acids loaded onto MCM-41," *Journal of Power Sources*, vol. 157, no. 1, pp. 35–44, 2006.

[240] S. Lu, D. Wang, S. P. Jiang, Y. Xiang, J. Lu, and J. Zeng, "HPW/MCM-41 Phosphotungstic Acid/Mesoporous Silica Composites as Novel Proton-Exchange Membranes for Elevated-Temperature Fuel Cells," *Advanced Materials*, vol. 22, no. 9, pp. 971–976, 2010.

[241] W. Feng, J. Wang, and Q. Wu, "Preparation and conductivity of PVA films composited with decatungstomolybdovanadogermanic heteropoly acid," *Materials Chemistry and Physics*, vol. 93, pp. 31–34, 2005.

[242] A. d. S. Gomes and J. C. Dutra Filho, "Hybrid membranes of PVA for direct ethanol fuel cells (DEFCs) applications," *International Journal of Hydrogen Energy*, vol. 37, no. 7, pp. 6246–6252, 2012.

[243] R. He, Q. Li, G. Xiao, and N. J. Bjerrum, "Proton conductivity of phosphoric acid doped polybenzimidazole and its composites with inorganic proton conductors," *Journal of Membrane Science*, vol. 226, pp. 169–184, 2003.

[244] S.-Y. Oh, T. Yoshida, G. Kawamura, H. Muto, M. Sakai, and A. Matsuda, "Inorganic-organic composite electrolytes consisting of polybenzimidazole and Cs-substituted heteropoly acids and their application for medium temperature fuel cells," *Journal of Materials Chemistry*, vol. 20, no. 30, pp. 6359–6366, 2010.

[245] M.-Q. Li, Z.-G. Shao, and K. Scott, "A high conductivity $Cs_{2.5}H_{0.5}PMo_{12}O_{40}$/polybenzimidazole (PBI)/H_3PO_4 composite membrane for proton-exchange membrane fuel cells operating at high temperature," *Journal of Power Sources*, vol. 183, no. 1, pp. 69–75, 2008.

[246] P. Staiti, "Proton conductive membranes based on silicotungstic acid/silica and polybenzimidazole," *Materials Letters*, vol. 47, no. 45, pp. 241–246, 2001.

[247] P. Staiti, M. Minutoli, and S. Hocevar, "Membranes based on phosphotungstic acid and polybenzimidazole for fuel cell application," *Journal of Power Sources*, vol. 90, no. 2, pp. 231–235, 2000.

[248] B. Xing and O. Savadogo, "The effect of acid doping on the conductivity of polybenzimidazole (PBI)," *Journal of New Materials for Electrochemical Systems*, vol. 2, pp. 95–101, 1999.

[249] D. R. Vernon, F. Meng, S. F. Dec, D. L. Williamson, J. A. Turner, and A. M. Herring, "Synthesis, characterization, and conductivity measurements of hybrid membranes containing a mono-lacunary heteropolyacid for PEM fuel cell applications," *Journal of Power Sources*, vol. 139, no. 12, pp. 141–151, 2005.

[250] A. Martinelli, A. Matic, P. Jacobsson, L. Brjesson, M. A. Navarra, D. Muna, S. Panero, and B. Scrosati, "A study on the state of PWA in PVDF-based proton conducting membranes by Raman spectroscopy," *Solid State Ionics*, vol. 178, no. 710, pp. 527–531, 2007.

[251] J. L. Malers, M.-A. Sweikart, J. L. Horan, J. A. Turner, and A. M. Herring, "Studies of heteropoly acid/polyvinylidenedifluoridehexafluoroproylene composite membranes and implication for the use of heteropoly acids as the proton conducting component in a fuel cell membrane," *Journal of Power Sources*, vol. 172, no. 1, pp. 83–88, 2007.

[252] W. Jang, S. Choi, S. Lee, Y. Shul, and H. Han, "Characterizations and stability of polyimidephosphotungstic acid composite electrolyte membranes for fuel cell," *Polymer Degradation and Stability*, vol. 92, no. 7, pp. 1289–1296, 2007.

[253] B. Smitha, S. Sridhar, and A. A. Khan, "Proton conducting composite membranes from polysulfone and heteropolyacid for fuel cell applications," *Journal of Polymer Science, Part B: Polymer Physics*, vol. 43, pp. 1538–1547, 2005.

[254] I.-Y. Jang, O.-H. Kweon, K.-E. Kim, G.-J. Hwang, S.-B. Moon, and A.-S. Kang, "Application of polysulfone (PSf) and polyether ether ketone (PEEK)tungstophosphoric acid (TPA) composite membranes for water electrolysis," *Journal of Membrane Science*, vol. 322, no. 1, pp. 154–161, 2008.

[255] M. L. Ponce, L. Prado, B. Ruffmann, K. Richau, R. Mohr, and S. P. Nunes, "Reduction of methanol permeability in polyetherketone-heteropoly acid membranes," *Journal of Membrane Science*, vol. 217, pp. 5–15, 2003.

[256] Y. S. Kim, F. Wang, M. Hickner, T. A. Zawodzinski, and J. E. McGrath, "Fabrication and characterization of heteropolyacid ($H_3PW_{12}O_{40}$)/directly polymerized sulfonated poly(arylene ether sulfone) copolymer composite membranes for higher temperature fuel cell applications," *Journal of Membrane Science*, vol. 212, no. 12, pp. 263–282, 2003.

[257] C. Zhao, H. Lin, Q. Zhang, and H. Na, "Layer-by-layer self-assembly of polyaniline on sulfonated poly(arylene ether ketone) membrane with high proton conductivity and low methanol crossover," *International Journal of Hydrogen Energy*, vol. 35, no. 19, pp. 10482–10488, 2010.

[258] Z. Cui, C. Liu, T. Lu, and W. Xing, "Polyelectrolyte complexes of chitosan and phosphotungstic acid as proton-conducting membranes for direct methanol fuel cells," *Journal of Power Sources*, vol. 167, no. 1, pp. 94–99, 2007.

[259] Z. Cui, W. Xing, C. Liu, J. Liao, and H. Zhang, "Chitosan/heteropolyacid composite membranes for direct methanol fuel cell," *Journal of Power Sources*, vol. 188, no. 1, pp. 24–29, 2009.

[260] C. Zhao, H. Lin, Z. Cui, X. Li, H. Na, and W. Xing, "Highly conductive, methanol resistant fuel cell membranes fabricated by layer-by-layer self-assembly of inorganic heteropolyacid," *Journal of Power Sources*, vol. 194, no. 1, pp. 168–174, 2009.

[261] M. I. Ahmad, S. M. J. Zaidi, S. U. Rahman, and S. Ahmed, "Synthesis and proton conductivity of heteropolyacids loaded Y-zeolite as solid proton conductors for fuel cell applications," *Microporous and Mesoporous Materials*, vol. 91, no. 13, pp. 296–304, 2006.

[262] T. Uma and M. Nogami, "Synthesis and characterization of phosphotungstic acid) glasses as electrolyte for low temperature H_2/O_2 fuel cell application," *Journal of Membrane Science*, vol. 280, no. 12, pp. 744–751, 2006.

[263] T. Uma and M. Nogami, "Properties of PWA/ZrO_2-doped phosphosilicate glass composite membranes for low-temperature H_2/O_2 fuel cell applications," *Journal of Membrane Science*, vol. 323, no. 1, pp. 11–16, 2008.

[264] T. Uma and M. Nogami, "Development of New Glass Composite Membranes and their Properties for Low Temperature H_2/O_2 Fuel Cells," *ChemPhysChem*, vol. 8, no. 15, pp. 2227–2234, 2007.

[265] U. Lavrenčič Štangar, N. Grošelj, B. Orel, A. Schmitz, and P. Colomban, "Proton-conducting solgel hybrids containing heteropoly acids," *Solid State Ionics*, vol. 145, no. 14, pp. 109–118, 2001.

[266] T. Inoue, T. Uma, and M. Nogami, "Performance of H_2/O_2 fuel cell using membrane electrolyte of phosphotungstic acid-modified 3-glycidoxypropyl-trimethoxysilanes," *Journal of Membrane Science*, vol. 323, no. 1, pp. 148–152, 2008.

[267] J.-D. Kim and I. Honma, "Synthesis and proton conducting properties of zirconia bridged hydrocarbon/phosphotungstic acid hybrid materials," *Electrochimica Acta*, vol. 49, no. 19, pp. 3179–3183, 2004.

[268] A. Anis, A. K. Banthia, and S. Bandyopadhyay, "Synthesis and characterization of polyvinyl alcohol copolymer/phosphomolybdic acid-based crosslinked composite polymer electrolyte membranes," *Journal of Power Sources*, vol. 179, no. 1, pp. 69–80, 2008.

[269] X. Zhao, H.-M. Xiong, W. Xu, and J.-S. Chen, "12-Tungstosilicic acid doped polyethylene oxide as a proton conducting polymer electrolyte," *Materials Chemistry and Physics*, vol. 80, no. 2, pp. 537–540, 2003.

[270] I. Honma, Y. Takeda, and J. M. Bae, "Protonic conducting properties of sol-gel derived organic/inorganic nanocomposite membranes doped with acidic functional molecules," *Solid State Ionics*, vol. 120, no. 14, pp. 255–264, 1999.

[271] I. Honma, H. Nakajima, O. Nishikawa, T. Sugimoto, and S. Nomura, "Amphiphilic organic/inorganic nanohybrid macromolecules for intermediate-temperature proton conducting electrolyte membranes," *Journal of The Electrochemical Society*, vol. 149, pp. A1389–A1392, 2002.

[272] H. Zhang, J. h. Pang, D. Wang, A. Li, X. Li, and Z. Jiang, "Sulfonated poly(arylene ether nitrile ketone) and its composite with phosphotungstic acid as materials for proton exchange membranes," *Journal of Membrane Science*, vol. 264, no. 12, pp. 56–64, 2005.

[273] M. Aparicio, Y. Castro, and A. Duran, "Synthesis and characterisation of proton conducting styrene-co-methacrylate-silica sol-gel membranes containing tungstophosphoric acid," *Solid State Ionics*, vol. 176, pp. 333–340, 2005.

[274] E. Fontananova, F. Trotta, J. C. Jansen, and E. Drioli, "Preparation and characterization of new non-fluorinated polymeric and composite membranes for PEMFCs," *Journal of Membrane Science*, vol. 348, no. 12, pp. 326–336, 2010.

[275] J. A. Asensio, S. Borrs, and P. Gmez-Romero, "Enhanced conductivity in polyanion-containing polybenzimidazoles. Improved materials for proton-exchange membranes and PEM fuel cells," *Electrochemistry Communications*, vol. 5, no. 11, pp. 967–972, 2003.

[276] M. A. Sweikart, A. M. Herring, J. A. Turner, D. L. Williamson, B. D. McCloskey, S. R. Boonrueng, and M. Sanchez, "12-Tungstophosphoric Acid Composites with Sulfonated or Unsulfonated Epoxies for High-Temperature PEMFCs," *J. Electrochem. Soc.*, vol. 152, pp. A98–A103, 2005.